Microelectronic devices, such as light-emitting diodes (LED), solar cells, computer chips, etc., are indispensable in modern society. Such products are becoming smaller, thinner, and more lightweight, while their functionality is being expanded in the form of, for example, flexibility and even stretchability. The down-sizing trend results in a large variety of materials (ceramics, polymers, metals) to be fabricated in a smaller volume.

Mechanical separation of the different material layers during fabrication and usage of microelectronic devices is considered to be one of the most critical failure mechanisms. Therefore, the mechanical adhesion properties of the interfaces must be measured within the actual device in order to predict and prevent failure of the material system.

This thesis describes the development of an experimental method to measure the relevant adhesion properties in microelectronic devices. A micro-mechanical testing device is developed to trigger separation of the materials in the microelectronic product. Microscopic techniques are used to capture the separation process in the form of images. By using computer simulations of the failure process, the experimentally acquired images are used directly to quantify the adhesion properties.

TU/e EINDHOVEN UNIVERSITY OF TECHNOLOGY

M2i materials innovation institute

PHILIPS

Identification of multi-layer interface systems

Andre Ruybalid

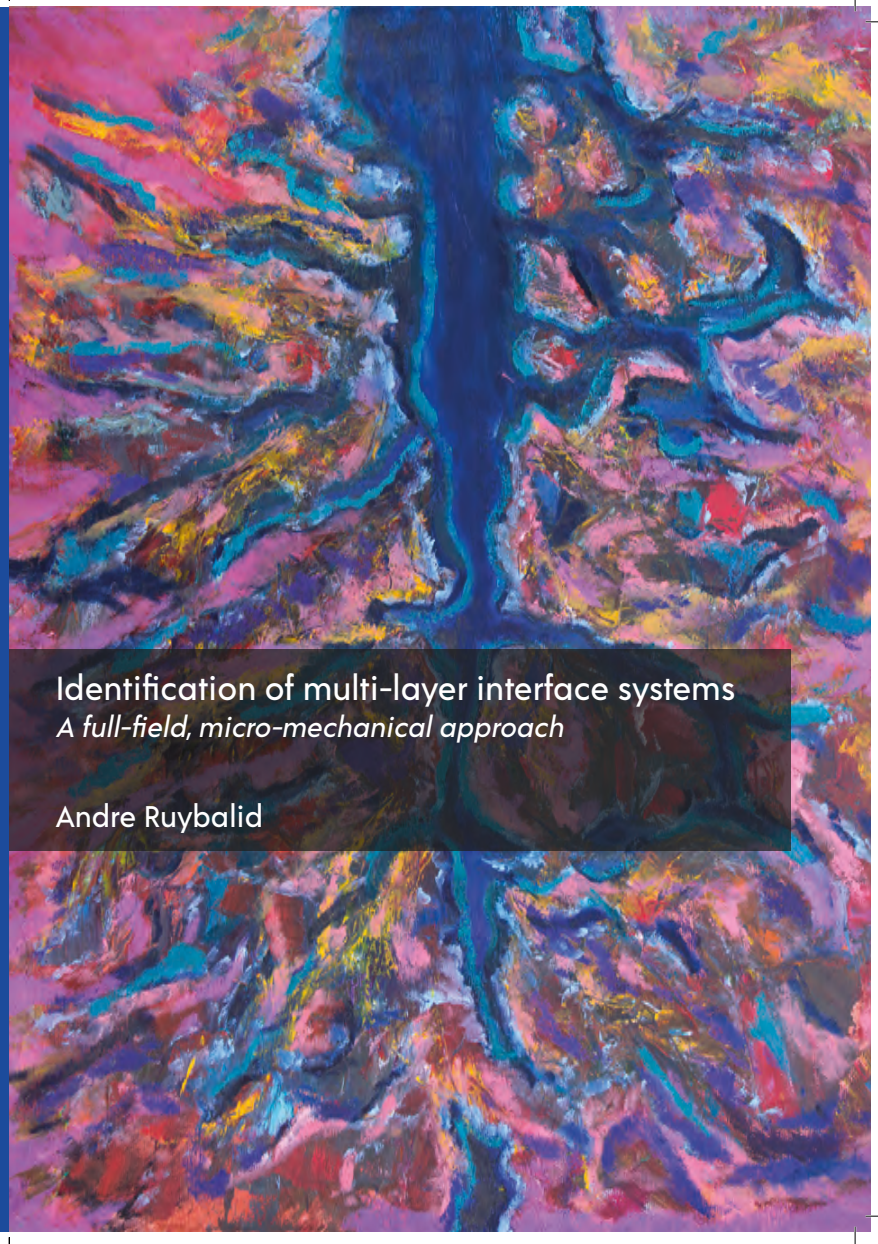

Identification of multi-layer interface systems

A full-field, micro-mechanical approach

Andre Ruybalid

IDENTIFICATION OF MULTI-LAYER INTERFACE SYSTEMS

A full-field, micro-mechanical approach

Andre Ruybalid

Identification of multi-layer interface systems: a full-field, micro-mechanical approach
by Andre Ruybalid

Technische Universiteit Eindhoven, 2019

A catalogue record is available from the Eindhoven University of Technology Library
ISBN: 978-90-386-4753-1

Printed by: Proefschriftmaken.nl

Summary translation by: Fleur van den Bergh

Cover artwork by: Jose I. Ruybalid
The cover shows an artistic reproduction - oil on canvas - of a scanning electron micrograph of an interfacial fracture between two 25 μm thick barrier-stack layers in an organic light-emitting diode (OLED):

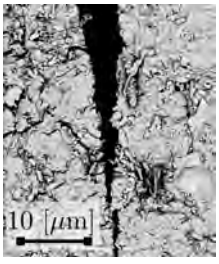

This research was carried out under the project number M62.2.12472 in the framework of the Research Program of the Materials innovation institute (M2i) in the Netherlands (www.m2i.nl).

Identification of multi-layer interface systems
A full-field, micro-mechanical approach

PROEFSCHRIFT

ter verkrijging van de graad van doctor aan de Technische Universiteit Eindhoven, op gezag van de rector magnificus prof.dr.ir. F.P.T. Baaijens, voor een commissie aangewezen door het College voor Promoties, in het openbaar te verdedigen op dinsdag 14 mei 2019 om 16.00 uur

door

Andre Paul Ruybalid

geboren te
Farmington, New Mexico, Verenigde Staten van Amerika

Dit proefschrift is goedgekeurd door de promotoren en de samenstelling van de promotiecommissie is als volgt:

voorzitter:	prof.dr. L.P.H. de Goey
1^{e} promotor:	prof.dr.ir. M.G.D. Geers
2^{e} promotor:	dr.ir. J.P.M. Hoefnagels
copromotor:	dr.ir. O. van der Sluis
leden:	dr. S. Bossuyt (Aalto University)
	prof.dr.ir. E.H. van Brummelen
	prof.dr. M. Grédiac (Université Clermont Auvergne)
	prof.dr. B. Wunderle (Technische Universität Chemnitz)

Het onderzoek of ontwerp dat in dit proefschrift wordt beschreven is uitgevoerd in overeenstemming met de TU/e Gedragscode Wetenschapsbeoefening.

"*Self-Knowledge is vital.*
All other forms of knowledge are of secondary importance, for a man's action, feeling, reasoning, and thinking are based on his idea of the Self."

Swami Nikhilananda

Contents

Summary

Identifying the adhesion properties of interfaces in multi-layer, microelectronic devices, e.g., light-emitting diodes, is challenging due to (1) the small-scale deformations requiring appropriate microscopic techniques, (2) the small, multi-directional forces within the different material layers and their interfaces, and (3) the complex loading conditions to which these systems are subjected during fabrication and operation. Because of the large variability in thermo-mechanical properties and fabrication-dependent loading conditions, identifying the relevant adhesion properties is most accurately done on actual microelectronic devices, rather than on dedicated specimens. This necessitates high resolution testing setups in combination with robust and accurate parameter identification tools, both of which are developed and realized in this dissertation. The strategy of investigation adopted here is to first generate virtual experimental data (by numerical methods) in order to develop and optimize the proposed methods, after which they are applied in real experiments.

The identification of mechanical model parameters can be achieved by utilizing full-field kinematic data in the form of micrographs, in combination with finite element simulations, as done in, e.g., Finite Element Model Updating (FEMU) and Integrated Digital Image Correlation (IDIC). In Chapter 2 of this work, the performances of these seemingly similar methods are compared in order to select the most appropriate of the two for mechanical characterization of microelectronic systems. Based on virtual experimentation, in which a variety of realistic error sources are investigated, it is concluded that IDIC is more reliable than FEMU, especially for cases involving the above-mentioned challenges that are typical for microelectronic devices.

The advancement of IDIC for identifying the mechanical parameters of a cohesive zone model is subsequently described in Chapter 3. The complications arising in microelectronic specimens are investigated by artificially imposing important error sources in a well-known test-case, involving a small-scale, virtual double cantilever beam specimen. Erroneous boundary conditions in the employed finite element model were identified as the most critical error source, mainly because the far-field boundary conditions applied in the experiment lie outside the microscopic field of view, and for which assumptions would be required. Instead of assuming the experimentally applied, far-field boundary conditions, a method is developed that enables adequate measurement and application of local boundary conditions in a finite element model that corresponds to the restricted, microscopic field of view. A mode-I interface delamination experiment on a real double cantilever beam specimen subsequently demonstrates that, when the elasticity parameters of the deforming cantilever beams are

known, no force data is required for accurately identifying cohesive zone parameters with the developed method.

Chapter 4 describes the extension of the method for identifying *mixed-mode* cohesive zone parameters from a single experiment on a small-scale, double cantilever beam specimen, i.e., without the need for performing multiple tests under different levels of mode-mixedness. Virtual experimentation provides a comprehensive understanding of the intricate role of the method's kinematic sensitivity towards the parameters of interest. By assessing kinematic sensitivity fields, the most appropriate experimental data and boundary conditions can be utilized in order to ensure high accuracy and robustness of the identification method. The method is validated by conducting real mixed-mode bending experiments on double cantilever specimens and identify the mixed-mode cohesive zone parameters.

To mechanically deform multi-layer material/interface systems, a micro-mechanical testing apparatus, composed of commercially available piezoelectric actuators, is devised and described in Chapter 5. The testing rig can impose a variety of loading paths in different directions (resulting in tension, compression, bending, shear, out-of-plane deformation, etc.) to approach the realistic loading conditions that microelectronic systems experience during fabrication and operation. A force measuring algorithm is developed and implemented in the actuators' controlling software, which solves the corrupting drift effects associated with piezoelectric actuators. High-resolution force measurements in all directions are thereby made possible, without the need for external force sensors. Furthermore, the compact design and the vacuum compatibility of the setup allow for in-situ testing of small-scale specimens in combination with a variety of microscopic techniques.

In Chapter 6, the realized micro-mechanical testing apparatus is used to deform a multi-layer barrier stack of a flexible, organic light-emitting diode (OLED), with the eventual goal of identifying the relevant adhesion properties by IDIC. Before parameter identification is realized, virtual experiments are conducted to simulate the loading conditions imposed by the mechanical test setup, in order to understand the required experimental conditions, as needed for reliable identification results. Subsequently, real experiments are used together with IDIC, extended with the developed methods for boundary condition application and kinematic sensitivity optimization, in order to identify the mechanical parameters of the considered material/interface system.

Samenvatting

Adhesie-eigenschappen van meerlaagse materialen en grensvlakken in micro-elektronische applicaties, zoals ledverlichting, zijn moeilijk te karakteriseren door (1) de kleinschaligheid van vervormingen waarvoor microscopische meetmethoden zijn vereist, (2) de kleine, multi-directionele krachten binnen de verschillende materiaallagen en hun grensvlakken, en (3) de complexe belastingscondities die optreden tijdens fabricage en gebruik van de applicatie. Vanwege de aanzienlijke verschillen in thermo-mechanische eigenschappen en fabricage-afhankelijke belastingscondities, worden relevante adhesie-eigenschappen nauwkeuriger gekarakteriseerd op werkelijke micro-elektronische producten dan op toegewijde proefstukken. Dergelijk onderzoek vereist daarom testopstellingen met hoge meetresolutie in combinatie met robuuste en accurate methoden om parameters te identificeren; beide zijn ontwikkeld en gerealiseerd in dit proefschrift. In de gehanteerde onderzoeksstrategie worden eerst virtuele experimenten uitgevoerd om de methodieken te ontwikkelen en te optimaliseren, om deze vervolgens toe te passen op echte experimenten.

Mechanische modelparameters kunnen het beste worden geïdentificeerd door *full-field* kinematische gegevens te gebruiken in de vorm van microscoopbeelden en deze te combineren met eindige elementensimulaties, zoals gedaan wordt in *Finite Element Model Updating* (FEMU) en *Integrated Digital Image Correlation* (IDIC). In Hoofdstuk 2 van dit proefschrift worden de prestaties van deze ogenschijnlijk equivalente methoden vergeleken om de meest geschikte te selecteren voor mechanische karakterisering van micro-elektronische systemen. Op basis van virtuele experimenten, waarin verschillende realistische foutbronnen worden nagebootst, wordt geconcludeerd dat IDIC betrouwbaarder is dan FEMU; met name wanneer de eerder genoemde uitdagingen van belang zijn, zoals het geval is voor micro-elektronische applicaties.

Verdere ontwikkeling van IDIC om mechanische parameters van een *cohesive zone*-model te karakteriseren, staat daaropvolgend beschreven in Hoofdstuk 3. Complicaties die bij micro-elektronische proefstukken optreden, worden onderzocht door op kunstmatige wijze belangrijke fouten op te leggen in een vertrouwde testcase met een kleinschalige, virtuele dubbele cantileverbalk (DCB). Er werd vastgesteld dat verkeerde randvoorwaarden in het gebruikte eindige elementenmodel de meest kritische foutbronnen zijn; voornamelijk omdat de randvoorwaarden buiten het microscoopbeeld vallen en er daarom aannames voor vereist zouden zijn. In plaats van deze externe randvoorwaarden aan te nemen, is er een methode ontwikkeld waarbij lokale randvoorwaarden gemeten en toegepast worden in een eindige elementenmodel dat overeenkomt met het microscopische gezichtsveld. Een Mode-I

delaminatieproef op een echte dubbele cantileverbalk toont vervolgens aan dat, wanneer de elasticiteitsparameters van de vervormende balken bekend zijn, er geen krachtgegevens zijn vereist om *cohesive zone*-parameters met de ontwikkelde methode nauwkeurig te kunnen bepalen.

Hoofdstuk 4 beschrijft de uitbreiding van de identificatiemethode voor *mixed-mode cohesive zone*-parameters uit een enkel experiment op een kleinschalige, dubbele cantileverbalk, en zonder de noodzaak om meerdere proeven uit te voeren met verschillende moduscombinaties. Virtuele experimenten bieden inzicht in de complexe rol van de kinematische gevoeligheid met betrekking tot de relevante parameters. Door gevoeligheidsvelden te analyseren, kunnen de meest geschikte experimentele gegevens en randvoorwaarden worden gebruikt om een hoge nauwkeurigheid en robuustheid van de identificatiemethode te realiseren. De methode wordt gevalideerd door echte *mixed-mode* buigproeven op dubbele cantileverbalken uit te voeren en vervolgens de betreffende *mixed-mode cohesive zone*-parameters te identificeren.

Om meerlaagse materiaalsystemen mechanisch te vervormen, is er een micro-mechanische proefopstelling ontworpen die is opgebouwd uit commerciële, piëzo-elektrische actuatoren (beschreven in Hoofdstuk 5). De proefopstelling kan verschillende belastingspaden in verschillende richtingen opleggen (resulterend in rek, afschuiving, compressie, buiging en deformatie uit het vlak etc.) om de belastingscondities te benaderen die echte micro-elektronische systemen ondervinden tijdens fabricage en gebruik. Er is een krachtmeetalgoritme ontwikkeld en geïmplementeerd in de besturingssoftware van de actuatoren dat de corrumperende drifteffecten oplost die onlosmakelijk aan piëzo-elektrische actuatoren zijn verbonden. Krachtmetingen met hoge resolutie in alle richtingen worden daardoor gerealiseerd, zonder dat er externe krachtsensoren nodig zijn. Bovendien maken het compacte ontwerp en de vacuümcompatibiliteit van de opstelling het in-situ testen - in combinatie met verschillende vormen van microscopie - van kleinschalige proefstukken mogelijk.

In Hoofdstuk 6 wordt de gerealiseerde micro-mechanische proefopstelling gebruikt om een meerlaagse beschermwand in een flexibele, organische led (*Organic Light-Emitting Diode* - OLED) te belasten en de relevante adhesie-eigenschappen met IDIC te karakteriseren. Voordat echte parameters kunnen worden geïdentificeerd, worden virtuele experimenten uitgevoerd. Hiermee kunnen de belastingscondities van de mechanische proefopstelling worden nagebootst om de vereiste experimentele omstandigheden te begrijpen, zoals nodig voor betrouwbare identificatie. Vervolgens worden er echte experimenten uitgevoerd. De ontwikkelde methoden voor randvoorwaarde-oplegging en gevoeligheidsoptimalisering worden toegepast om de mechanische parameters van het overwogen materiaalsysteem te karakteriseren met IDIC.

CHAPTER 1

Introduction

The trend of downsizing the substructures of devices, as seen in, e.g., the microelectronics industry, facilitates the sustainability of material resources, and the improvement of product capabilities [1, 2]. Central processing units become more powerful, solar cells become more efficient, and light-emitting diodes become more luminous, while also becoming cheaper and more compact, by which their accessibility increases. Novel production techniques, such as additive manufacturing (e.g., 3D printing) and roll-to-roll processing [3–5], have contributed to the emergence of new applications, including microelectronics in flexible and stretchable forms. For example, flexible displays are rapidly becoming more popular, as shown in Figure 1.1.

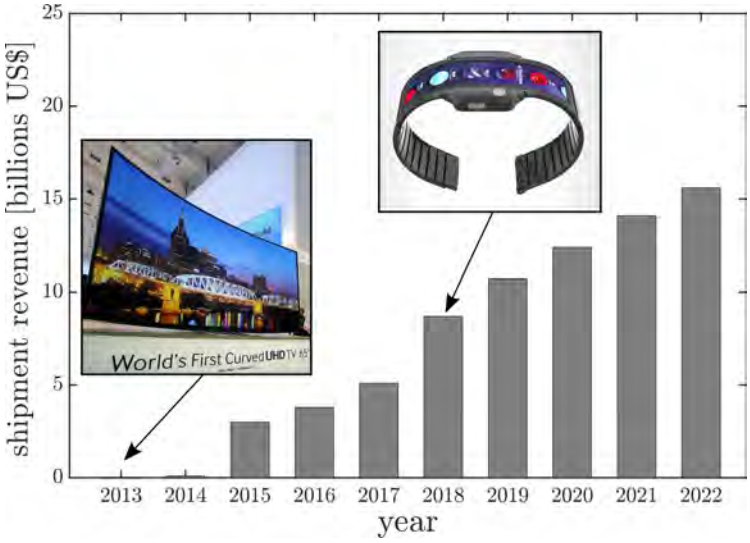

Figure 1.1. Forecast of the global, annual, shipment revenue of the flexible display market, and two examples of products: a curved television screen by Samsung and a bendable smartwatch by Nubia, that have marketed, showing the trend in the development of bendable/flexible electronics [6, 7].

To further miniaturize microelectronic systems, an increasing amount of dissimilar material must be fabricated into a dense stack, comprising an intricate three-dimensional design. The consequential increase in number of material interfaces per unit volume, combined with the mismatch in thermo-mechanical properties of the different material layers, results in interfacial delamination as one of the most critical failure mechanisms in microelectronic devices [8–10]. Accurate characterization of adhesion properties is, therefore, crucial for understanding and predicting the mechanical behavior of interfaces. This will assist the future development of highly reliable microelectronics, on which this research focuses. Yet, understanding and characterizing interfaces is also relevant to other types of material structures, e.g., carbon fiber reinforced polymers [11, 12] and additive manufactured components [13], comprising many interfaces that are prone to failure. Examples of interfacial failure in a variety of applications are shown in Figure 1.2.

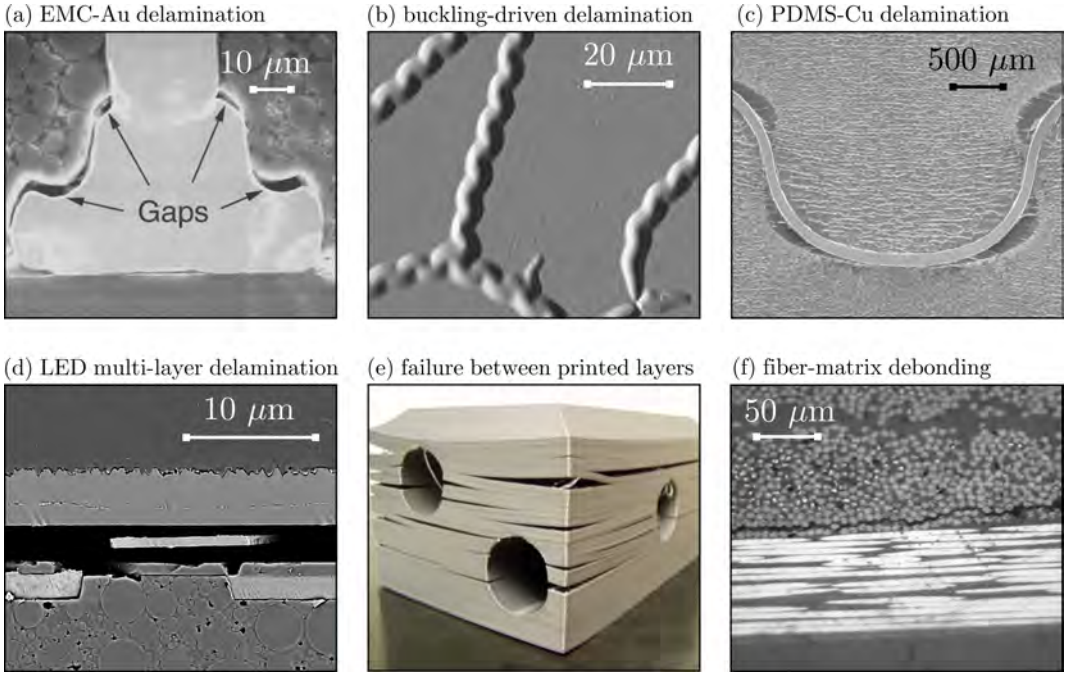

Figure 1.2. Examples of interfacial failure between (a)-(c) a variety of materials used in microelectronics (EMC: epoxy molding compound, PDMS: polydimethylsiloxane) [14], (d) multi-layer failure in a light-emitting diode, (e) failure between layers in an additive manufactured part [13], and (f) debonding between fiber and matrix in a carbon fiber reinforced composite [15].

Characterizing mechanical behavior is traditionally done using experiments that are carefully tailored to parallel modeling capabilities. For example, a uniaxial tensile test on a dog-bone shaped specimen targets uniformity in the region of interest. The stresses and strains in the gauge section of the specimen can easily be deduced from globally measured forces and displacements, i.e., the boundary conditions are well-known, yielding a closed-form solution to the problem. In other words, stringent demands on the experiment permit

to understand the problem with simple modeling techniques. However, it also limits the possibility of testing a material under more realistic conditions, where the material properties may be processing-dependent. In case of characterizing adhesion properties of interfaces, a large variety of experimental methods and setups exist [16]. They are generally restricted by the use of relatively simple, dedicated specimen geometries and straight-forward loading conditions in order to be able to model and understand the interface mechanics [17–26]. However, adhesion properties extracted from such experiments are found to be highly dependent upon the specific load-case and specimen geometry [14, 22, 27–31]. Furthermore, for microelectronic material systems, such strict experimental requirements put high demands on the fabrication processes of dedicated, small-scale specimens, and potentially introduce processing-induced size effects that affect the mechanical behavior [32, 33]. For these reasons, characterizing relevant adhesion properties calls for experiments that resemble the processing conditions and critical load-cases that actually occur during device operation or manufacturing procedures, which necessitates specimens that match the actual device in which the interfaces appear. This brings the additional advantage of circumventing costly and time-consuming fabrication of dedicated specimens.

However, respecting the real processing conditions and mimicking the actual loading of realistic samples require test configurations that trigger more intricate mechanics. In turn, this calls for more sophisticated models to achieve a comprehensive understanding of the mechanics. The increase in digital computing power since the 1980s has contributed to meet these requirements in two ways. Firstly, it has aided the expansion of modeling capabilities by, e.g., (further) development of the finite element (FE) method. Secondly, it gave rise to methods that can capture and process images (e.g., micrographs) of a mechanical deformation process to compute kinematic quantities (i.e., displacements or strains) in the entire, imaged field of view. Examples of such *full-field* measurement methods are: the grid method [34–36], digital holography [37, 38], speckle interferometry [39–41], and digital image correlation (DIC) [42–48]. The latter method does not require specialized equipment, is easily implemented, and can be applied to a large variety of problems at different length scales, because it can process images from various sources, e.g., digital camera sensors (also used together with optical microscopy), scanning electron microscopy, computed tomography, optical profilometry, etc. This makes it highly versatile and the most widely adopted method, which is therefore also employed in this work. The development of full-field measurement methods has, in turn, led to the emergence of identification techniques that utilize full-field kinematic data to identify constitutive model parameters. Various materials and mechanics problems have been analyzed by a variety of full-field identification techniques, such as the virtual fields method [49–51], the equilibrium gap method [52–54], the reciprocity gap method [55, 56], finite element model updating (FEMU) [57–63], and, integrated digital image correlation (IDIC) [64–66], of which overviews can be found in the literature [67–70].

A number of research papers have addressed the full-field identification of adhesion properties [71–77], although the type of configuration and the length scales at which microelectronic devices operate remained unexplored to a large extent. Major challenges therein involve: (1) the mixed-mode dependence of adhesion properties [28, 29], (2) the small specimen dimensions, causing practical difficulties regarding sample preparation, handling, and gripping, and (3) the small displacements and forces associated with deformation, requiring microscopic techniques and high resolution force sensors.

The goal of this research is, therefore, to accomplish major steps in realizing a method for on-device testing and identification of representative adhesion properties of interfaces in small-scale, multi-layer, microelectronic specimens. To this end, a setup for conducting in-situ, micro-mechanical experiments is devised, which applies multi-axial deformation and measures the associated forces in all three directions. An experimental-numerical framework, employing full-field identification, is established for characterizing interface mechanics. The following research questions (RQ) are addressed in this dissertation:

RQ.1 What is experimentally and methodologically required to realize on-device testing and identification of adhesion properties in small-scale, microelectronic components?

RQ.2 What are the main challenges for characterizing adhesion properties of small-scale, multi-layer material systems, as used in microelectronic applications?

RQ.3 What are the most critical error sources that affect the accuracy of inverse, full-field, mechanical parameter identification?

RQ.4 Which parameter identification method is preferred for identifying the mechanical adhesion properties of material interfaces in microelectronic applications?

The strategy to answering the above-stated research questions is outlined below, with references to the corresponding chapters in the thesis:

- Given the variety of available identification methods, in Chapter 2, a comparative performance assessment study of two seemingly similar methods is conducted. Herein, several realistic error sources are investigated by virtual experimentation in order to answer RQ.3. The investigation provides a clear view on the appropriateness of both methods for identifying adhesion properties of interfaces in microelectronic devices, yielding the answer to RQ.4

- Pure mode-I, and mixed-mode bending experiments on a bilayer material system are discussed in Chapters 3 and 4, respectively, in order to develop the identification framework for characterizing adhesion properties of small-scale specimens, relevant for microelectronic applications. Virtual experimentation is once again used to investigate the sensitivity of the identification method, in light of several error sources, in order to answer RQ.2, while broadening the answer to RQ.3. The insights gained from the virtual experiments are instrumental for optimizing the identification procedure. The method is validated in Chapter 3, using a well-understood test-case, i.e., a pure mode-I double cantilever beam test on a small-scale bilayer material system. In Chapter 4, the method is extended to identify the adhesion properties from mixed-mode bending experiments on a similar material system. The experiments in Chapters 3 and 4 are used to demonstrate and evaluate the identification method's potential and provide insight into the question raised in RQ.1.

- To work towards on-device testing for the identification of relevant adhesion properties of microelectronic material systems, an experimental setup is required that can impose realistic loading conditions. To this end, an in-situ, micro-mechanical setup with tri-axial force sensing and positioning is devised in Chapter 5, which contributes to answering RQ.1.

- The realized micro-mechanical setup of Chapter 5 and the identification method developed in Chapters 3 and 4 are employed in Chapter 6 to characterize adhesion properties of samples from a flexible, organic light-emitting diode (OLED) display, to elaborate on the answers to RQ.1 and 2.

CHAPTER 2

Full-field identification: a comparative study

Abstract

Full-field identification methods are increasingly used to adequately identify constitutive parameters to describe the mechanical behavior of materials. This chapter investigates the more recently introduced, *one-step* method of integrated digital image correlation (IDIC) with respect to the most commonly used, *two-step* method of finite element model updating (FEMU), which uses a subset-based digital image correlation algorithm.

To make the comparison as objective as possible, both methods are implemented in the most equivalent manner and use the same FE-model. Various virtual test-cases are studied to assess the performance of both methods when subjected to different error sources: (1) systematic errors, (2) poor initial guesses for the constitutive parameters, (3) image noise, (4) constitutive model errors, and (5) experimental errors.

Results show that, despite the mathematical similarity of both methods, IDIC produces less erroneous and more reliable results than FEMU, particularly for more challenging test-cases exhibiting small displacements, complex kinematics, misalignment of the specimen, and image noise.

Keywords: full-field identification; Integrated Digital Image Correlation; Finite Element Model Updating; inverse methods

Reproduced from:
A.P. Ruybalid, J.P.M. Hoefnagels, O. van der Sluis, M.G.D. Geers
Comparison of the identification performance of conventional FEM updating and integrated DIC
International Journal for Numerical Methods in Engineering, 2016, 106(4):298–320
doi: 10.1002/nme.5127

2.1 Introduction

Proper identification of constitutive model parameters is essential for quantifying material behavior. This enables trustworthy predictions of the mechanical response in arbitrary load cases, as required for optimization of material design and processing techniques. Traditionally, mechanical tests are conceived such that the kinematics in a tested material is adequately understood. The associated assumptions, e.g., a uniform strain in a uniaxial dog-bone shaped tensile specimen, allow material testing on the basis of limited measurement data (such as an LVDT displacement). However, in such tests, the restricted kinematic information does not represent the full mechanical behavior, which may result in inaccurate parameter identification. Moreover, difficulties arise from the fact that heterogeneous and anisotropic materials traditionally require various tests to identify the multiple constitutive parameters used in the corresponding material models.

Increased computing power now allows for large data sets to be processed efficiently, enabling more sophisticated identification techniques that take *full-field* kinematic information into account. Such field-data is typically acquired in a mechanical experiment through digital images of the entire deformation process during testing. The full displacement fields are then computed by digital image correlation (DIC) techniques, which obviously depend on the constitutive behavior of the deforming material. This makes it possible to identify the constitutive parameters through a single experiment, while relaxing design requirements on the specimen and loading conditions. The latter allows experiments to resemble practical, industrial applications more closely, which is especially of interest when the used materials are highly anisotropic and heterogeneous, e.g., in the microelectronic industry. Additional advantages of full-field measurements include: (1) the possibility to identify material parameters using small-scale specimens [78], where traditional techniques for measuring deformation do not suffice, and (2) enhanced accuracy of identified material parameters, due to the use of rich, full-field measurement data.

Various (inverse) identification approaches make use of full-field data, such as the virtual fields method [49–51], the equilibrium gap method [52–54], the reciprocity gap method [55, 56], and the constitutive gap method [79–81], of which overviews are given in the literature [67–70, 82, 83]. Undoubtedly, the most intuitive and widely used method is that of finite element model updating (FEMU) [57, 58, 60, 63]. In this technique, constitutive model parameters are optimized by comparing displacement fields from finite element (FE) simulation with displacement fields acquired through standard DIC procedures on experimental images.

More recently, a novel method has been introduced [66, 84–86], which intimately integrates mechanical descriptions of a material with full-field measurements to identify model parameters. The method is termed *integrated digital image correlation (IDIC)*, and eliminates the need for calculating displacements from (intensity) images prior to parameter identification. Instead, digital images are directly correlated by optimizing the mechanical parameters that govern the deformation of the imaged material. Thereby, the raw experimental data is used, i.e., intensity images, avoiding any processed derivatives of such data (e.g., displacement fields). Hence, the mechanical model steers the correlation procedure, which can be incorporated through, e.g., closed-form solutions [66, 73, 87–90] or FE-simulations [65, 84], as also done in this research. In IDIC, the correlation procedure

and identification procedure are integrated into a *one-step* approach, making it distinct from other methods, which are two-step approaches whereby post-processing of experimental data precedes the identification procedure.

This chapter aims to assess the performance of IDIC in an objective manner, considering the most important error sources: (1) systematic errors, (2) poor initial guesses for the parameters of interest, (3) image noise, (4) model errors, and (5) experimental errors. Therefore, a strategy is adopted in which the one-step method of IDIC is compared to a reference two-step method whose algorithmic procedure is most similar to IDIC: the commonly used FEMU method, implemented in a standard manner [62, 91–94], i.e., making use of subset-based DIC[1]. To make a fair comparison between IDIC and FEMU, the implementations of both methods are done equivalently, and are applied to the same experimental data. Furthermore, prior knowledge on the mechanical behavior is incorporated in both methods through the same constitutive model and the same FE-discretization. The investigation therefore focuses on the effect of a one-step approach versus a two-step approach, keeping all other implementation choices equal for both methods. Various mechanical test-cases are analyzed by FEMU and IDIC to identify the governing constitutive parameters. To exclude the effects of error sources that cannot be quantified, all tests are performed by *virtual* experimentation.

The structure of this chapter is as follows: after discussing the basics behind DIC and both identification methods, the virtual test-cases are introduced, and the results of the tests are presented, enabling the comparison between IDIC and FEMU. Both methods are assessed in terms of the accuracy of the identified model parameters upon varying different error sources. Even though the mathematical structures of IDIC and FEMU are highly similar, clear differences in performance are observed between the two methods, which become especially pronounced for more complex cases.

2.2 Digital image correlation

Digital image correlation (DIC) is an established technique for deformation measurements. Attention is therefore restricted to the general principles of DIC, which are needed further on. Section 2.3 continues with the extension of DIC towards both identification methods.

The objective of DIC is to determine full displacement fields on a deforming material sample. This is realized by correlating digital intensity images, which are experimentally acquired subsequently in time, as the material deforms. Typically, a random pattern is applied to the material in order to improve the uniqueness and robustness of the correlation approach. Implementations are based on cross-correlating pixel intensities within domains of images belonging to the reference material and the deformed material to extract full-field displacements [44, 46]. Instead of using cross-correlation, another common approach is solving for the unknown displacements by minimizing, in a least squares sense, the differences between the intensity in domains belonging to images of the reference and deformed material states [48]. The performance of these different DIC implementations has been assessed by Lava et al. [96]. In this research, the least squares approach is adopted, which is based on

[1] In the writing of this manuscript it came to the authors' attention that a very recent study also investigated IDIC and FEMU [95], however utilizing a less standard implementation of FEMU that uses a *global*, rather than a subset-based, DIC algorithm, and focusing on the influence of image noise as an error source.

the conservation of brightness. This principle is mathematically expressed as follows:

$$f(\vec{x}) \approx g\left(\vec{\Phi}(\vec{x})\right) = g \circ \vec{\Phi}(\vec{x}), \tag{2.1}$$

$$\vec{\Phi}(\vec{x}) = \vec{x} + \vec{U}(\vec{x}), \tag{2.2}$$

where f and g are the scalar intensity fields of, e.g., light sensed by a camera sensor, and $\vec{\Phi}$ represents the vector function that maps the pixel coordinates $\vec{x}$ of image f, corresponding to the reference material state, to the pixel coordinates of image g, corresponding to the deformed state. The DIC problem is schematically illustrated in Figure 2.1.

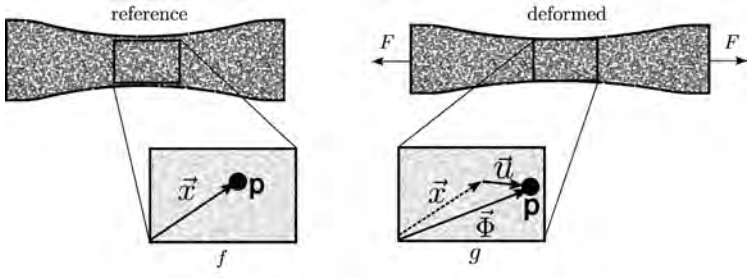

Figure 2.1. Schematic illustration of the DIC problem, where images f and g, respectively corresponding to reference and deformed (by force F) material states, are correlated to extract the displacement vectors of all other material points (e.g., point P), yielding the full displacement field $\vec{U}(\vec{x})$.

The displacement vector field $\vec{U}(\vec{x})$ is to be determined, with sub-pixel accuracy, by minimizing the *residual* Ψ between images f and g within the spatial domain Ω:

$$\Psi = \int_{\Omega} \frac{1}{2}\left(f(\vec{x}) - g \circ \vec{\Phi}(\vec{x})\right)^2 \mathrm{d}\vec{x}. \tag{2.3}$$

To solve this nonlinear least squares problem, an iterative solution scheme, such as the Newton-Raphson method [97, 98], is required. Newton-Raphson based algorithms have been reported as more accurate in comparison with other algorithms [99]. To solve the problem of [Eq. 2.3], images f and g must be evaluated at inter-pixel locations. Hence, an image-interpolation step is required, which introduces systematic errors to the DIC problem. It has been concluded in the literature that high-order interpolation polynomials result in the lowest systematic errors for images comprising speckle-patterns [96, 100, 101]. Additionally, the problem is ill-posed, and requires regularization in order to reduce the number of degrees of freedom [102]. Therefore, the true displacement field $\vec{U}(\vec{x})$, and consequently, the mapping function $\vec{\Phi}(\vec{x})$, are to be approximated by fields consisting of a reduced set of degrees of freedom λ_i:

$$\vec{U}(\vec{x}) \approx \vec{u}(\vec{x}, \lambda_i), \tag{2.4}$$

$$\vec{\Phi}(\vec{x}) \approx \vec{\phi}(\vec{x}, \lambda_i), \tag{2.5}$$

with λ_i being an array, with the values of the degrees of freedom; $\lambda_i = [\lambda_1, \lambda_2, \ldots, \lambda_n]^T$, where n is the total number of degrees of freedom. The minimization problem is now written as:

$$\frac{\partial \Psi}{\partial \lambda_i} = 0, \tag{2.6}$$

which, when solved by the Gauss-Newton method, yields the following system of equations:

$$M_{ij}\delta\lambda_j = b_i, \tag{2.7}$$

where $\delta\lambda_i$ contains the iterative updates of the degrees of freedom. The correlation matrix M_{ij} and b_i are written as:

$$\forall (i) \in [1, n], \quad b_i = \int_\Omega \vec{\varphi}_i(\vec{x}, \lambda_i) \cdot \vec{G}(\vec{x}, \lambda_i) \left(f(\vec{x}) - g \circ \vec{\phi}(\vec{x}, \lambda_i) \right) \mathrm{d}\vec{x}, \tag{2.8}$$

$$\forall (i, j) \in [1, n]^2, \quad M_{ij} = \int_\Omega \vec{\varphi}_i(\vec{x}, \lambda_i) \cdot \vec{G}(\vec{x}, \lambda_i) \vec{G}(\vec{x}, \lambda_i) \cdot \vec{\varphi}_j(\vec{x}, \lambda_j) \mathrm{d}\vec{x}, \tag{2.9}$$

$$\vec{\varphi}_i = \frac{\partial \vec{u}}{\partial \lambda_i}. \tag{2.10}$$

In this formulation, the '$\cdot$' notation represents an inner product. $\vec{G}$ is the gradient of the image with respect to the spatial coordinates. Different choices for the image gradient can be made, which have been explored by Neggers et al. [103]. Usually, the gradient of the reference image f is preferred for convenience. The vector columns $\vec{\varphi}_i$ are referred to as *shape functions*, controlling how the degrees of freedom approximate the displacement field in order to regularize the ill-posed problem.

Different regularization methods exist, whereby the most commonly used method is to subdivide the images into independent subsets, which encompass a number of pixels. The rigid translations of each subset's center is subsequently determined by minimizing the objective function of [Eq. 2.3] in the subset domains Ω. For this type of regularization, the DIC method is sometimes referred to as *local*, since the correlation problem is solved locally, i.e., separately in each subset. The full deformation field of the imaged material is composed by the individual subset-center displacements. Different types of shape functions $\vec{\varphi}_i$ within the subset domains are commonly implemented, allowing more complex deformation of the subsets, rather than a simple rigid translation [44, 96, 101]. The allowed subset morphology is referred to as rigid, affine, irregular, or quadratic (Figure 2.2). Allowing more complex subset morphology may reduce the residual, which drives the correlation procedure further, through which center displacements of subsets are determined more accurately. The size of the used subsets determines the resolution of the calculated displacement field. Smaller subsets may resolve more complex, spatially nonuniform displacement fields, but also entail more degrees of freedom, which results in less regularization of the ill-posed problem, reducing the robustness with respect to image noise [42, 101, 104].

Instead of dividing images into subsets, the domain Ω, in which the correlation problem is solved, may also be chosen to be as large as the entire image. In this case, the shape functions $\vec{\varphi}_i$, controlling the morphology of the large subset, have a global support (the entire

image), and therefore must be more complex than those used for small subsets. With this type of regularization, the DIC method is sometimes referred to as *global*. Shape functions with such global support exist as, e.g., polynomials [105] or B-splines [43]. Another common, global regularization method uses continuous meshes (with nodal supports), equivalent to FE-elements with Lagrangian shape functions [42, 47] or NURBS [106, 107]. Just as in the local regularization approach, the same trade-off exists between an increase of the kinematic complexity and a decrease of the noise robustness, when the global regularization method is used.

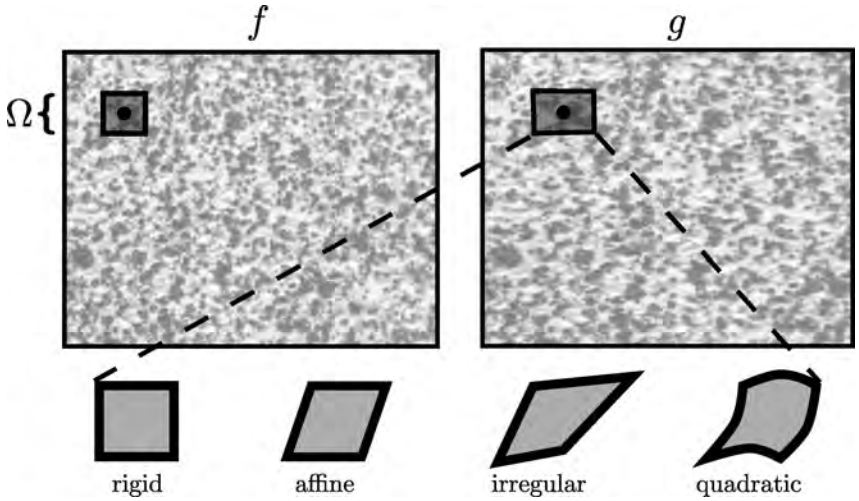

Figure 2.2. The principle of subset-based regularization in DIC, where the ill-posed minimization problem of [Eq. 2.3] is solved within subset domain Ω, yielding the subset-center displacement. The accuracy of the correlation method may be improved by allowing subsets to deform.

The use of global regularization in DIC is less standard than the use of local regularization. Differences between these two approaches have been investigated by Hild et al. [45], who concluded the global method to be more noise-robust due to the imposed continuity assumption. However, whether a global or local approach should be preferred is dependent on each specific test-case, and a general preference for a particular approach is difficult to justify.

It should be emphasized that the size of subsets, and the type of shape functions $\vec{\varphi}_i$ utilized in the regularization method, whether it be a local or global implementation, are among the most important choices in DIC, and directly affect the accuracy of the calculated displacement field. As will become clear, these choices are of importance for FEMU, yet not an issue for IDIC.

2.3 Full-field identification methods

The formulations of the two identification techniques used in this study are now briefly explained, starting with the FEMU method, followed by the IDIC approach. Both methods

are based on the previously discussed DIC methodology, and intrinsically make use of it. Since the objective of this investigation is to make a fair comparison between both identification methods, they must be implemented in a comparable manner. Several (modified) implementations of the FEMU [59, 61, 84, 95] and IDIC [73] approaches can be found in the corresponding literature, but will not be scrutinized further here.

2.3.1 Finite element model updating

In FEMU, the displacement measurement (through DIC) and the identification of constitutive parameters are performed sequentially. Measurement data, in the form of intensity images of a tested material, is analyzed by (local) DIC to calculate the displacement fields $\vec{m}$ of the deformed material. Simulation of a model of the experiment, making use of initial guesses for the constitutive parameters, yields simulated displacement fields $\vec{h}$. For a perfect model with accurate model parameters, the simulated field equals the measured field, assuming no errors are made in the determination of either of the fields. Hence, by minimizing a squared residual of the measured and simulated displacements, the model parameters used for simulation are updated in an iterative fashion. The objective function to be minimized is mathematically expressed as follows:

$$\vec{J} = \int_\tau \int_\Omega \frac{1}{2} \left(\vec{m}(\vec{x},t) - \vec{h}(\vec{x},t,\theta_i) \right)^2 \mathrm{d}\vec{x}\mathrm{d}t. \tag{2.11}$$

The data from all time instances is not sequentially processed, but considered in a single objective function. Displacement fields of different time instances are stacked to form displacement *blocks* $\vec{m}(\vec{x},t)$ and $\vec{h}(\vec{x},t,\theta_i)$, which are subtracted to produce the block residual $\vec{J}$. The residual is minimized at once for all displacements in space-time, which is defined by the spatial domain Ω and the temporal domain τ.

The simulated displacement fields also depend on array θ_i, which contains the unknown constitutive parameters. The nonlinear least squares problem is solved by the Gauss-Newton method:

$$\frac{\partial \vec{J}}{\partial \theta_i} = 0, \tag{2.12}$$

which yields the following system of equations:

$$L_{ij}\delta\theta_j = \kappa_i, \tag{2.13}$$

where $\delta\theta_i$ contains the updates of the parameters to be identified, and L_{ij} and κ_i are expressed as follows:

$$\forall (i) \in [1,p], \quad \kappa_i = \int_\tau \int_\Omega \vec{H}_i(\vec{x},t,\theta_i) \cdot \left(\vec{m}(\vec{x},t) - \vec{h}(\vec{x},t,\theta_i) \right) \mathrm{d}\vec{x}\mathrm{d}t, \tag{2.14}$$

$$\forall (i,j) \in [1,p]^2, \quad L_{ij} = \int_\tau \int_\Omega \vec{H}_i(\vec{x},t,\theta_i) \cdot \vec{H}_j(\vec{x},t,\theta_j) \mathrm{d}\vec{x}\mathrm{d}t. \tag{2.15}$$

The number of degrees of freedom p is equal to the number of sought parameters, since the degrees of freedom are, in fact, the constitutive parameters. Furthermore, $\vec{H}_i$ are referred

to as the *sensitivity maps*, since they govern the dependence of the simulated displacements on the parameters:

$$\vec{H}_i(\vec{x},t,\theta_i) = \frac{\partial \vec{h}(\vec{x},t,\theta_i)}{\partial \theta_i}. \tag{2.16}$$

In order to calculate the sensitivity maps $\vec{H}_i(\vec{x},t,\theta_i)$, a finite differences approach is used. The model response $\vec{h}^k(\vec{x},t,\theta_i^k)$ is calculated, by FE-simulation, for parameter set k. Each individual parameter θ_i^k, belonging to the set, is perturbed by $\Delta\theta_i^k$, to calculate the perturbed model response $\vec{h}^k(\vec{x},t,\ \theta_i^k+\Delta\theta_i^k)$. The sensitivity maps are subsequently determined as:

$$\vec{H}_i(\vec{x},t,\theta_i^k) = \frac{\vec{h}^k(\vec{x},t,\ \theta_i^k+\Delta\theta_i^k) - \vec{h}^k(\vec{x},t,\theta_i^k)}{\Delta\theta_i^k}. \tag{2.17}$$

Note that the sensitivity maps are calculated on the spatial coordinates $\vec{x}$, belonging to the subset-center locations in the measured displacement field $\vec{m}$. Hence, an interpolation step is required to determine the nodal displacements of $\vec{h}$ on these subset positions. To minimize interpolation errors, the interpolation scheme used is based on the FE-interpolation.

The linear system of equations in [Eq. 2.13] is solved in an iterative manner until a predefined convergence criterion is reached. The criterion used in this study is based on the Euclidean norm of the right-hand side of [Eq. 2.13]: $||\kappa_i|| < 10^{-5}$.

A flowchart of the FEMU method is shown in Figure 2.3(a), emphasizing that FEM updating is a *two-step* approach, consisting of (1) displacement measurement by DIC, followed by (2) the parameter identification process. Therefore, the choices associated with regularization in DIC (e.g., the size of subsets and the type of shape functions) must be made appropriately in order to ensure proper identification of the parameters.

In the implementation of FEMU adopted in this study, subset-based DIC is used to calculate the measured displacement fields $\vec{m}$. DIC is performed using the software 'MatchID', provided by the department of Materials Engineering of KULEUVEN (http://www.matchid.org).

2.3.2 Integrated digital image correlation

In integrated digital image correlation (IDIC), measurement of displacement fields by DIC does not precede parameter identification. Instead, images of a material's deformation process, taken during experimentation, are directly correlated by updating the constitutive parameters that govern the imaged deformation. To update the parameters, the most primary source of data, i.e., intensity images, is used, instead of processed derivatives of images (e.g., displacement fields).

A least squares problem, defined on the images (similar to [Eq. 2.3] for the conventional DIC method), is solved, for all time instances at once, by the Gauss-Newton optimization method:

$$\Psi = \int_\tau \int_\Omega \frac{1}{2}\left(f(\vec{x},t_0) - g\circ\vec{\Phi}(\vec{x},t)\right)^2 \mathrm{d}\vec{x}\mathrm{d}t, \tag{2.18}$$

yielding the following linear system of equations:

$$M_{ij}\delta\theta_j = b_i, \tag{2.19}$$

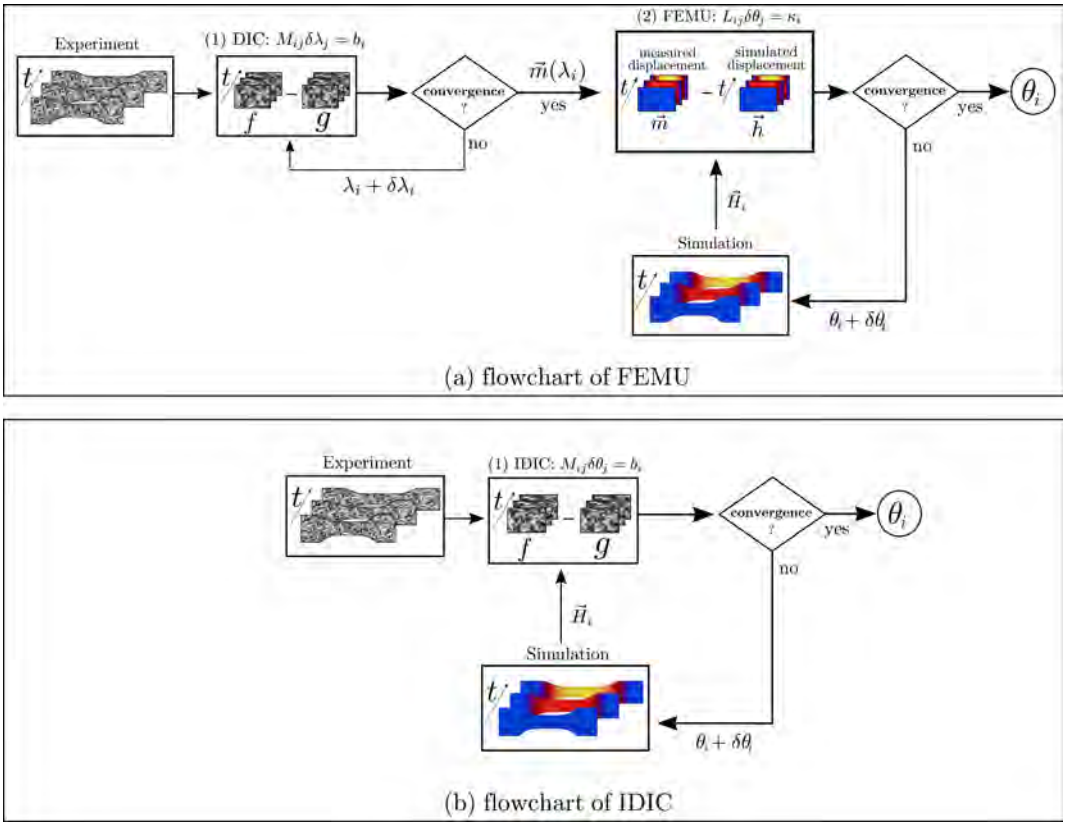

Figure 2.3. Flowcharts of (a) the two-step method of FEMU (note the two iteration loops) and (b) the one-step method of IDIC. In both methods, FE-simulations supply the identification procedure with sensitivity maps $\vec{H}_i$.

where the degrees of freedom in the correlation process correspond to the unknown constitutive parameters θ_i. The correlation matrix M_{ij} and the right-hand member b_i are written as follows:

$$\forall(i) \in [1,p], \quad b_i = \int_\tau \int_\Omega \vec{H}_i(\vec{x},t,\theta_i) \cdot \vec{G}(\vec{x},t,\theta_i) \left(f(\vec{x},t_0) - g \circ \vec{\phi}(\vec{x},t,\theta_i) \right) \mathrm{d}\vec{x}\mathrm{d}t, \tag{2.20}$$

$$\forall(i,j) \in [1,p]^2, \quad M_{ij} = \int_\tau \int_\Omega \vec{H}_i(\vec{x},t,\theta_i) \cdot \vec{G}(\vec{x},t,\theta_i) \vec{G}(\vec{x},t,\theta_i) \cdot \vec{H}_j(\vec{x},t,\theta_j) \mathrm{d}\vec{x}\mathrm{d}t. \tag{2.21}$$

It is obvious that this formulation is equivalent to the DIC formulation explained in Section 2.2. Analogously, in b_i, the mapping function $\vec{\Phi}(\vec{x},t)$ of [Eq. 2.18], which maps the coordinates $\vec{x}$ in the reference configuration to the coordinates in the deformed configuration, is approximated by a function that depends on the constitutive parameters: $\vec{\Phi}(\vec{x},t) \approx$

$\vec{\phi}(\vec{x}, t, \theta_i)$. Furthermore, unlike in the DIC formulations of [Eq. 2.8] and [Eq. 2.9], basis functions $\vec{\varphi}_i$ are not chosen independently. The sensitivity maps $\vec{H}_i$ now serve as basis functions, which are defined equivalently to the sensitivity maps of FEMU, see [Eq. 2.16]. Using the same finite differences approach of [Eq. 2.17], the FE-simulation of the experiment supplies these maps to the system of equations of [Eq. 2.19]. This means that the ill-posed DIC problem is now regularized by mechanics that controls how material deformation (captured in the images) depends on the constitutive parameters. This results in a highly regularized problem with a small number of degrees of freedom. Equivalent to the FEMU implementation, convergence is assumed when the Euclidean norm of the right-hand side of [Eq. 2.19] reaches a predefined criterion: $||b_i|| < 10^{-5}$.

A flowchart of the IDIC technique is shown in Figure 2.3(b). Its *one-step* nature can be recognized by the fact that the DIC routine is integrated within the identification loop. This direct integration of simulation and experimentation does not require additional choices associated with regularization of the ill-posed DIC problem.

2.3.3 Load residuals

So far, only kinematic information is considered in both identification methods, since the objective functions in [Eq. 2.11] and [Eq. 2.18] for FEMU and IDIC, respectively, are based on deformation-dependent displacement residuals and image residuals. However, loading data, which is typically measured during mechanical testing, is generally required in the identification process for certain parameters, as conventionally done in FEMU [91, 108] and similarly in IDIC [85]. This is mandatory for parameters that directly influence the force level when only Dirichlet boundary conditions are applied in the FE-simulation of the identification methods.

Similar to the displacement and image residuals, a load residual can be defined as:

$$\vec{P}_F = \int_\tau \left(\vec{F}_{\text{exp}}(t) - \vec{F}_{\text{sim}}(t, \theta_i) \right)^2 \mathrm{d}t, \tag{2.22}$$

where $\vec{F}_{\text{exp}}(t)$ is the experimentally measured force, and $\vec{F}_{\text{sim}}(t, \theta_i)$ is the numerically obtained reaction force, which depends on the constitutive parameters θ_i. This objective function is minimized by optimizing the parameters θ_i according to Gauss-Newton optimization, leading to the following system of equations, analogously to equations 2.13 and 2.19:

$$N_{ij} \delta\theta_j = c_i, \tag{2.23}$$

$$\forall (i) \in [1, p], \quad c_i = \int_\tau \left(\vec{\rho}_i \cdot \vec{P}_F \right) \mathrm{d}t, \tag{2.24}$$

$$\forall (i, j) \in [1, p]^2, \quad N_{ij} = \int_\tau \left(\vec{\rho}_i \cdot \vec{\rho}_j \right) \mathrm{d}t. \tag{2.25}$$

Herein, $\vec{\rho}_i$ represent force sensitivity maps, akin to the displacement sensitivity maps $\vec{H}_i$ in [Eq. 2.16], which are determined by a finite differences approximation on the FE-simulated forces:

$$\vec{\rho}_i(t, \theta_i^k) = \frac{\vec{F}_{\text{sim}}^k \left(t,\ \theta_i^k + \Delta\theta_i^k \right) - \vec{F}_{\text{sim}}^k \left(t, \theta_i^k \right)}{\Delta\theta_i^k}. \tag{2.26}$$

The objective function of the load residual is combined with the objective function of the displacement residual in FEMU or the image residual in IDIC by superposing [Eq. 2.23] on [Eq. 2.13] or [Eq. 2.19], respectively leading to the following coupled system of equations for FEMU:

$$\left((1-\alpha)\frac{1}{\beta_{[L]}}L_{ij}+\alpha\frac{1}{\beta_{[N]}}N_{ij}\right)\delta\theta_i=(1-\alpha)\frac{1}{\beta_{[L]}}\kappa_j+\alpha\frac{1}{\beta_{[N]}}c_j, \tag{2.27}$$

and the coupled system of equations for IDIC:

$$\left((1-\alpha)\frac{1}{\beta_{[M]}}M_{ij}+\alpha\frac{1}{\beta_{[N]}}N_{ij}\right)\delta\theta_i=(1-\alpha)\frac{1}{\beta_{[M]}}b_j+\alpha\frac{1}{\beta_{[N]}}c_j, \tag{2.28}$$

where $\beta_{[]}$ is a normalization factor, corresponding to the maximum absolute value of the variable inside the subscripted brackets. In this way, both kinematic and load data enter the optimization problem to identify the parameters θ_i. Furthermore, $\alpha \in [0,1]$ is a weight factor, controlling the contributions of each objective function.

2.4 Virtual experimentation

In order to quantitatively assess the errors made by IDIC and FEMU and exclude effects of errors that cannot be quantified, virtual experiments are conducted. An artificial speckle pattern in reference image $f(\vec{x},t_0)$ is deformed by numerically imposing displacements to produce subsequent images $g(\vec{x},t)$. The altering speckle pattern represents a virtual material that mechanically deforms over time. The finite element (FE) method was used in this study to simulate the reference displacement fields by which the speckle patterns were deformed to generate images. Since the reference parameters used for virtual experimentation are known, the accuracy of the parameters identified by IDIC and FEMU can be quantitatively assessed.

Uniaxial tensile tests (2D plane stress simulations) were performed on a virtual tensile bar of 30 x 46 x 0.9 [mm^3], with two circular notches with a radius of 11 [mm], of which an illustration is shown in Figure 2.4. The speckle patterns were stored in 8-bit, gray-valued images of 2048 x 1536 pixels, corresponding to an imaged region of 27 x 20 [mm^2]. In order to come to these images, a reference speckle pattern is firstly built by superposing randomly drawn gray values from three standard normal distributions with different widths (4, 35, and 300 pixels), thereby realizing features of different sizes. These gray values are stored in a high resolution image of 4096 x 3072 pixels. Subsequently this reference speckle pattern is deformed using FE-simulated displacement fields from a model built with a finer mesh than that is eventually used in the identification procedures, which involves interpolation of the reference gray values to new (displaced) spatial positions. The images are then coarsened by a factor of four in order to realize images of a realistic resolution (as mentioned above) of typical cameras used for experimentation. The use of a high resolution reference image and a finer FE-model in this virtual experiment is done to reduce interpolation errors possibly introduced during the generation of the images of the 'deformed' speckle patterns.

The imaged region of Figure 2.4 does not include the edges of the specimen geometry, because it is well known that for subset-based DIC (as used within the FEMU procedure) the subsets encompassing these edges do not correlate successfully, as for instance shown

in [109], potentially causing erroneous identification results for FEMU. Since this study aims at comparing the performance of IDIC to FEMU with respect to other realistic error sources and in a most objective and honest manner, a most optimized form of FEMU was implemented, and image regions in which unsuccessful subset correlation may occur were excluded from the minimization problem. However, in one specific test-case that involves a highly notched specimen geometry, introduced in Section 2.5.7, part of the specimen geometry edges are included in the region of interest, since in that test-case those regions contain the mechanically relevant information.

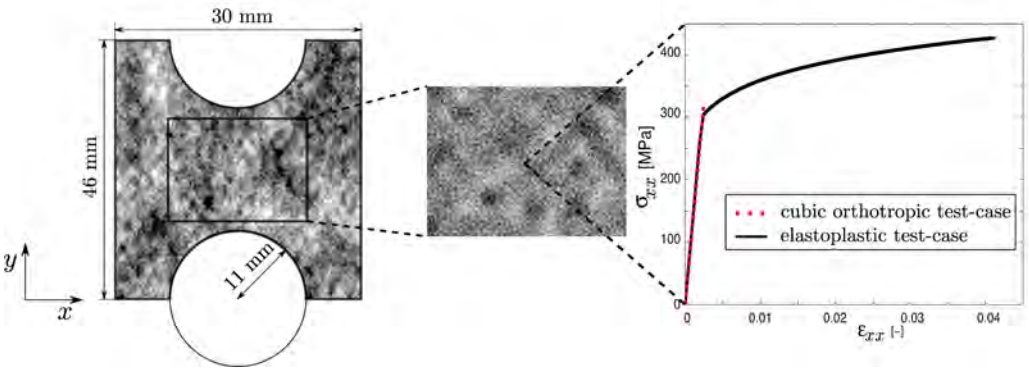

Figure 2.4. Sketch of a tensile bar with circular notches, used in virtual uniaxial tensile tests, in which loading is applied in the x-direction. The indicated imaged region of the tensile specimen is used for parameter identification purposes. Two test-cases were studied, for which tensile stress-strain curves illustrate the corresponding constitutive behavior.

To trigger different realistic complexities in material parameter identification, two types of test-case materials were studied, using the above-described specimen and speckle pattern. Tensile stress-strain curves of both test-cases are also shown in Figure 2.4.

One test-case concerns an isotropic, elastoplastic material, of which the elastic behavior is described by Young's modulus $E = 134$ [GPa] and Poisson's ratio $\nu = 0.36$ [-]. A Von Mises plasticity model is used with isotropic power-law hardening that describes the relation between the yield stress σ_y and the equivalent plastic strain $\bar{\varepsilon}_p$ [110]:

$$\sigma_y = A\left(\varepsilon_{y_0} + \bar{\varepsilon}_p\right)^m, \tag{2.29}$$

where ε_{y_0} is the strain corresponding to the initial yield stress, and A and m are two plastic material parameters, with reference values 632 [MPa] and 0.12 [-], respectively. The initial yield strain ε_{y_0} is not an independent parameter, since it depends on the other two plastic parameters A and m, and Young's modulus E:

$$\varepsilon_{y_0} = \sqrt[m-1]{\frac{E}{A}}, \tag{2.30}$$

at the onset of yielding, when the equivalent plastic strain $\bar{\varepsilon}_p$ equals zero, and the yield stress is $\sigma_{y_0} = E\varepsilon_{y_0}$. Therefore, this test-case has four independent parameters; E, ν, A, and

m, to be identified. Application of a horizontal displacement of 200 [μm] to the specimen's edges results in strains with maximum values up to 4%. Inhomogeneous deformation is induced due to the notched specimen geometry.

The second test-case corresponds to a cubic orthotropic, linear elastic material, which is described by three independent model parameters [111]; Young's modulus $E_x = 130$ [GPa], Poisson's ratio $\nu_{xy} = 0.28$ [-], and the shear modulus $G_{xy} = 79.6$ [GPa]. The orthotropy axes coincide with the x- and y-direction of Figure 2.4. The virtual tensile bar is loaded in x-direction by an applied horizontal tensile force of 2500 [N]. This results in small displacements with an average value of 0.64 pixel and a maximum strain of 0.25%, in the center of the tensile specimen (where the strain is largest due to the presence of the notches). Such small displacements, which are realistic in, e.g., silicon, are challenging for the identification methods, since it puts high demands on the required resolution of the DIC method, which must be capable of capturing these fine kinematics.

Both identification methods; FEMU and IDIC, will be used to identify the parameters of the two test-case materials. Different error sources will be considered in order to assess the methods' robustness to (1) the presence of image noise, (2) poor initial guesses for the constitutive parameters, (3) modeling errors, and (4) experimental errors. The results for the different error sources considered will be presented in the next Section.

2.5 Results and discussion

The results of IDIC and FEMU are here presented in terms of the relative error on the identified parameters, which is defined as follows:

$$\epsilon_i = \frac{\theta_i - \theta_i^{\text{ref}}}{\theta_i^{\text{ref}}} \times 100\%, \tag{2.31}$$

where θ_i represents the i^{th} identified parameter. The corresponding input *reference* parameters θ_i^{ref} are used in the virtual experiment to generate the images used in the identification procedures.

Before results are presented, certain choices are clarified, which relate to the experimental conditions if applied to real experiments. Then, the results of IDIC and FEMU on the different test-cases are presented. As an overview, the comparative analyses of FEMU and IDIC, for the different imposed error sources, are summarized in Table 2.1. The markers indicate which method produces more accurate results.

2.5.1 Experiment conditions

To properly assess FEMU and IDIC, some necessary choices must be clarified. First of all, the choice of the subset size, used in the DIC procedure within the FEMU framework, is important. The subset size directly affects the spatial resolution of the DIC process [101], and therefore influences the accuracy of the entire FEMU method. It is emphasized that these subsets are not used in the IDIC method. Because of the notched virtual specimens, relatively small subsets are needed to adequately capture the inhomogeneous deformation. To what extent the subset size affects the accuracy of the identified parameters in FEMU will be discussed later in Section 2.5.7. For now, the subset size for the DIC algorithm within the FEMU implementation was chosen to be 15 pixels in length and width.

	test-case	tested error source	FEMU vs. IDIC
1	elastoplastic (large deformation)	systematic errors	○ ● ○
2		poor initial guess	○ ● ○
3		modeling error	○ ● ○
4		experimental error	○ ○ ●
5		image noise	○ ○ ●
6	cubic orthotropic elastic (small deformation)	systematic errors	○ ○ ●
7		poor initial guess	○ ● ○
8		modeling error	○ ● ○
9		image noise	○ ○ ●
10	higher complexity	DIC subset size	○ ○ ●

Table 2.1. Summary of results for comparative analyses of FEMU and IDIC. Marked circles indicate which method (FEMU or IDIC) performs better, in terms of accuracy of identified constitutive parameters.

Another important experimentally related condition is the coarseness of the (artificial) speckle pattern of which images consist. The coarseness is governed by the size of the pattern's features. To enable proper correlation, the pattern must be fine enough so that the subset encompasses several features. The generated pattern therefore exhibits speckle features of 2 pixels in width, as previously reported in Section 2.4.

The most important settings chosen in the implementations for FEMU and IDIC are listed in Table 2.2. Some settings, indicated in the Table by (v), are varied in some analyses, as will become clear in the results hereafter.

Settings	**FEMU**	**IDIC**
convergence criterion	10^{-5}	10^{-5}
max. number of iterations	20	20
perturbation factor $\Delta\theta_i$	10^{-4}	10^{-4}
weight factor α	0.01 (v)	0.01 (v)
image interpolation	cubic spline	cubic spline
DIC subset size	15 pixels (v)	N/A
DIC subset shape functions	affine	N/A
DIC search area	100 x 100 pixels	N/A
DIC convergence criterion	0.001 (update)	N/A

Table 2.2. Summary of implementation settings chosen in IDIC and FEMU. The settings regarding subset-based DIC are only applicable to FEMU, and relate to the 'MatchID' software.

Finally, it must be mentioned that the boundary conditions applied in the simulations of both IDIC and FEMU, are ideal boundary conditions, meaning that they correspond exactly to the boundary conditions applied during virtual experimentation. In Section 2.5.5 a test-case will be discussed in which the influence of misalignment of the specimen with respect to the loading direction is investigated. This has the effect that the boundary conditions of the simulations in both identification methods do not coincide with the ones applied during

virtual experimentation.

2.5.2 Sensitivity to systematic errors

Firstly, the sensitivity to systematic errors is investigated for IDIC and FEMU. Systematic errors propagate to the identification results, even though the identification procedure is initialized with perfect initial guesses for the parameters, and no noise is present in the images. Systematic errors originate from (1) interpolation steps needed in the identification algorithms, as described in Sections 2.2 and 2.3, and (2) regularization of the ill-posed problem in DIC.

For the elastoplastic test-case, shown in Figure 2.5(a), the relative errors for all parameters due to systematic errors, for both IDIC and FEMU stay well below 0.5%, and no significant difference is observed between IDIC and FEMU. This conclusion is indicated in row 1 of Table 2.1.

Schreier et al. showed that interpolation errors become more pronounced for high-frequency fluctuations in the speckle patterns [100], and Pan et al. showed that the resulting bias can be reduced by smoothing the images with a Gaussian low-pass filter before correlation [112]. To verify that the observed parameter errors are indeed mainly due to interpolation errors, a Gaussian smoothing kernel of 5 × 5 pixels was used to blur the images for the elastoplastic test-case. The resulting relative parameter errors are also presented in Figure 2.5(a), and indicated in the legend accordingly. The error contrast changes slightly for IDIC, supporting the hypothesis that the parameter errors are caused by interpolation errors. For FEMU, however, blurring with a 5 × 5 pixel Gaussian kernel, resulted in unsuccessful correlation of the images in the DIC procedure, because the subset size of 15 pixels was too small to encompass the larger (blurred) pattern features [113]. Since the artificial speckle pattern was built by superposing three Gaussian distributions, blurring these images with a Gaussian low-pass filter is equivalent to generating a coarser pattern with wider Gaussian peaks. Consequently, the relative errors of the identified parameters drastically increased, highlighting the importance of the correct choice for the subset size within the FEMU procedure.

For the cubic orthotropic elastic test-case, shown in Figure 2.5(b), the relative errors on Poisson's ratio ν_{xy} and the shear modulus G_{xy} are considerably higher than the errors on the parameters for the elastoplastic test-case (mind the different scales of the two plots). Since the displacements in the imaged tensile specimen are small, with an average value of 0.64 pixel (x-displacement), systematic errors in the identification algorithms have a more pronounced influence on the identified parameters. This is confirmed by an additional virtual experiment in which the applied loading is twice as high. For these larger deformations the resulting relative errors of the identified parameters decrease significantly for both IDIC and FEMU. The corresponding error values, which are equivalent for both identification methods, are also plotted in Figure 2.5(b), and are indicated in the legend by their corresponding labels.

Interestingly, for the original cubic orthotropic elastic test-case, IDIC is somewhat less sensitive to systematic errors than FEMU, which can be rationalized as follows. Since FEMU is a two-step approach, it contains more systematic error sources than the one-step IDIC method, resulting in more erroneous parameter identification. The separate DIC-algorithm of FEMU typically requires a much higher number of degrees of freedom (i.e.,

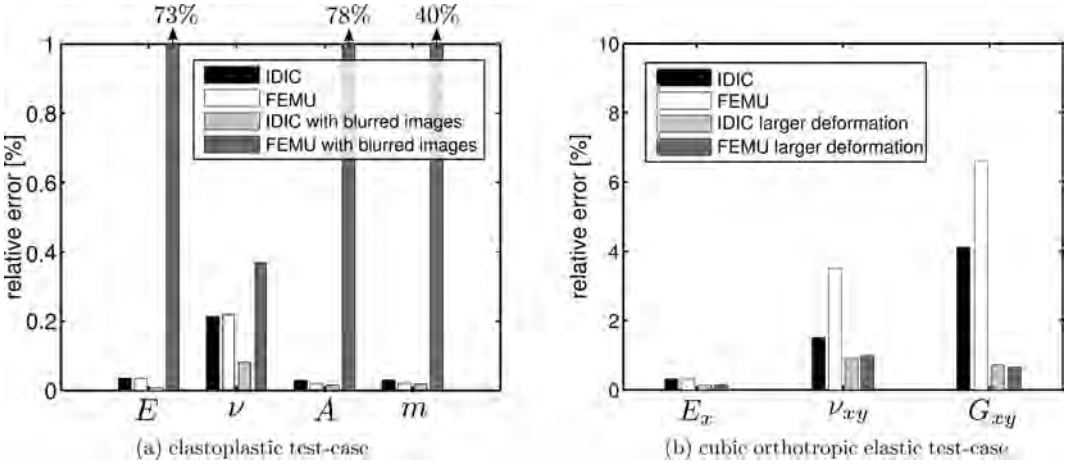

Figure 2.5. Influence of systematic errors on the identified parameters for IDIC and FEMU, when initialized with perfect initial guesses for the parameters, and no noise is present in the images.

less regularization), depending on, e.g., the number of local subsets, the degree of global polynomial shape functions, or the number of connected finite elements. It is known that the choice of regularization is important in DIC and directly affects the accuracy of the DIC-results [96, 104]. Errors made in the separate DIC routine within FEMU propagate into its identification results and therefore result in an additional systematic error source, besides the interpolation error sources present in both IDIC and FEMU. In IDIC, however, this extra regularization step is absent, and the ill-posed DIC problem is directly regularized by the mechanics imposed by the FE-simulation. This conclusion is shown in row 6 of Table 2.1. Note, however, that the difference is small and only noticeable in test-cases in which small displacements dominate the kinematics, such as the virtual experiment on the considered cubic orthotropic elastic material.

Another observation applies to the cubic orthotropic elastic test-case: the identified Poisson's ratio ν_{xy} and shear modulus G_{xy} are significantly less accurate than Young's modulus E_x, for both IDIC and FEMU. The corresponding error contrast of Figure 2.5(b) can be understood by studying the sensitivity maps $\vec{H}_i$, as defined in [Eq. 2.16]. The same sensitivity maps are used in IDIC and FEMU (see Section 2.3), and reveal the sensitivity of the displacement fields, calculated by FE-simulation, to each (mechanical) parameter used in the material model. The maps in Figure 2.6 display the sensitivity of the displacement in x-direction to each parameter for the cubic orthotropic elastic test-case (normalized with their respective maximum values $\hat{\theta}_i$, which are shown above each subfigure). The values $\hat{\theta}_2$ and $\hat{\theta}_3$ are significantly lower than $\hat{\theta}_1$, implying that the x-displacement field is less sensitive to Poisson's ratio ν_{xy} and the shear modulus G_{xy} compared to Young's modulus E_x.

For the subsequent results, the testing conditions, as described in Section 2.5.1, are used. This means that images are not blurred for the elastoplastic test-case, and for the cubic orthotropic elastic test-case the applied displacements at the boundaries of the virtual specimen are not increased.

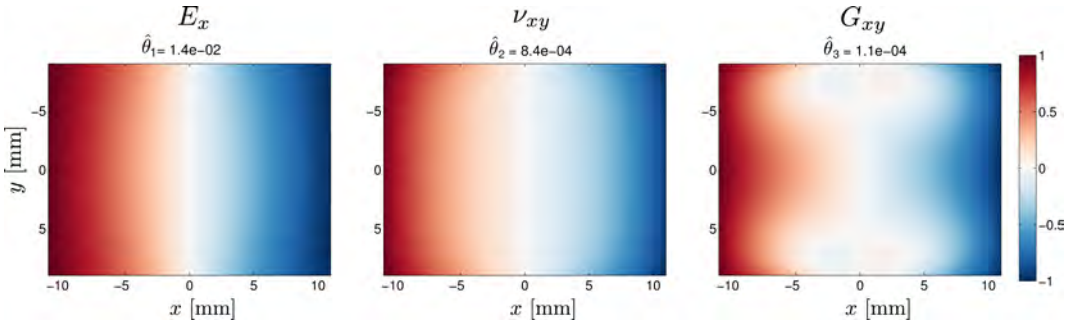

Figure 2.6. Normalized sensitivity maps of the x-displacement field corresponding to the three elastic parameters for the cubic orthotropic elastic test-case.

2.5.3 Errors due to deviating initial guesses

IDIC and FEMU both make use of an iterative Gauss-Newton scheme, which requires initial guesses for each of the parameters to initialize the identification procedure. In the previous discussion about systematic errors, these initial guesses coincided with the exact parameter values with which the virtual experiment was performed. In reality, however, the initial guesses may deviate substantially from the optimum parameter values. The data used for identification of these parameters differs for both methods, since FEMU makes use of displacement fields, while IDIC uses speckle-pattern images directly. It is therefore relevant to investigate whether differences in robustness (sensitivity to initial guesses) exist between IDIC and FEMU.

Both methods are used to identify the parameters for both test-cases, initialized with parameters at different distances from their respective reference values. This distance is expressed as a percentage of the exact value. For example, -20% distance represents an initial guess that is 20% lower than the reference value, and a 20% distance indicates an initial guess that is 20% higher than the reference value. Examples of the displacement and image residuals, for FEMU and IDIC respectively, before and after optimization of elastoplastic parameters, are shown in Figure 2.7.

Figure 2.8 presents the results for both test-cases, which shows that a distance up to 80% below the reference parameter values still leads to convergence. Note that for the elastoplastic test-case, the largest initial guess distance that was tested is 30%, because Poisson's ratio approaches its physical limit value of 0.5 for larger distances. This physical limit does not apply for the cubic orthotropic elastic case.

The main conclusions from these results are indicated in rows 2 and 7 of Table 2.1: no difference between IDIC and FEMU is observed in terms of initial guess robustness, despite the different data used by the methods. Apparently, both IDIC and FEMU attain a global minimum in the solution space, leading to the same solution irrespective of the initial guess for the parameters. Hence, the errors on the parameter values do not deviate from those caused by systematic errors, as presented earlier in Figure 2.5.

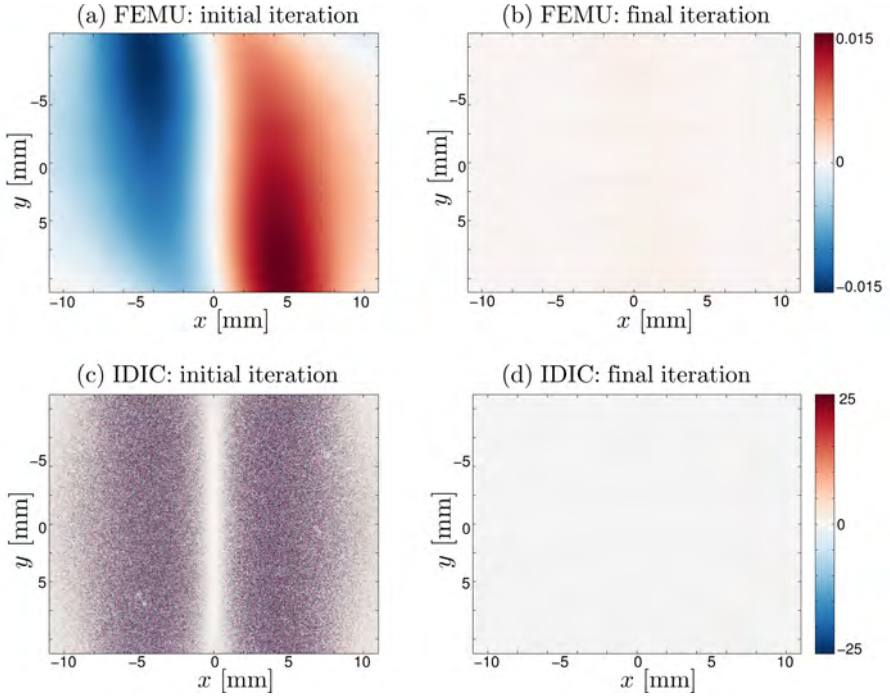

Figure 2.7. Examples of typical displacement residual fields, in [mm], for the FEMU method and image residual fields, in [%] of the image dynamic range, for the IDIC method, initialized with incorrect elastoplastic parameter guesses ((a) and (c)), and after convergence of the parameters ((b) and (d)).

2.5.4 Modeling errors

Invalid assumptions in material models may trigger substantial errors in the identification of model parameters by full-field identification methods that rely on FE-simulation, such as FEMU and IDIC. To assess the performance of IDIC and FEMU in the presence modeling errors, discrepancies between the virtual experiment and the FE-model used in the identification procedures are deliberately applied for the two test-cases.

For the elastoplastic test-case, a discrepancy between the virtual experiment and the constitutive model used for identification is implemented by modifying the virtual experiment, while still using the plasticity model with power-law hardening of [Eq. 2.29] to describe plastic behavior in the identification methods. This time, to generate images in the virtual experiment, a Von Mises plasticity model is used together with experimental tabular stress-strain input capturing the elastic and plastic hardening behavior. The input data is experimentally acquired from mechanical tests on copper foil as used for stretchable electronic systems. This data is adopted from literature [30], and shown in Figure 2.9. In this reference, Young's modulus and Poisson's ratio are $E = 84.58$ [GPa] and $\nu = 0.30$, respectively. Since realistic tabular stress-strain input is used in the virtual experiment, the plastic model parameters determined by the identification procedures cannot be compared to any

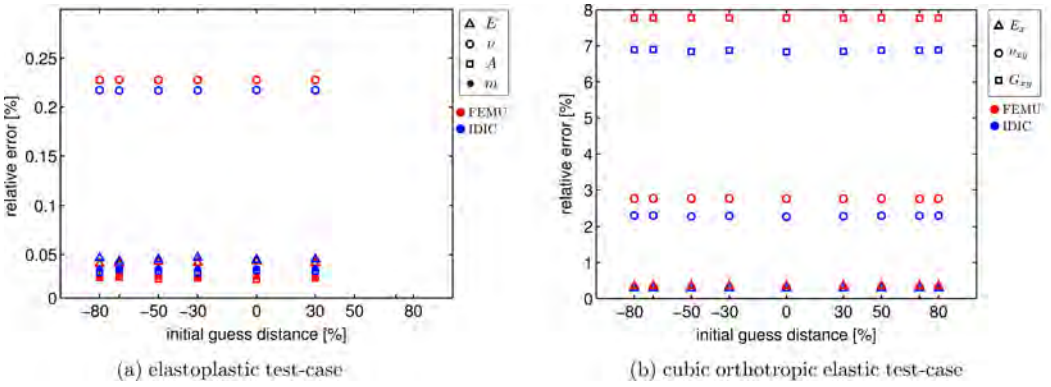

(a) elastoplastic test-case (b) cubic orthotropic elastic test-case

Figure 2.8. The relative errors for the parameters when initialized with different distances from their reference values.

reference values. Therefore, the global stress-strain curves, resulting from FE-simulation with the elastoplastic power-law model and the four identified elastoplastic parameters, are compared to the stress-strain curve from the experimental data used as tabular input in the virtual experiment. It is, however, still possible to compute the relative error for the two elastic parameters. The results for IDIC and FEMU, in which parameters were initialized with a -30% distance from their reference values, are shown in Figure 2.9. Different initial guesses were used, yielding equivalent results, concurring with the conclusions of the initial guess robustness study. The weight-factor α, which controls the contribution of the load and kinematic residuals, as explained in Section 2.3.3, was varied. With a low value for α more weight is put on the kinematic data, while a high value increases the contribution of the load data. Three different values for α were used; 0.01, 0.5, 0.8. The relative errors for the elastic parameters are also shown in the right panel of Figure 2.9, and are also labeled to indicate results for different values for α. Furthermore, for each value of α, the mean absolute values for the image residuals $\bar{\Psi}$ (IDIC) and displacement residuals $\bar{J}$ (FEMU) are given in Figure 2.9 as well.

The first observation is that both identification methods produce equivalent results in identifying the four parameters of the elastoplastic model. Secondly, when most weight is put on the load residual (i.e., $\alpha = 0.8$), the global stress-strain response fits the experimental input data best, while the opposite is true for the lowest α-value equals 0.01. However, when the global response fits the experimental stress-strain data best, the residuals $\bar{\Psi}$ and $\bar{J}$ are highest, indicating that the local kinematics are less well resolved. The identification methods, based on the adopted power-law to describe plastic hardening, cannot perfectly capture the elastoplastic behavior of the virtual experiment and either optimize the four power-law parameters so that the global stress-strain curves fit the experimental curves (high α-value), or so that the kinematic data is correlated (low α-value).

For the cubic orthotropic elastic test-case, an *isotropic* linear elastic model is used in the identification procedures, while the virtual experiment was performed with a cubic orthotropic linear elastic material model. Hence, only two elastic parameters are identified; Young's modulus E and Poisson's ratio ν, while the kinematics in the virtual experiment

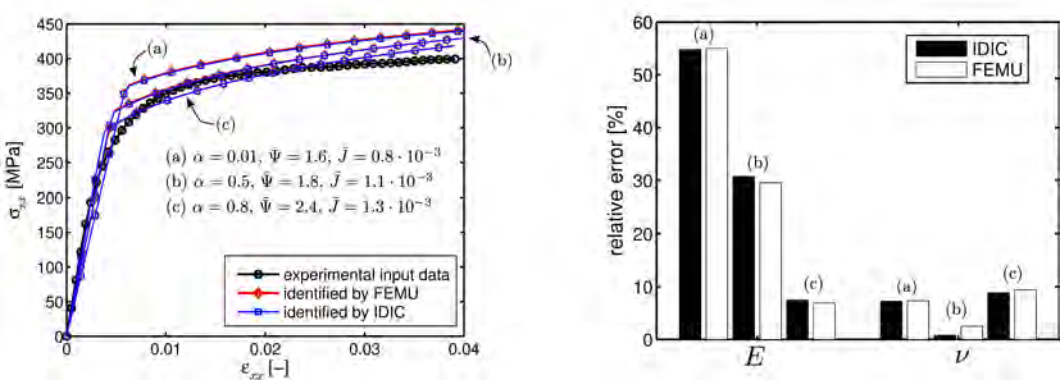

Figure 2.9. The performance of IDIC and FEMU in the presence of modeling errors for the elastoplastic test-case: global stress-strain curves (left) and relative errors of elastic parameters (right). Different values for weight-factor α produce different results. The curves and error bars corresponding to these different α-values are labeled by (a), (b), and (c).

is governed by three elastic parameters (as described in Section 2.4). The two isotropic parameters were initialized with different initial guesses, yielding equivalent results. The relative errors were found to be 3% and 21%, for E and ν respectively. Since no differences were observed between IDIC and FEMU, the detailed results are not shown. Furthermore, because the utilized FE-model is load-controlled, in which the same load is applied in the FE-simulations within the identification methods as was applied in the virtual experiment, the force residual is zero, and there is no use in varying weight-factor α.

The main conclusion for both test-cases is that IDIC and FEMU perform equally in the presence of modeling errors. This is indicated in rows 3 and 8 of Table 2.1.

2.5.5 Experimental errors

Another realistic error source is considered: experimental errors, originating during experimentation, of which an example is here investigated in the form of misalignment of the tensile loading direction with respect to the specimen. This is considered to be an experimental error, since the applied loading during (virtual) experimentation unintentionally deviates from the intended load application.

Three extra virtual experiments were performed on the notched elastoplastic tensile specimen shown in Figure 2.4, with different degrees of misalignment. Misalignment is introduced by additional boundary conditions during virtual experimentation, in the form of a displacement in y-direction, corresponding to angular misalignment of the loading direction with respect to the specimen of 0.5°, 1°, and 2°. No noise was added to the images and the parameters were initialized (initial guess) with a distance of -30% from their reference values.

The relative errors for the four elastoplastic parameters identified by IDIC and FEMU are, respectively, shown as black circles and green squares in Figure 2.10. These results show that the errors for FEMU increase for increasing degree of misalignment and are orders of magnitude higher than for IDIC, in which the errors remain below 0.5% without showing

a significant increase for increasing degree of misalignment. Therefore, it is concluded that FEMU is more sensitive to misalignment. Analysis of the objective function revealed the reason for this difference in performance, i.e., the objective function minimized in FEMU, comprising the displacement residual of [Eq. 2.11], is smoother than the objective function minimized in IDIC, comprising the image residual of [Eq. 2.18]. The latter contains the locally, strongly varying speckle pattern, while the former contains smoothly varying displacement field differences, which results in a broader global minimum. Because of this relatively broad global minimum, less accurate results may be obtained. This is verified by comparing the converged displacement fields, corresponding to the identified parameters, to the reference displacement fields with which the deformed images were generated during virtual experimentation. The converged displacement fields from FEMU deviated more from the reference input fields than those from IDIC. This indicates that convergence to the real solution is never completely reached by FEMU, which explains the larger errors on the elastoplastic parameters.

In order to improve the identification procedure to deal with possible misalignment, extra degrees of freedom can be added in order to account for it. This may be done by allowing rigid body motion, i.e., translation and rotation. It was found that this does not improve the identification results of either method and, surprisingly, even causes complete divergence from the solution. This is likely due to a shear component, caused by misaligned loading, not to be resolved for by these additional rigid body modes. Since both methods did not converge toward a sensible solution, these results are not presented.

A more accurate way of dealing with possible misalignment is to consider the additional y-displacement (causing misalignment) as a degree of freedom (DOF) in the identification procedures. To do this, the y-displacement is iteratively updated and applied as boundary condition (B.C.) in the FE-simulations and is thereby optimized along with the mechanical parameters. This can be done for both FEMU and IDIC, and the results are shown in Figure 2.10, labeled "FEMU w B.C. as DOF" and "IDIC w B.C. as DOF", from which it is concluded that especially FEMU is significantly improved by this additional DOF, whereas for IDIC the results were already accurate for the case when no extra DOF was added. Both methods produce equivalent results for this case, with errors of similar magnitude as those for the case without applied misalignment.

These results are summarized in row 4 of Table 2.1, where IDIC is considered to be more robust against such an experimental error, because it also produces accurate results even when no extra DOF is added to the routine.

2.5.6 Image noise

Since both full-field identification methods rely on digital image correlation, image noise is an important potential error source, which may affect the accuracy of the identification process. The robustness of IDIC and FEMU with respect to image noise is investigated by artificially applying white noise, with a variety of levels, to the images used in IDIC and FEMU. The amplitude of the noise levels represents the standard deviation of the applied Gaussian noise field expressed in a percentage of the root mean square of the image intensity. The applied noise levels range from 1% to 60%. To eliminate a possible bias due to specific noise realizations, four random realizations of each noise level were generated. The results, i.e., relative errors of the identified parameters, were averaged, and are shown

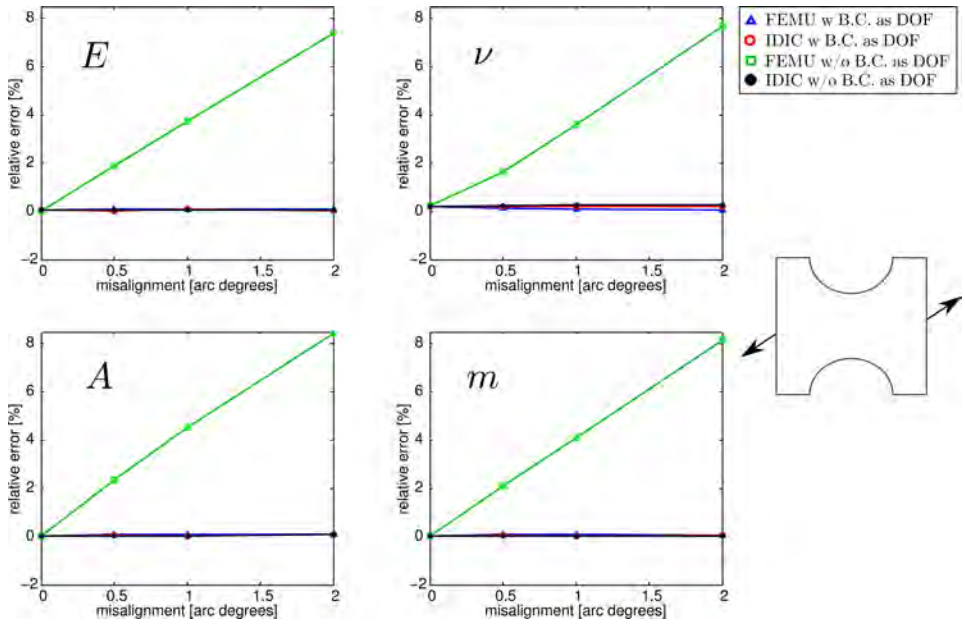

Figure 2.10. Relative errors of elastoplastic parameters (each in a separate plot) identified by FEMU and IDIC for the case of misalignment of the specimen with respect to the loading direction (schematically illustrated on the right), either with (w) or without (w/o) the boundary condition (B.C.) of y-displacement as a degree of freedom (DOF) in the procedure.

on a logarithmic x-scale in Figure 2.11. For both identification methods, the parameters were initialized with a -30% distance from their reference values.

For low noise levels up to 3%, IDIC and FEMU produce similar results, equivalent to the results of tests without any noise, presented previously in Figure 2.5. However, for higher noise levels, IDIC shows lower relative error values for the identified parameters. For instance, for the elastoplastic test-case, at a noise level of 30%, Poisson's ratio is determined with a 23% error by FEMU, while the error for the parameter identified by IDIC is below 1%; a difference of 22 percentage points ([pp]). For even higher noise levels of 60%, FEMU does not converge to a solution, due to the lack of successfully correlated subsets by the DIC routine. IDIC, however, is still capable of identifying the elastic parameters with relative error values in the order of 1%, and even 0.1% for the plastic parameters A and m.

For the cubic orthotropic elastic test-case, a similar result is observed, yet, due to the larger standard deviation, the increasing trend is less obvious for parameter ν_{xy}. In particular, the shear modulus G_{xy} highlights a difference between FEMU and IDIC, since it is determined with a 30 [pp] lower error by IDIC than by FEMU at a noise level of 10%. This difference is even more pronounced at a noise level of 30%, at which the error for G_{xy} is 50 [pp] lower when identified by IDIC than when identified by FEMU.

The observation that IDIC is more robust with respect to image noise than FEMU, (as marked in rows 3 and 8 of Table 2.1), is due to the higher degree of regularization in

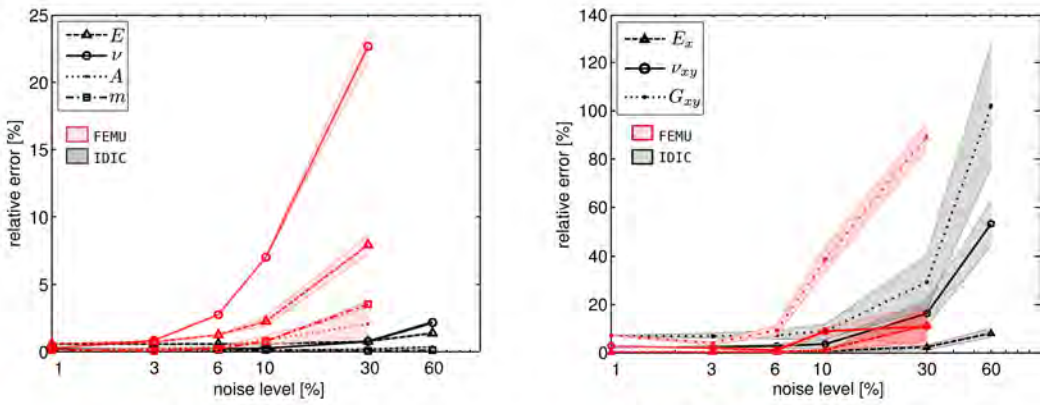

Figure 2.11. The relative errors of the parameters plotted against different noise levels for (a) the elastoplastic and (b) cubic orthotropic elastic test-cases.

the correlation procedure. Since IDIC is a one-step approach, entire images are directly correlated for the identification process, making use of global regularization by mechanical sensitivity maps, see [Eq. 2.16]. FEMU, however, is a two-step approach. Though making use of the same sensitivity maps in the identification procedure as IDIC, the first step (DIC) is performed on the images, making use of local, subset-based regularization. Less data is taken into account in correlating the relatively small, independent subsets, decreasing the signal-to-noise ratio, and increasing the sensitivity to noise [45]. This results in errors in the calculated displacement fields, which propagate to the FEMU identification procedure. Note that a global DIC routine is known to be more robust with respect to image noise than a subset-based approach [45], because the DIC problem becomes more regularized. Using such a global DIC method within FEMU, as done by Mathieu et al. [95], may therefore significantly improve noise robustness if the regularization approach in the DIC procedure is well chosen. The high degree of regularization in the IDIC method by the small number of degrees of freedom and associated level of noise robustness is, however, unlikely to be reached by a global DIC routine within FEMU.

Comparing the results from the cubic orthotropic elastic test-case to those from the elastoplastic test-case, it is concluded that the mean relative errors are higher and the standard deviations increase substantially for higher noise levels. This is, once again, attributed to the small displacements occurring in the virtual cubic orthotropic elastic specimen, which are in the same order of magnitude as the spatial length-scale over which the applied noise varies; 1 pixel. The accuracy of resolving parameters using such fine kinematics is more noticeably affected by noise than in the elastoplastic test-case, where larger displacements occur between subsequently captured images.

2.5.7 Complex test-case: sharply notched tensile bar

So far, the performances of IDIC and FEMU have been investigated with respect to realistic error sources, under optimal conditions described in Section 2.5.1. In the following results, the performance of both methods is further examined using a virtual, tensile specimen with two vertically oriented sharp notches. The notches do not extend during experimentation, but invoke highly localized plastic deformation in their proximity. Once again the material behaves elastoplastically, with the four parameters being: E, ν, A, and m. The geometry with the notches is shown in Figure 2.12. The virtual experiment is conducted with the

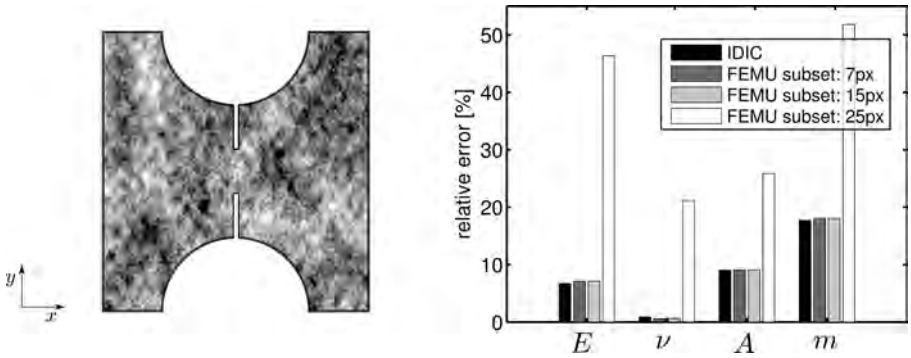

Figure 2.12. Virtual, sharply notched, elastoplastic tensile bar (left). The results of IDIC and FEMU using different subset sizes in the DIC procedure reveal the importance of this regularization choice in FEMU.

same reference image (and pattern), boundary conditions, and material model (Von Mises model with power-law hardening) as the elastoplastic test-case described in Section 2.4. The notch, which widens as deformation increases throughout the (virtual) experiment, exposes free surfaces of the specimen (at the edges of the notch). These free edges and the tip of the notch hold most of the meaningful kinematic information, such as localization of deformation, and must therefore be included in the region of interest of the identification procedure (for both IDIC and FEMU). White noise with an amplitude of 3% is added to the images, which is a level at which no difference between IDIC and FEMU was observed in the previous elastoplastic experiment (Figure 2.11(a)). In order to eliminate possible bias due to specific noise realizations, three random realizations of noise were generated. IDIC and FEMU are used to identify the four elastoplastic parameters; E, ν, A, m, using the same material model as used in the virtual experiment, and starting with an initial guess distance of -30% from the reference parameter values. The averaged results, in terms of relative errors on the parameters, are shown in Figure 2.12, and indicated in row 10 of Table 2.1.

The importance of the subset size in the DIC procedure was already shown in Figure 2.5(a), where it was concluded that subsets smaller than pattern features result in inaccurate parameter identification by FEMU. The present results reveal that larger subsets of 25 pixels (px) in length and width, although encompassing sufficient pattern features, produce erroneous parameter values. This is caused by the loss of spatial resolution of the DIC procedure, due to larger subsets, through which it fails to capture the localized kine-

matics surrounding the sharp notches. Interestingly, this shortcoming is difficult to assess from the depicted deformation fields, and is better quantified by investigating the correlation coefficients. The latter coefficient is used to assess the success of the subset correlations in local DIC algorithms [96, 97], and is formulated as:

$$C = 1 - \frac{\Psi}{\int_\Omega f^2 \mathrm{d}\vec{x}}, \tag{2.32}$$

where Ψ is the residual of each subset (with spatial domain Ω) between images f and g, as defined in [Eq. 2.3]. The normalization with $\int_\Omega f^2 \mathrm{d}\vec{x}$ leads to a correlation coefficient C between 0 and 1, corresponding to no correlation and perfect correlation, respectively. Figure 2.13 shows correlation coefficient fields, at the end of the applied deformation (final time increment), for the DIC analysis, using the two different subset sizes of 15 and 25 pixels. It

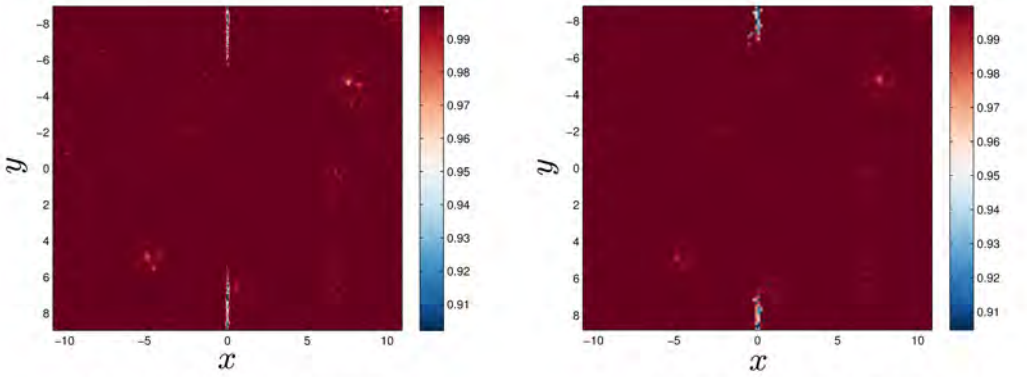

(a) subset size: 15 by 15 pixels (b) subset size: 25 by 25 pixels

Figure 2.13. Correlation coefficient fields of DIC between the reference image f and the final image g, corresponding to the final loading increment.

is obvious that subsets positioned on or near the notches of the specimen are not successfully correlated. For both subset sizes the mean absolute value for C is 0.999, which indicates an adequate correlation. However, as seen in the result of Figure 2.12, when using the displacement results from the DIC analysis with subsets of 25 by 25 pixels, erroneous parameters are identified by the FEMU method. This implies that critical choices, associated with regularization of the DIC process, which are also required in a global DIC approach, may have a significant influence on the FEMU performance. Since in IDIC, the DIC problem is integrated with the identification procedure, this extra choice regarding the subset size and other DIC settings that were not tested, e.g., the shape functions used within subsets and the initial guess choice within the DIC algorithm, are absent.

2.6 Conclusions

To investigate the performance of an IDIC-based parameter identification procedure, it was compared to its most similar equivalent: the conventional FEMU method. Although

both methods utilize DIC and FEM to identify model parameters, there is an important difference. FEMU is a two-step approach, requiring two iterative procedures: (1) local DIC to calculate full-field displacements and (2) the minimization procedure that uses these fields to identify constitutive parameters of a FE-model. IDIC, on the other hand, is a one-step approach, with one iterative procedure to identify the model parameters. In the latter method, the most rudimentary experimental data is used for parameter optimization: intensity images, instead of using processed derivatives, e.g., displacement fields. The goal of this research was to make an objective comparison between FEMU and IDIC, in order to gain understanding of the influence of a one-step approach with respect to a two-step approach. The method of IDIC has very recently been validated against FEMU with a *global* DIC implementation by Mathieu et al. [95]. In the current research, the most standard form of FEMU was used; making use of subset-based DIC to calculate displacement fields and both methods were implemented equivalently. Two virtual test-cases, involving notched tensile bars with cubic orthotropic elastic and elastoplastic material models, were studied to assess the performance of both methods when subjected to the most important realistic sources of error: systematic errors, poor initial guesses, modeling errors, and image noise. These test-cases were chosen because of their imposed challenges for the identification methods regarding small displacements (cubic orthotropic elastic case), localized deformation (due to geometry), and localized mechanical response (plasticity in the elastoplastic case).

It was found that FEMU and IDIC are equally robust with respect to poor initial guesses for parameters with which the identification procedures are initialized and equally sensitive to errors made in the utilized FE-model.

Significant differences between the methods were revealed in the presence of (1) systematic errors leading to erroneous identification, (2) image noise, and (3) experimental error. Because of its two-step nature, FEMU contains more sources of systematic error than IDIC, leading to slightly higher errors on the identified parameters. This becomes more pronounced in test-cases exhibiting small displacements (such as the cubic orthotropic elastic case). Moreover, IDIC is less sensitive to image noise than FEMU. This results from the high level of regularization of the image correlation procedure by a limited set of degrees of freedom: the mechanical parameters. On the contrary, in FEMU, local subsets are individually correlated, requiring a large number of degrees of freedom. The ill-posed DIC problem is thereby less regularized, and the signal-to-noise ratio within each subset is lower. For the case of misalignment of the specimen with respect to the loading direction, IDIC is found to be more robust when no extra degrees of freedom (DOF) are considered in the identification routine. This is regarded to be caused by the narrower global minimum in the objective functions minimized in IDIC. However, when the y-displacement is considered to be an additional DOF that is optimized along with the mechanical parameters, the FEMU routine is improved and produces results with similar accuracy as IDIC.

Furthermore, a test-case of higher complexity, involving a tensile specimen with two sharp notches, reveals the criticality of the subset size in the DIC algorithm of FEMU. Subsets that are too large to capture fine kinematics result in erroneous identification of model parameters, as do subsets smaller than speckle-pattern features. The correctness of the chosen subset size is difficult to assess from the DIC results (e.g., correlation coefficient), jeopardizing the reliability of FEMU results. The choices regarding such DIC-related settings are absent in IDIC.

Because of the versatility of the underlying FE-simulations used in IDIC and FEMU, both methods are applicable to a wide range of problems involving complex material behavior and inhomogeneous specimen geometries. However, the two-step nature of FEMU requires critical regularization choices in the DIC algorithm, the optimization of which are intricate and tedious. The robustness of FEMU with respect to image noise may be improved by using a global DIC routine, instead of a subset-based method as used in this research. Nonetheless, the choices associated with a global regularization scheme (e.g., a mesh with Lagrangian shape functions, global polynomials, B-splines, NURBS) are expected to be even more extensive than in a subset-based scheme. Especially for complex, inhomogeneous specimen geometries (such as a sharply notched specimen), global DIC would require additional procedures, such as image masking, in order to locally eliminate global continuity of the regularization functions. It is therefore concluded that, despite their mathematical resemblance, IDIC is less laborious than FEMU and, more importantly, contains less potential error sources because of its one-step nature, resulting in more reliable identification results. This becomes especially pronounced for test-cases involving small displacements, significant image noise, misalignment of the specimen with respect to the loading direction, or more complex kinematics.

Acknowledgments

This research was carried out under the project number M62.2.12472 in the framework of the Research Program of the Materials innovation institute (M2i) in the Netherlands (www.m2i.nl). Furthermore, Jan Neggers is acknowledged for his contribution to the identification software used for this research and Leo Wouters is acknowledged for maintaining the used computer cluster.

CHAPTER 3

Full-field identification of mode-I cohesive zone parameters

Abstract

Accurate characterization of adhesion properties in microelectronic systems is challenging due to (1) the far-field load application that often falls outside the microscopic field of view, (2) the ultra-small loads associated with specimen deformation, and (3) the load-case and specimen dependent interface response. To overcome these challenges, a generic method based on Integrated Digital Image Correlation (IDIC) is proposed, which identifies cohesive zone model parameters (of an arbitrary model not intrinsic to the identification method), by correlating images of a delamination process from a restricted field of view at the microscopic scale, whereby far-field loading data cannot be exploited.

To quantify the effects of potential error sources on the performance of the proposed IDIC-routine, virtual experimentation is first conducted. Inaccurate application of boundary conditions in the FE-model of IDIC is thereby shown to be the most critical source of error. Subsequently, a real double cantilever beam (DCB) experiment has been analyzed as a well-defined test-case for characterization of adhesion properties. Since the Young's modulus of the bulk material is generally well known, the imaged, elastically deforming bulk material acts as a force sensor. External load measurement can therefore be omitted from the identification process, thereby rendering the interface identification method independent of the particular test method. The implemented IDIC-algorithm is shown to be robust for accurately identifying the two cohesive zone parameters of interest: the work of separation G_c and the critical opening displacement δ_c.

Keywords: Digital Image Correlation; full-field identification; inverse methods; cohesive zone parameters; finite element model

Reproduced from:
A.P. Ruybalid, J.P.M. Hoefnagels, O. van der Sluis, M.G.D. Geers
Image-based interface characterization with a restricted microscopic field of view
International Journal of Solids and Structures, 2018, 132-133:218–231
doi: 10.1016/j.ijsolstr.2017.08.020

Nomenclature

BC	boundary condition(s)
CZ	cohesive zone
DCB	double cantilever beam
DIC	digital image correlation
FE	finite element
IDIC	integrated digital image correlation
LVDT	linear variable differential transformer
MMMB	miniaturized mixed mode bending
ROI	region of interest
VE	virtual experiment

3.1 Introduction

Further down-scaling in the microelectronics industry requires the fabrication of dissimilar materials into a dense stack with a complex 3D geometrical structure. Thereby, the number of interfaces per unit of volume increases, as well as the loads on these interfaces due to the mismatch between the coefficients of thermal expansion of the interfaced materials. Interface failure therefore jeopardizes the integrity of the entire system. Hence, the strength and toughness of such interfaces are of great importance during fabrication and usage of microelectronic devices. In the microelectronics industry, the micro-fabrication processing scheme of microelectronic devices with adopted process parameters is typically strongly regulated and restricted. Therefore, the optimization of the microelectronic design for preventing interface failure is currently based on a lengthy (and costly) trial and error procedure. In order to improve the design geometry by means of predictive numerical failure analysis instead, the mechanical behavior of the critical interfaces needs to be characterized in detail. This requires interface tests to be performed on specimens with the same micro-structure, residual stress conditions, and thermo-mechanical deformation history in the layers as in the actual application, since all of these aspects may strongly influence the interface behavior. In other words, the test specimens should be processed using the same micro-fabrication process as the actual device, including restrictions on maximum in-plane dimensions, thus ruling out dedicated blanket specimens with a simplified material layer stack. Only then can the identified interface behavior truly be used in a predictive fashion to further optimize the geometry of the microelectronic design. Conventional methods rely on accurate knowledge of the applied forces (or moments) to induce interface delamination, and their use is restricted to simplified specimen geometries that do not resemble the actual application [17, 18, 21, 24, 25, 114–116]. Because of the complex multilayer material structure in microelectronic devices, both of these prerequisites are not trivially met for specimens extracted directly from these devices. In contrast, the present proposal is set up specifically to realize an identification method that is independent of such requirements, and that can be used on intricate specimen designs that are fabricated with the same processing scheme as the application. Measuring the ultra-small loads associated with mechanical testing of microelectronic specimens imposes additional demands on the sensitivity of the load mea-

surement, which therefore requires non-commercial, highly specialized measuring equipment that is difficult to use [117].

As a first step towards realizing microelectronic interface characterization, here, a generic method for the identification of cohesive zone (CZ) model parameters is developed. A general, yet arbitrary cohesive zone model is employed here, and it is stressed that the chosen model is not intrinsic to the method, meaning that other models may also be used. To this end, the method of *Integrated Digital Image Correlation (IDIC)* is investigated, which employs finite element (FE) simulations to correlate images of a mechanical deformation process. Literature has demonstrated IDIC to be a versatile and robust method for mechanical parameter identification in general [73, 85, 87, 95, 118, 118]. Interface behavior, however, can only be observed indirectly by analyzing its kinematic effect on the surrounding bulk material during a mechanical experiment, which puts additional demands on the sensitivity of the IDIC-routine. The typical measurement resolution of DIC is ~ 0.01 of a digital pixel [90, 96, 100, 119]. In combination with a smallest pixel size approaching ~ 100 nm for commercially-available optical microscopes, this is sufficient for capturing the displacements associated with the delamination of microelectronic material layers in the order of nanometers. Hence, the required sensitivity can only be achieved through microscopic investigation of the deforming bulk material with sufficient magnification. Under these conditions, the load application generally falls outside the microscopic field of view and a proper method is required to substitute these inaccessible, far-field boundary conditions (BC) of the experiment by local BC applied to the FE-model within the restricted field of view. A problem that consequently arises is the validation of the local reaction forces, which generally differ from the measured force at the location of load application in the experiment (because of the reduction of a system of forces at another location). However, when stiffness properties (e.g., Young's modulus) of deforming adjacent material layers are known, it should be possible to identify CZ-parameters from the elastic deformation of the adjacent layers only, i.e., without using the (possibly measured) applied load. This brings the additional advantage of the proposed method not requiring this load data which in many small-scale experiments cannot be measured accurately. The demanded high sensitivity of IDIC to the kinematic effects of the CZ-parameters requires the method to be rather insensitive to various potential error sources. Experimental errors result from the imaging technique and modeling errors arise from (1) the applied geometry in the FE-model, (2) the boundary condition application, and (3) the adopted constitutive model.

Therefore, the goal of this chapter is to develop an IDIC method that properly transforms the far-field boundary conditions to local boundary conditions in a FE-model matching the restricted microscopic field of view. The developed method is applied to the well-known double cantilever beam (DCB) test-case for interface characterization in microelectronic systems, which makes validation of the method accessible. Firstly, virtual DCB experiments are performed to analyze the performance of IDIC when subjected to various artificially applied error sources, with special focus on the application of boundary conditions. The optimized method is then validated using single and double cantilever beam experiments.

This manuscript briefly reviews the underlying theory and methods of IDIC and CZ-models in Section 3.2. The development and validation of an appropriate IDIC-methodology, adopting local boundary conditions, and its experimental results are presented in Sections 3.3–3.6, followed by general conclusions in Section 3.7.

3.2 Methods

To characterize interfaces, the following methods are required: (1) Integrated Digital Image Correlation, see Section 3.2.1, and (2) a cohesive zone model to be employed in FE-simulations, see Section 3.2.2.

3.2.1 Integrated digital image correlation

Integrated digital image correlation is a full-field identification method allowing to directly identify the constitutive parameters of a material model [66, 84, 86]. Images of a deformation process, taken at different moments in time t (e.g., by a digital camera sensor), are correlated [45, 48, 65, 103] by optimizing the constitutive parameters of a material model that governs the deformation. A random pattern is typically applied to the tested material to promote uniqueness of contrast in the images.

Conservation of brightness in the images is assumed and forms the starting point of the optimization procedure:

$$f(\vec{x}, t_0) \approx g\left(\vec{\Phi}(\vec{x}, t)\right) = g \circ \vec{\Phi}(\vec{x}, t), \tag{3.1}$$

$$\vec{\Phi}(\vec{x}, t) = \vec{x} + \vec{U}(\vec{x}, t), \tag{3.2}$$

where f and g are the scalar intensity fields of, e.g., light detected by an optical camera. The vector function $\vec{\Phi}$ maps the pixel position vector $\vec{x}$ in image f (corresponding to the reference material state at time t_0), to the pixel position vector in image g (corresponding to the deformed state at time t). The displacement field $\vec{U}(\vec{x}, t)$ can be approximated by the results from a FE-simulation of the experiment: $\vec{U}(\vec{x}, t) \approx \vec{h}(\vec{x}, t, \theta_i)$, which, in turn, depends on the constitutive model parameters $\theta_i = [\theta_1, \theta_2, \ldots, \theta_n]^T$, where n is the total number of unknown parameters. The mapping function is therefore also directly dependent upon these parameters: $\vec{\Phi}(\vec{x}, t) \approx \vec{\phi}(\vec{x}, t, \theta_i)$. A least squares residual problem is introduced as follows:

$$\Psi = \int_\tau \int_\Omega \frac{1}{2} \left(f(\vec{x}, t_0) - g \circ \vec{\phi}(\vec{x}, t, \theta_i)\right)^2 \mathrm{d}\vec{x}\mathrm{d}t. \tag{3.3}$$

This residual is minimized simultaneously at all pixel intensity levels in space-time, defined by a spatial domain Ω and a time domain τ, by optimizing the constitutive parameters θ_i by the Gauss-Newton method [103]:

$$\frac{\partial \Psi}{\partial \theta_i} = 0, \tag{3.4}$$

yielding the following linear system of equations:

$$M_{ij} \delta\theta_j = b_i, \tag{3.5}$$

where, the correlation matrix M_{ij} and the right-hand side b_i are:

$$\forall(i) \in [1,n], \quad b_i = \int_\tau \int_\Omega \vec{H}_i(\vec{x},t,\theta_i) \cdot \vec{G}(\vec{x},t,\theta_i) \left(f(\vec{x},t_0) - g \circ \vec{\phi}(\vec{x},t,\theta_i) \right) \mathrm{d}\vec{x}\mathrm{d}t, \tag{3.6}$$

$$\forall(i,j) \in [1,n]^2, \quad M_{ij} = \int_\tau \int_\Omega \vec{H}_i(\vec{x},t,\theta_i) \cdot \vec{G}(\vec{x},t,\theta_i) \vec{G}(\vec{x},t,\theta_i) \cdot \vec{H}_j(\vec{x},t,\theta_j) \mathrm{d}\vec{x}\mathrm{d}t, \tag{3.7}$$

in which $\vec{G}$ is the gradient of the image with respect to the spatial coordinates, for which different choices can be made, which have been explored in detail in [103]. For convenience, the gradient of reference image f is used here. Furthermore, $\vec{H}_i$ are the *kinematic sensitivity maps*, representing the dependence of the simulated displacements $\vec{h}(\vec{x},t,\theta_i)$ on each parameter θ_i:

$$\vec{H}_i(\vec{x},t,\theta_i) = \frac{\partial \vec{h}(\vec{x},t,\theta_i)}{\partial \theta_i}. \tag{3.8}$$

In order to calculate the sensitivity maps $\vec{H}_i(\vec{x},t,\theta_i)$, a finite difference approach is used. The model response $\vec{h}^k(\vec{x},t,\theta_i^k)$ is calculated, through the FE-simulation, for parameter set k. Each individual parameter θ_i^k, belonging to the set, is perturbed by $\Delta\theta_i^k$, to calculate the perturbed model response $\vec{h}^k(\vec{x},t,\ \theta_i^k + \Delta\theta_i^k)$. The sensitivity maps are subsequently determined as:

$$\vec{H}_i(\vec{x},t,\theta_i^k) = \frac{\vec{h}^k(\vec{x},t,\ \theta_i^k + \Delta\theta_i^k) - \vec{h}^k(\vec{x},t,\theta_i^k)}{\Delta\theta_i^k}. \tag{3.9}$$

The sensitivity maps $\vec{H}_i$ are supplied to the system of equations [Eq. 3.5], by which the ill-posed IDIC problem is thus strongly regularized by the mechanics from FE-simulation.

Even though force correlation is not strictly necessary, as argued previously, it is included here for completeness. Besides correlating images, a squared residual of the applied load can be taken into account in the correlation routine, which is defined as:

$$\vec{P}_F = \int_\tau \frac{1}{2} \left(\vec{F}_{\mathrm{exp}}(t) - \vec{F}_{\mathrm{sim}}(t,\theta_i) \right)^2 \mathrm{d}t, \tag{3.10}$$

where $\vec{F}_{\mathrm{exp}}(t)$ is the experimentally measured force, and $\vec{F}_{\mathrm{sim}}(t,\theta_i)$ is the computed reaction force, depending on the constitutive parameters θ_i. This objective function is minimized by optimizing the parameters θ_i leading to a system of equations analogous to [Eq. 3.5]:

$$N_{ij}\delta\theta_j = c_i, \tag{3.11}$$

comprising *load sensitivity functions* that can be calculated in a similar manner as the kinematic sensitivity functions of [Eq. 3.8]. The objective function of the load residual is combined with the objective function of the image residual by superposing [Eq. 3.11] and [Eq. 3.5], leading to the following coupled system of equations:

$$\left((1-\alpha)\frac{1}{\beta_{[M]}} M_{ij} + \alpha \frac{1}{\beta_{[N]}} N_{ij} \right) \delta\theta_j = (1-\alpha)\frac{1}{\beta_{[M]}} b_i + \alpha \frac{1}{\beta_{[N]}} c_i, \tag{3.12}$$

where $\beta_{[]}$ is a normalization factor, corresponding to the maximum absolute value of the variable inside the subscripted brackets. In this way, both kinematic and load data enter the optimization problem to identify the parameters θ_i. Furthermore, $\alpha \in [0, 1]$ is a weight factor, controlling the contributions of each objective function. Convergence is assumed when the Euclidean norm of the right-hand side of [Eq. 3.12] reaches a predefined criterion.

3.2.2 Cohesive zone model

Cohesive zone (CZ) models are widely used to describe a large variety of mechanical interfaces [22, 120–125]. In general, CZ-models lump all damage processes near the crack tip in the interface plane by relating the normal and shear components (indicated by subscripts n and s, respectively) of the traction vector $\vec{T} = T_n\vec{e}_n + T_s\vec{e}_s$ to the opening displacement vector $\vec{\delta} = \delta_n\vec{e}_n + \delta_s\vec{e}_s$ between the separating material surfaces, where $\vec{e}$ is the unit vector. An effective opening displacement Δ is defined as:

$$\Delta = \sqrt{\delta_n^2 + \beta^2\delta_s^2}, \tag{3.13}$$

where β is the ratio between the maximum shear traction $T_{s,\max}$ and the maximum normal traction $T_{n,\max}$. Although other relations are possible [126, 127], the CZ-model adopted here makes use of an exponential relation that originates from the binding energies during atomic separation in bimetallic interfaces [128], which was shown to be suitable for different types of interfaces [23, 121, 129], including epoxy adhesives as used in this research [130]. The effective traction T [Nm^{-2}] can be expressed with respect to the effective separation Δ [m] [131]:

$$T = G_c\frac{\Delta}{\delta_c^2}\exp\left(-\frac{\Delta}{\delta_c}\right), \tag{3.14}$$

where the work of separation G_c [Jm^{-2}] and the critical opening displacement δ_c (corresponding to the maximum effective traction $T_{\max}$) are the CZ-parameters. The effective traction T reads:

$$T = \sqrt{T_n^2 + \beta^{-2}T_s^2}. \tag{3.15}$$

The FE-software *MSC.Marc/Mentat* is used in the present analyses, in which the CZ-model of [Eq. 3.14] describes the interfacial debonding between adjacent bulk material layers, using four-node elements with linear interpolation. The bulk material is described using a linear elastic material model and bilinear quadrilateral elements. Furthermore, a plane strain condition is assumed. A mesh convergence study was conducted to optimize the FE-discretization.

3.3 Double cantilever beam experiment

A DCB-specimen is made by gluing two 300 [μm] thin spring steel beams together with an Araldite 2020 epoxy glue layer ($\sim$ 10 [μm] thin). The glue thickness is controlled by applying a 10 [kN] pressure force to the glued beams, allowing excess glue to flow out from the sides of the specimen. The interface between the beams contains a 3 [mm] pre-crack. The dimensions of the specimen are shown in Figure 3.1. A speckle-pattern is applied to the

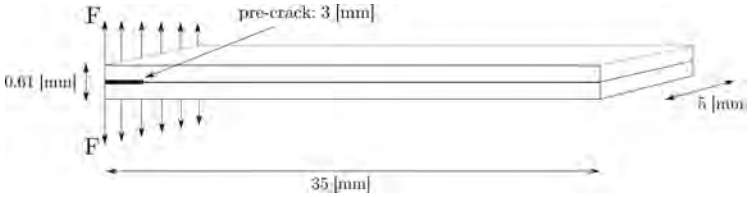

Figure 3.1. Illustration (not to scale) of the DCB-specimen with a pre-crack of 3 [mm].

specimen by spray-painting. A micro tensile tester (manufactured by Kammrath & Weiss), in combination with the Miniaturized Mixed Mode Bending (MMMB) test setup developed by Kolluri et al. [114, 132], is used to delaminate the two beams under a pure mode-I loading condition. In order to later compare the IDIC-results with results from conventional identification methods, global force-displacement data is measured at one of the two tensile tester's gripper clamps by a load cell and an LVDT measuring the total opening where the DCB-specimen is attached to the MMMB setup. Furthermore, images are acquired by optical microscopy and capture the deformation of the beams and the progressive failure of the glue interface. A total of 15 images, consisting of 1300×512 pixels with a physical pixel size of 5.45×5.45 [μm^2], are used for the IDIC-routine. The global experimental data of the reference specimen configuration and the deformed specimen are shown in Figure 3.2.

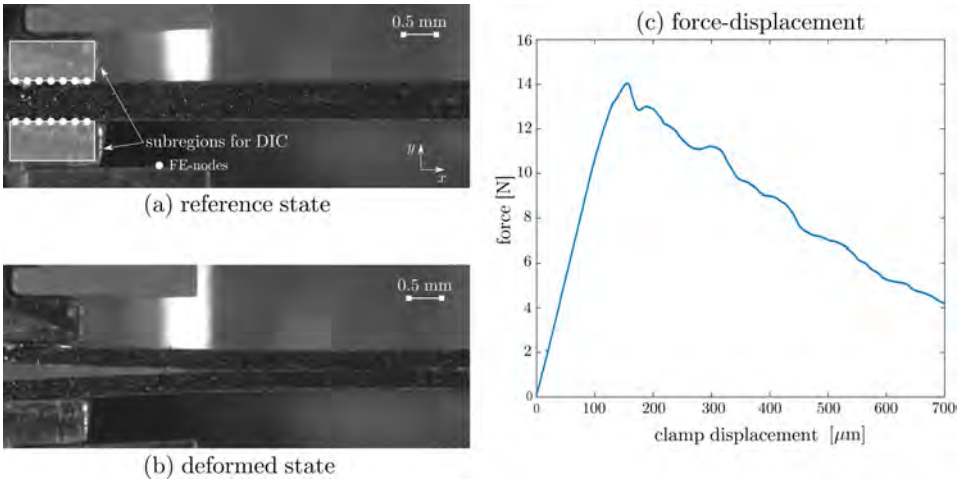

Figure 3.2. Experimental images of the DCB-specimen in (a) the reference configuration before deformation and (b) the deformed configuration; (c) global force-displacement data measured at one of the tensile tester's gripper clamps. Subregions used to extract boundary conditions by global DIC are highlighted in (a), together with the approximate positions of FE-nodes at which kinematic boundary conditions are applied in the model.

Both spring steel beams are assumed to deform linear-elastically with elastic parameters (as specified by the supplier): Young's modulus $E = 210$ [GPa] and Poisson's ra-

tio $\nu = 0.33$ [-]. Between the two modeled beams, CZ-elements are inserted to represent the interface, except in the 3 [mm] long pre-crack region. As is typical for (more complex) microelectronic systems, the load application of the experiment falls outside the field of view (see introduction). For the DCB test-case in this chapter, only part of the specimen is captured in the images. Therefore, the kinematic boundary conditions for the FE-model must be extracted from the experimental images. To this end, a global digital image correlation procedure [105] is conducted on selected subregions of the images that correspond to the clamps of the MMMB-setup that are glued to the specimen's top and bottom beams. From these DIC-analyses, displacements in x- and y-direction are acquired and applied as kinematic boundary conditions to the corresponding beam nodes in the FE-model. The subregions used for DIC and the FE-nodes at which kinematic boundary conditions are applied in the model are highlighted in Figure 3.2.

IDIC is used to identify the two mechanical parameters of the CZ-model: G_c and δ_c. Without any precautions or without properly applying the boundary conditions in the FE-model, IDIC may not converge, or may converge to a non-unique parameter set. At the start of the IDIC-procedure, initial guesses must be provided for the CZ-parameters: $G_c^i = 33$ [Jm^{-2}] and $\delta_c^i = 16$ [μm], which were values adopted from the experiments conducted by Kolluri et al. [22]. Figure 3.3 shows the convergence behavior of this case, in terms of the image residual (shown as a percentage [%] of the dynamic range of the images) and the Euclidean norm of the parameter updates $||\delta\theta||$. The poor convergence is mostly observed in

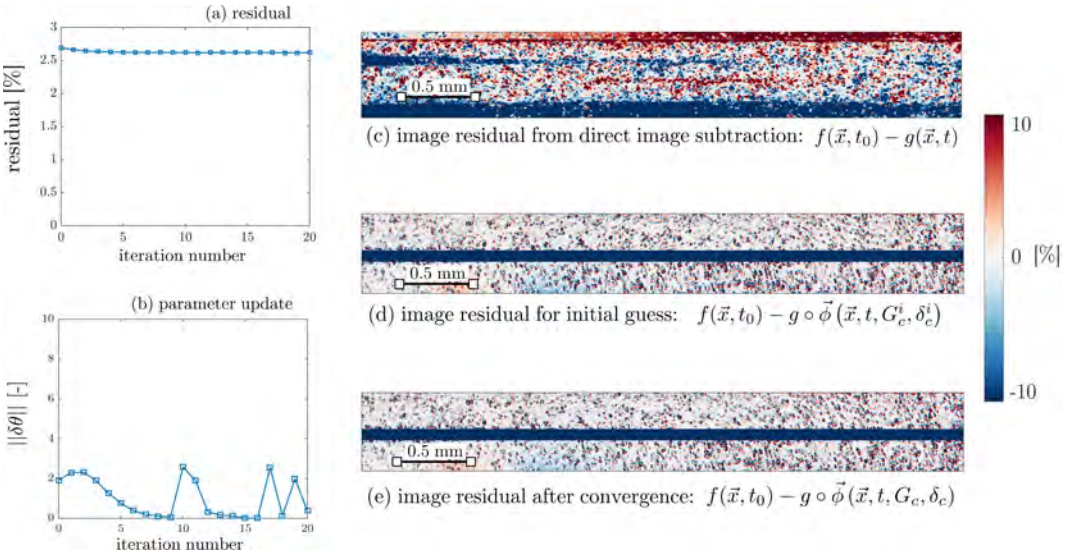

Figure 3.3. Results from IDIC on the 15 experimental images. The convergence behavior is plotted in (a) and (b). The image residual fields (between the reference image at time t_0 and the final image at time t) are shown in (c), (d), and (e) in which the colors represent the percentage [%] of the dynamic range of the images. The blue band in the center of residual images (d) and (e) represents an image region that is not taken into account (masked) for correlation, because of pattern degradation near the crack region during delamination.

the fluctuating parameter update (Figure 3.3(b)) and in the relatively high remaining image residual values (Figure 3.3(a)). This is confirmed by the image residual after convergence, in which distinct pattern features can be clearly identified. To illustrate how the image residual should be assessed, the initial residual between the reference image f and the image of the deformed configuration g is shown in Figure 3.3(c). This is the computation of the objective function (image residual) without any displacement, even before an initial guess is given or boundary conditions are applied in the IDIC-routine. Patterns present in both images are clearly visible in this residual. The large improvement of Figure 3.3(d) with respect to Figure 3.3(c), in which the displacement field is calculated with the initial guess ($G_c^i = 33$ [Jm^{-2}] and $\delta_c^i = 16$ [μm]), but not minimized by the IDIC-routine, is caused by the fact that this displacement field includes rigid body motion and an approximate DCB opening profile. IDIC optimization, however, does not give any improvement to this initial guess residual, as evident by comparing Figure 3.3(e) with Figure 3.3(d). Several revisions of the IDIC-routine and FE-model were tested by varying the assumed thickness of the beams, the pre-crack length, and Young's modulus, but without any improvement to the disappointing results presented above.

The results from IDIC on data from DCB-experiments showed that proper convergence towards a reliable solution is not readily achieved. To improve on the method's robustness and accuracy, virtual experiments are conducted to probe the method's performance when subjected to various potential error sources.

3.4 Virtual experimentation

To better understand the problems associated with interface characterization, virtual experiments (VE) are performed using the DCB test-case. Special attention is given to a proper application of the local kinematic boundary conditions in the FE-simulation.

An artificial speckle pattern in reference image $f(\vec{x}, t_0)$ is deformed by imposing displacements from a FE-simulation to produce subsequent images $g(\vec{x}, t)$. The virtual images are then used in the IDIC-routine to identify the CZ-parameters of the model. Since the parameters are now known in advance, the accuracy of IDIC can be assessed quantitatively. The reference parameter values are: $G_c = 33$ [Jm^{-2}] and $\delta_c = 16$ [μm]. The virtual experiment is performed on a 2D model of the entire DCB-specimen (see Figure 3.1 for the specimen dimensions). The kinematic boundary conditions are applied at the outer-left corner nodes of both beams, as illustrated in Figure 3.4(a). In order to reproduce the conditions of the real experiment, the magnitude of the prescribed nodal displacements in the virtual experiment is specified such that the resulting opening between the beams corresponds to the opening observed during the real experiment. Furthermore, similar to the real experiment, a total of 15 images were generated in the virtual experiment. To reduce interpolation errors possibly introduced during the generation of the virtual images, the element size used in the model of the virtual experiment is twice as small as the element size in the model used in the IDIC-routine. To test the performance of IDIC when more realistic (thus less ideal) patters are used, a micrograph of a real specimen was also virtually deformed. Figure 3.5 shows two sets of virtual images: one image with an artificial speckle pattern generated by a combination of different Gaussian intensity peaks that is virtually deformed, and a second image taken from the real experimental reference image that is virtually deformed.

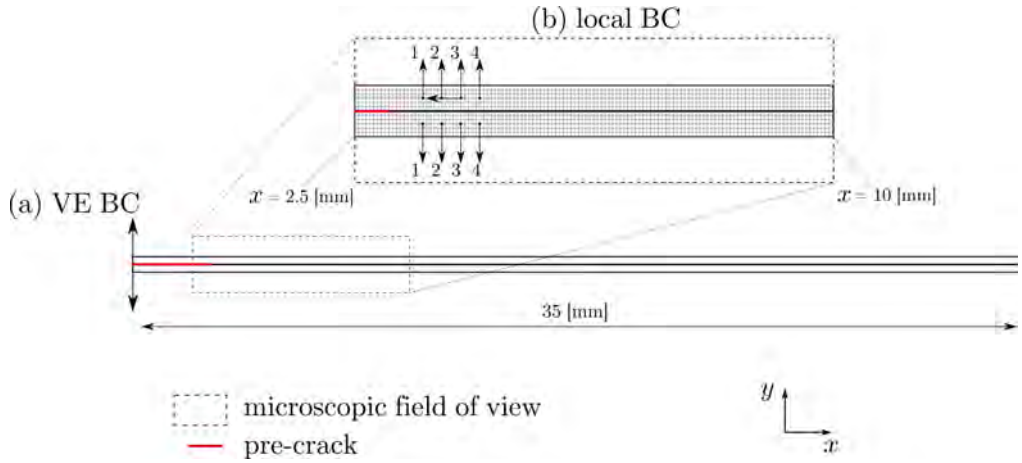

Figure 3.4. Illustration of the far-field kinematic boundary conditions (BC) as applied in the virtual experiment (a). To realize adequate boundary condition application within the restricted field of view, local boundary conditions are applied in the simulation used for IDIC (b), as explained in Section 3.5 (not yet employed in current Section 3.4).

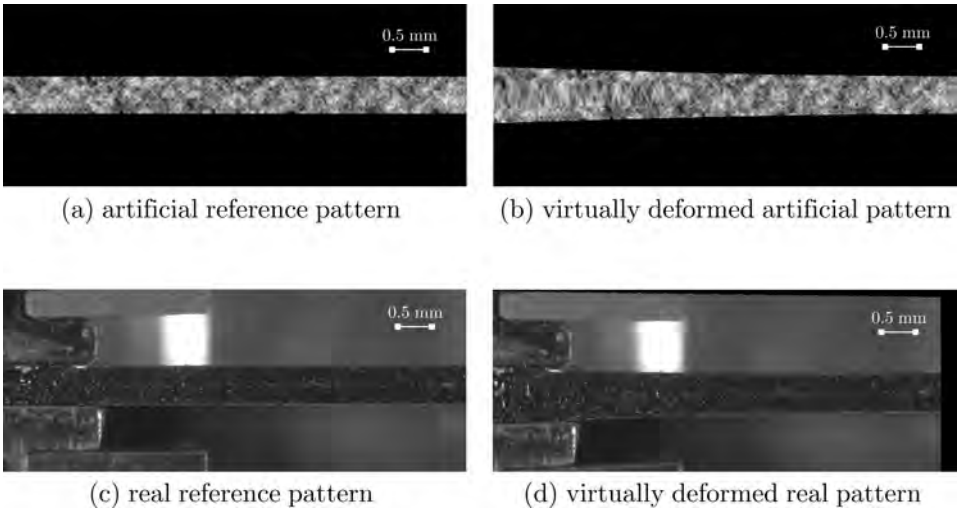

Figure 3.5. Images resulting from virtual experimentation on an artificial speckle pattern (a) and (b), and the experimental image (c) and (d). The stretched pattern in between the delaminated beams (in both of the virtually deformed images) behind the crack tip is an artifact from the interpolation procedure used for image generation. For a real (physical) experiment, such artifacts are not present in this form, however, similarly, new intensity levels of pixels in between the delaminated beams appear from the background (see Figure 3.2).

3.4.1 Error sources

Different errors were probed by virtual experimentation, assessing the robustness of IDIC against image noise, the existence of a unique solution, the adequacy of the real speckle pattern, and the size of the assumed pre-crack in the model. For these tests, the model and its boundary condition application employed in the IDIC-routine are exactly the same as in the virtual experiment, shown in Figure 3.4(a), i.e., no reduced model corresponding only to a restricted field of view is used. An overview of the different test-cases and resulting errors are given in Table 3.1. Relative errors ϵ of the identified CZ-parameters with respect to the reference values used in the virtual experiment are specified in percentages. The elastic parameters of the beams were kept at their reference values: $E = 210$ [GPa] and $\nu = 0.33$ [-].

Table 3.1. Overview of different virtual test-cases and resulting errors.

OBJECTIVE	METHOD OF TESTING	RESULTS	CONCLUSIONS
test effect of images of different parts of deformation process	compare results when all images, or images of only the delamination regime, are used for correlation	for both cases $\epsilon < 1\%$	only use images from delamination regime to reduce computational costs
test artificial vs. real speckle pattern	compare results from IDIC with artificial, or with real pattern	for both cases $\epsilon < 1\%$	real pattern is adequate
test effect of image noise	artificial application of white noise of 3% to the images	$\epsilon < 1\%$	IDIC robust against noise
test effect of erratic rigid body motion as in real test	extract displacements from real experiment by DIC and apply as boundary conditions in VE	$\epsilon < 1\%$	IDIC robust against erratic motion
test uniqueness of solution	initial guesses G_c^i, δ_c^i up to 10 times higher/lower than reference	$\epsilon < 1\%$	IDIC finds unique solution
test influence of incorrect assumption of pre-crack length	pre-crack length of 2 [mm] instead of 3 [mm] as in VE	$\epsilon < 1\%$	IDIC robust against pre-crack length in model

The results presented in Table 3.1 are briefly explained in the order in which they appear in the table. To understand whether specific images should be taken into account, results were compared for correlation of all 15 images or only 8 images taken during delamination. Both cases converged to the same, accurate solution with errors well below 1%, i.e., correlating only the 8 final images corresponding to the delamination regime during the DCB test is

sufficient. Accurate results were obtained when IDIC was conducted with the actual speckle pattern of the real DCB test, meaning that the pattern is adequate. An image noise level of 3%, applied to the images, does not negatively influence the parameter identification results, meaning that the method is robust against such realistic levels of image noise. Furthermore, it was shown that image blurring, in order to smooth possible image noise, did not improve results. In fact, the errors on the CZ-parameters increased to 2.5%, meaning that image blurring should not be used. This indicates a pronounced sensitivity of the CZ-parameter identification with respect to the local kinematics. Image blurring decreases the spatial resolution of IDIC, meaning that the method becomes less sensitive to local kinematics. The erratic rigid body motion observed in the real experiment is applied as a boundary condition in a virtual experiment in order to assess IDIC's performance under these conditions (see Figure 3.5(d)). IDIC produced accurate results for the CZ-parameters with errors well below 1% and is therefore robust against erratic rigid body motion (as adopted here). To test the robustness of IDIC with respect to distinct initial guesses for the CZ-parameters, the parameters were initialized with different values, up to 10 times higher/lower than the reference values used in the virtual experiment. For different initial guesses, IDIC consistently converges to the same unique solution, meaning that IDIC is robust against poor initial guess values. Furthermore, IDIC is, at least for this test-case, concluded to be robust against a possible error in the assumption of the pre-crack length, of which the measurement is nontrivial in a real experiment.

Based on the influence of the potential error sources listed in Table 3.1, the data acquired during experimentation should be adequate, allowing for a proper identification of the CZ-parameters with IDIC. The unsuccessful IDIC analysis of the DCB experiment in Section 3.3 is therefore attributed to the imprecise application of the boundary conditions in the FE-model employed within IDIC. As mentioned earlier, the proper application of boundary conditions in the FE-simulation is a challenge of IDIC, because the actual location of the applied load in the experiment lies outside the microscopic field of view. This calls for transforming the far-field boundary conditions of the experiment to local boundary conditions in the FE-model that corresponds to the limited, microscopic field-of-view. Applying the displacements extracted by DIC on the subregions as shown in Figure 3.2 is likely to be erroneous, since the subregions do not correspond to material of the DCB-specimen, but to the MMMB-setup's clamping stubs, which may partly delaminate from the specimen and slightly rotate. Furthermore, the displacements of the subregions' edges are eventually applied as boundary conditions to nodes at the beam edges. It is known that this DIC method [105] is accurate away from the edges of its subregions. It is therefore quite plausible that the kinematic boundary conditions extracted from these subregions constitute an inaccurate description of the actual displacements transferred from the stubs to the specimen during experimentation.

3.5 Optimization of IDIC boundary conditions

In order to review the role of the prescribed boundary conditions in IDIC, a systematic study using virtual experiments is performed. Analogously to the real experiment, where the load application falls outside the field of view, the far-field boundary conditions applied in the virtual experiment will not be captured within the virtually generated images. Instead,

local boundary conditions are applied in the simulation used within the IDIC-routine, which correctly capture the kinematics resulting from the far-field boundary conditions. To extract these local kinematic boundary conditions, precautions must be taken with respect to the following points: (1) to measure displacements, digital image correlation (DIC) is performed on a limited set of subregions within the images, which is referred to as the "DIC pre-step"; (2) measured displacements should be applied to a minimum number of nodes in the FE-model to prevent over-constraining the kinematics; (3) the boundary condition nodes must be sufficiently spaced in order to prevent stress fluctuations of ~ 100 [MPa] in the FE-simulation (an estimate based on the typical DIC resolution of ~ 0.01 [px] [90, 96, 100, 119] and the employed nodal spacing of ~ 15 [px]). Because of the simple far-field boundary conditions applied in the virtual experiment, resulting in pure mode-I opening of the DCB-specimen, two boundary regions suffice for the corresponding local boundary conditions to establish kinematic equivalence: one subregion within each beam on the left side of the field of view. The nodal locations where the boundary condition are applied are chosen as close as possible to the neutral axes of the beams to assure that the beams can only comply to the applied nodal displacements by bending and not by shear. Transverse displacements are applied to the selected nodes, which are spatially separated in the longitudinal (horizontal) direction. To account for any rigid horizontal translation, a horizontal displacement is applied as a boundary condition to one node. Illustrations of the far-field boundary conditions of the virtual experiment and the local boundary conditions within the limited field of view are shown in Figure 3.4. The required number of boundary condition nodes per region is investigated next.

In a real experiment, the displacements are extracted in the DIC pre-step. In order to bypass the influence of potential error sources associated with the DIC extraction method, nodal displacements are first directly taken from the virtual experiment results and subsequently applied as local boundary conditions in the FE-simulation of the IDIC-routine. The displacement results from the FE-simulation with local boundary conditions are then compared to the displacement results from the virtual experiment with the far-field boundary conditions. Error fields are calculated at the final loading increment, as presented in Figure 3.6. As the number of incorporated boundary condition nodes increases, the error decreases. Obviously, using a single node in each boundary region does not result in deformation that is kinematically equivalent to the far-field boundary conditions applied in the virtual experiment.

3.5.1 IDIC with improved boundary conditions

To determine the required number of boundary condition nodes for the FE-model, IDIC is performed using boundary conditions involving different numbers of prescribed nodes (i.e., increasing the kinematic constraint). Images with a real speckle pattern, as deformed in the virtual experiment, see Figures 3.5(c) and (d), are used. The IDIC-routine is initialized with the same reference values for the CZ-parameters as those used in the virtual experiment, i.e., perfect initial guesses. The image residual to be minimized is assessed at the first iteration of the IDIC-routine (prior to convergence) in terms of percentage [%] of the dynamic range of the images. Furthermore, the mean absolute values of the displacement error fields (of Figure 3.6) of all time increments, and the converged CZ-parameters after minimization of the image residual are evaluated with respect to the number of adopted boundary condition

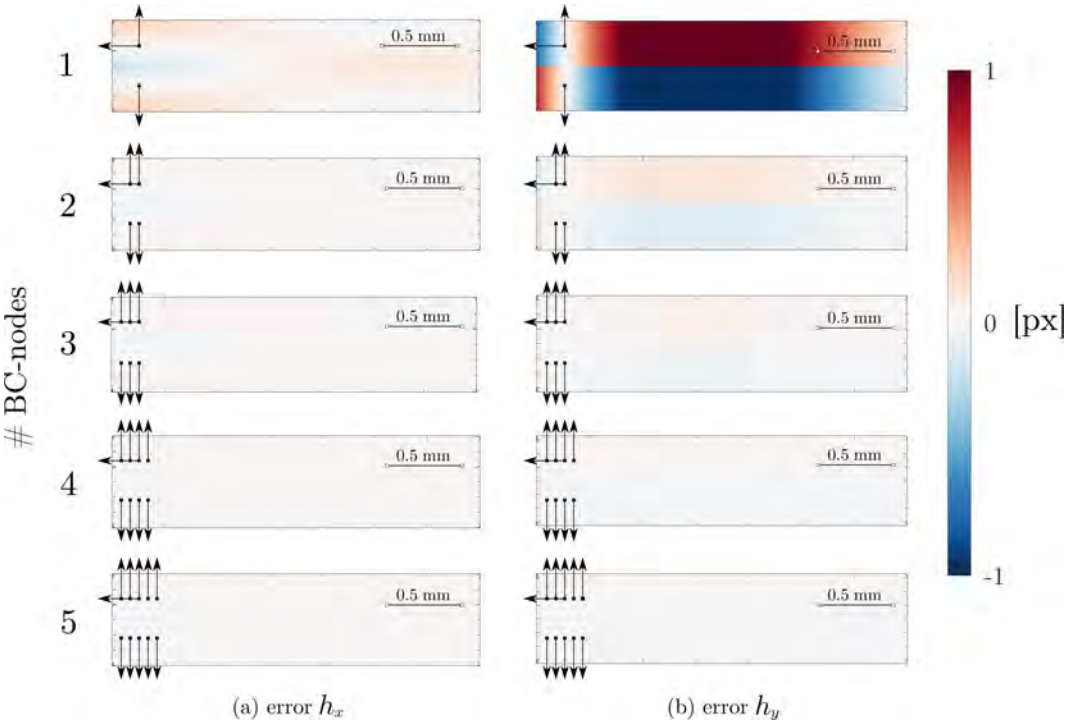

Figure 3.6. Error fields in terms of pixels of the simulated displacements h_x and h_y, for kinematic boundary conditions applied to a different number of nodes within each boundary region. The arrows indicate the boundary conditions applied in the FE-simulation. In all cases, the x-displacement is prescribed to only one node. Near those locations the errors are zero, because the boundary conditions extracted from the virtual experiment are exact here.

nodes per boundary region. The results are presented in Figure 3.7.

The reduction of the far-field force system at a different location requires a minimum of two local boundary condition nodes. From Figure 3.7(a), it is clear that the image residual is relatively high when only a single boundary condition node in each region is prescribed. Consequently, during IDIC, the CZ-parameters converge to erroneous values, see Figure 3.7(c). By prescribing two or three nodes, respectively, the slope and the curvature of the bending beams can be captured, which improves the results. Optimal results are obtained by prescribing four nodes (spaced ten elements apart), because it allows to capture the essential beam kinematics, i.e., the curvature and its linear gradient over the length of the beams, without over-constraining the problem. Using four boundary condition nodes, the image residual in IDIC is relatively low, and consequently, the parameter identification is accurate, see Figure 3.7(c). Prescribing more than four boundary condition nodes does not improve the results and induces a stiff constraint instead, resulting in increased errors on the CZ-parameters. Hence, for this DCB test-case, it is concluded that locally prescribing four boundary condition nodes per subregion adequately establishes kinematic equivalence

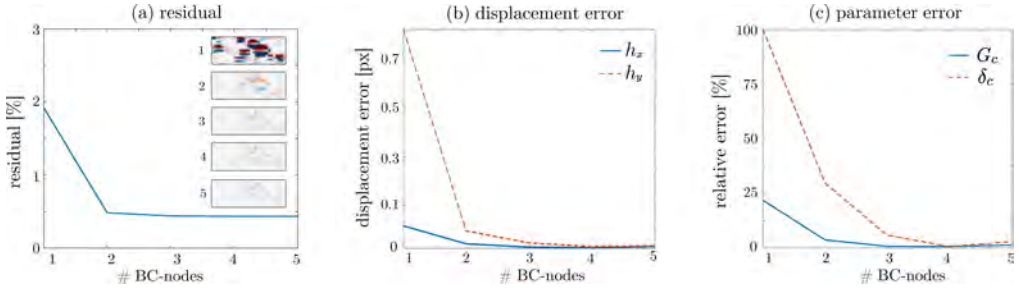

Figure 3.7. The influence of the number of boundary condition nodes per subregion on the image residual (a), the absolute displacement error (b), and the error on the converged CZ-parameters (c). The subfigures in (a) show a zoomed-in region of the image residual fields after convergence of the IDIC-procedures using different numbers of boundary condition nodes in the FE-model, with a color scale ranging from -10 to 10 [%] similar to Figure 3.3(c)-(e).

with respect to the far-field boundary conditions of the virtual experiment.

So far, the influence of boundary condition application was investigated without making use of the DIC pre-step to extract the boundary condition displacements, as required in a real experiment. The virtual experiment is subsequently revised using the full procedure: (1) performing a DIC pre-step on subregions of the images to measure displacements; (2) applying the measured displacements as boundary conditions in the DCB simulation; (3) performing IDIC on the virtually deformed images to identify the CZ-parameters of the interface. Whereas the local boundary conditions are here needed because of the restricted field of view, they also allow to reduce the size of the FE-model in IDIC for other problems. It suffices to only model the part of the specimen that is captured within the field of view, which reduces computational costs. The finite element size is ~ 15 [px]. The discretization and boundary conditions are shown in Figure 3.8 together with the imaged specimen, the subregions used for the DIC pre-step, and the region of interest taken into account in IDIC. The local boundary conditions applied in the model to the four nodes per subregion are also depicted. The DIC pre-step is implemented using global polynomial basis functions [105] for measuring the kinematic boundary conditions in the subregions of the images.

Results of the DIC pre-step in the top-left and bottom-left subregions of the virtually deformed images are presented in Figure 3.9. The residual fields, in terms of percentage [%] of the dynamic range of the images, are noticeably small. Furthermore, the differences of the displacements measured by DIC with respect to the nodal displacements of the virtual experiment are in the order of 0.01 [px], which is representative for a typical DIC resolution [90, 96, 100]. It is therefore expected to be sufficiently accurate to determine the kinematic boundary conditions for the FE-simulation of the IDIC-routine.

Identification results are presented in Figure 3.10 for two different IDIC cases with $\alpha = 0.3$ (see [Eq. 3.12]) and $\alpha = 0$. Identifying CZ-parameters without force correlation ($\alpha = 0$) is only possible when Young's modulus of at least one of the beams is known and kept constant during optimization of the CZ-parameters, because the deflection of the delaminated beams with known stiffness effectively acts as a force sensor. The CZ-parameters were initialized with the following values: $G_c^i = 330$ [Jm^{-2}] and $\delta_c^i = 160$ [μm], which are ten times larger

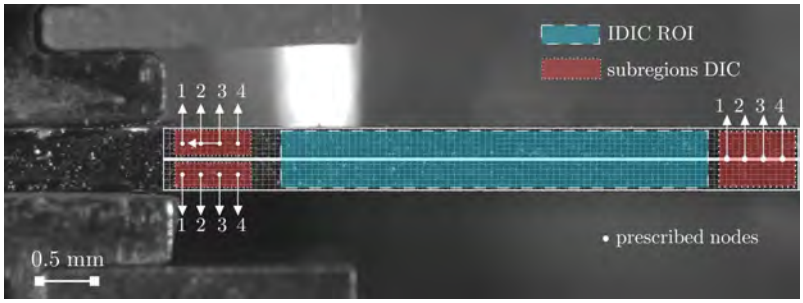

Figure 3.8. Illustration of the application of local kinematic boundary conditions. A restricted view of the DCB test is used in the FE-simulation within IDIC (for visualization clarity the FE-mesh is drawn a factor two coarser in horizontal dimension than it is in the simulation). The subregions used for the DIC pre-step for capturing the boundary condition displacements, and the region used in IDIC for parameter optimization, are highlighted. The subregion on the right of the field of view is only used in the real experiment (described in Section 3.6) and not in the virtual experiment.

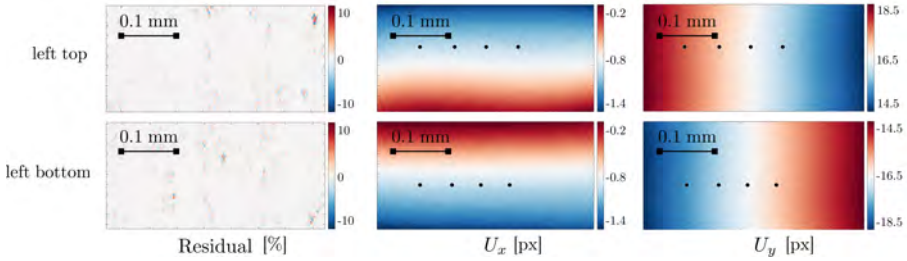

Figure 3.9. Results from the DIC pre-step in the two subregions of the virtual images to extract the kinematic boundary conditions. The residual fields in terms of [%] of the dynamic range of the images, and the displacement fields in x- and y-directions in terms of [px] are shown at the final time increment. The black dots indicate the nodal positions at which the corresponding displacement fields' values are applied as boundary conditions in the FE-simulation for IDIC.

than the reference values used in the virtual experiment (see Section 3.4). The elasticity parameters of the beams are assumed to be known and given by: $E = 210$ [GPa] and $\nu = 0.33$ [-]. For both cases, the CZ-parameters properly converged towards the reference values. The remaining relative errors on the CZ-parameters are: $\epsilon_{G_c} = 1.72\%$, $\epsilon_{\delta_c} = 4.59\%$ for the case with force correlation and: $\epsilon_{G_c} = 0.65\%$, $\epsilon_{\delta_c} = 1.25\%$ for the case without force correlation. Surprisingly, the latter is concluded to be more accurate, meaning that force correlation is not only unnecessary, but here also deteriorates the accuracy of the method. This counter-intuitive result is explained as follows. For the case in which force correlation is taken into account, the IDIC-routine uses both kinematic data (images) and force data (see [Eq. 3.12]). However, the transformed locations of the boundary condition nodes in the local FE-model do not trivially allow for direct validation of the corresponding vertical reaction forces to the far-field force in the virtual experiment. Furthermore, the above mentioned stress fluctuations may be of influence at the boundary condition locations. The

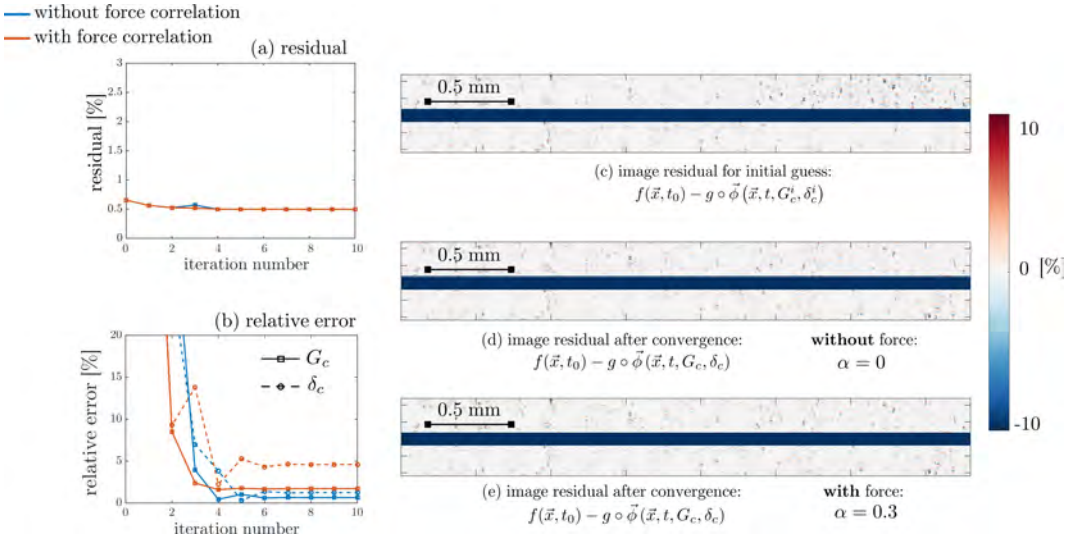

Figure 3.10. Results from IDIC on the virtually deformed images. The boundary conditions are extracted by a DIC pre-step from the subregions and next applied to the FE-simulation. Two IDIC-routines are tested: one in which force correlation is taken into account and one in which force correlation is omitted. For both cases the elasticity parameters of the bulk material are well known. The convergence behavior is plotted in (a) and (b), and the image residual fields (between reference and final image) are shown in (c), (d), and (e), in terms of [%] of the dynamic range of the images.

region of interest (ROI) used for image correlation is therefore taken at a distance from these locations, as seen in Figure 3.8 (IDIC ROI). At this distance kinematic fluctuations will not have a significant influence because of Saint-Venant's principle.

3.5.2 Force data exclusion

From the previously presented results it is concluded that if boundary conditions in the FE-model of IDIC are applied in subregions that do not correspond with the location of the physical boundary conditions, the corresponding reaction forces cannot be used for force correlation, as they would lead to less accurate results. In a physical experiment, experimental errors obviously play an important role. The forces are measured by a load cell far from the field of view, and may not fully represent the forces applied to the specimen. There are two main reasons for this: (i) the kinematic boundary conditions are prescribed at locations that do not correspond to the physical (far-field) load application, hence, reaction forces differ due to the reduction of a system of forces from one location to another; (ii) in between the load cell and the specimen is the complex body of the Miniaturized Mixed Mode Bending setup [114, 132] that transfers the load and deformation from a tensile tester's clamps to the specimen by a series of elastic flexure hinges. Although optimally designed, minute sliding, friction or misalignment in the setup may cause deviation from the assumed load transfer and jeopardizes accurate comparison of the measured forces to the forces on the clamps.

An additional practical problem is time synchronization of the different measurements: load measurement and image capturing of the deformation process for the duration of the shutter time. Unintended, asynchronous measurements effectively cause an error in the assumed load at a moment in time (corresponding to a snapshot of the specimen). For all these reasons, force correlation cannot be taken into account in IDIC for micro-scale tests with such a restricted field of view.

Recently, a paper was published that also addressed the challenge of identifying the interface parameters from delamination tests [71]. In that paper FEM updating (FEMU) was employed to simultaneously identify mixed-mode interface parameters from the combination of a DCB test and crack lap shear (CLS) test. However, the authors concluded that it is mandatory to include force correlation in the minimization of the objective functional (together with image correlation) to enable accurate parameter identification, a conclusion that was also drawn for parameter identification using only the DCB test. This conclusion varies from the one drawn here that force correlation is redundant. This contradiction can be explained by the different method for boundary condition application in the FE-model. In [71] all nodes of the entire top and bottom edge of the modeled DCB specimen geometry are kinematically constrained (with Dirichlet boundary conditions), which results in lower *kinematic* sensitivity to the parameters of interest than the less constraining boundary conditions advocated here, which explains the necessity for load data in [71]. Furthermore, in [71], the reaction forces are not evaluated at the locations of the physically applied boundary conditions, but at model locations, rendering the force reduction nontrivial and sensitive to errors.

As mentioned in the introduction, the goal of this chapter is to establish a generic identification method. Since the microscopic field of view is restricted, the physical (far-field) boundary conditions are not captured, and the real load transfer is not measured. This calls for replacing the far-field boundary conditions of the experiment by local boundary conditions in the FE-model within the actual field of view, making force correlation impossible. Moreover, there are purely kinematic testing setups in which forces cannot be measured at all, and IDIC must be employed without force correlation.

Before applying the developed method for a restricted field of view with Dirichlet boundary conditions to the DCB analysis, it has first been validated on a fully-defined single clamped beam bending experiment (with load data available) on an aluminum specimen without an interface (which is described in Appendix A).

3.6 The double cantilever beam revisited

The double cantilever beam experiment introduced in Section 3.3 is now revisited using the knowledge gained through virtual experimentation. The goal is to properly identify the CZ-parameters of the FE-model. Boundary conditions are measured in image subregions by a DIC pre-step and applied to four nodes in corresponding subregions of the FE-model, as described in Section 3.5.

3.6.1 DIC pre-step results

Because of rigid translations and rotation of the specimen during experimentation, a third subregion is incorporated to extract and impose boundary conditions. This subregion is po-

sitioned at the right-hand side of the field of view, as illustrated in Figure 3.8. Similar to the other two subregions on the left of the field of view, four nodes are kinematically prescribed in a corresponding subregion of the FE-model. Another reason for implementing the third subregion is to allow for more complex load-cases, involving mixed-mode delamination (not further analyzed here). The DIC pre-step results, in terms of final image residuals and displacement fields, are shown in Figure 3.11 for each subregion. The low image residual fields

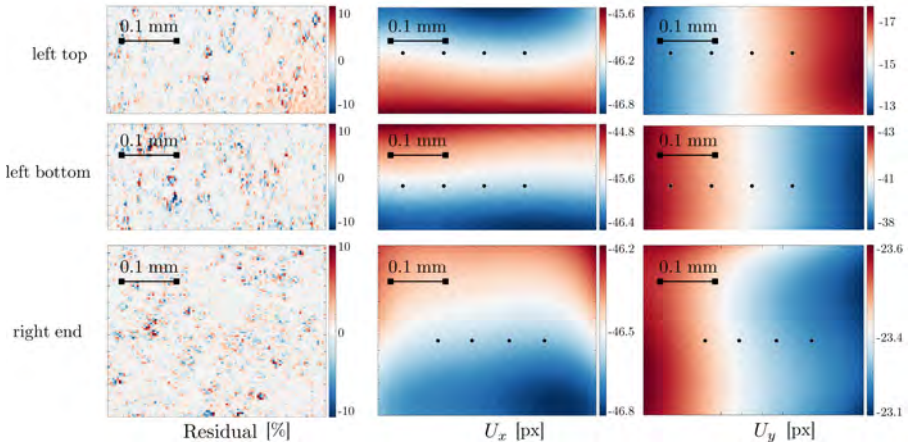

Figure 3.11. Results of the DIC pre-step on the three subregions in the experimental images to extract the kinematic boundary conditions. The image residual, in terms of [%] of the dynamic range of the images, and the displacement fields in x- and y-direction, in terms of [px], are shown at the final time increment. The black dots indicate the nodal positions where displacements are applied as kinematic boundary conditions in the FE-simulation for IDIC.

(compared to Figure 3.3) confirm the adequacy of the local kinematic boundary conditions in the FE-model.

3.6.2 Sensitivity maps

A sensitivity analysis is performed in order to assess the sensitivity of the displacement fields to each of the CZ-parameters. Sensitivity maps are defined in [Eq. 3.8], representing the sensitivity of the displacements h_x and h_y, with respect to a change of a CZ-parameter. A high sensitivity indicates a good identifiability of the corresponding parameter. The perturbation factor (relative to each parameter) used to calculate sensitivity maps is set to 5×10^{-4}. In order to compare the sensitivity maps for the two parameters of interest, they are multiplied with the respective parameter values, i.e., the resulting maps can be assessed in terms of pixels [px]. Sensitivity maps corresponding to the ROI used for IDIC are shown in Figure 3.12. As expected, the horizontal displacement h_x is less sensitive to the CZ-parameters than the vertical displacement h_y, since the DCB-experiment exhibits pure mode-I loading during which the vertical displacements dominate. Both parameters have a similar kinematic influence in the spatial domain, since the sensitivity fields take a similar distribution. However, the vertical displacement h_y is clearly more sensitive to the work of separation G_c than it is to the critical opening displacement δ_c (note the scale

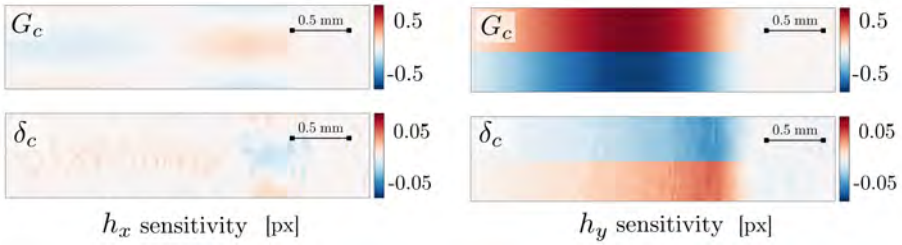

Figure 3.12. Sensitivity maps for displacement fields h_x and h_y in terms of pixels [px] with respect to each CZ-parameter, corresponding to the ROI used for IDIC at the final time increment.

bars). Accordingly, G_c can be identified with a higher accuracy than δ_c, which is not a general conclusion, but is specific to this DCB test-case, including the used materials and the boundary conditions applied in the FE-simulation.

Considering the measurement resolution of DIC (~ 0.01 [px]), the relevant h_y-sensitivities are adequate for proper identification of both CZ-parameters. Note that the sensitivity maps outside the ROI (not shown here) are negligible near the boundary subregions in which the boundary conditions are applied. Indeed, in those subregions the FE-model response follows the prescribed nodal displacements which are insensitive to the mechanical parameters.

3.6.3 Interface parameter identification

IDIC is conducted with 8 images taken during the delamination regime of the deformation process, without the physical boundary conditions within the field of view, and employing local boundary conditions. To test robustness and uniqueness, a total of eleven IDIC-routines are conducted, each of them initialized with different initial guesses for the CZ-parameter values. Forces are not correlated, and hence the elasticity parameters of the beam material are to be known in advance: $E = 210$ [GPa] and $\nu = 0.33$ [-]. To demonstrate the minimization of the objective function, examples of image residuals at the first and final iteration are shown in Figure 3.13. More results of the IDIC-routines are presented in Fig-

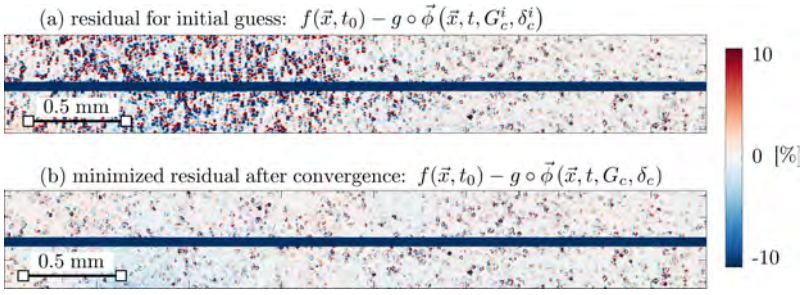

Figure 3.13. The image residuals in terms of [%] of the dynamic range of the images, corresponding to IDIC-routine H marked in Figure 3.14, before minimization (a), and after convergence towards the final CZ-parameters (b).

ure 3.14 for different initial guess values of the CZ-parameter. The convergence behavior in Figure 3.14 is shown in terms of (a) the image residual [%], and (b) the Euclidean norm of the iterative updates of the two CZ-parameters $||\delta\theta||$ (also showing the previously reported "failed" identification results of Section 3.3). An initial guess map is shown in (c), indicating different combinations of the initial guesses and the corresponding converged values of the CZ-parameters. The ranges of initial guess values are: $0.5 \leq G_c^i \leq 3000$ [Jm^{-2}] and $0.1 \leq \delta_c^i \leq 160$ [μm]. The robustness of this IDIC procedure is thereby demonstrated, as it

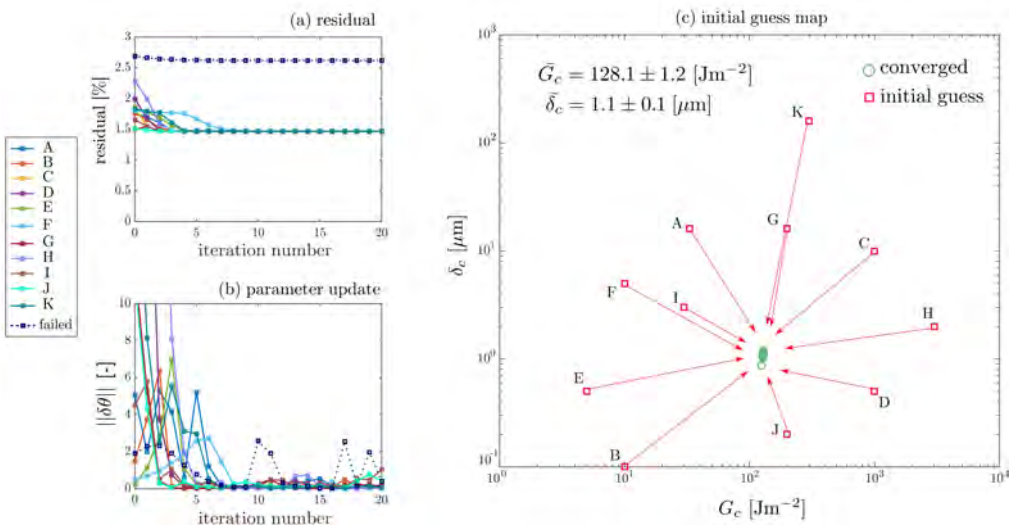

Figure 3.14. Convergence behavior is shown in (a) and (b) for IDIC-routines with different initial guesses for the CZ-parameters. The initial guess map in (c) is a log-log graph that shows the different initial guess combinations of the CZ-parameters and their converged values.

minimizes the image residual for initial guesses that differ orders of magnitude. Uniqueness appears as all routines converge to identical values for the CZ-parameters. The average values and the corresponding standard deviations of the two identified cohesive zone parameters are: $\bar{G}_c = 128.1 \pm 1.2$ [Jm^{-2}] and $\bar{\delta}_c = 1.1 \pm 0.1$ [μm], where it is stressed that the standard deviations do not reflect the total uncertainty of the method, but merely indicate the standard deviation on the average parameter values, acquired by initializing the IDIC-procedure with different initial guess values for the cohesive zone parameters. They reveal the robustness of the optimization routine. The critical opening displacement δ_c is determined with a relatively larger standard deviation than the work of separation G_c. This is consistent with the sensitivity analysis of Section 3.6.2. The value for the critical work of separation G_c lies within 10% of the value determined by the Andersson-Stigh [18] method from the global measurement data of Figure 3.2(c): $G_c = 138$ [Jm^{-2}]. This difference, although small, may be caused by a number of possible systematic errors. Firstly, a different choice for the shape of the traction-separation relation could yield different identification results, although the existence of a model error should reveal itself in the image residual fields. Assessment of this image residual (Figure 3.13) does not indicate that a different shape of the traction-

separation model is needed, therefore, the shape of the employed traction-separation model was not further investigated. Secondly, errors due to three-dimensional kinematics, e.g., anticlastic bending, have not been investigated, however, a three-dimensional model can easily be used with this method. The use of a three-dimensional model will surely be necessary in future work for interface characterization in real microelectronic applications exhibiting complex three dimensional micro-structures.

3.7 Conclusions

To enable the characterization of interfaces in microelectronic systems, typically performed with testing equipment in which the location of load application falls outside the microscopic field of view, a generic and robust identification method based on Integrated Digital Image Correlation was developed. As a proof of principle test-case, a double cantilever beam (DCB) experiment was performed and images of the deformation process were acquired through optical microscopy.

A systematic study, making use of virtual experimentation, was conducted to develop IDIC into an adequate methodology for the identification of interface parameters of a general, arbitrary cohesive zone model that is not intrinsically part of the identification method (i.e., other models may be used). As typical for micro-scale specimens, the physical boundary conditions applied during an experiment fall outside the microscopic field of view, and require a method to substitute these far-field boundary conditions by local boundary conditions within the microscopic field of view (modeled in the IDIC-routine). To extract the local kinematic boundary conditions, a DIC pre-step must first be conducted on the experimental images. General criteria for the DIC-based measurement and application of boundary conditions were formulated. For the DCB test-case, these criteria result in the following simple local boundary conditions: the measured transverse displacements are optimally applied to four longitudinally spaced nodes in a boundary subregion of the FE-model. Using this method, the identification method becomes truly sensitive to the kinematic influence of the interface parameters on the imaged bulk materials. Because of the reduction of the far-field boundary conditions to the local boundary conditions, the corresponding reaction forces from FE-simulation may not trivially correspond to the force measured at the far-field location during (virtual) experimentation. Virtual experimentation showed IDIC to be accurate, without using the far-field force, which is only possible when the elasticity parameters of the deforming bulk material are well known.

The current method for boundary condition application is specific for this test-case comprising a DCB experiment. The key to success here was the optimization of boundary conditions using virtual experimentation. For a different test-case that does not consider DCB kinematics, the kinematics within the microscopic field of view that are imposed by the inaccessible far-field boundary conditions can be assessed in two ways. Firstly, by measuring the kinematics by digital image correlation. Secondly, if possible, by assessing the kinematics from finite element simulations in which the far-field boundary conditions are applied. Such measurements and simulations can be used to develop adequate boundary conditions (and their locations for application). Subsequently, the adequacy of the boundary conditions and their locations can be assessed and optimized using virtual experimentation, as was also done in the DCB test-case analyzed here.

The adequacy of the method to apply the local boundary conditions was first validated on a single cantilever beam experiment, see Appendix A. Subsequently, the optimized IDIC-routine was applied to experimental images, without load data, taken from the DCB experiment. The work of separation G_c and the critical opening displacement δ_c of a cohesive zone model were to be identified. A sensitivity analysis revealed that identification is more sensitive to the former parameter than to the latter parameter. A series of IDIC-analyses with different initial guesses for the parameters all converged to nearly the same solution for the CZ-parameters, indicating that the optimization routine is robust and a unique solution exists. The work of separation G_c lies within 10% of the value determined by the Andersson-Stigh method.

The proposed local boundary conditions applied within a restricted field of view in this chapter, in combination with IDIC with force correlation excluded, proved to be adequate by considering the DCB experiment as a model test-case. Thereby, a generic method based on IDIC has been developed for accurately identifying CZ-parameters, which omits (the invisible) far-field load application and does not require load measurement (when load data is missing or unreliable), but which exploits the elasticity of one of the deforming material layers as an implicit force sensor.

Acknowledgements

This research was carried out under project number M62.2.12472 in the framework of the Research Program of the Materials Innovation Institute (M2i) in the Netherlands (www.m2i.nl). Furthermore, Matthijs Baan and Cédric Guimier are acknowledged for conducting the experiments, and Marc van Maris is acknowledged for facilitating and supervising the experiments.

CHAPTER 4

Mixed-mode cohesive zone parameter identification

Abstract

Mixed-mode loading conditions strongly affect the failure mechanisms of interfaces between different material layers as typically encountered in microelectronic systems, exhibiting complex material stacking and 3D microstructures. The integrated digital image correlation (IDIC) method is here extended to enable identification of mixed-mode cohesive zone model parameters under arbitrary degrees of mode-mixedness. Micrographs of a mechanical experiment with a restricted field of view and without any visual data of the applied far-field boundary conditions are correlated to extract the cohesive zone model parameters used in a corresponding finite element simulation. Reliable or accurate force measurement data is thereby not available, which constitutes a complicating factor. For proof-of-concept, a model system comprising a bilayer double cantilever beam specimen loaded under mixed-mode bending conditions is explored. Virtual experiments are conducted to assess the sensitivities of the technique with respect to mixed-mode loading conditions at the interface. The virtual experiments reveal the necessity of (1) optimizing the applied local boundary conditions in the finite element model and (2) optimizing the region of interest by analyzing the model's kinematic sensitivity relative to the cohesive zone parameters. From a single virtual test, exhibiting a range of mode-mixedness, the mixed-mode cohesive zone model parameters are accurately identified with errors below 1%. The IDIC-procedure is shown to be robust against large variations in the initial guess values for the parameters.

Real mixed-mode bending experiments are conducted on bilayer specimens comprising two spring steel beams and an epoxy adhesive interface, under different levels of mode-mixedness. The mixed-mode cohesive zone model parameters are identified, demonstrating that IDIC is a powerful technique for characterizing interfaces, imaged with a limited field of view, which is relevant for microelectronic applications.

Keywords: full-field identification; Digital Image Correlation; inverse methods; mixed-mode cohesive zone parameters; finite element model

Reproduced from:
A.P. Ruybalid, J.P.M. Hoefnagels, O. van der Sluis, M.P.F.H.L. van Maris, M.G.D. Geers
Mixed-mode cohesive zone parameters from integrated digital image correlation on micrographs only
International Journal of Solids and Structures, 2019, 156–157:179–193
doi: 10.1016/j.ijsolstr.2018.08.010

Nomenclature

BC	boundary condition(s)
CZ	cohesive zone
DCB	double cantilever beam
DIC	digital image correlation
FE	finite element
FOV	field of view
IDIC	integrated digital image correlation
LVDT	linear variable differential transformer
MMMB	miniaturized mixed mode bending
ROI	region of interest
VE	virtual experiment

4.1 Introduction

Development trends in the microelectronics industry require dissimilar material layers to be more densely fabricated into a small volume, while often being subjected to stringent thermo-mechanical loading conditions. The interfaces between the materials are therefore of increasing significance to the device's mechanical and functional integrity, making proper characterization of interfaces of critical importance. The specimen-dependent loading conditions and process-dependent adhesion properties suggest that parameter identification should ideally be conducted on the actual device, bypassing the costly fabrication of dedicated specimens. Characterizing interfaces in such small specimens with complex 3D geometries requires micro-scale imaging whereby the far-field load application is no longer captured in the restricted field of view. Direct interface characterization methods that rely on simplified 2D geometries and well-defined loading conditions [18, 19, 21, 24] are therefore not applicable.

In the previous chapter [133], a method has been proposed to substitute such inaccessible far-field loading conditions on a double cantilever beam (DCB) experiment by *local* boundary conditions (BC) in a corresponding finite element (FE) model, in order to identify cohesive zone (CZ) parameters under mode-I loading conditions using integrated digital image correlation (IDIC) [73, 85, 87, 118]. It has been shown that global force data is not required for the identification of the mode-I cohesive zone parameters, provided that the elasticity parameters of one of the deforming material layers are known (serving as a local force sensor) [133].

Mixed-mode delamination typically occurs in microelectronic systems with 3D microstructures due to the elastic and thermal mismatch between the different material layers. Therefore, the present chapter extends the mode-I IDIC method of [133] to the considerably more complex mixed-mode load cases. A model system is used to assess the developed methodology, consisting of a bilayer specimen loaded in mixed-mode bending. After introducing the identification method of IDIC in Section 4.2, virtual experiments (VE) are analyzed in Section 4.3 on virtual bilayer specimens loaded under different degrees of mode-mixedness. The performance and the limits of the IDIC-based identification technique are thereby in-

vestigated, allowing to assess the complexity accompanying mixed-mode loading conditions. Special attention is given to optimizing the kinematic sensitivity of the IDIC-procedure with respect to the mixed-mode cohesive zone parameters. In Section 4.4, IDIC is subsequently applied to real bilayer specimens bonded with an industrial epoxy adhesive and loaded in mixed-mode bending. Mixed-mode cohesive zone parameters are properly identified using the microscopic images only, and without using global force data (replaced by known elasticity properties of the beams). Conclusions on the effectiveness of the approach are summarized in Section 4.5.

4.2 Methodology

4.2.1 Mixed-mode bending experiments

In order to establish a generic method for the identification of interface parameters of microelectronic systems under mixed-mode loading conditions, a model system is used. This system consists of bilayer specimens loaded in a Miniaturized Mixed Mode Bending (MMMB) setup, developed by Kolluri et al. [114, 132]. The specimens consist of two spring steel beams that are bonded with an industrial epoxy adhesive, i.e., Araldite 2020. The glue layer thickness is approximately 10 [μm], and is applied by filling the micro-scale roughness depressions of the adherends (beams) with glue. To ensure a uniform glue thickness, a razor blade is used to remove excess glue above the adherends' roughness profile. Subsequently, a compressive force of 10 [kN] is applied to bond the beams. The dimensions of each beam are $35 \times 5 \times 0.3$ [mm^3]. After curing of the adhesive at room temperature, an interface pre-crack of 3 [mm] is made by an ultra-thin razor blade, and, subsequently, a speckle pattern is applied to the specimen by spray painting, resulting in speckles with a typical size of ~ 10 [μm]. The specimen is attached to the MMMB setup by dovetail-shaped insets that slide into a fixed position of the MMMB setup (see Figure 4.1).

The MMMB setup is used in combination with a small-scale tensile stage (Kammrath & Weiss), occupying a load cell with a capacity of 50 [N]. The full range of mode-mixedness (i.e., from pure mode-I to pure mode-II) can be imposed by changing the position of the fixture of the MMMB setup, called the "mode selector", to the tensile stage [114, 132]. In-situ MMMB tests are conducted under optical microscopy using a digital camera to capture the deformation process. The 8-bit images, each comprising 2720×2200 pixels, are subsequently used for the integrated digital image correlation (IDIC) identification process. The experimental setup, together with examples of images of the specimen, are shown in Figure 4.1.

4.2.2 Virtual mixed-mode experimentation

To extend the identification technique (explained in Section 4.2.3) and quantify its accuracy in a controlled manner, virtual experiments are conducted before real experiments are performed. As MMMB tests on bilayer specimens are used as a model system, virtual MMMB experiments are carried out by finite element simulations on a model of the bilayer specimen. Artificial images are reproduced from the simulated deformations. Figure 4.2 shows an illustration of the MMMB setup, the mode selector position, and a schematic representation of the externally applied *far-field* boundary conditions. To avoid modeling the entire MMMB setup, the boundary conditions in the virtual experiment are implemented by a nodal tying

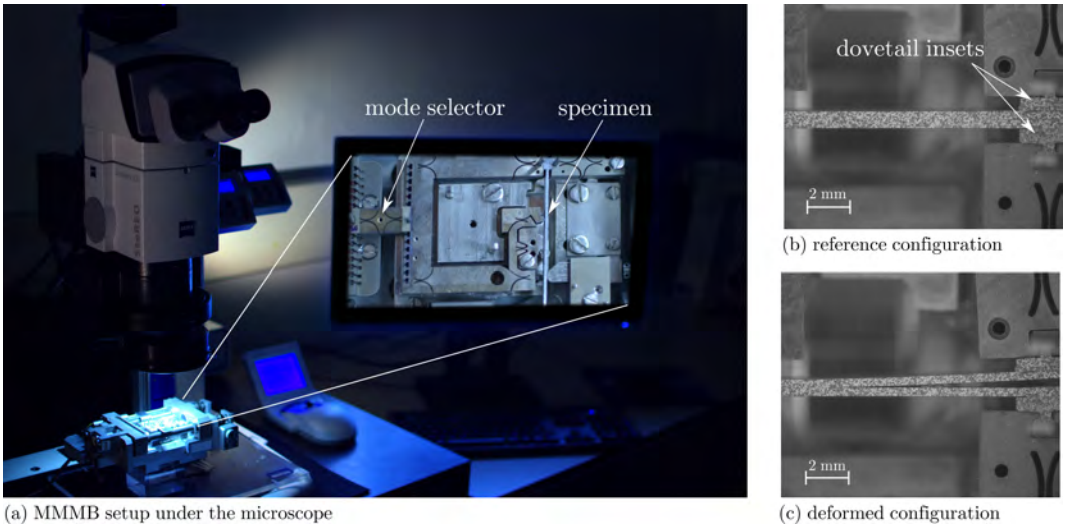

(a) MMMB setup under the microscope (b) reference configuration (c) deformed configuration

Figure 4.1. (a) Miniaturized Mixed Mode Bending (MMMB) setup inside a micro-scale tensile stage imaged with an optical microscope. (b)-(c) Microscopic images of a mixed-mode bending test on a bilayer specimen.

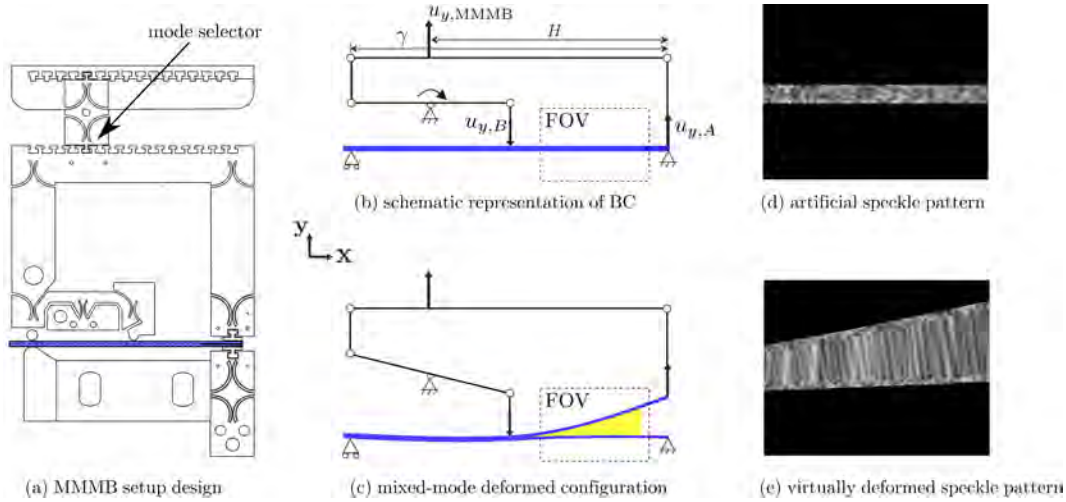

(a) MMMB setup design (b) schematic representation of BC (c) mixed-mode deformed configuration (d) artificial speckle pattern (e) virtually deformed speckle pattern

Figure 4.2. (a) Miniaturized Mixed Mode Bending (MMMB) setup design. (b)-(c) A schematic representation of the applied boundary conditions for virtual experimentation, and an example of a mixed-mode deformed configuration, with the bending beams in blue and the damaged interface in yellow. (d)-(e) Examples of virtual images, corresponding to the indicated field of view (FOV), of an artificial speckle pattern in the reference and the deformed configuration.

relation that reflects the ideal kinematics of the MMMB setup (see [134] for details), and

which reads:

$$u_{y,A} = \frac{1}{1-\xi} u_{y,\mathrm{MMMB}} + \frac{\xi}{1-\xi} u_{y,B}, \tag{4.1}$$

$$\xi = \frac{H}{\gamma}. \tag{4.2}$$

The vertical displacement $u_{y,\mathrm{MMMB}}$ represents the displacement that the tensile stage imposes on the MMMB setup, which is the far-field prescribed kinematic boundary condition in the virtual experiment. The normalized mode selector position ξ defines the amount of mode-mixedness imposed on the bilayer specimen and takes a value between 0 (pure mode-I) and 1 (end notch flexure, i.e., shear plus compression), while pure mode-II is realized at $\xi \approx 0.75$, depending on the specimen specifics, such as its dimensions and mechanical properties [130].

The interface is modeled using an exponential cohesive zone model [125–128, 131] that lumps all damage processes near the crack-tip in the interface plane between two material surfaces. The model implemented here was originally developed by Van den Bosch et al. [135] to describe fibrillating interfaces. It relates the traction vector $\vec{T} = T\vec{e}\,[\mathrm{Nm}^{-2}]$ to the opening displacement vector $\vec{\Delta} = \Delta\vec{e}\,[\mathrm{m}]$ of the separating material surfaces, where $\vec{e}$ is a unit vector along the line that links two associated material points at opposite sides of the interface:

$$T = G_{c,n} \frac{\Delta}{\delta_c^2} \exp\left(-\frac{\Delta}{\delta_c}\right) \exp\left(\ln(\zeta)\frac{d}{2}\right), \tag{4.3}$$

where the work of separation $G_{c,n}$ $[\mathrm{Jm}^{-2}]$ and the critical opening displacement δ_c (corresponding to the maximum effective traction $T_{\max}$) are the model parameters. The local state of mode-mixedness (at every interface location, hence not to be confused with the globally imposed mode-mixedness ξ) is represented by d. In case of pure mode-I opening, $d = 0$, and in case of pure mode-II opening, $d = 2$, while $0 < d < 2$ for intermediate levels of mode-mixedness. Further details of the model can be found in [135]. The model can account for mode-dependency through the parameter ζ, which defines the ratio between the critical work of separation in the tangential (t) and normal (n) direction as follows:

$$\zeta = \frac{G_{c,t}}{G_{c,n}}. \tag{4.4}$$

The cohesive zone model has been implemented by user-defined, planar elements in a three-dimensional finite element model, using the software package *MSC.Marc*. The goal of this research is to be able to identify interface parameters for predictive FE-simulations, in which the interface is modeled with infinitely thin cohesive zone elements. Thereby, different failure mechanisms, physically occurring at a smaller, microscopic scale, are lumped into the cohesive zones of the model, without discriminating between, e.g., cohesive and adhesive failure. The bulk material is described using a linear-elastic material model with Young's modulus E and Poisson's ratio ν corresponding to known values: $E = 210$ [GPa] and $\nu = 0.33$ [-]. A mesh convergence study was conducted to optimize the finite element discretization: for each of the two beams, six elements are used over the thickness, and the

length and width of the elements near the interface are ~ 15 [μm], amounting to approximately 130 elements within the fracture process zone, which typically has a length of several millimeters (the exact length depending on the test-case).

The model effectively allows for the identification of $G_{c,n}$ and $G_{c,t}$. To this end, convenient use is made of the fact that the mode angle, defined as: $\psi = \tan^{-1}\left(\frac{\delta_t}{\delta_n}\right)$, varies significantly along the fracture process zone of the interface [21, 23], as visible in Figure 4.3 for three test-cases with different mode selector positions ξ. In these (and all other) illustrations, the initial crack-tip is located at $x = 32$ [mm] with respect to the origin on the left-end of the specimen, and extends 3 [mm] to the right-end of the specimen. The crack subsequently propagates from right to left during delamination. The variation of the mode angle

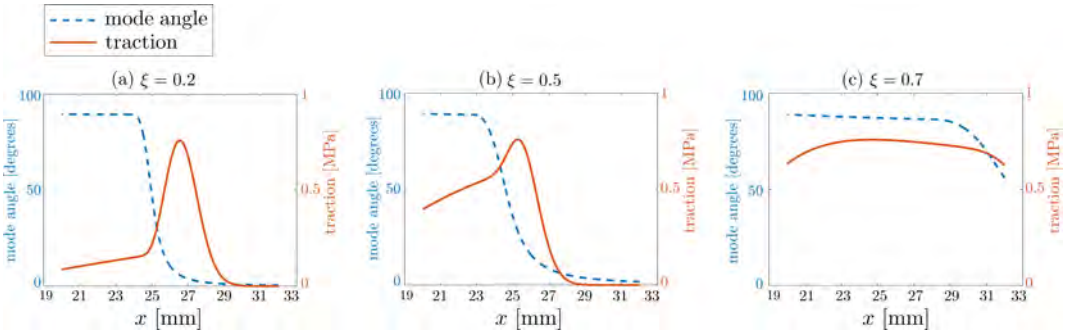

Figure 4.3. The traction and mode angle profiles along the interface (x-coordinate), for virtual test-cases with mode selector positions $\xi = 0.2$, $\xi = 0.5$, and $\xi = 0.7$, plotted for one time increment of the virtual experiment.

depends on the applied boundary conditions, i.e., the amount of mode-mixedness induced by the mode selector position ξ. For the case with $\xi = 0$, exhibiting pure mode-I kinematics through symmetric bending of the two beams, the mode angle does not vary and remains 0° along the entire interface (not shown), since $\delta_t = 0$. For the case with $\xi = 0.7$, exhibiting mostly mode-II kinematics, the mode angle varies to a limited extent, but is relatively high along the entire interface (Figure 4.3(c)). For the test-cases with $\xi = 0.2$ and $\xi = 0.5$, the mode angle varies strongly along the fracture process zone (cf. Figures 4.3(a) and (b)). A spatially varying mode angle can be used to identify both parameters $G_{c,n}$ and $G_{c,t}$ from a single test under mixed-mode loading conditions.

The model described above is next used for conducting virtual mixed-mode bending experiments with different mode selector positions $\xi = 0.0, 0.2, 0.4, 0.5, 0.6, 0.7, 0.75$, spanning the range of mode-mixedness between pure mode-I and pure mode-II. An artificial image of a bilayer specimen in the undeformed reference configuration was created by superposing random gray pixel spots from three standard normal distributions with different widths (3, 8, and 18 pixels), thereby realizing speckle features of different sizes. The speckle pattern was stored in an 8-bit, gray-valued image with 700×550 pixels, corresponding to an imaged field of view (FOV) of 7.1×5.9 [mm^2]. The reference speckle pattern was subsequently deformed using the simulated displacement fields from the virtual experiment by interpolation of the reference gray values to displaced spatial pixel positions. Multiple images were thereby cre-

ated at selected time increments in order to capture the deformation process of the virtual specimen over time. Examples of a reference image and a deformed image are shown in Figures 4.2(d)-(e). In order to quantitatively investigate the effects of mixed-mode loading on the accuracy of the identified cohesive zone parameters, the supplementary (detrimental) effect of image noise is deliberately disregarded, i.e., no image noise is artificially added to the images in the virtual experiment.

4.2.3 Integrated digital image correlation

To identify the cohesive zone parameters, the integrated digital image correlation method [66, 84, 86] is used. Images of a deformation process are correlated by directly optimizing the mechanical parameters of a corresponding finite element model. To this end, residual images are calculated by back-deforming the images of the deformed material configurations, using the displacement fields from finite element simulations, and subtracting them from the image of the undeformed reference configuration:

$$\Psi = \int_\tau \int_\Omega \frac{1}{2} \left(f(\vec{x}, t_0) - g \circ \vec{\phi}(\vec{x}, t, \theta_i) \right)^2 \mathrm{d}\vec{x}\mathrm{d}t, \tag{4.5}$$

where f and g are the scalar intensity fields (e.g., gray values) of the undeformed reference configuration at time t_0 and the deformed configurations at time t, respectively. The symbol $\circ$ is used to denote a function composition, i.e., image g is a function of the mapping function $\vec{\phi}$ that maps the pixel position vector $\vec{x}$ in image f to the pixel position vector in image g [103] by

$$\vec{\phi}(\vec{x}, t, \theta_i) = \vec{x} + \vec{h}(\vec{x}, t, \theta_i), \tag{4.6}$$

using the displacement field $\vec{h}(\vec{x}, t, \theta_i)$ from a finite element simulation of the experiment that depends on the constitutive model parameters $\theta_i = [\theta_1, \theta_2, \ldots, \theta_n]^T$ (where n is the total number of unknown parameters). Subsequently, the Gauss-Newton method is applied to iteratively minimize the square image residual of [Eq. 4.5] for all pixels in the space domain Ω and the time domain τ by updating the finite element model parameters to be identified [103, 118]:

$$\frac{\partial \Psi}{\partial \theta_i} = 0, \tag{4.7}$$

yielding the following linear system of equations:

$$M_{ij} \delta\theta_j = b_i, \tag{4.8}$$

where the correlation matrix M_{ij} and the right-hand side b_i are:

$$\forall (i) \in [1, n], \quad b_i = \int_\tau \int_\Omega \vec{H}_i(\vec{x}, t, \theta_i) \cdot \vec{G}(\vec{x}, t, \theta_i) \left(f(\vec{x}, t_0) - g \circ \vec{\phi}(\vec{x}, t, \theta_i) \right) \mathrm{d}\vec{x}\mathrm{d}t, \tag{4.9}$$

$$\forall (i, j) \in [1, n]^2, \quad M_{ij} = \int_\tau \int_\Omega \vec{H}_i(\vec{x}, t, \theta_i) \cdot \vec{G}(\vec{x}, t, \theta_i) \vec{G}(\vec{x}, t, \theta_i) \cdot \vec{H}_j(\vec{x}, t, \theta_j) \mathrm{d}\vec{x}\mathrm{d}t, \tag{4.10}$$

in which $\vec{G}$ is the gradient of the image with respect to the spatial coordinates, for which different choices can be made, which have been explored in detail in [103]. For convenience, the gradient of reference image f is used here. Furthermore, $\vec{H}_i$ are the *kinematic sensitivity maps*, representing the dependence of the simulated displacements $\vec{h}(\vec{x}, t, \theta_i)$ on each parameter θ_i:

$$\vec{H}_i(\vec{x}, t, \theta_i) = \frac{\partial \vec{h}(\vec{x}, t, \theta_i)}{\partial \theta_i}. \tag{4.11}$$

In order to calculate these sensitivity maps $\vec{H}_i(\vec{x}, t, \theta_i)$, a finite difference approach is used, which requires the model response for a parameter set and the perturbed model responses for each perturbed parameter.

The problem of interest focuses on IDIC combined with microscopy where local images of the deformation process are recorded. Due to the required magnification, the load application, i.e., the physical boundary conditions (BC) typically lie outside the microscopic field of view. In Chapter 3, a method has been developed to substitute these inaccessible far-field boundary conditions by local, kinematic boundary conditions within the microscopic field of view corresponding to the finite element model employed in IDIC [133]. The method requires a digital image correlation (DIC) pre-step to extract the displacements in a limited set of subregions of the images of the deforming specimen. Subsequently, it has been shown that the resulting displacements should be applied to a minimum number of nodes in the finite element model to prevent over-constrained kinematics. These results, however, were confined to mode-I interface delamination only. The more involved local boundary conditions under mixed-mode loading conditions are studied and optimized in Section 4.3.1, using virtual experiments. Furthermore, it is emphasized that IDIC does not rely on explicit tracking of the crack-tip during experimentation. Instead, the experimental data in the form of images is used within the IDIC-procedure to optimize the cohesive parameters of the constitutive model used within the FE-simulations. The image correlation procedure within IDIC thereby minimizes the image residual, implicitly resulting in the crack-tip's location to be validated by the FE-simulation, omitting the need to track the crack-tip.

4.3 Mixed-mode parameter identification using virtual MMMB experiments

The purpose of virtual experimentation is to assess the sensitivities of the identification method to interface delamination under mixed-mode loading in well-defined conditions. In order to capture the required kinematics in microelectronic systems, sufficient magnification is required, which results in an image with a restricted field of view. Appropriate local boundary conditions under mixed-mode loading conditions are therefore established using the model system specified in Section 4.3.1. The importance and the optimization of the kinematic sensitivity of IDIC with respect to the cohesive zone parameters is discussed in Section 4.3.2. Finally, identification results from virtual experimentation with different levels of mode-mixedness are discussed in sections 4.3.3 and 4.3.4, by quantifying the relative errors on the identified cohesive zone parameters. First, the optimization of the IDIC-routine is performed by identifying the effective parameters G_c and δ_c for a mode-insensitive cohesive

zone model, i.e., with the mixed-mode parameter fixed at the value: $\zeta = 1$. After the routine has been optimized, new virtual experiments are performed from which the mixed-mode parameters are also identified, which is described in Section 4.3.4.

4.3.1 Local boundary conditions in a restricted field of view

Figure 4.4 illustrates the restricted microscopic field of view, which for the considered experiments has a horizontal field width (HFW) of 7.1 [mm]. The field of view neither captures the locations at which the loading is applied and measured (far-field locations not shown in the illustration), nor the full length of the specimen. The recently introduced method [133] is extended for substituting the far-field boundary conditions of the (virtual) experiment by local boundary conditions in a finite element model that corresponds to the restricted field of view, here for mixed-mode loading conditions. The procedure for applying local

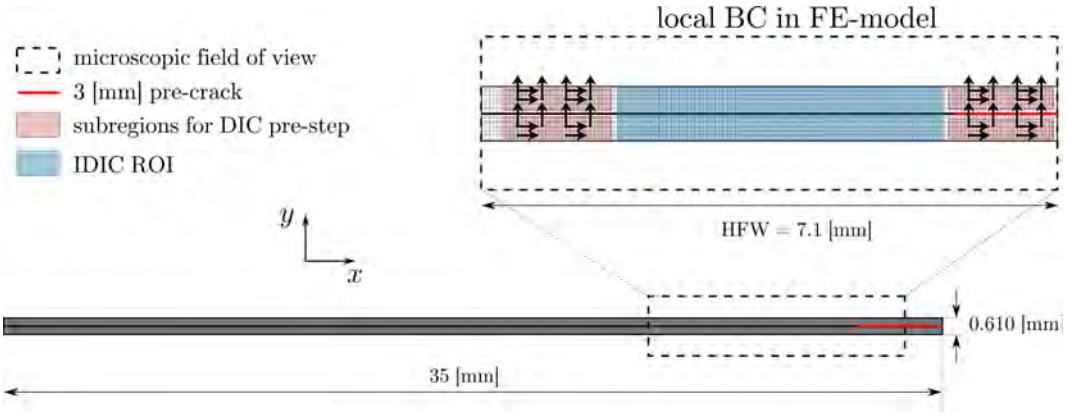

Figure 4.4. Illustration of the local boundary condition (BC) application in the 2D finite element (FE) model of IDIC, where arrows indicate in which direction (x or y) the measured displacements from the DIC pre-step are prescribed to the corresponding BC-nodes. The subregions used for the DIC pre-step and the region of interest (ROI) used for IDIC are highlighted.

boundary conditions is: (1) displacements are measured in four subregions of the images (two per beam) by a digital image correlation (DIC) "pre-step"; (2) the measured normal displacements (in y-direction) are applied to four longitudinally aligned nodes in each subregion of the finite element model to accurately capture the bending kinematics of the beams with a limited number of boundary condition nodes to prevent over-constraining [133]; (3) additionally, and different from the mode-I DCB test-case of [133], the tangential displacement (in x-direction) are prescribed at four nodes in each subregion to accurately capture the linearly varying shear deformation, associated with mixed-mode kinematics in which the beams do not bend symmetrically. Again, a limited number of additional boundary condition nodes is used in order to prevent over-constraining. An additional advantage of using a local model with local boundary conditions is that only the specimen geometry corresponding to the imaged field of view needs to be modeled, reducing computational costs in the finite element simulation, and thus, in the identification procedure. Because of the reduction of the far-field boundary conditions to the local boundary conditions, the

corresponding reaction forces from finite element simulations do not trivially compare to the force measured at the far-field location during (virtual) experimentation. However, as shown in [133], the elastically deforming beams act as an implicit force sensor, making force validation unnecessary, if, and only if, the elasticity parameters of the beams are well known. An additional advantage of this approach is the fact that it circumvents frictional losses in the test-setup which are influencing the measured far-field forces.

The digital image correlation "pre-step" procedure, used to measure the kinematic boundary conditions for the local finite element model, and its optimization are discussed in Appendix B. The accuracy of the DIC pre-step is improved when using images of higher resolution. Therefore, instead of using the images described earlier in Section 4.2.2 with 700×550 pixels, high resolution images with 2600×2024 pixels are used in all the subsequently discussed (virtual) experiments. The above described method of extracting and applying local boundary conditions was validated (see Appendix B) and applied for all the mixed-mode test-cases.

4.3.2 Sensitivity analysis

The virtual test-case with mode selector position $\xi = 0.7$ is analyzed. In this test-case a total of 18 images were used for the IDIC-routine: 1 reference configuration and 17 virtually deformed configurations. Figure 4.5 shows the displacement fields restricted to the imaged field of view indicated in Figure 4.2 and the reaction force in the test-setup at the location where $u_{y,\mathrm{MMMB}}$ is prescribed in the virtual experiment (Figure 4.5). A cross-section of the displacement field at a fixed y-level is indicated by the dotted red line and plotted in time. The sudden force drop and the accompanying abrupt opening of the interface at increment # 10 are caused by the rapid release of elastic energy that was built up in the beams, triggering unstable interface crack propagation. After the initial drop, the force increases again as the interfacial crack-tip approaches the central pressure point that imposes displacement $u_{y,\mathrm{B}}$ (see Figure 4.2), which arrests the unstable crack propagation.

The sensitivity of the kinematics with respect to the two effective cohesive zone parameters (in this case of the mode-insensitive model with $\zeta = 1$) is investigated by assessing the sensitivity maps $\vec{H}_i$ as defined in [Eq. 4.11] and shown in Figure 4.6. The perturbation factor $\delta\theta$ for calculating the kinematic sensitivity fields having unit [px/$\delta\theta$] (where px indicates a pixel unit), is taken as 1% of the cohesive parameter θ_i to which the sensitivity field corresponds. Figure 4.6 reveals that the displacement fields become insensitive to the cohesive zone parameters for $t > 9$, which corresponds to the time increment at which the interfacial crack propagates instantaneously through the entire field of view. Since the beams have hereafter delaminated, the beam kinematics are locally no longer directly influenced by the interface, at least not within the field of view.

Another important observation is that the sensitivity is zero near the locations at which the local boundary conditions are applied in the finite element model, around $x = 27$ [mm] and $x = 31.5$ [mm]. This is obvious because at these locations the kinematics are dictated by the boundary conditions and therefore not sensitive to the cohesive zone parameters.

In order to improve the sensitivity of the IDIC-routine with respect to the cohesive zone parameters, the region of interest is improved in space and time. Since the crack propagates through the field of view of the images and even beyond, there is no gain in shifting the region of interest more toward the center (to the left) of the specimen. However, from the

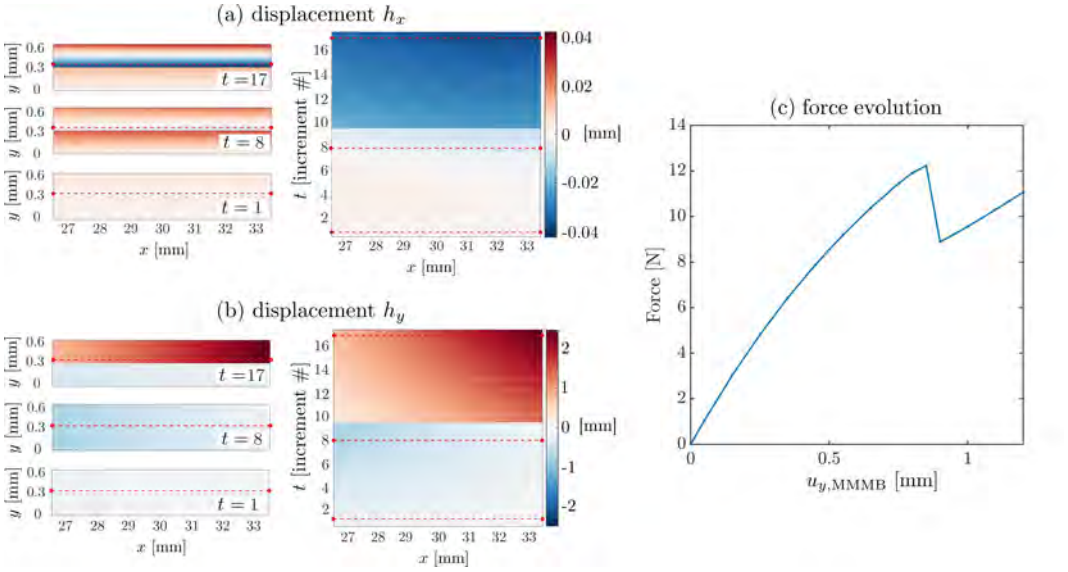

Figure 4.5. (a)-(b) The x- and y-components of the displacement fields (within the field of view) from the virtual experiment with mode selector position $\xi = 0.7$ for three time increments and for a single y-cross-section for all time increments t, and (c) the force evolution versus the prescribed displacement of the virtual experiment.

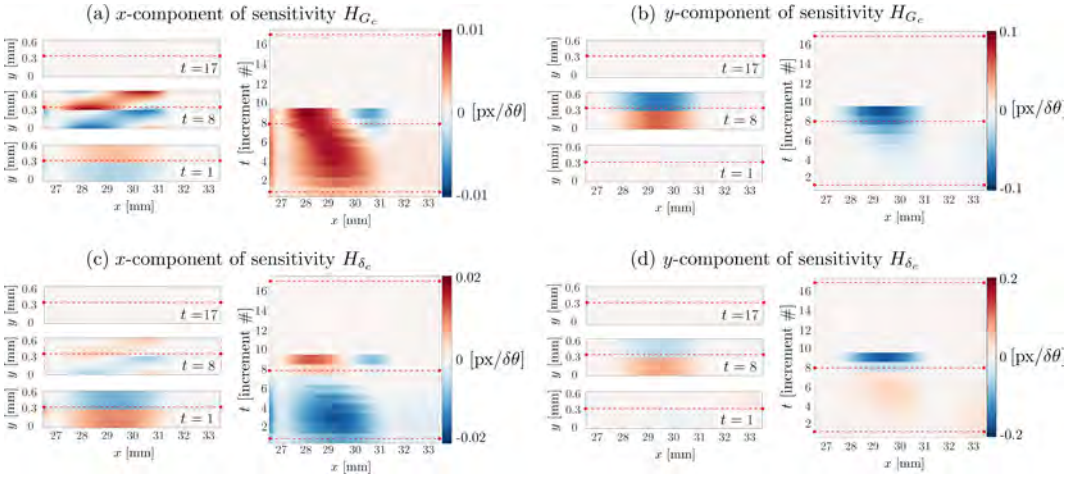

Figure 4.6. x- and y-components of the sensitivity fields in [px/$\delta\theta$] for the two parameters G_c and δ_c for three time increments and for a single y-cross-section for all time increments.

sensitivity fields of Figure 4.6 it is clear that the kinematic sensitivity is deficient near the initial crack-tip at $x = 32$ [mm], because of the selected locations of the subregions in which local boundary conditions are applied. Therefore, these boundary condition subregions are

shifted toward the right end of the specimen, extending the region of interest used for IDIC by ~ 1 [mm] and thereby capturing the initial crack-tip location. Furthermore, the images corresponding to the time increments in which the sensitivity is lost are neglected, i.e., for this case, from increment # 10 onward. This results in only 10 images to be taken into account for IDIC, corresponding to the delamination regime before the unstable force drop. The sensitivity fields corresponding to this expanded region of interest are presented in Figure 4.7 and reveal that the region in which the kinematics are sensitive to the cohesive zone parameters has been increased by ~ 1 [mm]. The moving crack-tip location (from

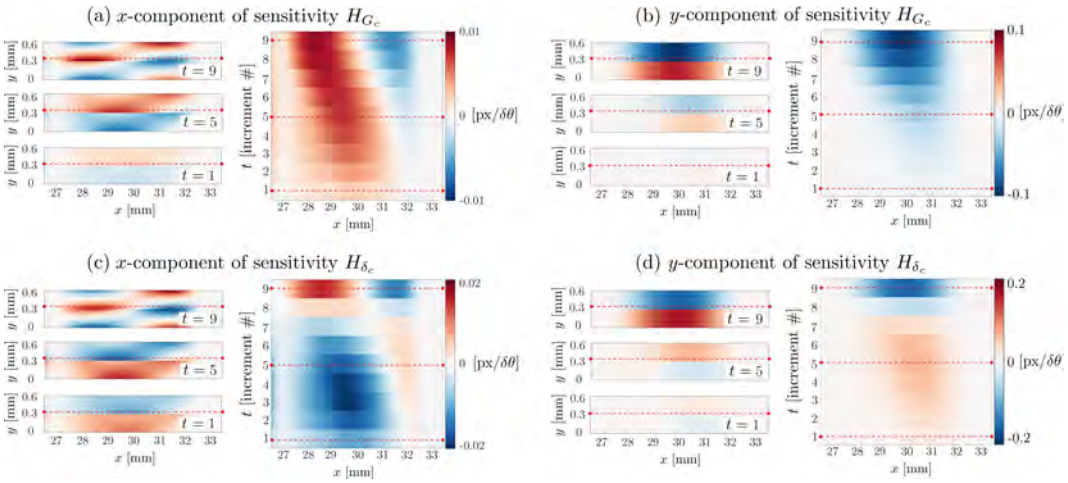

Figure 4.7. x- and y-components of the sensitivity fields in [px/$\delta\theta$] for the two parameters G_c and δ_c for three time increments and for a single y-cross-section for all time increments.

the right at the first increment to the left at the final increment) is clearly visible in the x-components of the sensitivity maps.

The sensitivity study demonstrates that by optimizing the region of interest used in IDIC in space and time, the kinematic sensitivity of IDIC with respect to the cohesive zone parameters can be significantly improved.

4.3.3 Results for mode-independent cohesive zone parameter identification under mixed-mode conditions

The parameters of a mode-independent cohesive zone model, in which the mixed-mode parameter is set to $\zeta = 1$, are next identified for the virtual test-cases with different global levels of mode-mixedness, i.e., different mode selector positions ξ. The results are summarized in Table 4.1 in terms of the relative errors ϵ_i on the identified cohesive zone parameters, which are calculated as follows in [%]:

$$\epsilon_i = \frac{\theta_i - \theta_{\text{ref}}}{\theta_{\text{ref}}} \times 100\%, \tag{4.12}$$

where θ_i is the identified parameter value after convergence of the IDIC-procedure, and θ_{ref} is the reference value used in the virtual experiment. The parameters were given an erroneous

initial guess at the start of the identification procedure with values of: $G_c^i = 1500$ [Jm^{-2}], i.e., an error of 4545% and $\delta_c^i = 4600$ [μm], i.e., an error of 28295%, with respect to the reference values θ_{ref} , also shown in Table 4.1. The IDIC-routine successfully minimizes the

Table 4.1. Identified cohesive zone parameters and their relative errors ϵ_i in [%] of all the virtual test-cases with different mode selector positions.

	θ_{ref}	$\xi = 0.0$	$\xi = 0.2$	$\xi = 0.4$	$\xi = 0.5$	$\xi = 0.6$	$\xi = 0.7$	$\xi = 0.75$
G_c [Jm^{-2}]	33.0	33.5	33.7	33.3	33.4	32.8	33.0	31.0
ϵ_{G_c} [%]	-	1.6	2.1	1.0	1.2	−0.5	0.0	−6.2
δ_c [μm]	16.2	16.5	16.4	16.3	16.5	16.1	16.0	15.1
ϵ_{δ_c} [%]	-	1.9	1.2	0.6	1.9	−0.6	−1.2	−6.8

image residuals, of which examples for one test-case with mode selector position $\xi = 0.7$ are shown in Figures 4.8(a) and (e). The blue horizontal band in the residual images is a masked region not taken into account in the IDIC-procedure, since pattern degradation occurs within that region due to the interface opening, which would corrupt the correlation procedure. The average absolute residual value taken over all pixels in space and time is plotted against the iteration number in Figure 4.8(b) for all virtual test-cases, showing its minimization during IDIC. Convergence towards the reference cohesive zone parameter values of the virtual experiment is achieved for all test-cases, see Figures 4.8(c)-(d).

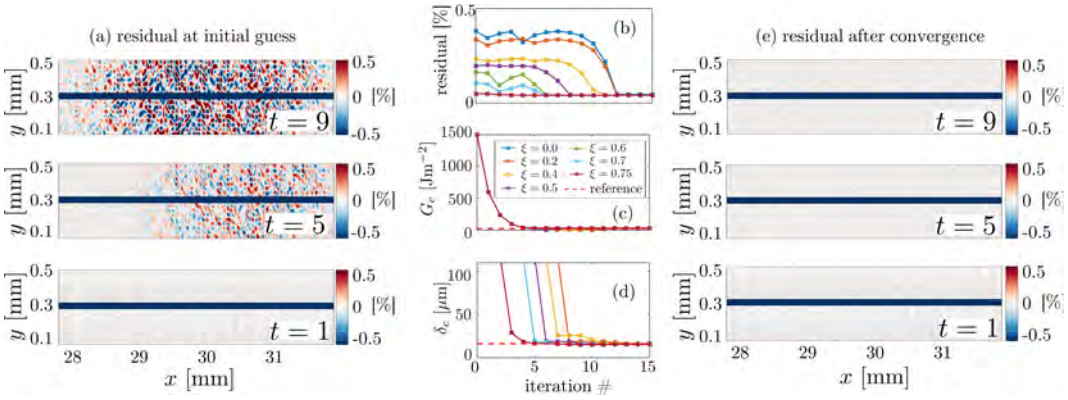

Figure 4.8. Examples of residual fields, in percentages [%] of the images' dynamic range, at three time increments for the initial guess of the IDIC-routine (a), and after convergence (e) for the virtual test-case with mode selector position $\xi = 0.7$. Convergence behavior (b)-(d) of the IDIC-routine in terms of the image residual and the cohesive zone parameter values for all virtual test-cases with different mode selector positions ξ. The blue band in the image residuals represents a masked region not taken into account in IDIC.

From these results it is concluded that the effective cohesive zone parameters are adequately identifiable under mixed-mode conditions. Only for the case with nearly pure mode-II loading conditions, i.e., mode selector position $\xi = 0.75$, errors on the identified

cohesive zone parameters above 5% emerge (cf. Table 4.1).

4.3.4 Mode-dependent cohesive zone parameter identification under mixed-mode conditions

So far, a mode-independent cohesive zone model has been used of which the effective parameters G_c and δ_c have been identified. However, for realistic applications, different values for the cohesive zone model parameters in the normal (n) and tangential (t) directions are required to adequately describe the mode-dependent behavior. Several virtual test-cases with different levels of mode-mixedness, i.e., mode selector positions $\xi = 0.0, 0.2, 0.5, 0.7$, are investigated with the objective to identify the parameters, $G_{c,n}$, δ_c, and ζ of the mixed-mode cohesive zone model described in Section 4.2.2.

Sensitivity analysis

To assess the potential for identifying the mixed-mode cohesive zone model parameters $G_{c,n}$, δ_c, and ζ ($G_{c,t}$ is extracted through [Eq. 4.4]), a sensitivity analysis is first performed. Because of the additional degree of freedom ζ, the sensitivity analysis is more intricate and it becomes more insightful to investigate the sensitivity matrix M_{ij} [Eq. 4.10], as suggested in [45, 65, 136]. The sensitivity matrix M_{ij} is symmetric, and it represents the Hessian of the Gauss-Newton scheme of [Eq. 4.8]. As becomes clear from [Eq. 4.10], it reflects the sensitivity of the optimization routine to each parameter and indicates potential cross-sensitivity that may jeopardize the optimization of cohesive zone parameters. Cross-sensitivity means that optimizing one parameter provokes the same (or highly similar) change in the kinematics as the optimization of another parameter, resulting in non-uniqueness in identifying the corresponding parameters. Spectral decomposition of the real-valued, symmetric sensitivity matrix M [45, 65] allows to extract and visualize the cross-sensitivity and is mathematically written in matrix form (omitting the index notation) as:

$$M = QDQ^T, \tag{4.13}$$

where Q is an orthogonal matrix comprising columns that represent the eigenvectors q_i, and D is a diagonal matrix containing the corresponding eigenvalues d_i. The eigenvalues in this matrix are typically ordered from large (the left-most diagonal element of D) to small (the right-most diagonal element of D) to which also the arrangement of the eigenvector columns q_i correspond, i.e., q_1 corresponds to the largest eigenvalue d_1 and q_3 corresponds to the lowest eigenvalue d_3. The M-matrix, normalized by its maximum value, the corresponding eigenvalue matrix D, and the orthonormal eigenvector matrix Q are shown in Figure 4.9 for different test-cases with different mode selector positions ξ.

For the case with $\xi = 0.0$, in which no mode-II kinematics is triggered by the boundary conditions, the M-matrix clearly indicates that the sensitivity towards ζ is indeed insignificant, since the sensitivity field $\vec{H}_\zeta$ takes near-zero values in nearly the entire spatial and temporal domain (not shown here). For that reason, this test-case is obviously not suitable for identifying ζ. For the test-cases with higher mode-mixedness, the sensitivity towards ζ clearly increases.

The eigenvalue analysis allows to assess the independence of the parameter sensitivities. When the eigenvalues d_i are distinct, then the eigenvectors q_i form an orthogonal set, i.e.,

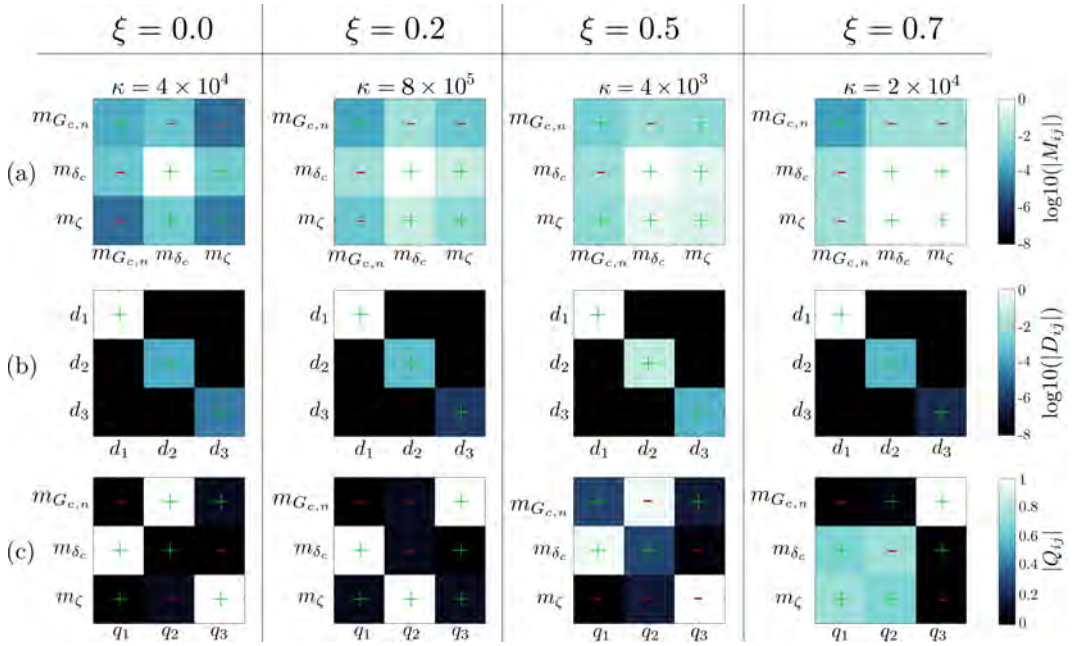

Figure 4.9. (a) The sensitivity matrix M, with κ being the condition number of M, (b) the eigenvalue matrix D, and (c) the eigenvector matrix Q, for virtual test-cases with different levels of mode-mixedness ξ. The log-scales in M and D are used to improve the visible discreteness of the colors, and the signs of the values are plotted in each matrix element.

the vectors q_i are linearly independent [137]. The Q-matrix reveals the relation between the eigenvectors q_i and the original sensitivity vectors m_i. Particularly for the test-case with $\xi = 0.7$, the first two eigenvectors (first two columns of Q) are each predominately composed of combinations of two of the original vectors in M: m_{δ_c} and m_ζ. This reveals that the original sensitivity vectors m_i do not form an orthogonal set for the case $\xi = 0.7$, indicating that there is more cross-sensitivity than for the other cases, in which the eigenvectors are more or less dominated by only one of the original vectors of M. This may cause the corresponding interface parameters to be less uniquely identifiable for the test-case with $\xi = 0.7$. For all the other test-cases, with $\xi = 0.0$, $\xi = 0.2$ and $\xi = 0.5$, insignificant cross-sensitivity is to be expected. However, the test-case with $\xi = 0.5$ shows the highest sensitivity for all parameters, as seen in the corresponding M-matrix. From the relatively high sensitivity seen in the M-matrix, in combination with the diagonal dominance of the M-matrix as concluded from the eigenvalue analysis, and which is also confirmed by the relatively low condition number κ of the M-matrix (printed above the M-matrix in Figure 4.9), it is expected that the test-case with mode selector position $\xi = 0.5$ yields the most accurate identification results for the mixed-mode cohesive zone parameters $G_{c,n}$, δ_c, and ζ.

Results for mode-dependent cohesive zone parameters

The results for the different test-cases are shown in Table 4.2. All test-cases were initialized with imperfect initial guess values for the IDIC-procedure. The test-case with mode selector position $\xi = 0.5$ yields the most accurate results as expected from the sensitivity analysis above. Examples of image residual fields are shown in Figures 4.10(a) and (f) for the test-

Table 4.2. The reference mixed-mode cohesive zone parameters as used for virtual experimentation, the identified parameters and their relative errors ϵ_i [%] of all the virtual test-cases with different ξ.

	reference	$\xi = 0.0$	$\xi = 0.2$	$\xi = 0.5$	$\xi = 0.7$
$G_{c,n}$ [Jm^{-2}]	33.0	33.0	34.3	33.1	51.7
$\epsilon_{G_{c,n}}$ [%]	-	-0.1	3.9	0.4	56.6
δ_c [μm]	16.2	16.3	16.8	16.1	10.4
ϵ_{δ_c} [%]	-	-0.4	3.5	0.6	-35.8
ζ [-]	3.0	3.3	2.0	3.0	1.4
ϵ_ζ [%]	-	11.2	-33.7	0.5	-52.4

case with mode selector position $\xi = 0.5$. The average absolute residual value taken over all pixels in space and time is plotted against the iteration number in Figure 4.10(b) for all mixed-mode virtual test-cases, showing its minimization during IDIC. The convergence plots of the cohesive zone parameters are shown in Figures 4.10(c)-(e). For all virtual test-cases the image residuals are properly minimized, even for the test-cases with significant errors on the parameter ζ (cf. Table 4.2). This emphasizes that the image residual does not reflect the insensitivity towards certain parameters, which highlights the importance of the additional sensitivity analysis. Furthermore, for the test-case with mode selector position $\xi = 0.0$, exhibiting no mode-II kinematics, the insensitivity towards ζ (resulting in a significant error for ζ) does not negatively affect the identification of the two other parameters $G_{c,n}$ and δ_c. For the test-case with mode selector position $\xi = 0.7$, the cross-sensitivity, as identified in the corresponding sensitivity matrices of Figure 4.9, results in relatively large errors on all the mixed-mode cohesive zone parameters, revealing that cross-sensitivity has a more detrimental effect on the accuracy of the affected parameters than the insensitivity with respect to another single parameter.

The robustness of the IDIC-method is evaluated for the test-case with mode selector position $\xi = 0.5$ by initializing the IDIC-procedure with different initial guess value combinations for the three parameters. Figure 4.11 shows a logarithmic initial guess map for the following initial guess ranges: $1 \leq G_{c,n}^i \leq 1500$ [Jm^{-2}], $1.8 \leq \delta_c^i \leq 110$ [μm], and $0.05 \leq \zeta^i \leq 7.4$ [-], and the corresponding values after convergence. The mean values and the corresponding standard deviations are: $\bar{G}_{c,n} = 33.1 \pm 0.0007$ [Jm^{-2}], $\bar{\delta}_c = 16.3 \pm 0.0002$ [μm], $\bar{\zeta} = 3.0 \pm 0.0001$ [-]. The uniqueness of the solution is indicated by the small standard deviations and signifies the robustness of the IDIC-routine.

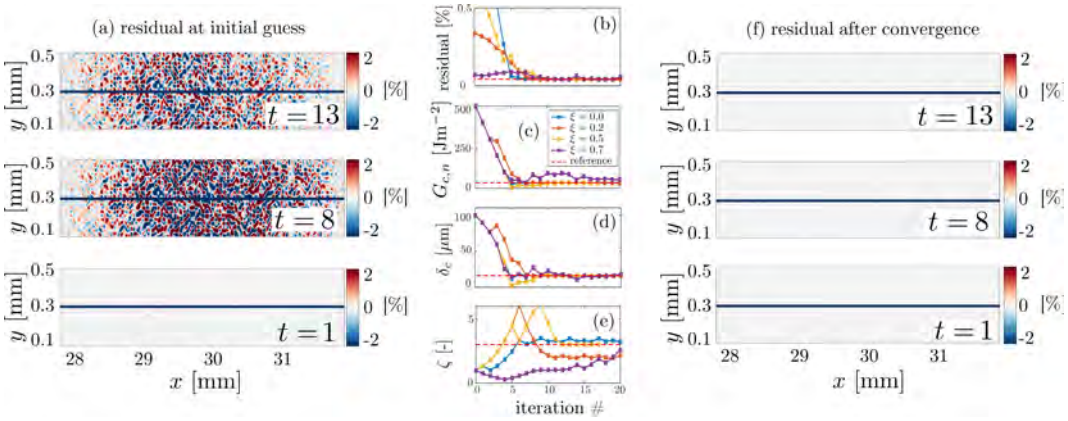

Figure 4.10. Examples of residual fields, in percentages [%] of the images' dynamic range, at three time increments for the initial guess of the IDIC-routine (a), and after convergence (f) for the virtual test-case with mode selector position $\xi = 0.5$. Convergence behavior (b)-(e) of the IDIC-routine in terms of the image residual and the mixed-mode cohesive zone parameter values for all virtual test-cases with different mode selector positions ξ. The blue band in the image residuals represents a masked region not taken into account in IDIC.

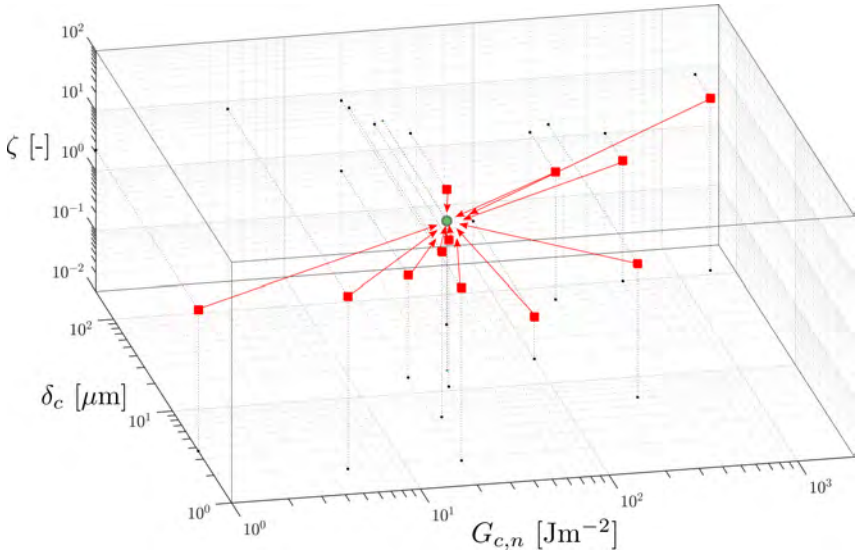

Figure 4.11. Log-log initial guess map depicting the different initial guess combinations of the mixed-mode cohesive zone parameters (red squares) and the corresponding converged values (green circles, which are all in close proximity to one another).

4.4 Identification results from real experiments

The identification method is now applied to experimental results from real MMMB tests (cf. Figure 4.1) in which different levels of mode-mixedness are imposed on the bilayer specimens: $\xi = 0, 0.25, 0.5, 0.63$. The acquired insights from virtual experimentation regarding the increase of kinematic sensitivity by selecting a proper region of interest for IDIC in space and time (see Section 4.3.2), are applied. The real experiments are meant to prove the concept of the identification procedure and demonstrate its applicability in a real test-case. In other words, the identification procedure of IDIC, rather than the identification results for the specific interface used as a test-case, is the main focus of this Section.

4.4.1 Digital image correlation pre-step

The same DIC pre-step procedure as explained in Section 4.3.1 and Appendix B was used for extracting the kinematic boundary conditions from the experimental images, yielding low image residual fields of which an example is shown in Figure 4.12. The mean absolute value of this image residual equals 0.45 [%], validating the use of the extracted displacements as local kinematic boundary conditions in the finite element model.

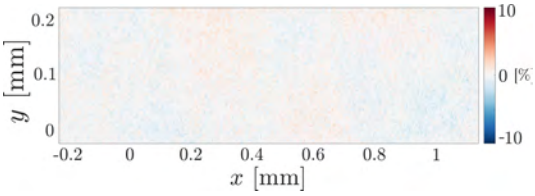

Figure 4.12. Residual field between the deformed configuration at the final time increment and the reference configuration, expressed in [%] of the dynamic range of the images, of the DIC pre-step in the bottom-right subregion (see Figure 4.4) of the experimental images.

4.4.2 Force evaluation

Although force data is not used for identification purposes, the evaluation of the measured force gives insight in the stability of the crack propagation process. It was found that realizing consistent specimens was challenging due to improper mixing of the two-component adhesive. After a batch of specimens showed unstable crack propagation in the corresponding force-displacement curves from MMMB tests with $\xi = 0$ (not shown), the mixing ratio between the resin and the hardener was changed to 100:25, instead of the ratio 100:30 as prescribed by the adhesive's manufacturer. Consequently, stable crack propagation is observed for cases with $\xi = 0$ and $\xi = 0.25$ in the force-displacement curves of Figure 4.13 as measured by a load cell and an LVDT at the location of the applied far-field boundary conditions. For most test-cases the force increases to a maximum after which it decreases. The case with $\xi = 0.5$ shows a sudden force-drop (snap-through), and therefore less stable crack propagation. The decreasing force is associated with a propagating, fully developed fracture process zone, resulting in delamination of the interface. The case with $\xi = 0.63$ does not show such a decreasing force, indicating that the interface has not failed before the experiment terminates when the maximum deflection limits of the MMMB setup's flexure

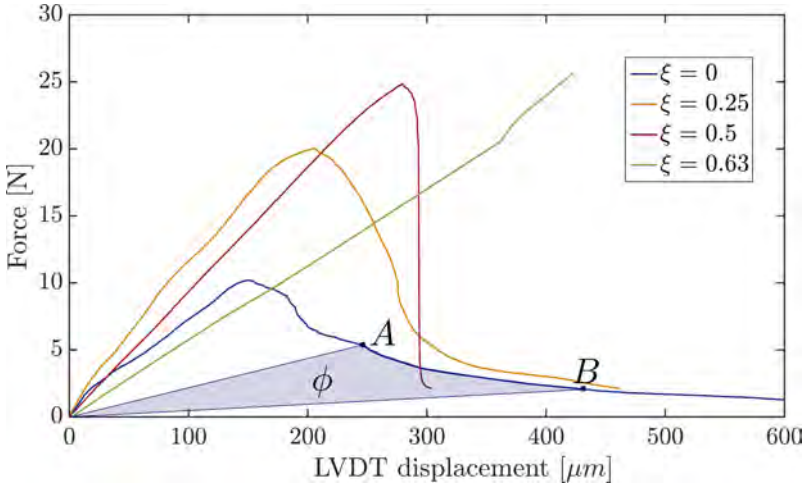

Figure 4.13. Force evolution of four MMMB test-cases with different mode selector positions ξ. The area underneath the curve for the case with $\xi = 0$ indicates the energy ϕ dissipated during delamination from point A to point B.

hinges have been reached. The intact interface between the beams is also noticeable in the experimental image corresponding to the final force data point, in which no interface opening is visible (not shown). Although the true loading state is difficult to assess locally, it is likely that for the case with $\xi = 0.63$ a loading condition beyond pure mode-II is present at the interface, i.e., approaching an end notch flexure test, involving interface compression that may impede delamination through friction between the surfaces of the two spring steel beams. For the above-mentioned reasons, the experimental results for the case of $\xi = 0.63$ are excluded from further analysis.

From the force-displacement curve for $\xi = 0$, the dissipated energy ϕ [J] can be calculated from the area underneath the curve, as indicated in Figure 4.13. The work of separation G_c [Jm^{-2}], which is the energy needed for the creation of new material surface during delamination, can then be calculated as follows:

$$G_c = \frac{\phi}{(a_B - a_A)w}, \tag{4.14}$$

where $w = 5$ [mm] represents the width of the specimen, and a_A and a_B are the crack lengths corresponding to points A and B on the force-displacement curve in Figure 4.13. The work of separation calculated from the force-displacement curve for the test-case with $\xi = 0$ equals $G_c = 44.2$ [Jm^{-2}]. The force-displacement data may, however, contain inaccuracies due to friction and clearances in the MMMB-setup, inducing errors in the determination of G_c based on the area underneath the curve. Particularly for the cases with higher mode-mixedness ($\xi > 0$), G_c cannot be calculated from the force-displacement data straightforwardly due to the multi-directional nature of the applied forces on the setup for which a unidirectional force measurement is inadequate (if the forces due to lateral constraints in the clamps are not measured).

4.4.3 Mode-dependent cohesive zone parameter identification

The mixed-mode cohesive zone model parameters $G_{c,n}$, δ_c and ζ are identified by IDIC. Prior to initializing the IDIC-routine, a sensitivity analysis as described in Section 4.3.4 is performed for two cases with mode selector positions $\xi = 0.25$ and $\xi = 0.5$. The sensitivity matrix M, the corresponding eigenvalue matrix D, and the eigenvector matrix Q are shown in Figure 4.14.

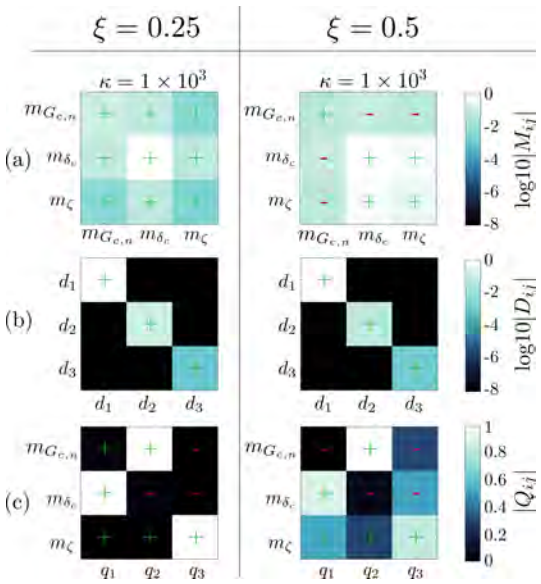

Figure 4.14. (a) The sensitivity matrix M, with κ being the condition number of M, (b) the eigenvalue matrix D, and (c) the eigenvector matrix Q, for real test-cases with different levels of mode-mixedness ξ. The log-scales in M and D are used to improve the visible discreteness of the colors, and the signs of the values are plotted in each matrix element.

From the analysis of the M-matrices, it is concluded that the test-case with $\xi = 0.5$ yields the highest sensitivity for all parameters. However, the corresponding Q-matrix indicates significant cross-sensitivity, while the test-case with mode selector position $\xi = 0.25$ shows the most linearly independent (orthogonal) sensitivity vectors m_i, indicating that the test-case with $\xi = 0.25$ allows for the most unique determination of the parameters $G_{c,n}$, δ_c, and ζ (since the corresponding eigenvalues d_i are distinct). Therefore, the test-case with mode selector position $\xi = 0.25$ is used for the identification of the mixed-mode cohesive zone parameters. The test-case with $\xi = 0.5$ was also analyzed (not shown), but did not reach stable convergence toward a unique solution due to the cross-sensitivity, as expected from the sensitivity analysis (Figure 4.14). Figure 4.15 shows the convergence behavior of IDIC for test-case $\xi = 0.25$, initialized with the following initial guess values: $G^i_{c,n} = 20$ [Jm^{-2}], $\delta^i_c = 4$ [μm], and $\zeta^i = 0.1$ [-] in which proper minimization of the image residual is achieved. The blue horizontal band in the residual images is a masked region not taken into account in the IDIC-procedure, since pattern degradation occurs within that region due to the interface

opening.

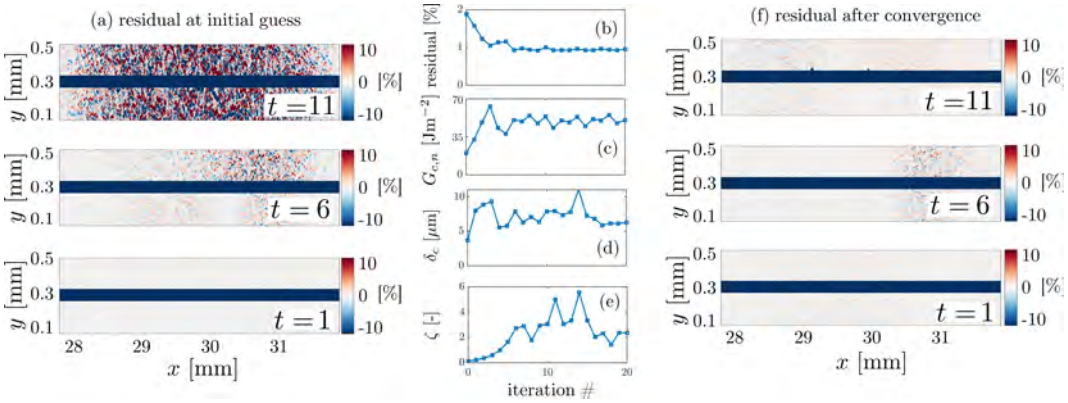

Figure 4.15. Residual fields, in percentages [%] of the images' dynamic range, at three time increments for (a) the initial guess of the IDIC-routine, and (f) after convergence for the test-case with mode selector position $\xi = 0.25$. (b)-(e) The corresponding convergence behavior of the IDIC-routine in terms of the image residual and the cohesive zone parameter values. The blue band in the image residuals represents a masked region not taken into account in IDIC.

Similar to the analysis of the virtual experiments in Section 4.3.4, the robustness of IDIC is evaluated for the real test-case with mode selector position $\xi = 0.25$ by initializing the IDIC-procedure with different initial guess value combinations for the three parameters. Figure 4.16 shows the initial guess map for the following ranges of initial guess values: $1 \leq G_{c,n}^i \leq 500$ [Jm^{-2}], $0.12 \leq \delta_c^i \leq 75$ [μm], and $0.05 \leq \zeta^i \leq 35$ [-], and the corresponding values after convergence. For all cases, the image residual is minimized properly, while the procedure converges in a stable manner, leading to the conclusion that the method is robust against wrong initial guesses. The mean values and corresponding standard deviations of the identified parameters are: $\bar{G}_{c,n} = 49.8 \pm 4.0$ [Jm^{-2}], $\bar{\delta}_c = 7.3 \pm 1.4$ [μm], and $\bar{\zeta} = 3.3 \pm 1.3$ [-]. Considering the wide initial guess ranges it is concluded that the technique is also robust for real experiments. The identified value for $G_{c,n}$ deviates 10% from the value for G_c as determined from the globally measured force-displacement data of Figure 4.13, reported in Section 4.4.2. Note that no force measurement data was utilized in the applied IDIC-method, making it insensitive to force measurement inaccuracies.

4.5 Conclusions

Mixed-mode delamination is an important failure mechanism in multi-layered microelectronic systems for which the local forces cannot be measured in general. Characterizing interfaces under mixed-mode loading conditions is therefore essential for the development of highly reliable microelectronic devices.

Given the specific application conditions, a characterization method requiring simplified test specimens cannot be used. Instead, an identification technique based on integrated digital image correlation (IDIC) has been developed for the characterization of interfaces loaded under mixed-mode conditions that does not rely on force measurement data nor on simplified

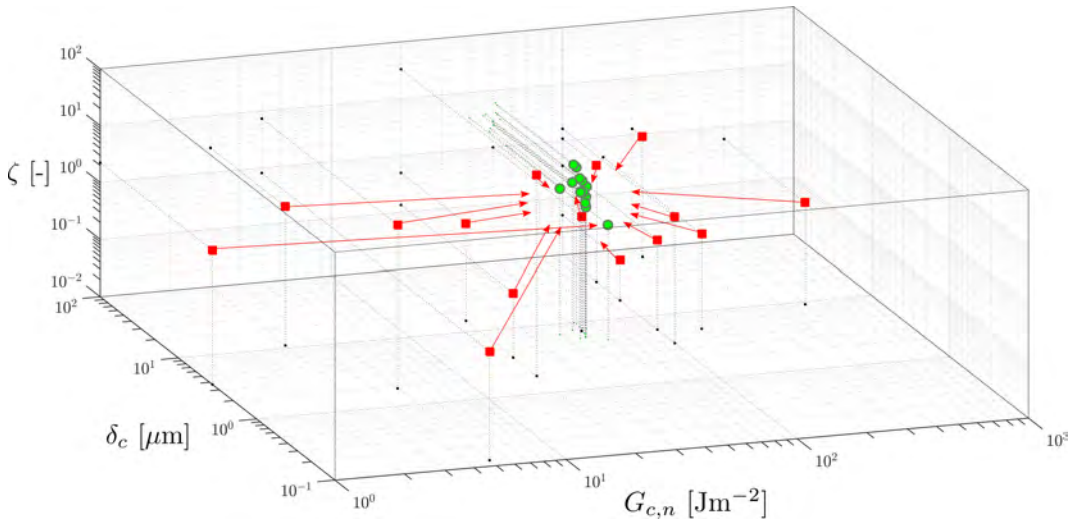

Figure 4.16. Log-log initial guess map depicting the different initial guess combinations (red squares) and the corresponding converged solution values (green circles, which are all in close proximity to one another) of the cohesive zone parameters of the fibrillation model of Van den Bosch et al. [135].

(2D) test specimens. Evidently, this is only possible when the elasticity parameters of one of the elastically deforming bulk materials are known, acting as a local force sensor [133]. Virtual experiments have been used to optimize the method proposed in [133] for mode-I conditions, allowing to apply local boundary conditions in the finite element model. To account for bending and shear under mixed-mode loading, a limited number of finite element nodes must be kinematically prescribed in both x- and y-directions at the outer edges of the imaged field of view. A sensitivity analysis has been carried out, revealing that the region of interest used for IDIC should be optimized in space and time. It is important to include the initial crack-tip location within the region of interest, whereas images in which the crack has fully propagated through the field of view should be omitted from the IDIC-procedure.

Convenient use was made of the strongly varying mode-angle along the fracture process zone under mixed-mode loading, enabling the identification of all mixed-mode cohesive zone parameters ($G_{c,n}$, δ_c, and ζ in the tested example) from a single (virtual) experiment. A sensitivity analysis was conducted, based on the sensitivity matrix M, its corresponding eigenvalue matrix D and its eigenvector matrix Q. This allows to convincingly assess the level of independence of the kinematic sensitivity vectors corresponding to each parameter.

Exploiting the analysis based on virtual experimentation, the applicability of IDIC was demonstrated on real images acquired from small-scale, mixed-mode bending experiments to identify the interface parameters of an epoxy adhesive. The mixed-mode parameters $G_{c,n}$, δ_c and ζ of a cohesive zone model were identified for a particular test configuration that was selected on the basis of the sensitivity analysis based on the M, D, and Q-matrices. The robustness of the identification technique was validated for the real experiments by

initializing the IDIC-routine with different initial guess values in a wide range for the three cohesive zone parameters.

In the experiments, a homogeneous interface with constant cohesive zone parameters along the entire interface, was assumed. This assumption may be invalid for realistic specimens, especially when the specimens are manually produced, as was the case in the experiments performed here. Although not demonstrated, the variability of the FE-model used within the IDIC-algorithm allows for characterizing heterogeneous interfaces by implementing a model with different cohesive zones along the interface, each with its own set of parameters. In that case, the procedure here presented for analyzing the (cross-) sensitivity of IDIC with respect to the different parameters is advised.

Integrated digital image correlation constitutes a promising, versatile technique for characterizing interfaces when (1) mixed-mode loading conditions are present at the interface, (2) the far-field boundary conditions lie outside the imaged field of view, and (3) the force measurement is unfeasible or inaccurate and the elasticity parameters of one of the bulk materials are known instead. This is particularly interesting for microstructures and microelectronic specimens with intricate 3D geometries and complex material layer stacking, although the application of IDIC on actual microelectronic devices is yet to be demonstrated in future work. Furthermore, IDIC allows for identifying mixed-mode cohesive zone model parameters from a single test as long as the mode-angle changes rapidly along the fracture process zone during the experiment.

Acknowledgements

This research was carried out under project number M62.2.12472 in the framework of the Research Program of the Materials Innovation Institute (M2i) in the Netherlands (www.m2i.nl).

CHAPTER 5

An *in-situ*, micro-mechanical setup with tri-axial force sensing and positioning

Abstract

To enable accurate characterization of the mechanical behavior of materials at the micro-scale, e.g., in micro-systems, experiments are required that are representative of the actual (often multi-axial) loading conditions to which these materials are subjected during fabrication and operation. Equally important is the acquisition of mechanical data in the form of multi-axial force measurements, and the measurement of kinematics by in-situ microscopic techniques.

To this end, a micro-mechanical testing rig is here realized using commercially available piezoelectric actuators. It is shown that the setup measures forces with a resolution of ~ 0.3 [mN] in the x- and y-directions, and ~ 50 [mN] in the z-direction, over a range of 10 [N], yielding a high dynamic (force) range. Furthermore, displacements can be imposed with a resolution of ~ 1 [nm] over a range of 200 [μm], in all three directions (x, y, z). The setup is compact, vacuum compatible, and specimens are loaded on top of the setup so that the field of view is unobstructed, allowing for in-situ testing with optical and scanning electron microscopy, and optical profilometry. A generic method is developed for extracting quasi-static forces from the piezoelectric actuators. Furthermore, challenges raised from the use of commercial actuators, for which the public technical specifications are generally incomplete, are overcome and the solution strategy is described.

Proof-of-concept experiments on flexible, organic, light-emitting diodes demonstrate the potential of the setup to provide rich micro-mechanical data in the form of tri-axial force and displacement measurements. The commercial availability of the piezoelectric actuators, combined with the proposed engineering solutions lead to a generally accessible micro-mechanical test setup to investigate small-scale specimens under realistic, multi-axial loading conditions.

Keywords: micro-mechanics; tri-axial force measurement; in-situ testing; mechanical setup; piezoelectric actuator

Reproduced from:
A.P. Ruybalid, J.P.M. Hoefnagels, O. van der Sluis, M.G.D. Geers
An in-situ, micro-mechanical setup with accurate, tri-axial, piezoelectric force sensing and positioning, Submitted to journal

5.1 Introduction

Mechanical characterization of materials in microelectronics devices, e.g., light emitting diodes, computer chips, and solar cells, is challenging due to: (1) the associated small-scale deformation, (2) the small, multi-directional forces at play within the material layers and their interfaces, and (3) the complex loading conditions to which these systems are subjected during fabrication and operation. To accurately characterize microelectronic materials, high-resolution measurement techniques in terms of displacements and forces are required. Conventional methods are based on experiments in which over-simplified sample geometries and loading conditions are applied, e.g., micro-beam bending or tensile testing of dedicated, micro-fabricated specimens [78, 138–141]. This typically puts high demands on the fabrication processes of dedicated small-scale specimens, while introducing changes to the material behavior, e.g., due to processing-induced size effects [32, 33]. Moreover, these highly specific and simplified experiments do not represent the realistic conditions to which these material systems are subjected during fabrication and/or operation [142–144]. Therefore, to capture the realistic, multi-axial loading conditions in an experiment, while overcoming the above-mentioned challenges, a novel testing rig is here proposed. It is designed to mechanically test samples of actual devices, rather than dedicated specimens that are specifically fabricated for one idealized test-case.

Besides the necessity of imposing realistic loading conditions, a major challenge resides in the measurement of the mechanical quantities of interest, i.e., the forces and the displacements in all three directions. Multi-axial force transducers have been realized for, e.g., gripping and passive sensing applications (robotics) [145–147], in-situ scratch testing [148], and biaxial testing of relatively small, cruciform samples [149]. Although tri-axial load-cells are commercially accessible at the larger scale, multi-axial force measurement is not available for the purpose of in-situ, mechanical testing, where deformation must accurately be applied to a small-scale specimen, while measuring forces and imaging the deforming by high-magnification, microscopic techniques. The mechanical testing rig, presented in this chapter, is compact and vacuum compatible, and specimen loading is performed on top of the setup to realize an unobstructed field of view for in-situ optical and scanning electron microscopy. It consists of two adjacent, and oppositely positioned piezoelectric actuator stacks, enabling an autonomous actuation and force measurement along three perpendicular motion axes (x, y, z). The apparatus is described in Section 5.2, with a particular focus on the methodology proposed for the force measurement.

The piezoelectric actuators were commercially acquired, making this an economically attractive setup, which is easily accessible to the research community. However, the use of commercially available actuators also raises problems to solve. Indeed, the publicly available technical specifications of commercial actuators is generally incomplete, requiring an extensive characterization of the technical properties of the piezoelectric actuators, the procedure of which is described in Section 5.3. The potential of the realized mechanical test setup is demonstrated by proof-of-concept experiments in Section 5.4, and the findings are summarized in the concluding Section 5.5.

5.2 Methodology

This section presents a method for adapting a commercial, piezoelectric actuator system, consisting of two piezoelectric actuator stacks, in order to realize a mechanical testing rig with accurate, quasi-static force measuring capabilities in three perpendicular, independent directions, without requiring additional load cells.

5.2.1 Experiment setup

Two identical, commercially available, vacuum compatible, piezoelectric actuator stacks (manufacturer: Mad City Labs, model type: "nano-3D200") are positioned oppositely to each other, see Figure 5.1(b), and secured to a bottom plate. Each stack consists of three, independent, piezoelectric actuators in order to realize a displacement in three perpendicular directions (x, y, z), without cross-talk between the axes. The displacement of each stack's platform is accomplished by applying an electric voltage to the piezoelectric element within each actuator (i.e., each independent axis), which thereby deforms mechanically due to the reversed piezoelectric effect. The resulting motion is guided and amplified by an unknown, internal, elastic flexure hinge system to realize a positional range of 200 [μm], and a positioning resolution of 1 [nm], in each direction. Each actuator can be controlled with or without a closed feedback control loop. Piezoresistive sensors measure the motion of each actuator, which is used in the feedback control loop for accurate positioning [150]. These motion sensors, intrinsic to the device, will be utilized for force measuring purposes, as explained in Section 5.2.2.

The setup enables the deformation of small-scale microelectronic specimens between the two actuator stacks in a variety of ways, accommodating tension, compression, bending, shearing, and any arbitrary combination of these loading conditions. The multi-axial load application enables replication of complex conditions to which microelectronic devices are subjected during their fabrication and operation.

5.2.2 Force measurement principle

The electric charge generated by a piezoelectric element is proportional to the mechanical force acting on its free surfaces. The quasi-static force measurement, based on this piezoelectric effect, is known to be challenging due to free charge carriers drifting toward the dipoles under static stress in the piezoelectric crystal, leading to leakage of electric charge and current in the electronic circuit and causing significant drift of the measured force quantity [151, 152]. Solutions proposed in the literature require detailed knowledge and precise manipulation of the system's electronic circuit, and/or of the environmental conditions (e.g., ambient temperature, humidity) to which the system is subjected during operation [152–155]. For off-the-shelf, commercially available piezoelectric actuators, this information is not readily available. However, this problem can be overcome by calibrating one piezoelectric stage against a second piezoelectric stage. Specifically, to measure quasi-static forces in the setup presented here, the embedded piezoresistive motion sensors are utilized, together with an algorithm to circumvent the drift effects. The method is demonstrated in Figure 5.2 for an experiment on a linear elastic coil spring loaded along its axis in between the two piezoelectric actuators. For each motion axis, the piezoelectric actuator of one of the two piezo-stacks is used to accurately apply deformation to the spring, in axial direction. A

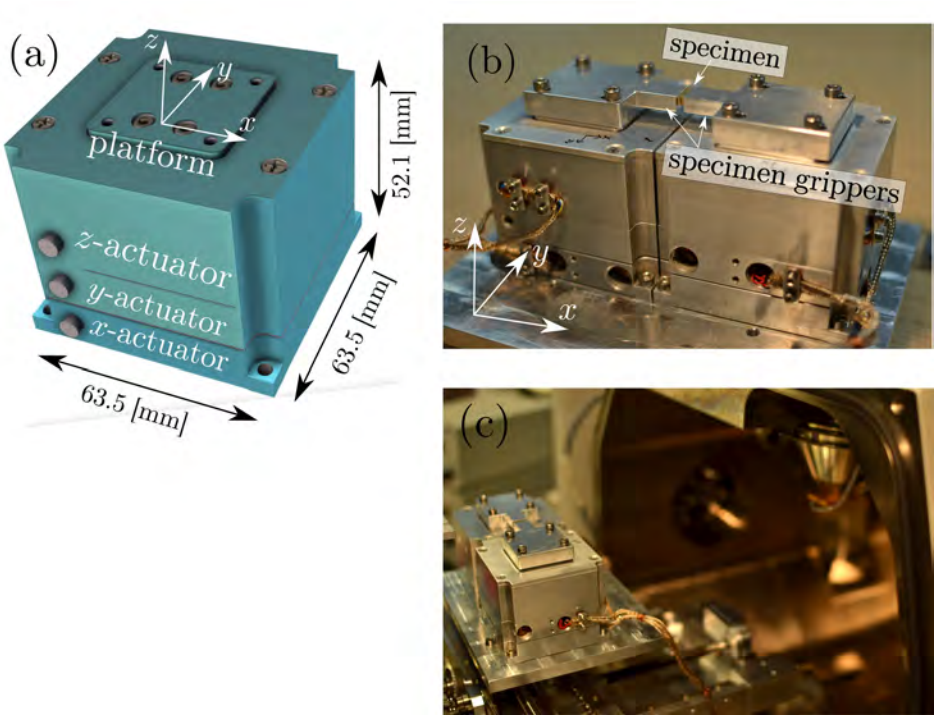

Figure 5.1. (a) CAD drawing of a single, tri-axial, piezoelectric actuator stack, consisting of three independent actuators to realize a displacement in three perpendicular, independent directions. Two identical actuator stacks are oppositely positioned to realize a mechanical testing setup, shown in (b), which is used for in-situ testing with, e.g., (c) scanning electron microscopy (SEM).

feedback control mechanism (see Figure 5.2(a)) is thereby used, with a positioning resolution of approximately 1 [nm] (minor deviations may be caused by fluctuating environmental conditions, e.g., vibrations). This piezoelectric actuator operates in the closed-loop configuration, and is henceforth called the "closed-loop actuator". The opposite piezoelectric actuator is used without the feedback control mechanism to measure the positional change of the actuator, again in axial direction of the coil spring, caused by the force acting on it (see Figure 5.2(b)). This load-sensing piezoelectric actuator is henceforth called the "open-loop actuator". To make the force measurement insensitive to drift, a step-wise positioning of the closed-loop actuator is required, while measuring the resulting positional change of the open-loop actuator. The closed-loop actuator applies a displacement step, and keeps the applied displacement constant for a short period of time ($\sim$ 50 [ms]). Because of noise and drift affecting the uncontrolled open-loop actuator, the constant displacement applied by the closed-loop actuator does not appear as a constant plateau in the open-loop actuator response. Linear regression is therefore applied to this regime in the open-loop actuator data (see the red fit-lines of Figure 5.2(b)-(c)). This procedure allows to effectively eliminate noise and drift effects that occur in between the driving steps induced by the closed-loop

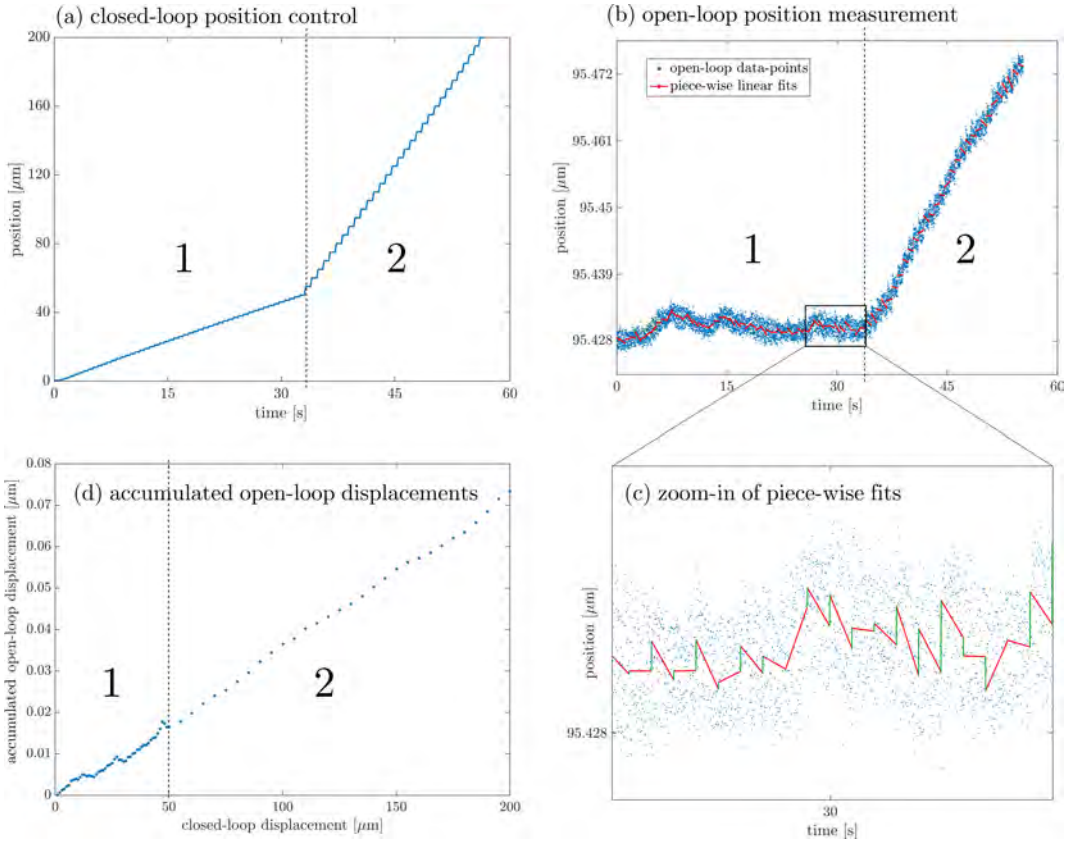

Figure 5.2. Illustration of the procedure (b)-(c) used to eliminate the noisy plateau regions of the piezoresistive displacement measurement by the actuator operating without a feedback control mechanism, i.e., the "open-loop" actuator. Thereby, the displacement jumps (green lines in (c)), induced by the step-wise positioning (a) of the actuator operating with the feedback control mechanism, i.e., the "closed-loop" actuator, are recorded and accumulated (d). The force can be calculated from the accumulated open-loop displacement jumps when the system stiffness is known. Two regimes are indicated in the figures: (1) a slow increase of the displacement, followed by (2) a fast increase of the displacement.

actuator. The remaining displacement jumps (linking up the linear fits) of the open-loop actuator (see the green lines of Figure 5.2(c)) are thereby effectively recorded and accumulated. The accumulated displacements jumps of the measuring open-loop actuator (see Figure 5.2(d)) correspond linearly to the jumps in the axial force when the stiffness of the elastic hinge system of the actuator is known, the calibration of which will be discussed in Section 5.3.1. The algorithm is applied on-the-fly, meaning that the force can be measured real-time during a mechanical experiment (i.e., the force is not post-processed), and the setup can operate autonomously, employing a digital input file for driving the closed-loop actuators of each loading axis (x, y, z). In this fashion, intermittent displacement control

with quasi-static force measurement is possible. Force control, for mechanical creep experiments, and fully static force measurement, for relaxation experiments, are unfeasible, due to the long-term, nonlinear drift effects corrupting such measurements. As will be discussed in further detail in Section 5.3, proper operation requires the calibration of the system's characteristics, such as the stiffness of the elastic flexure hinges in all three directions, and the machine compliance.

5.3 Characterization of the setup

Since the mechanical test setup consists of commercially acquired piezoelectric actuators, detailed technical specifications are not provided to the end user. Therefore, to measure force and displacement accurately, the technical specifications of the setup must be quantitatively assessed first.

This section discusses the assessment procedures and results: (1) the measurement of the axial, machine compliance, affecting the measurement accuracy of the displacement imposed on a test specimen, (2) the calibration of the internal stiffness of the elastic mechanism underlying each loading axis, affecting the force measurement accuracy of the open-loop piezoelectric actuators, (3) the cross-axial compliance that may corrupt the force measurement in the z-direction. Finally, after the setup has been assessed and calibrated, the actual force resolution for each loading axis is determined.

5.3.1 Axial machine compliance and internal stiffness

Because the testing rig has a finite stiffness, it will deform during a mechanical test. Consequently, accurate measurement of the relative clamp displacement requires knowledge of the machine compliance in each loading direction (x, y, z). The measured displacement of the closed-loop stage of each axis should be corrected in order to recover the actual relative displacement of the specimen clamps. Various factors may contribute to the machine compliance, e.g., the deformation of the elastic flexure hinge system, clearances in the setup, deformation of the machine frame, etc. It is impossible to quantify the individual contributions of such factors in a commercially acquired piezoelectric actuator. The objective here is therefore to quantify the total machine compliance, instead of identifying and characterizing the contributing factors individually.

To measure the machine compliance along each of the three axes, the two piezoelectric stacks are rigidly connected by a relatively thick steel plate, with a cross-sectional area of 30×10 [mm^2], which shows negligible deformation under the maximum applicable load of the system (10 [N], as specified by the manufacturer). For each loading axis (x, y, z), a calibration experiment is conducted, where the displacement at the closed-loop actuator is prescribed, while the corresponding open-loop actuator's displacement is monitored. When the connection is indeed rigid, the displacement difference between the open-loop actuator and the closed-loop actuator represents the machine compliance Δ_{mc}, i.e., the displacement that is not transferred from the driven closed-loop actuator to the corresponding open-loop actuator. The results of the compliance calibration experiments for each axis are shown in Figure 5.3(e), where U_{CL} and U_{OL} are the displacements of the closed-loop (driving) actuator and the open-loop (force measuring) actuator, respectively. The similarity between the axial compliance in the x- and y-directions, and the noticeably different axial compliance

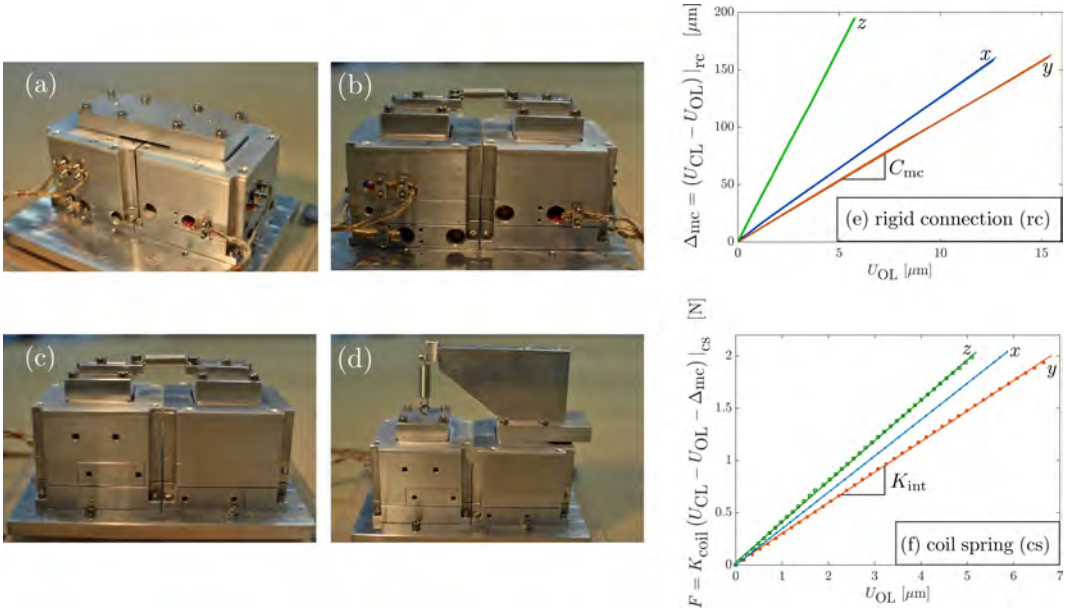

Figure 5.3. (a) Photograph of the experiment with a rigid connection (rc) between the two actuator stacks for identifying the machine compliance for all three axes from the data in (e), providing the machine compliance factors C_{mc}. A coil spring (cs) with a stiffness of $K_{coil} = 1.1 \times 10^4$ [Nm^{-1}] is loaded along the (b) x-, (c) y-, and (d) z-axis for determining the corresponding internal stiffness K_{int} from the data in (f). To load the spring axially, yet trigger the internal stiffness of the y-axis of the setup (recall Figure 5.1), the two actuator stacks are both rotated 90° so that their y-axis corresponds with the spring axis. Solid lines represent linear regressions through the data in figures (e)-(f).

in the z-axis results from the likely equivalence in design of the former two stages, since they both drive in the horizontal plane. The z-stage, however, drives in the vertical, out-of-plane direction, which is therefore expected to exhibit a different design than the x- and y-stages. The solid lines represent linear regressions through the data, from which it is concluded that the machine compliance Δ_{mc} in each direction is linearly dependent on the open-loop displacement U_{OL} in that direction, i.e.:

$$\Delta_{mc} = C_{mc} U_{OL}. \tag{5.1}$$

The constant, compliance factors C_{mc}, determined from the linear regressions of Figure 5.3(e), are listed in Table 5.1. [Eq. 5.1] is used to compute the compliance C_{mc}, and thereby the relative clamp displacement U_{clamp} between the open-loop and closed-loop actuators of each axis, during a mechanical experiment:

$$U_{clamp} = U_{CL} - U_{OL} - \Delta_{mc}. \tag{5.2}$$

To convert the open-loop actuator's deformation response to a measured force, the internal stiffness K_{int} of the elastic hinge system of each piezoelectric actuator must first

Table 5.1. The machine compliance factor C_{mc} [-], and the internal stiffness [Nm^{-1}] of each loading axis, based on linear regression on the data in Figures 5.3(e)-(f), including the 95% confidence intervals of the identified parameters.

Axis	x	y	z
C_{mc} [-]	12.42 ± 0.02	10.46 ± 0.02	33.64 ± 0.03
K_{int} [Nm^{-1}]	$(3.476 \pm 0.002) \times 10^5$	$(2.925 \pm 0.016) \times 10^5$	$(3.867 \pm 0.023) \times 10^5$

be identified. This is done by using a linear elastic coil spring with a known stiffness of $K_{\mathrm{coil}} = 1.1 \times 10^4$ [Nm^{-1}] as a reference specimen and applying deformation with the closed-loop actuator, while measuring the deformation response of the oppositely positioned open-loop actuator, as explained in Section 5.2.2. The response of the open-loop actuator can now be translated into a force by the known stiffness of the coil spring and the measured relative clamp displacement of [Eq. 5.2], for which the machine compliance factors C_{mc} are required:

$$F = K_{\mathrm{int}} U_{\mathrm{OL}} = K_{\mathrm{coil}} U_{\mathrm{clamp}}. \tag{5.3}$$

The results of the coil spring experiments are shown in Figure 5.3(f). As expected, the relationship between the force in the coil spring and the open-loop response of each actuator is linear (linear regressions are represented by solid lines in Figure 5.3(f)). From the relation in [Eq. 5.3] and the results of Figure 5.3(f), the internal stiffness K_{int} along each axis (x, y, z) is identified, the values of which are listed in Table 5.1.

5.3.2 Cross-axial compliance

A different type of compliance may jeopardize force measurements in the z-direction. Because experiments are performed on top of the setup (to enable an unobstructed field of view for in-situ microscopy testing), the alignment with respect to the force measuring actuator in the z-direction is not optimal. When forces are applied in the x- and y-directions, a force will also be registered in the z-direction. The in-plane forces: F_x and F_y, induce a moment to the open-loop stage's platform, which thereby rotates around its x- and/or y-axis (see Figure 5.1(a)). The piezoresistive displacement sensor of the z-axis, whose internal position is not disclosed to the user by the manufacturer, measures a displacement u_z in the z-direction due to the platform's rotation, which does not represent a displacement caused by a force acting in the z-direction. The situation is illustrated in Figures 5.4(a)-(b). The occurrence of this rotation is verified by optical profilometry measurements of a mirror surface, with a sub-nanometer roughness profile, placed on the stage's platform. The profilometry measurements before and after application of forces of 5 [N] in the x- and y-directions, reveal an angular rotation of 0.17° of the platform around the x- and y-axes. An illustration of this cross-axial coupling and the optical profilometry measurements are shown Figure 5.4.

To quantify the cross-axial compliance that affects the measurement of the force in the z-direction, an additional experiment is conducted with a rigid connection between the platforms of the two stages. Both x- and y-axes are driven in compression and tension directions, across their full ranges and in a scanning manner, while the forces in all directions are recorded. Because of the rigid connection between the stages' platforms, any force

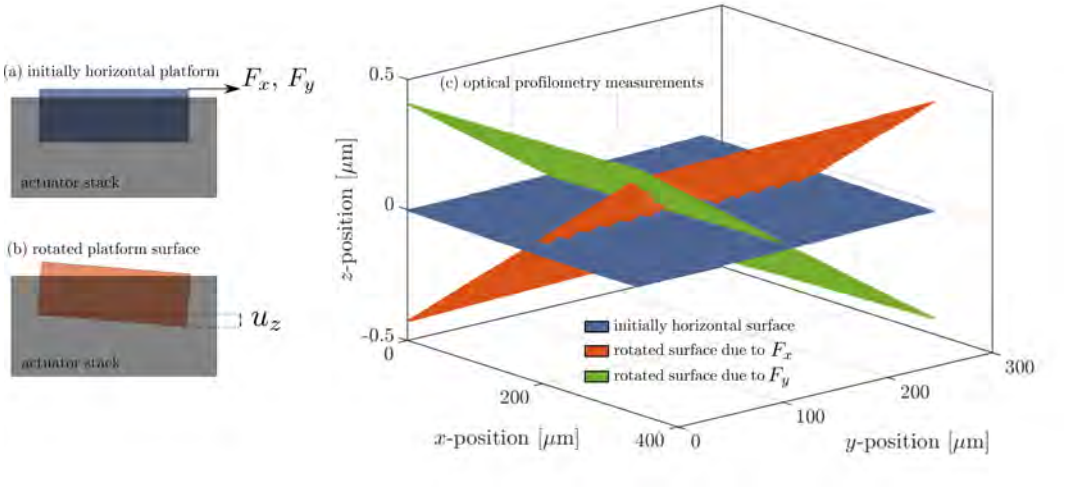

Figure 5.4. (a)-(b) An illustration of the 0.17° angular rotation caused by in-plane forces F_x and/or F_y, resulting in a measured displacement u_z, and (c) the optical profilometry measurements of the stage's platform, verifying its rotation as a result of the applied forces F_x and F_y with a magnitude of 5 N.

measured in the z-direction should be considered as artificial. The artificial force $F_{z,a}$ is thus a function of the forces F_x and F_y, and its relation appears to be linear, as shown in Figure 5.5, i.e., it can be expressed as:

$$F_{z,a} = C_{z,x}F_x + C_{z,y}F_y, \tag{5.4}$$

where $C_{z,x}$ and $C_{z,y}$ are called the *cross-compliance* factors. The two cross-compliance factors can be straightforwardly characterized from a linear, planar regression through the measured data points of Figure 5.5(a). In order to investigate a potential dependence on the positive and negative regimes of the applied forces F_x and F_y, four planar regressions are made: one in each quartile Q_{1-4} of positive and negative combinations of F_x and F_y. Moreover, the test has been repeated three times over a period of 1 hour, and with 15 minutes intervals in between each test. While the first and third test are performed under equal conditions, the second test is conducted with an added force of 1 [N] in the z-direction, induced by a displacement step of the closed-loop actuator of the z-axis. This was done to investigate the dependence of the cross-compliance on the applied force in the z-direction. The four quartiles and the three tests yield a total of twelve test-cases for the linear regressions. The identified parameters, i.e., the cross-compliance factors, for each test-case are shown in Figure 5.5(b)-(c). The spread on the data in 5.5(b)-(c) is mainly governed by the quartile location (distinguished by the colors of the data points), and less by the different tests (distinguished by the marker symbols of the data points). The dependence of the cross-compliance factors on the four quartiles suggests that a linear, planar regression on all data points is inadequate, since it does not properly capture the dependence of $F_{z,a}$ upon

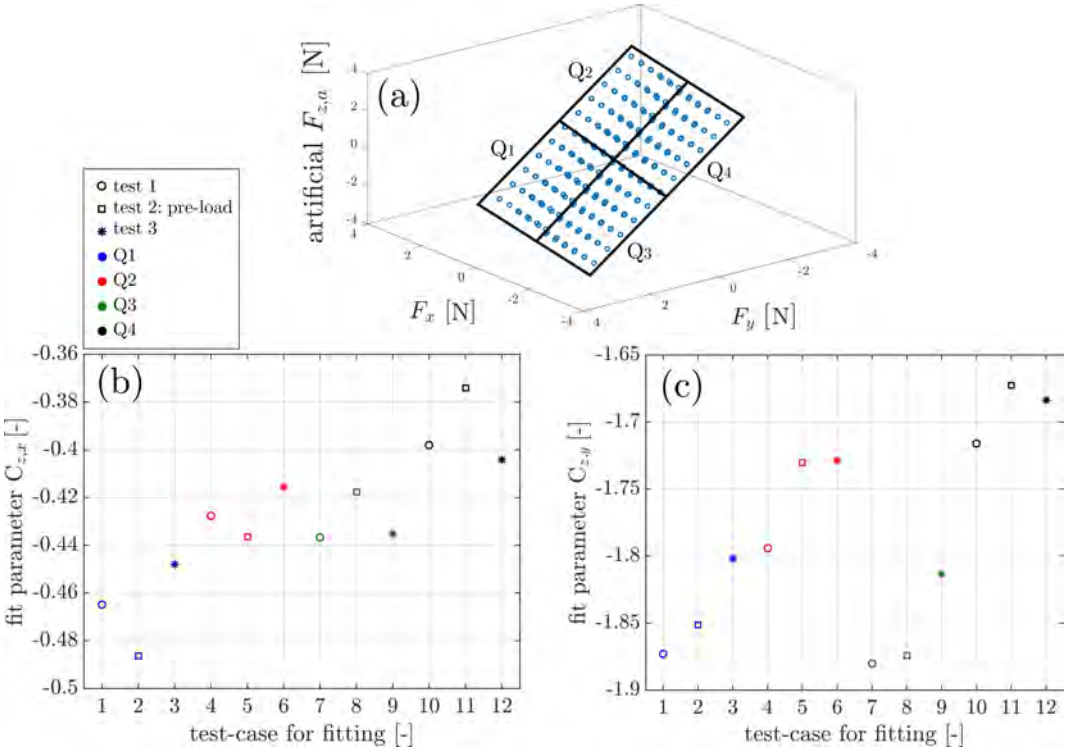

Figure 5.5. (a) The artificial force $F_{z,a}$ in the z-direction is caused by the forces F_x and F_y. Separate linear regressions are made on the data in the quartiles Q1, Q2, Q3, and Q4, and for three separate tests, to determine cross-compliance factors $C_{z,x}$ and $C_{z,y}$ for all twelve test-cases, the values of which are graphically shown in (b) and (c), respectively.

F_x and F_y. Accordingly, [Eq. 5.4] should be extended. To this end, polynomial regressions of different orders are made on all data points of all three tests combined. The root-mean-square of deviation (RMSD) between regressions and the measured data points is plotted against the polynomial order of the regressions, as shown in Figure 5.6(b). It is clear that the linear regression is significantly less adequate than the higher order regressions. A second order regression polynomial yields an improvement of 34% with respect to the linear one. Higher (than second) order polynomial regression introduces higher order fluctuations, due to non-physical measurement noise, while not reducing the RMSD significantly with respect to the second order polynomial regression. Hence, a second order polynomial regression is adopted and the artificial force $F_{z,a}$ is written as:

$$F_{z,a} = C_{z,x}F_x + C_{z,y}F_y + C_{z,xx}F_x^2 + C_{z,xy}F_xF_y + C_{z,yy}F_y^2, \tag{5.5}$$

where $C_{z,i}$ are the cross-axial compliance factors as determined from the second order polynomial fit through the data from the calibration experiment, as shown in Figure 5.6(a) and listed in Table 5.2. [Eq. 5.5] is used to correct the force extracted from the open-loop

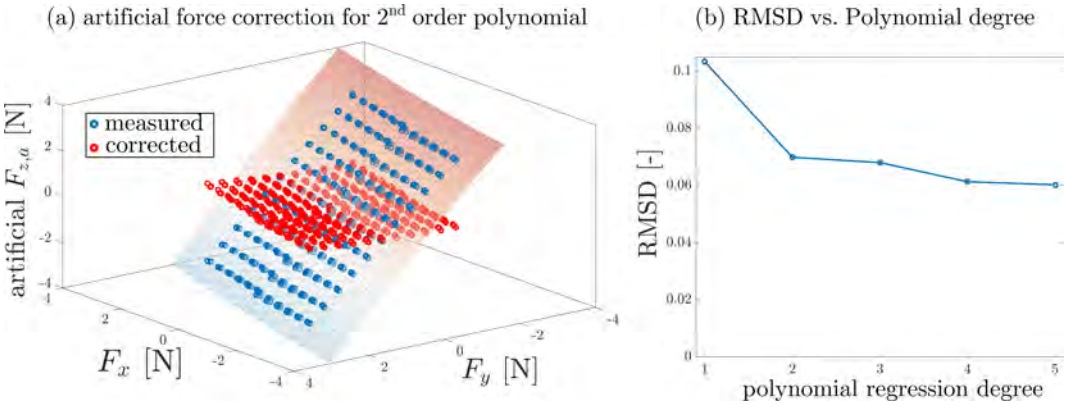

Figure 5.6. (a) Measurement of the artificial force in the z-direction (blue data points). A second order polynomial regression is made on the data points, and used to determine the cross-axial compliance factors, which is subsequently used to correct for the artificial force $F_{z,a}$, as is illustrated by the red data points. (b) RMSD vs. order of polynomial regression.

Table 5.2. The cross-axial compliance factors $C_{z,i}$ [-] with the 95% confidence intervals, as determined from a second order polynomial regression through the calibration data of Figure 5.6(a).

$C_{z,x}$	$C_{z,y}$	$C_{z,xx}$	$C_{z,xy}$	$C_{z,yy}$
-0.4222 ± 0.0027	-1.7920 ± 0.0040	-0.0136 ± 0.0015	-0.0286 ± 0.0030	-0.0393 ± 0.0031

displacement $U_{\mathrm{OL},z}$ as measured by the open-loop actuator in the z-axis:

$$F_z = K_{\mathrm{int},z} U_{\mathrm{OL},z} - F_{z,a}, \tag{5.6}$$

where $K_{\mathrm{int},z}$ is the stiffness of the respective actuator system (see Table 5.1). For the calibration experiment, the measured z-force is thereby reduced to nearly zero, as shown by the red data points in Figure 5.6(a).

In spite of this correction, the artificial force may still negatively affect the resolution of the force measurement in the z-direction, as will be shown in the next section.

It was also verified whether artificial forces also occur in the x- and y-directions, for which a displacement is imposed along each of the two other axes, while measuring the corresponding forces by the open-loop actuators (not shown). To this end, the in-plane displacements, measured by the piezoresistive motion sensors of the open-loop x- and y-actuators (used for force measurements) were also measured by 2D digital image correlation on images of the moving stage platform. It was found that the x- and y-displacement of the platform correspond to that of the piezoresistive sensors within measurement accuracy. Therefore, it can be concluded that the cross-axial machine compliance can be neglected for the x- and y-force measurements.

5.3.3 Force resolution

To quantify the force resolution of the calibrated system, a coil spring specimen, with a (very low) stiffness of 125 [Nm^{-1}], is elongated by 200 [μm] by the closed-loop actuator, while the

force is measured by the open-loop actuator. The measurement is conducted separately for each direction, where the spring is loaded along its axis, equivalent to the test configurations shown in Figures 5.3(b)-(d). The resulting force-displacement curves are shown in Figure 5.7. The linear regressions verify the ability of the measurement algorithm to capture the linear elastic behavior of the coil spring. The root-mean-square deviation (RSMD) with respect

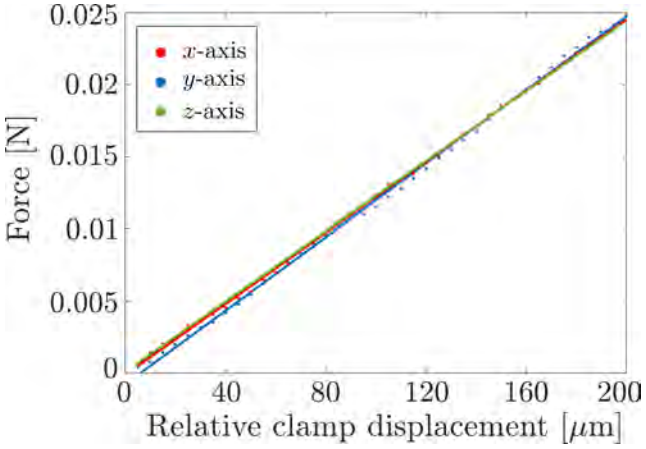

Figure 5.7. Linear regressions on the force-displacement curves from uni-axial experiments of linear elastic coil spring specimens loaded in three different directions. The root-mean-square deviation with respect to the regressions reveals the force measurement resolution for each axis.

to the linear regression represents the resolution of the force measurement by the open-loop actuator of each axis. The force resolution values are listed in Table 5.3, while the maximum allowed force for these piezoelectric actuators is specified by the manufacturer at 10 [N]. However, for the z-direction, the RSMD of the second order polynomial regression through the artificial z-force data in Figure 5.6 is two orders of magnitude larger than the RMSD of the regression from Figure 5.7. Here, the cross-compliance will still corrupt the force resolution in the z-direction (if x- and y-loads are present). Therefore, the RSMD of the artificial z-force regression is taken as a measure for the resolution instead, as seen in Table 5.3. Since the actuators have a load bearing capacity of 10 [N], the dynamic range,

Table 5.3. The force measurement resolution in [N], for open-loop actuator of each axis, which should be compared to the load range of 10 [N], yielding the dynamic range.

Axis	x	y	z
Resolution [N]	1.8×10^{-4}	2.8×10^{-4}	7.0×10^{-2}
Dynamic range [-]	5.6×10^{4}	3.6×10^{4}	1.4×10^{2}

defined as the ratio between the maximum load and the force resolution, is particularly high for the x- and y-directions.

5.4 Proof-of-concept measurements

First, a three-point-bending experiment is described in Section 5.4.1, characterizing a well-defined spring steel rod specimen. The potential of the setup is further demonstrated with several other proof-of-concept experiments in Section 5.4.2.

5.4.1 Three-point bending experiment

A three-point bending experiment is conducted on a cylindrical, spring steel rod. The results are validated by analytic calculation, making use of the Euler-Bernoulli beam theory. Since special grippers are used for this experiment, the previously measured machine compliance in the x-direction (direction of bending) may be incomplete. Therefore, the total machine compliance in x-direction is measured again for the system, now including the specific grippers: $C_{\mathrm{mc},x} = 18.738 \pm 0.02$ [-].

The cylindrical rod specimen has a length of $L = 4.07 \pm 0.006$ [mm] (measured optically between the outer loading points), and a diameter of $D = 400 \pm 1$ [μm]. The force F is measured in the x-direction, along which the bending deformation is applied, by the corresponding open-loop actuator, see Figure 5.8. The relative displacement of the two piezoelectric

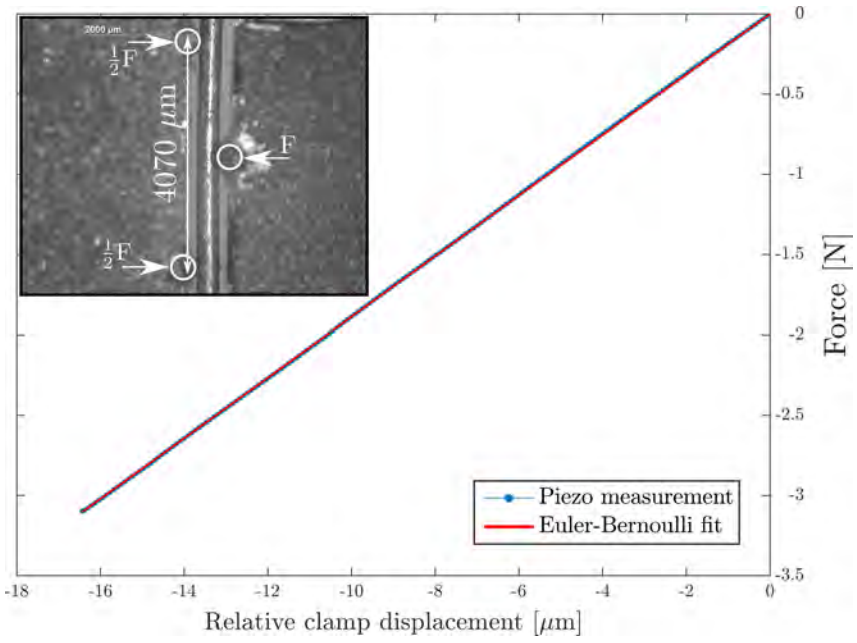

Figure 5.8. Force versus relative clamp displacement in the drive direction x, as measured by the piezo testing rig. The inset shows the part of the image that contains the three-point-bending experiment.

actuators represents the deflection of the bending rod. Using the Euler-Bernoulli equation

for this problem, the maximum deflection w at $x = \frac{1}{2}L$ is:

$$w|_{x=L/2} = \frac{FL^3}{48EI}, \tag{5.7}$$

where E is Young's modulus and I is the second moment of area of this cylindrical specimen. Using Young's modulus as the unknown material parameter, applying [Eq. 5.7] on the experimental data allows to identify the Young's modulus as: 211 ± 5 [GPa], which is in agreement with the expected Young's modulus of the spring steel: 210 [GPa]. The error bounds on the computed value of the Young's modulus are determined from the error margins on the variables of [Eq. 5.7], as specified throughout this chapter. This experiment demonstrates that a setup based on two commercially available piezoelectric actuator stacks can indeed be used to perform highly accurate mechanical tests on small-scale specimens.

5.4.2 Organic light-emitting diode

Samples from a flexible sheet of an organic light-emitting diode (OLED) are mechanically deformed to demonstrate the potential of the setup for tri-axial, micro-mechanical testing. The samples consist of a polyethylene naphthalate (PEN) substrate with three moisture barrier layers, each consisting of an acrylate (organic) coating for planarization (OCP) [156, 157], and a 150 ± 1 [nm] thick Si_3N_4-coating. The thickness of the PEN substrate is $H = 160 \pm 1$ [μm], and the total thickness of all three (equally thick) OCP-layers is $h = 75 \pm 1$ [μm]. The specimens are cut to a size of 7 ± 0.01 [mm] in length and 4 ± 0.01 [mm] in width, by a thin razor blade with a thickness of ~ 10 [μm]. To facilitate viewing and recording of the deformation of the specimen over its cross-section and along its length-direction by optical microscopy, it is ground by using consecutively finer sanding paper, with ~ 5.5 [μm] particles for the finest step. The specimen is, thereafter, glued to the grippers of the mechanical testing rig, at the side of the substrate over the full length and width of the specimen, and partially at the side of the OCP-layers over a length of ~ 2 mm and the full width of the specimen. A schematic illustration of the OLED specimen and the locations at which it is loaded by the mechanical testing rig (the boundary conditions), is shown in Figure 5.9.

Four in-situ experiments are conducted in which interface delamination between the OCP-layers is triggered under different loading modes: (a) normal opening by driving the stage 100 [μm] along the x-axis, (b) in-plane shear opening by driving the stage 100 [μm] along the y-axis, (c) out-of-plane tearing by driving the stage 100 [μm] along the z-axis, and (d) a combination of the former loading modes, with 100 [μm] along x, and 50 [μm] along y and z, consecutively imposed in that order. In each of the four mechanical tests interface crack propagation was observed and the delamination was induced in the OCP-stack between the first and second OCP-layers (counting from the substrate), as illustrated in Figure 5.9(b). Before the specimens were loaded, a pre-crack was first produced by loading the specimen in the x-direction, while observing the force evolution. The moment when the force in the x-direction was observed to suddenly drop, the loading was stopped. The result of this loading path is a pre-crack of ~ 2 [mm], spanning the length of the specimen over which the right-hand boundary condition (glue) is applied, see Figure 5.9(a). The pre-cracked specimen was first unloaded before being reloaded in one of the four experiments (a)-(d).

The forces in all directions were recorded during the four experiments, see Figure 5.10,

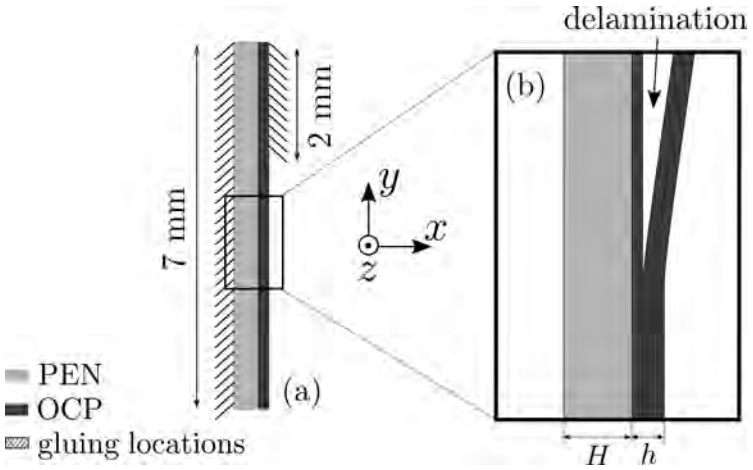

Figure 5.9. Illustration of the OLED specimen. The specimen is glued to the grippers of the mechanical testing rig, at the schematically indicated locations. After loading in, e.g., horizontal direction, delamination is triggered between the OCP-layers (b). $H = 160 \pm 1$ [μm], $h = 75 \pm 1$ [μm].

together with several micrographs of the deformation which occurred during the experiments. The progressive increase of the x-force in the normal opening test-case of Figure 5.10(a)

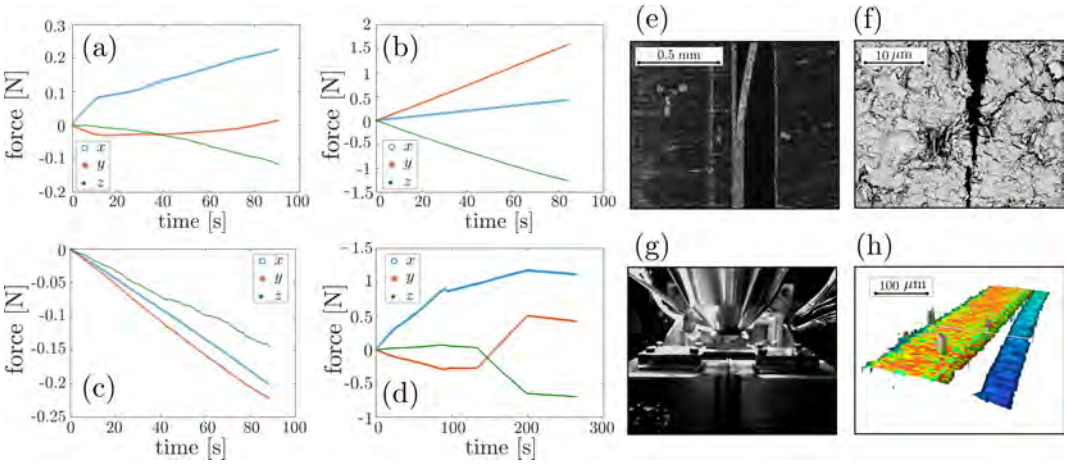

Figure 5.10. Force evolution in all directions (x, y, z), as measured by the open-loop actuators of the mechanical setup during in-situ tests under (a) normal opening, (b) in-plane shearing, (c) out-of-plane tearing, and (d) a combination of loading modes, consecutively imposed in the order as mentioned above. The induced delamination is visualized by (e) optical microscopy, (f) scanning electron microscopy (SEM), of which a photograph of the setup inside the vacuum chamber is seen in (g), and optical profilometry (h).

can be explained by the fact that the delaminating layers are stretched as the experiment

progresses and the interface crack propagates. Interfacial failure is visualized by optical microscopy, as shown in Figure 5.10(e), and more detailed visual information of, e.g., the crack-tip is captured by scanning electron microscopy, as seen in Figure 5.10(f). The induced delamination is not purely mode-I, thereby preventing the measured force to reach a plateau or decrease, as is typically observed for pure mode-I loading conditions. For the in-plane shearing and the out-of-plane tearing test-cases, no significant decrease in the force slopes is observed at all, yet crack propagation, and thus delamination, is clearly observed in both experiments. The specimen of the tearing test-case shows crack propagation along the length of the interface. By using surface metrology techniques, such as optical profilometry, the out-of-plane delamination of OCP-layers subjected to tearing, can be quantitatively visualized, see Figure 5.10(h).

The specimen processing method, prescribed above, does not produce specimens with a consistent, reproducible pre-crack length, and therefore does not allow for comparison of the results between different samples. The experiments only serve to demonstrate the tri-axial capabilities of the device. The setup's in-situ microscopic testing capabilities assists in acquiring high resolution images of the underlying microscopic (failure) mechanisms that dominate the mechanics, which facilitates the identification and validation of small-scale mechanical models. Hence, the tri-axial force measurements, in combination with high resolution microscopy and computational modeling tools, e.g. finite element method, provide rich, mechanical data, which allows for in-depth investigation of realistic, three-dimensional mechanics, which would be impossible with conventional, uni-axial mechanical tests, such as bending or tensile testing.

5.5 Conclusion

Understanding the intricate, mechanical behavior of densely stacked materials, as used in, e.g., microelectronic applications, requires mechanical experiments that mimic the realistic setting in which these material systems are fabricated and used. This chapter presents a versatile experimental approach to measure quasi-static, tri-axial forces using commercially available piezoelectric actuators. A tri-axial, micro-mechanical testing rig with sub-millinewton force sensing resolution, a high dynamic (force) range, and nanometer positioning resolution has been realized.

The leakage of charge in piezoelectric materials poses a major challenge in measuring quasi-static forces by the piezoelectric effect. The generic solution, proposed in this work, relies on the use of two piezoelectric actuators for each loading axis (x, y, z) of the mechanical testing rig. One actuator is used with closed-loop feedback control to impose mechanical deformation to a specimen in a step-wise manner. The other actuator is used without the feedback control loop to measure the force in the specimen. Because of the step-wise method for driving the closed-loop actuators, the corrupting drift effects, resulting from charge leakage, can be eliminated.

The use of commercial actuators makes the device accessible, but also presents particular challenges, since the design details are not disclosed by the manufacturer. This problem is overcome through a series of dedicated calibration experiments, allowing to characterize the device's technical properties, i.e., the internal stiffness, and the axial and cross-axial machine compliance.

This work resulted in an accurate, in-situ, tri-axial, mechanical testing rig with a relatively simple design, and constructed from commercially available components, which makes it highly accessible for academic research or industrial investigatory applications. A shortcoming of the setup is, however, its incapability of performing mechanical creep or relaxation experiments. The setup demonstrates its potential for conducting realistic, micro-mechanical, quasi-static experiments to provide rich, multi-axial, mechanical information. In combination with high-resolution microscopy, such experiments allow to investigate and characterize the mechanical behavior of microelectronic material systems in a more realistic, micro-mechanical setting.

Acknowledgements

This research was carried out under project number M62.2.12472 in the framework of the Research Program of the Materials Innovation Institute (M2i) in the Netherlands (www.m2i.nl).

CHAPTER 6

Identifying mixed-mode adhesion properties of a flexible OLED

Abstract

The identification of relevant adhesion properties is important for the development of microelectronic systems, e.g., microprocessors, light-emitting diodes, etc. This is best done on an actual device, rather than on dedicated specimens, because such properties are highly specimen specific. This paper discusses how the full-field identification method of integrated digital image correlation (IDIC) can be used to identify three mixed-mode cohesive zone parameters of a flexible, organic light-emitting diode (OLED) from a single mechanical test. A tri-axial, micro-mechanical testing setup is employed for the in-situ, on-device delamination experiment, employing optical microscopy.

The microscopic magnification, required for capturing the relevant kinematics, prevents the experimentally imposed loading conditions to be captured within the field of view. Virtual experiments are firstly conducted to optimize the local boundary conditions therefore required by the finite element simulation within the IDIC-framework, and which constitutes the cohesive zone model. The virtual experiments also allow for selecting an adequate load-case for the actual experiment, in order to maximize the kinematic sensitivity of IDIC with respect to the three mixed-mode cohesive zone parameters, and identify them accurately. The image residual, minimized in IDIC, together with the convergence behavior towards the associated global minimum, provide adequate measures for assessing the trustworthiness of the solution.

The optimized load-case is subsequently used to trigger delamination of a 50 [μm] thick barrier stack from its substrate in a real in-situ experiment on a flexible OLED. The optimized boundary conditions from the virtual experiments are used in a corresponding simulation for identifying the three mixed-mode cohesive zone parameters by IDIC. The optimization scheme within IDIC was found to be robust against deviating initial guesses, and consistently converged to a unique solution for the cohesive zone parameters.

Keywords: adhesion properties; mixed-mode cohesive zone model; full-field identification; in-situ testing; microelectronics; flexible electronics

Reproduced from:
A.P. Ruybalid, O. van der Sluis, M.G.D. Geers, J.P.M. Hoefnagels
Full-field identification of mixed-mode adhesion properties in a flexible, multi-layer microelectronic material system, Submitted to journal

6.1 Introduction

Interfacial delamination is one of the key failure mechanisms in microelectronic devices consisting of dissimilar material layers [8–10, 14]. An extensive number of experimental approaches has been applied in the literature to measure the adhesion properties of thin films on substrates and other microelectronic material systems [26, 158–168], although they are mainly based on the use of dedicated specimens and/or specifically induced load-cases (e.g., nanoindentation, blister tests, etc.). Adhesion properties are, however, known to be highly load-case specific and specimen-dependent [14, 22, 27–31]. Therefore, identification of relevant adhesion properties is most accurately done by conducting mechanical experiments that impose in-situ loading conditions to samples directly taken from actual microelectronic devices [169]. To this end, the specimen must be loaded in a multi-axial setting, in order to reproduce the mixed-mode conditions induced during fabrication processes by thermo-mechanical mismatch of the material layers. Because the loading conditions in such experiments are not well-defined, globally measured force-displacement data cannot straightforwardly be used for identifying the relevant adhesion properties, making full-field identification methods necessary.

In this chapter, a tri-axial, micro-mechanical testing setup is employed to induce mixed-mode delamination in specimens from a flexible, organic light-emitting diode (OLED). In-situ mechanical tests are conducted in combination with optical microscopy to capture images of the interfacial failure process. The mixed-mode parameters of a cohesive zone model are identified by correlating the images, using full-field integrated digital image correlation (IDIC) [64–66]. Since the loads in the experiment are applied outside the microscopic field of view, local boundary conditions are measured within the field of view, and subsequently applied in the finite element model, as done in previous studies [133, 170]. Prior to conducting real experiments, the identification procedure is optimized by virtual experimentation, which has proven to be instrumental for investigating the accuracy of the full-field identification method in a controlled manner. Virtual experiments facilitate the selection of a proper test configuration in order to maximize the sensitivity of the identification routine with respect to the unknown parameters. A mixed-mode cohesive zone model is thereby used to describe the interfacial behavior of the OLED stack.

Before the virtual and real experiments are discussed in Sections 6.3 and 6.4, respectively, the adopted cohesive zone model, the full-field identification method, and the experimental setup and procedures are described in Section 6.2.

6.2 Methodology

Identifying the parameters of a mixed-mode cohesive zone model is based on integrated digital image correlation (IDIC). This section describes (1) the in-situ mechanical experiment and the used specimens, (2) the cohesive zone model used within a finite element framework, and (3) the method of integrated digital image correlation.

6.2.1 Experiment setup and specimen processing

To trigger delamination in a sample from an organic light-emitting diode, a mechanical testing rig, based on piezoelectric actuators, is used [171]. The setup has the capability

of applying displacement controlled loading with nanometer resolution and over a range of 200 [μm], in all three directions (x, y, z), while measuring the corresponding forces with sub-millinewton resolution over a range of 10 [N]. This mechanical testing rig allows for imposing a variety of loading modes, by simultaneous loading in different directions, which is required for mixed-mode delamination tests on the interfacing material layers in the specimen. Optical microscopy is used to capture the delamination process in images with a horizontal field width of 1104 [μm], comprising pixels with a physical size of 0.5 [μm].

Specimens are processed from a multi-layer barrier sheet as used for flexible, organic light-emitting diodes (OLED). The specimen consists of a 130 [μm] thick polyethylene naphthalate (PEN) substrate and a multi-layer barrier consisting of three 25 [μm] thick, acrylate (organic) coatings for planarization (OCP) with 150 [nm] thin films of Si_3N_4 in between the OCP-layers. The multi-layer OCP-Si_3N_4 stack serves as a barrier, protecting the functional OLED layers against moisture and oxidation [172–175]. The mechanical experiment requires preparation of the specimens, for which the following protocol is pursued:

1. Specimens are cut out from a larger sheet, to a size of 9×3 [mm^2], by a tool consisting of two parallel, ultra-thin razor blades each having a blade thickness of 5 [μm].

2. The specimens are adhered in between two stainless steel beams, each beam having the same length and width as the OLED specimen, i.e., 9×3 [mm^2], and a thickness of 1 mm. The specimen's side of the PEN-substrate is adhered to one steel beam over its full length and width, while the OCP-side of the specimen is adhered along $\sim$ 2.5 [mm] of its total length (9 mm). An illustration of the specimen, the confining steel beams, and the glued regions are shown in Figure 6.1.

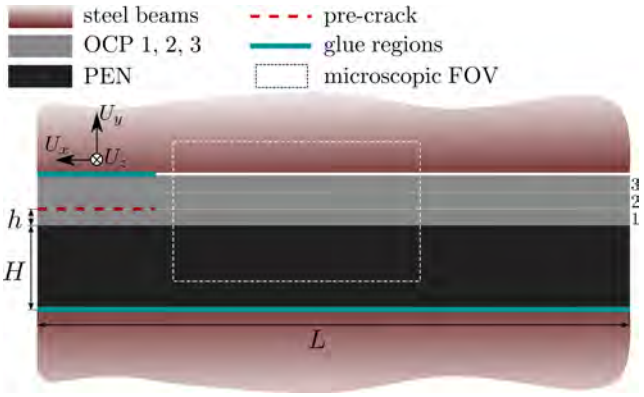

Figure 6.1. Side-view illustration of the specimen (not to scale) with a length $L = 9$ [mm], consisting of a PEN-substrate with a thickness $H = 130$ [μm], and three OCP-layers (numbered: 1, 2, 3), each with a thickness $h = 25$ [μm], amounting to a total stack thickness of 205 [μm]. For testing, the specimen is adhered in between two 1 [mm] thick steel beams along the regions indicated in blue. The testing rig can impose displacements U_x, U_y, and U_z to the top layer of the specimen, depending on the desired testing configuration, while keeping the bottom layer fixed. The thin Si_3N_4-films are not shown in this illustration. For the identification procedure (explained in Section 6.2.3), micrographs are captured within the indicated field of view (FOV).

3. The excess adhesive on the sides of the specimen, sandwiched in between the steel beams, is removed by grinding with sandpaper grit sizes of 1200, 2000, and 4000. The grinding process is done dry, i.e., without water, since moisture creeping in between the layers may be taken up by the polymers, causing the layers to swell and the interfaces to fail prematurely.

4. One longitudinal edge of the specimen is sputter coated with 20 [nm] of gold by physical vapor deposition, in order to increase the light reflection for optical microscopy used during the in-situ experiments. No additional speckle pattern is needed, since the micro-scale roughness, induced by the grinding steps, in combination with the highly reflective gold layer provides sufficient contrast for the digital image correlation procedure used within the identification method.

5. A pre-crack is made by forcing a razor blade in between OCP-layers 1 and 2 (See Figure 6.1), since preliminary experiments have consistently shown this particular interface to be the weakest in the stack and prone to fail before other interfaces do. The pre-crack is made on the left side in Figure 6.1, with approximately the same length as the region by which the OCP-layer is adhered to the steel beam, i.e., ~ 3 [mm]. Note that the exact pre-crack length may vary from specimen to specimen. The pre-crack in the material stack is clearly visible in Figure 6.2(c).

6. Finally, the sandwich (OLED specimen in between the two steel beams) is adhered in between the grippers of the mechanical testing rig. The thickness of the steel beams (1 [mm]) prevents excess adhesive to flow over and in between the specimen's material layers.

The identification method makes use of local boundary conditions, extracted from images of the delamination process, which will be explained in detail in Section 6.2.3. Note that, therefore, the requirements regarding the lengths of the adhered regions and the pre-crack are not stringent. Photographs of the mechanical setup and a specimen are shown in Figure 6.2.

6.2.2 Simulation of the experiment

Simulations are required for the virtual experiments, by which the identification method can be optimized, which is explained in Section 6.3. The integrated digital image correlation procedure is explained in Section 6.2.3.

For the virtual experiments, the full specimen is modeled, having a length of 9 [mm], a width of 3 [mm] and a total stack thickness of 205 [μm], in order to simulate the real experiment by the finite element (FE) method. The steel beams holding the specimen in the experiment are not modeled.

The bulk material layers of the OLED, i.e., OCP and PEN, are described by linear-elastic material models, governed by a Young's modulus E and a Poisson's ratio ν. Three-point bending experiments are conducted by the mechanical test setup of Section 6.2.1 to measure the Young's moduli of the PEN-substrate and the OCP-layers. The experimental results of these bending tests are shown in Figure 6.3, and are used together with Euler-Bernoulli analyses to extract the Young's moduli of PEN and OCP, which are listed in Table 6.1. The

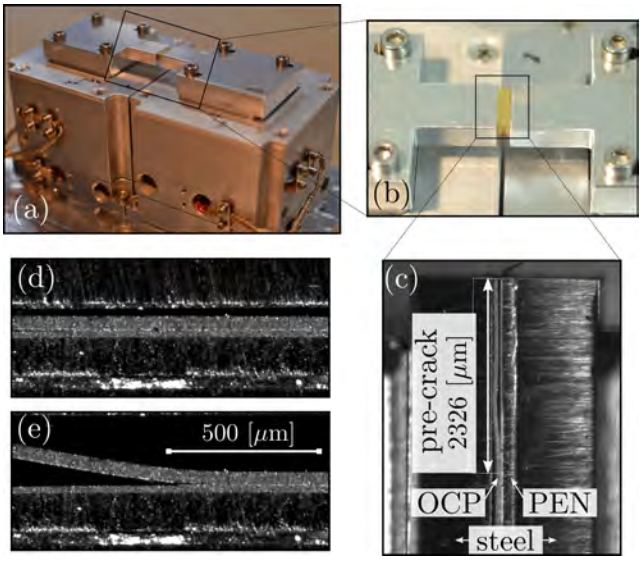

Figure 6.2. (a) Photograph of the micro-mechanical setup, with (b) a zoom-in of the grippers to which (c) the specimen, sputter coated with gold and sandwiched in between two steel beams, is glued. In (c), a pre-crack of ~ 2.3 [mm] made by a razor blade can be seen. (d)-(e) show examples of optical micrographs of the delamination process used for the integrated digital image correlation procedure (Section 6.2.3).

reported mean values are used in the FE-models employed in the remainder of this chapter, unless stated otherwise. The uncertainties reported on the Young's moduli stem from the

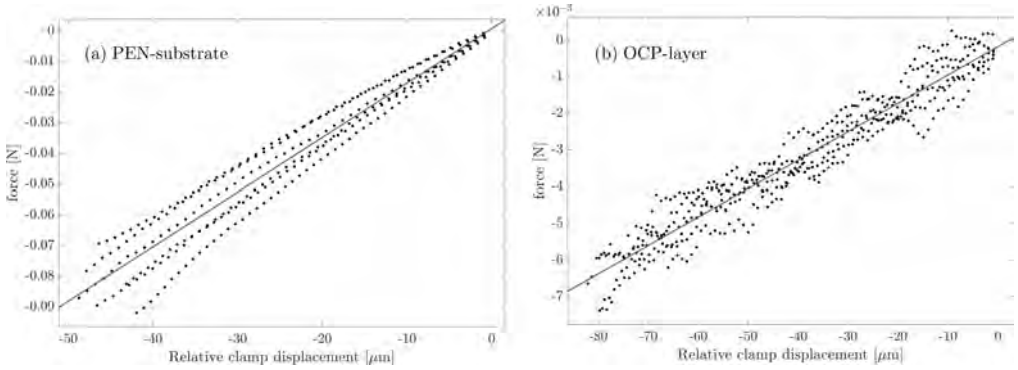

Figure 6.3. Three-point bending tests on (a) six PEN-substrates, and (b) six OCP-layers. The blue lines represents linear regressions through the collective data from six experiments for each material.

variations in specimen widths, which have been measured optically for each tested specimen.

Table 6.1. The elastic properties of PEN and OCP.

material	E [GPa]	ν [-]
PEN	4.91 ± 0.15	0.4
OCP	3.90 ± 0.12	0.3

To model the weakest interface between the first and second OCP-layers (see Figure 6.1), an exponential cohesive zone model [135] is used. The model relates the effective traction $\vec{T} = T\vec{e}$ [Nm^{-2}] to the effective opening displacement $\vec{\Delta} = \Delta\vec{e}$ [m] between originally coinciding, interfacing material points. The unit vector $\vec{e}$ represents the direction of the effective separation between two associated material points at opposite sides of the interface. The traction-separation relation for normal opening is:

$$T = \frac{G_{c,n}}{\delta_c^2}\Delta \exp\left(-\frac{\Delta}{\delta_c}\right), \tag{6.1}$$

where the work of separation $G_{c,n}$ [Jm^{-2}] and the critical opening displacement δ_c (corresponding to the maximum effective traction $T_{\max}$) are the model parameters. This direct scalar relation between T and Δ is often observed between interfacing polymer materials [23, 130, 176]. Numerous studies reveal that the behavior of many interfaces is not equal under normal and tangential opening conditions [20, 28, 29, 121, 130, 177–180]. The adopted model can account for this. The degree of mode-mixedness is defined by the scalar $d = ||\vec{d}_1 - \vec{d}_2||$, which is determined by the direction $\vec{e}$ of the opening vector $\vec{\Delta}$ between two separating material points, see Figure 6.4. In case of pure mode-I (normal) opening, $d = 0$,

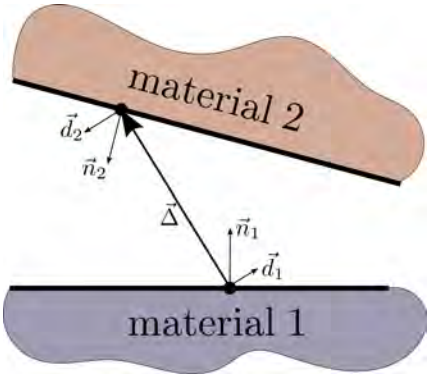

Figure 6.4. Illustration of delamination between two material points that separate by $\vec{\Delta}$ (reproduced from [181]). The unit vectors $\vec{n}_i$ are the normal directions of the material surfaces, and the vectors $\vec{d}_i$ are their orthogonal projections on the direction perpendicular to the opening vector $\vec{\Delta}$.

and in case of pure mode-II (tangential) opening, $d = 2$, while $0 < d < 2$ for intermediate degrees of mode-mixedness. Together with the ratio between the work of separation in the tangential and normal directions, represented by a parameter ζ, the model response varies

for different degrees of mode-mixedness d:

$$T = \frac{G_{c,n}}{\delta_c^2}\Delta \exp\left(-\frac{\Delta}{\delta_c}\right)\zeta^{\frac{d}{2}}, \tag{6.2}$$

$$\zeta = \frac{G_{c,t}}{G_{c,n}}. \tag{6.3}$$

The cohesive zone model has been implemented between OCP-layers 1 and 2 (see Figure 6.1) by user-defined, planar elements in a three-dimensional finite element model, using the software package *MSC.Marc*. As explained above, the cohesive zone model has three governing parameters: $G_{c,n}$, δ_c, and the ratio ζ. Identifying these parameters for the interface between OCP-layer 1 and 2 in the OLED-specimen is the goal of this investigation. Since the interface between OCP-layers 1 and 2 is the weakest, other interfaces in the specimen are neglected, i.e., no cohesive zone elements are implemented between the other layers. Furthermore, the thin Si_3N_4-films are also neglected in the model, since the magnification of the microscopic technique employed in the experiments does not allow to visualize these layers. They can be considered to be part of the interface between the OCP-layers, since a cohesive zone model typically lumps the fine-scale damage processes (e.g., failure of Si_3N_4) at the crack-tip in a plane.

The model used for the virtual experiment incorporates Dirichlet boundary conditions, by fixing the bottom nodes of the modeled PEN-substrate in all three directions, and by kinematically prescribing the top nodes of the OCP-layer that correspond to the glued region of the experiment (cf. Figure 6.1). The finite element discretization was optimized by a mesh convergence study, yielding elements with a size of ~ 5 [μm]. Furthermore, the pre-crack of 3 [mm] is included in the model (i.e., a region without cohesive zone elements). Illustrations of the model with the pre-crack, the applied boundary conditions, and the finite element mesh, are shown in Figure 6.5.

6.2.3 Integrated digital image correlation

The three cohesive zone parameters of interest are identified by integrated digital image correlation (IDIC) [66, 84, 86]. For the problem addressed here, the residual difference between a reference image of the undeformed material configuration and images of the deformed material configurations is minimized, using the displacement fields from the finite element simulations:

$$\Psi = \int_\tau \int_\Omega \frac{1}{2}\left(f(\vec{x}, t_0) - g \circ \vec{\phi}(\vec{x}, t, \theta_i)\right)^2 \mathrm{d}\vec{x}\mathrm{d}t, \tag{6.4}$$

where f and g are the scalar intensity fields of the reference configuration at time t_0 and the deformed configurations at time t, respectively. Furthermore, the symbol $\circ$ denotes a function composition. Image g is a function of the mapping function $\vec{\phi}$ that maps the pixel position vector $\vec{x}$ in image f to the pixel position vector in image g [103] by:

$$\vec{\phi}(\vec{x}, t, \theta_i) = \vec{x} + \vec{h}(\vec{x}, t, \theta_i), \tag{6.5}$$

using the displacement field $\vec{h}(\vec{x}, t, \theta_i)$ from the finite element simulation, incorporating the cohesive zone model of [Eq. 6.2] with its model parameters $\theta_i = [\theta_1, \theta_2, \ldots, \theta_n]^T$ (where n

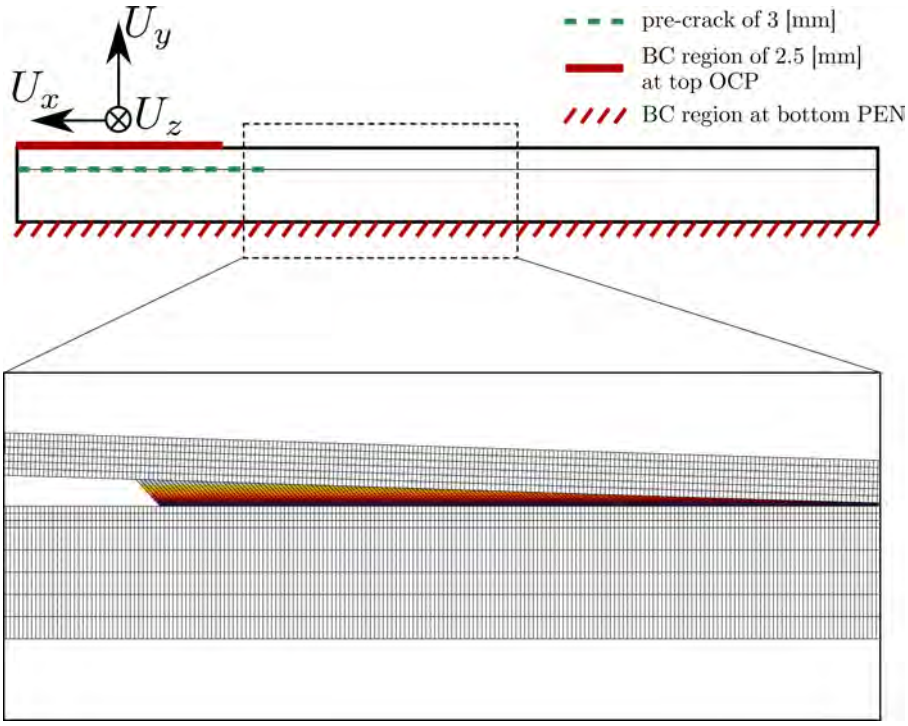

Figure 6.5. The top panel illustrates the full-length model (not to scale) with the pre-crack and the applied boundary condition (BC) regions. The bottom BC-nodes (PEN) are fully fixed in all directions and the top BC-nodes (OCP) can be kinematically prescribed by a combination of displacements U_x, U_y, U_z, depending on the desired test configuration. The bottom panel shows a sub-region of the actual FE-model (deformed), where the finite element discretization is noticeable, and in which the opened cohesive zone elements are colored.

is the total number of unknown parameters). Using the Gauss-Newton method, the square image residual of [Eq. 6.4] is minimized for all pixels in the space domain Ω and the time domain τ by optimizing the model parameters in an iterative fashion:

$$\frac{\partial \Psi}{\partial \theta_i} = 0, \tag{6.6}$$

yielding a linear system of equations:

$$M_{ij}\delta\theta_j = b_i, \tag{6.7}$$

where the correlation matrix M_{ij} and the right-hand side b_i are:

$$\forall(i) \in [1,n], \quad b_i = \int_\tau \int_\Omega \vec{H}_i(\vec{x},t,\theta_i) \cdot \vec{G}(\vec{x},t,\theta_i) \left(f(\vec{x},t_0) - g \circ \vec{\phi}(\vec{x},t,\theta_i) \right) \mathrm{d}\vec{x}\mathrm{d}t, \tag{6.8}$$

$$\forall(i,j) \in [1,n]^2, \quad M_{ij} = \int_\tau \int_\Omega \vec{H}_i(\vec{x},t,\theta_i) \cdot \vec{G}(\vec{x},t,\theta_i) \vec{G}(\vec{x},t,\theta_i) \cdot \vec{H}_j(\vec{x},t,\theta_j) \mathrm{d}\vec{x}\mathrm{d}t, \tag{6.9}$$

The gradient $\vec{G}$ is here taken to be the spatial gradient of the reference image f, but different choices are possible [103]. Furthermore, $\vec{H}_i$ represent the kinematic sensitivities of the simulated displacement fields $\vec{h}(\vec{x},t,\theta_i)$ with respect to each parameter θ_i:

$$\vec{H}_i(\vec{x},t,\theta_i) = \frac{\partial \vec{h}(\vec{x},t,\theta_i)}{\partial \theta_i}, \tag{6.10}$$

which are here calculated by a forward finite difference approach that requires the model response for a parameter set and the perturbed model responses for each perturbed parameter. In practice, this means that $n+1$ simulations must be run for each iteration of the IDIC routine.

6.3 Virtual experimentation

Virtual experimentation exploits numerical simulations to generate virtual "experimental" data, in order to validate a method, in this case, the identification method of IDIC, for a known solution. In this case, the generated data consists of a set of intensity images representing a virtual specimen, i.e., gray values. Virtual experiments have proven to be instrumental for investigating and optimizing the identification method's sensitivity towards the parameters of interest, as well as for understanding the detrimental effect of potential error sources [65, 95, 118, 133, 170]. This section discusses several virtual experiments in order to optimize IDIC for identifying the three cohesive zone parameters of an OLED barrier stack.

6.3.1 Boundary conditions

As explained in the introduction, microscopy is required for capturing the relevant kinematics associated with the interfacial failure triggered during a micro-mechanical experiment. When magnifying a local area of interest, the loads applied at far-field locations during a mechanical experiment are not visible in the imaged field of view. This is of concern, because previous work has identified inadequate boundary conditions to be the most critical source of error for IDIC [133, 170, 182]. A solution to this problem is to avoid inaccurate assumptions on the invisible, far-field loading conditions applied during the experiment. Instead, local, kinematic boundary conditions are measured from within the imaged field of view, and subsequently applied in the finite element model of the visualized part of the specimen (which also decreases the computational costs with respect to modeling the full specimen). It is thereby essential that (1) the kinematics, induced by the far-field boundary conditions, are adequately captured by the local boundary conditions, while (2) not over-constraining

the kinematic model response. The latter is important in order to assure that the model is sufficiently sensitive to the kinematic influence of the three cohesive zone parameters: $G_{c,n}$, δ_c, ζ, so that they can be accurately identified by IDIC [170].

Virtual experiments provide direct insight in the role of the local boundary conditions, and are used here to select an optimal method for applying them. To this end, a virtual experiment is conducted in which the interface is opened in the normal direction by applying a total displacement $U_y = 150$ [μm] at the boundary condition region of the top layer in the full model of the material system, as illustrated in Figure 6.5. A total of 150 increments is used for the simulation, i.e., 1 [μm] per increment is imposed. The displacements U_x and U_z are prescribed to be zero, and the bottom nodes of the modeled PEN-substrate are fixed in all directions. Opening in the normal direction by U_y, as opposed to opening in the tangential direction, yields the largest nonlinear deformation in the form of bending and stretching of the top OCP-layers in the modeled system. Note that this will not trigger pure mode-I delamination, since the top OCP-layers will also stretch, due to the imposed zero displacement U_x, resulting in a significant mode-II opening component as well. Since, in a real experiment, the images used for IDIC only capture a limited, spatial region of the entire specimen, the model used for IDIC in this virtual experiment should also correspond to the restricted field of view with its locally applied boundary conditions. The method for applying such local boundary conditions can be assessed and optimized by extracting displacements from the full-model simulation (virtual experiment), and imposing those displacements to a limited number of nodes in the model corresponding to the restricted field of view of the images used for IDIC. To this end, the kinematic model responses of the full model (virtual experiment), which uses the far-field boundary conditions, and the cropped model that uses locally applied boundary conditions, are compared by subtraction, yielding a displacement difference field. Note that for this first investigation, IDIC is not yet employed. Figure 6.6 shows the difference fields from the two model responses for the final time increment of the simulations, for different locally applied boundary conditions. The left-most column in Figure 6.6 illustrates the locally prescribed boundary condition (BC) nodes. The local boundary conditions should capture the kinematics "entering" the limited field of view sufficiently accurately to impose the correct kinematic response in the interior of the cropped model. Firstly, the boundary conditions required for the modeled OCP-stack are scrutinized. The FE-nodes near the left and right edges of the modeled OCP-stack should therefore be kinematically prescribed, while leaving the middle part of the modeled OCP-stack unconstrained. To capture the kinematics associated with bending, it is rationalized that a minimum of four horizontally spaced nodes should be used to prescribe the y-displacements on each side (left and right), because four nodes are needed to enforce the curvature of the bending layers and its linear variation along the horizontal direction [170]. To account for the shearing component, the x-displacement is prescribed in four nodes, horizontally and vertically spaced, at each side (left and right). The resulting BC are illustrated in the first column of row (a), in Figure 6.6. Since the focus lies on examining the boundary conditions for the OCP-stack, the bottom nodes of the modeled PEN-substrate are, initially, all prescribed with zero-displacements, as in the virtual experiment (full model). For this first set of local boundary conditions, shown in row (a), the difference fields still yield significant errors in the order of 1×10^{-4} [mm]. A shear component may be missing. Therefore, another row of four nodes prescribing the y-displacement is added on either

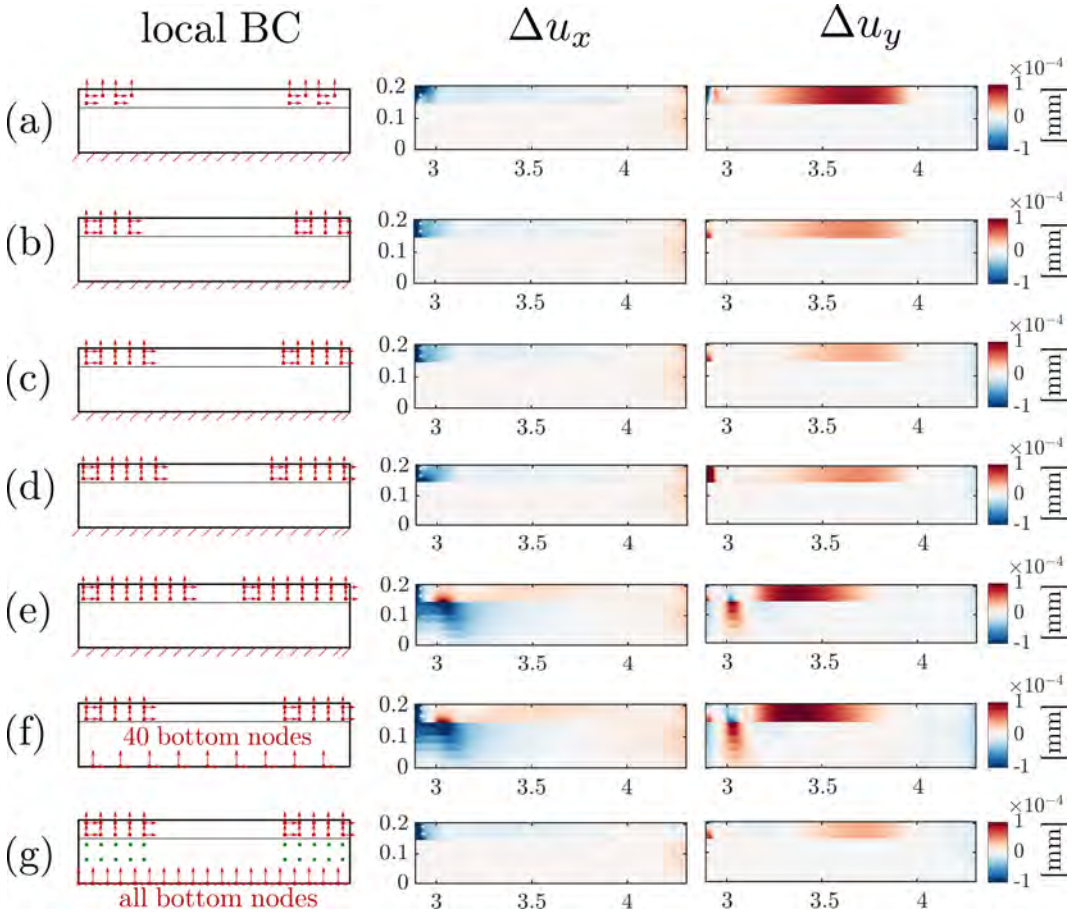

Figure 6.6. Displacement difference fields Δu_x and Δu_y in [mm] between the full model response and the cropped model response, using local boundary conditions as illustrated in the left column. The difference fields are only shown for the final simulated increment.

side (left and right), as seen in row (b). The differences Δu_x and Δu_y thereby decrease. Gradually, more nodes are added to investigate the effect on the displacement fields. It becomes clear that the boundary conditions, employing two rows of five nodes to prescribe the y-displacement and four nodes to prescribe the x-displacement, on either side (left and right) of the OCP-stack, yields the smallest error, as seen in row (c) of Figure 6.6. Prescribing more nodes in the OCP-stack has a detrimental effect on the accuracy of the model response. Moreover, with more prescribed nodes, the size of the kinematically free center region of the model decreases. This, in turn, reduces the kinematic sensitivity to changes in the material parameters, and with that, the accuracy with which these parameters are identified [133, 170]. Row (f) of Figure 6.6 shows a variation of the number of the bottom nodes prescribed in the PEN-substrate. Prescribing only a fraction of those bottom nodes

(e.g., 40) is inadequate, since the PEN-layer is fully fixed in all directions in the (virtual) experiment. It is thereby verified that it is indeed necessary to prescribe all bottom nodes of the modeled PEN-substrate, as was done in all the other BC (except in row (f) to test this particular effect). Furthermore, to capture kinematics entering from the left and right sides into the PEN-substrate, equivalent local boundary conditions as used in the top OCP-stack are applied in the PEN-substrate as well. These local boundary conditions are illustrated by green squares in row (g) of Figure 6.6, without arrows for the sake of visual clarity. The additional boundary conditions for the modeled PEN-substrate decrease the maximum displacement difference (e.g., for Δu_y) from $\sim 5 \times 10^{-5}$ in Figure 6.6(c) to $\sim 2 \times 10^{-5}$ [mm] in Figure 6.6(g). To conclude, the boundary conditions of row (g) in Figure 6.6 are the most adequate and will be adopted in the model used for IDIC.

6.3.2 Test-case selection

The virtual experiment used for the boundary condition optimization in Section 6.3.1 does not allow for identifying all three cohesive zone parameters (identification results not shown), because the sensitivity towards the parameters is insufficient. Therefore, the test configuration required for properly identifying all three mixed-mode cohesive zone parameters is investigated in detail. Four different virtual experiments are conducted, in between which the load application is varied. The simulated displacement fields from the virtual experiment are subsequently used to generate images embodying the deformation of a reference image of the virtual specimen. The reference speckle pattern is constructed by the superposition of three standard normal distributions of random gray levels, each distribution having a different width of 5, 20, and 100 pixels, see Figure 6.7(a). Thereby, the constructed reference image contains a random pattern of speckles with different sizes, and is stored in an 8-bit gray-valued image, comprising 2752×910 pixels, which corresponds to a physical field of view of 1.189×0.393 [mm^2], i.e., the pixel size is: 0.43 [μm]. Subsequently, images of the deformed, virtual specimen are generated by interpolating the pixel gray values of the reference image on displaced pixel positions, using the simulated displacements, see Figures 6.7(b)-(c).

The four different virtual test-cases, labeled (a) to (d), are described next, and are illustrated in column I of Figure 6.8, which also shows the loading paths in terms of the applied displacements U_x and U_y. See Figure 6.5 to recall how the loading is applied in different directions in the (virtual) experiment. The required test-case should trigger a combination of normal an tangential delamination, so that all three mixed-mode cohesive zone parameters: $G_{c,n}$, δ_c, and ζ, can be identified from a single experiment.

To investigate whether both normal and tangential delamination are sufficiently triggered at the interface, the mode angle is evaluated along the fracture process zone of the numerical simulation that corresponds to the field of view used within IDIC. The mode angle is calculated as: $\psi = \tan^{-1}\left(\frac{\Delta_t}{\Delta_n}\right)$, where Δ_t and Δ_n are the tangential and normal components of the effective opening vector $\vec{\Delta}$, respectively. The mode angle approaches $\psi \approx 0^\circ$ when the normal opening component dominates, and approaches $\psi \approx 90^\circ$ when the tangential opening component dominates. The mode angle profiles along the fracture process zone (the x-direction) are shown in column II of Figure 6.8 for each test configuration, together with the traction profile. Previous work revealed that significant spatial variations of the mode

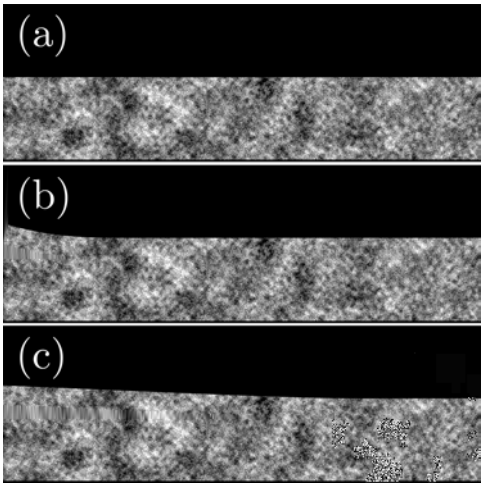

Figure 6.7. Examples of generated images from a virtual experiment, where (a) shows the virtual specimen in the reference configuration, and (b)-(c) show the deformed virtual specimen.

angle within the imaged fracture process zone are required for identifying all mixed-mode cohesive zone parameters from a single test [170]. The interfacial crack propagates from left to right, along x, and the region where the traction is nonzero corresponds to the fracture process zone.

Load-case (a), see Figure 6.8(a):

The first attempt to trigger mixed-mode delamination is to firstly apply a total displacement of $U_y = 200$ [μm] in a pre-step to open the interface in the normal direction. The field of view visualizes a section of the (virtual) specimen, in front of the crack tip, in which the interface has not yet opened due to the application of the pre-step. Therefore, this pre-step is omitted from the IDIC-analysis. The interface is subsequently loaded in the tangential direction. To this end, a displacement of $U_x = 100$ [μm] is applied gradually in time, while the normal opening displacement is kept constant at $U_y = 200$ [μm], resulting in an interfacial crack that propagates through the field of view of the images. These images are used for parameter identification by IDIC. As seen in column II of Figure 6.8(a), the variation of the mode angle is limited within the fracture process zone (FPZ). To achieve accurate identification of mixed-mode cohesive zone parameters, it is important that the mode angle varies from $\psi = 0°$ to $\psi = 90°$ within the FPZ, as was shown in [170]. Therefore, the load-case is adapted in order to try to maximize the variation of ψ within the FPZ.

Load-case (b), see Figure 6.8(b):

The virtual experiment of load-case (b) simultaneously applies a total of $U_x = 25$ [μm] and a total of $U_y = 12.5$ [μm], i.e., a ratio of $\frac{U_y}{U_x} = 0.5$, gradually in time. The applied tangential component causes rapid crack propagation through the entire field of view, hence the applied

displacements are limited, and much smaller as opposed to the displacements applied in the load-case (a). As can be seen in column II of Figure 6.8(b), the variation of the mode angle is even more limited. Especially the normal opening component, corresponding to $\psi = 0°$ is poorly triggered.

Load-case (c), see Figure 6.8(c):

To trigger more normal opening, and thereby induce a more strongly varying mode angle, a total of $U_x = 100$ [μm] and a total of $U_y = 70$ [μm] are applied, i.e., a ratio of $\frac{U_y}{U_x} = 0.7$, gradually in time. Although the normal opening component is better represented than in load-case (b), the mode angle does not vary much within the fracture process zone. This load-case is rather similar to load-case (a).

Load-case (d), see Figure 6.8(d):

The previous load-cases do not trigger both normal and tangential delamination in a balanced manner. A more intricate loading path is therefore investigated, where pure mode-I opening is targeted first, followed by a transition that targets mode-II opening. To this end, firstly, displacements $U_y = 150$ [μm] and $U_x = -30$ [μm] are simultaneously applied gradually in time. The normal opening component is thereby initialized strongly, and is gradually leveled off, while the negative tangential displacement compensates for the stretching of the delaminating OCP-stack in the tangential direction. This results in a strong normal opening component by which pure mode-I loading conditions are approached. Subsequently, the normal displacement is gradually decreased to $U_y = 15$ [μm], while the tangential displacement is gradually increased to $U_x = 30$ [μm]. By doing so, the dominant loading mode gradually switches from mode-I to mode-II. As a result, the mode angle now varies significantly within the fracture process zone, see Figure 6.8(d). Therefore, it is expected that load-case (d) will yield the most accurate identification of the mixed-mode cohesive zone parameters.

Sensitivity analysis

The sensitivity fields of [Eq. 6.10] represent the kinematic sensitivity of the IDIC-routine towards the degrees of freedom, i.e., the cohesive zone parameters. For accurate parameter identification, the sensitivity must fulfill two requirements. Firstly, the sensitivity towards each parameter must be sufficient, and secondly, the amount of cross-sensitivity should be limited. Cross-sensitivity causes the objective function, i.e., the right-hand member of [Eq. 6.7], to be minimized by the update of more than one parameter, and potentially leads to a non-unique solution. Because a multitude of images in time are correlated at once, and three degrees of freedom are thereby simultaneously optimized, it is difficult to cross-analyze all sensitivity fields with respect to each parameter of interest. The sensitivity is more conveniently assessed by evaluating the Hessian of the Gauss-Newton scheme of [Eq. 6.7], i.e., the "correlation matrix" M_{ij}. The correlation matrix is defined in [Eq. 6.9], and it represents the kinematic sensitivity towards all parameters of interest. The diagonal terms, M_{ii}, each represent the scalar product of the kinematic sensitivity towards the corresponding parameter and itself, whereas the cross-terms in M_{ij} each represent the scalar product of the sensitivity towards one parameter and the sensitivity towards another parameter.

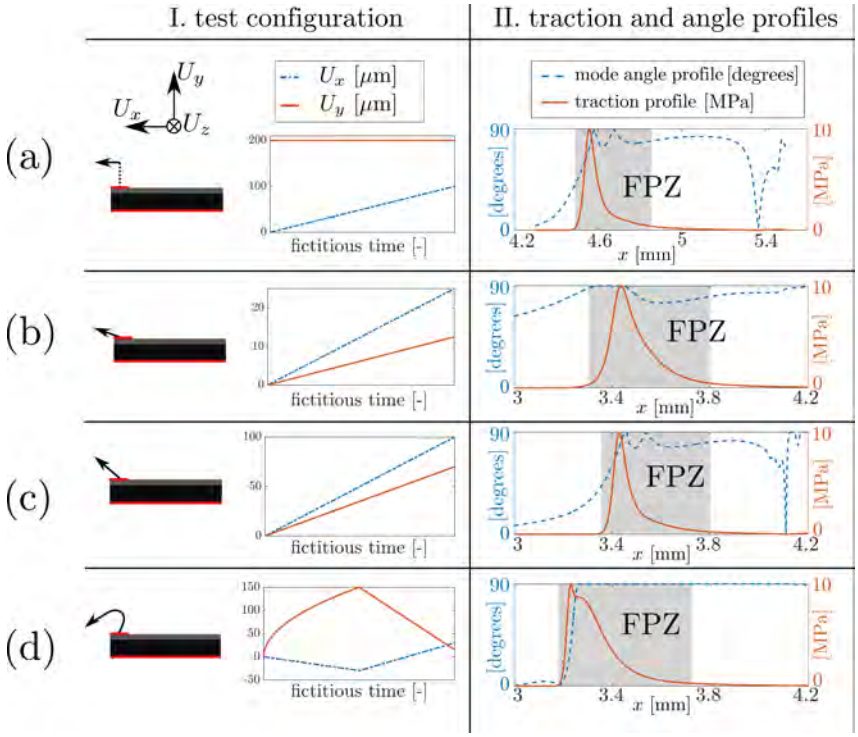

Figure 6.8. Column I shows illustrations of the four load-cases (a)-(d) used in the corresponding virtual experiments. Column II shows the effective traction and the mode angle profiles along the fracture process zone (FPZ) along x of the simulations used for IDIC with the reference parameter values: $G_{c,n} = 10$ [Jm^{-2}], $\delta_c = 0.368$ [μm] and $\zeta = 1.65$ [-].

Therefore, when the M_{ij}-matrix is diagonally dominant, the amount of cross-sensitivity is less pronounced. To evaluate the cross-sensitivity more rigorously, a spectral decomposition of the real-valued, symmetric M_{ij}-matrix is computed. Omitting the index notation, the spectral decomposition is written as:

$$M = QDQ^T, \tag{6.11}$$

where the diagonal matrix D contains the eigenvalues d_i, and matrix Q comprises the corresponding eigenvectors q_i in each column. When the eigenvalues are distinct, the eigenvectors compose an orthogonal set and are linearly independent. Each eigenvector q_i is composed of a combination of the original sensitivity vectors m_i. Since Q discloses the relation between the orthogonal eigenvectors q_i and the original sensitivity vectors m_i, it reveals the level of independence of m_i. When q_i consists of one vector m_i, the latter is considered to be parallel to the former. In other words, Q reveals the orthogonality of the sensitivity vectors m_i. In case of cross-sensitivity, the sensitivity vectors m_i do not align with the orthogonal eigenvectors q_i, and the corresponding parameters are less uniquely identifiable. The M-matrix and its spectral decomposition matrices D and Q are shown in Figure 6.9, as computed for

the four load-cases (a)-(d). The eigenvalues are arranged from large (left) to small (right) in D, and the eigenvectors in Q are arranged accordingly.

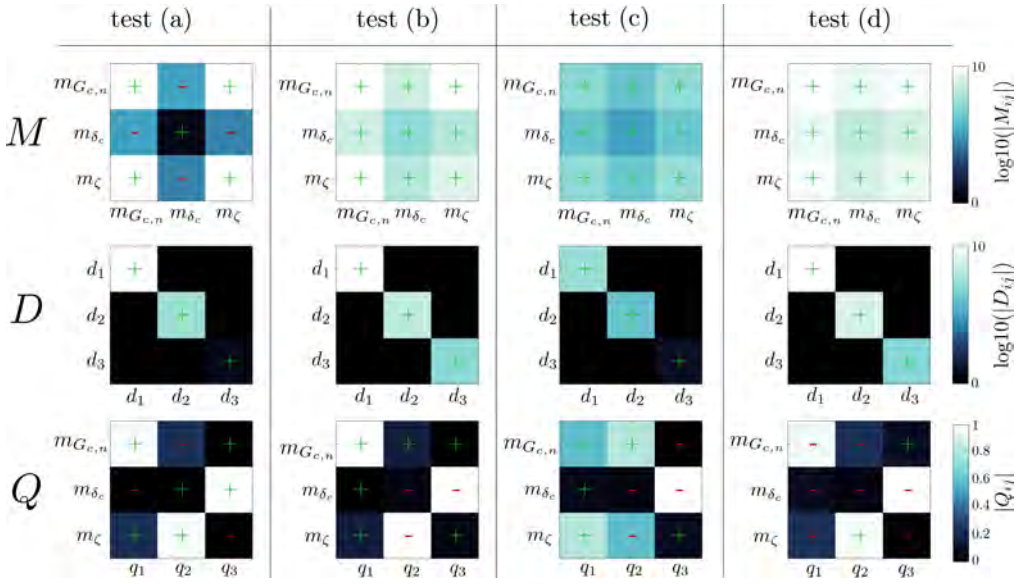

Figure 6.9. The sensitivity matrix M, its eigenvalue matrix D, and its eigenvector matrix Q, representing the kinematic sensitivity for the four different virtual tests constituting the load-cases (a)-(d). The log-scales in M and D are used to improve the visible discreteness of the colors, and the signs of the values are plotted in each matrix element.

The M-matrix of load-case (a) reveals that mainly the sensitivity towards δ_c is relatively low with respect to the sensitivity towards the other two parameters. Moreover, for load-case (a), the third eigenvalue, D_{33}, is extremely low. This eigenvalue is associated with the eigenvector q_3 in Q, which is aligned with the sensitivity vector m_{δ_c}. These observations imply that, for load-case (a), δ_c could be challenging to identify accurately. The same holds for load-case (c), although to a lesser extent, since the lowest eigenvalue in D, of which the corresponding eigenvector q_3 also aligns with m_{δ_c}, is higher than in load-case (a). Furthermore, the Q-matrix of load-case (c) indicates that the sensitivity vectors m_i do not align well with he orthogonal eigenvectors. Cross-sensitivity is therefore expected to occur for that load-case, mainly between the parameters $G_{c,n}$ and ζ (see eigenvectors q_1 and q_2), potentially causing these two parameters to be less uniquely identifiable. In contrast, the eigenvectors of the Q-matrices of load-cases (a), (b) and (d) are each composed of predominantly one sensitivity vector m_i, so cross-sensitivity is expected to be limited, since also the corresponding eigenvalues in D are distinct. Since the matrices M and D of load-case (d) exhibit the largest (eigen)values, followed by those of load-case (b), it is expected that the cohesive zone parameters are most accurately identified in load-case (d), followed by load-case (b).

Identification results

Integrated digital image correlation is applied to the images generated by the four virtual experiments. The local boundary conditions, as described in Section 6.3.1, are employed in the FE-model. To investigate the isolated effect of the different load-cases on the accuracy of the identified parameters, the displacements used for the boundary conditions are extracted directly from the simulations used in the virtual experiments. Using exact boundary conditions ensures that the nodal constraints are prescribed without introducing any additional error. For each load-case, the adequacy of the boundary conditions was validated by evaluating the displacement difference fields Δu_x and Δu_y (not shown), which, for all cases, were equivalently low and similar to Figure 6.6(g). This allows for a clean comparison between the different load-cases, without disturbances from experimental error sources. Furthermore, no globally measured force data is used for IDIC. The known elasticity parameters of the elastically deforming material layers (PEN and OCP) serve as an intrinsic force sensor, as has been shown in previous studies [133, 170].

For each load-case, IDIC is initialized with perfect initial guess values for the parameters, and the identification results are shown in Figure 6.10. The identified parameter values and their corresponding relative errors with respect to the known reference values, are listed in Table 6.2.

Table 6.2. The reference mixed-mode cohesive zone parameters as used in the virtual experiments of the four different test configurations, and the identified parameters and their relative errors ϵ_i [%].

	reference	load-case (a)	load-case (b)	load-case (c)	load-case (d)
$G_{c,n}$ [Jm^{-2}]	10	10.61	11.44	18.83	10.60
$\epsilon_{G_{c,n}}$ [%]	-	6.12	14.38	88.30	6.00
δ_c [μm]	0.368	0.082	0.377	0.38	0.378
ϵ_{δ_c} [%]	-	−77.86	2.49	4.35	2.66
ζ [-]	1.65	1.41	1.33	1.02	1.51
ϵ_ζ [%]	-	−14.46	−19.29	−38.07	−8.41

For load-case (a), the largest error is on the parameter δ_c, as was predicted by the sensitivity analysis, cf. Figure 6.9. The image residual, seen in column II of Figure 6.10(a), has not been properly minimized. The image residual is the most direct measure for evaluating the adequacy of IDIC. Remaining image residuals are a clear indicator of an inaccurate solution, even if the IDIC-analysis seems to have converged.

Load-case (c) comprises the second larges error on δ_c, after load-case (a), which is in line with the corresponding sensitivity analysis. The cross-sensitivity between the sensitivity vectors $m_{c.n}$ and m_ζ, as seen in Figure 6.9(c), has also resulted in large remaining errors on $G_{c,n}$ and ζ, and an inhomogeneously minimized image residual, as seen in column II of Figure 6.10(c). Although the sensitivity towards δ_c, as seen in M of Figure 6.9(c), is the lowest with respect to the other two sensitivities, δ_c is identified more accurately than $G_{c,n}$ and δ_c. This implies that cross-sensitivity can have a more detrimental effect on the accuracy of the solution than a low sensitivity towards a single parameter.

Load-case (b) shows a more properly minimized image residual, although inhomogeneity

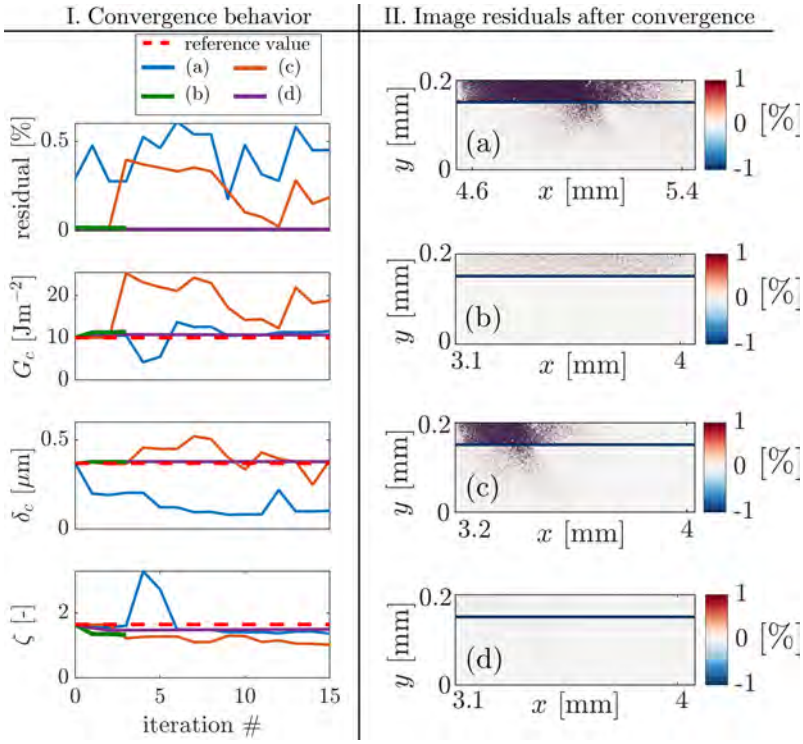

Figure 6.10. Column I shows the convergence behavior of the IDIC-analyses, in terms of the mean value of the image residual over the entire spatial and temporal domains, and the three mixed-mode cohesive zone parameters. Column II shows image residual fields for each load-case (a)-(d), after convergence of the corresponding IDIC-analysis. The blue band in the image residuals represents a masked region not taken into account in IDIC.

can be identified in the residual reflecting the OCP-stack. Since other regions in the residual field have reached an even lower minimum (PEN-substrate region), further minimization of the residual region regarding the OCP-stack should also be possible. It is thereby noted that for these virtual experiments there are no other mechanisms, such model errors, lighting issues or pattern degradation, by which the brightness conservation may have been jeopardized locally within the field of view. Since this is a controlled virtual experiment, these error sources do not apply, so the only remaining reason for significant spatial variation of the image residual, are inaccurate cohesive zone parameters. Although seemingly insignificant in magnitude, the inhomogeneous image residual reveals non-negligible identification inadequacy, which is verified by the significant errors on the identified parameters.

As expected from the sensitivity analysis in Section 6.3.2, as well as the traction and mode angle profiles of Figure 6.8, it is concluded that load-case (d) allows for identifying all three parameters with a reasonable accuracy, since the remaining errors are all below 10%, whereas the other cases show significantly larger errors. This is reflected by the low, homogeneously minimized image residual field in column II of Figure 6.10(d). Although for load-case (d)

the cross-sensitivity regarding parameters $G_{c,n}$ and ζ was concluded to be minimal, the sensitivity vectors $m_{G_{c,n}}$ and m_ζ, do not align perfectly with the orthogonal eigenvectors, cf. Figure 6.9(d). The slight cross-sensitivity is believed to be the reason for the persistent errors on the corresponding parameters $G_{c,n}$ and ζ. Load-case (d) invokes mode-I dominant interfacial mechanics in the initial phase of the experiment, and gradually evolves to mode-II delamination as the test progresses, see column I in Figure 6.8(d). This should yield sufficient kinematic sensitivity and minimal cross-sensitivity, to enable the identification of all three, mixed-mode cohesive zone parameters from a single test. The loading conditions applied in load-case (d) should therefore be used to identify the mixed-mode parameters of the cohesive zone model of [Eq. 6.2] from real experiments.

6.3.3 Robustness against deviating initial parameter guesses

The robustness of IDIC against deviating initial guess values is evaluated for the virtual load-case (d). For load-cases (a)-(c) of Section 6.3.2, initial guesses that deviated only 10% from the perfect, reference values caused divergence in the optimization routine of IDIC. This highlights the importance of the employed load-case for identifying the mixed-mode cohesive zone parameters. Only load-case (d) allowed for larger initial guess distances, as will be discussed below.

Instead of using perfect boundary conditions, extracted directly from the VE-simulation, the boundary conditions are now captured by global digital image correlation (GDIC) in the regions where the local boundary conditions are applied in the FE-model, cf. Figure 6.6(g). To this end, polynomial basis functions up to the fifth degree are used in the GDIC analysis. Subsequently, the extracted displacements are interpolated onto the nodal locations of the corresponding FE-model.

A total of eight IDIC-analyses on the images from the virtual test (d) are initialized with different initial guess values for the mixed-mode cohesive zone parameters. The initial guess values lie within the following ranges: $2 \leq G_{c,n}^i \leq 20$ [Jm^{-2}], $0.08 \leq \delta_c^i \leq 3.68$ [μm], and $1.11 \leq \zeta^i \leq 2.72$ [-]. The results are shown in Figure 6.11, where the colored lines are used to distinguish between the different initial guess cases. The mean values and corresponding standard deviations of the identified parameters are: $\bar{G}_{c,n} = 11.12 \pm 1.10$ [Jm^{-2}], $\bar{\delta}_c = 0.379 \pm 0.002$ [μm], $\bar{\zeta} = 1.42 \pm 0.20$ [-] (recall Table 6.2 for the reference parameter values used within the virtual experiment). The consistent convergence towards equivalent results for a variety of initial guesses, indicates that a global minimum of the objective function, i.e., the image residual, is found. The image residual is the most important measure for evaluating the identification, which can be considered to be trustworthy when:

1. The residual fields for the solution are low throughout space and time, with respect to the residual fields for other parameter values (e.g, erroneous initial guesses).

2. The residual fields have minimized in a homogeneous fashion throughout space and time.

3. For different initial guesses, the image residual minimizes consistently towards the same, or highly equivalent, minimum, while the parameters converge to equivalent values.

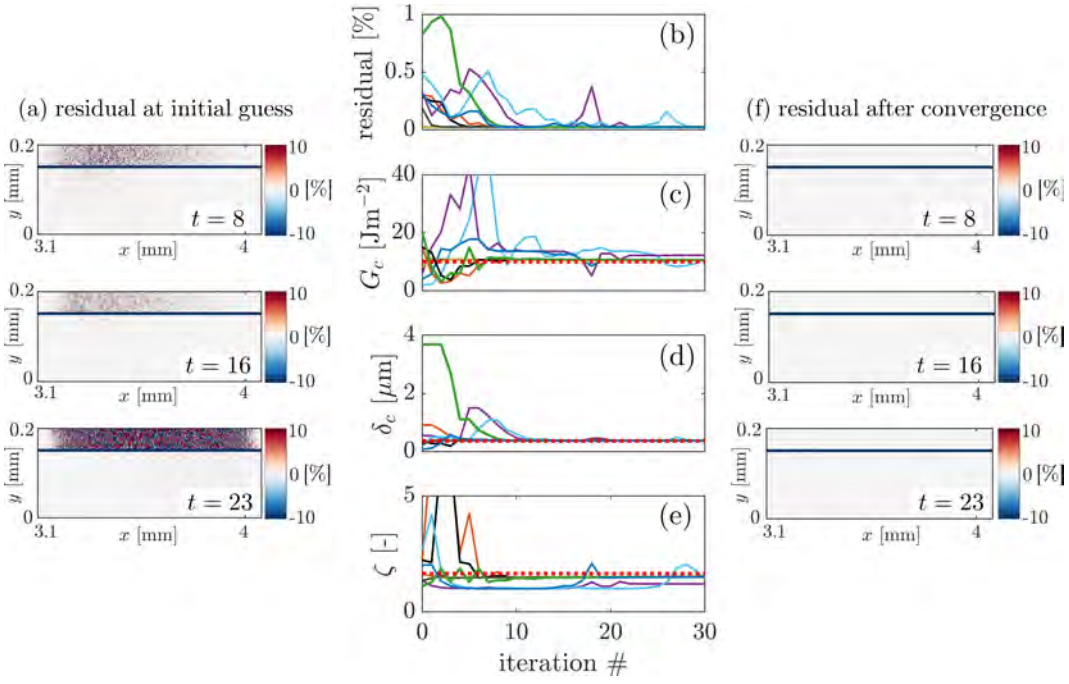

Figure 6.11. The convergence behavior of IDIC for different initial guess values, in terms of (b) the image residual, in percentages [%] of the images' dynamic range, and (c)-(e) the mixed-mode cohesive zone parameter values. The lines are colored to distinguish between the optimization routines initialized with different initial guesses. The red, dotted, horizontal lines indicate the reference values for the cohesive zone parameters used in the virtual experiment. (a) Examples of residual fields, at three time increments t for the initial guess of the IDIC-routine corresponding to the case represented by the green curve in (b)-(e), and after convergence (f). The blue band in the image residuals represents a masked region not taken into account in IDIC.

When these observations on the results can be made, the solution is trustworthy, and is considered to be accurate.

6.3.4 The effect of erroneous elasticity parameters

The global forces associated with the applied deformation are not trivially recovered, due to the complex, multi-directional loading conditions imposed on the specimen, and the restricted field of view. When elasticity parameters of elastically deforming layers are known, and the elastic deformation is captured within the field of view, cohesive zone parameters can be identified without using globally measured force data [133, 170]. However, adopting erroneous values for the elasticity parameters may jeopardize the accuracy of the identified cohesive zone parameters. The effect of wrong elasticity parameters is therefore investigated. The uncertainty on the measured Young's moduli of OCP and PEN, as reported in Table 6.1 of Section 6.2.2, are employed in the FE-model used for IDIC, while the mean values of Table 6.1 have been used in the virtual experiment. Four cases, each with a different

variation of one of the elastic parameters, are analyzed by IDIC, of which the results are reported in Table 6.3. By comparing these results to the previously reported results for

Table 6.3. The influence of erroneous Young's moduli of OCP and PEN on the accuracy of the identified cohesive zone parameters. The Young's moduli are reported in [GPa]. The reference values for the elastic parameters used in the virtual experiment are the mean values listed in Table 6.1. The reference values for the cohesive zone parameters are listed along with the relative errors ϵ_i [%] after convergence of IDIC.

	ref.	$E_{OCP} = 4.05$	$E_{OCP} = 3.75$	$E_{PEN} = 5.06$	$E_{PEN} = 4.75$
$G_{c,n}$ [Jm^{-2}]	10	11.09	10.29	10.69	10.65
$\epsilon_{G_{c,n}}$ [%]	-	10.89	2.89	6.94	6.52
δ_c [μm]	0.368	0.375	0.378	0.381	0.375
ϵ_{δ_c} [%]	-	1.79	2.73	3.76	1.97
ζ [-]	1.65	1.49	1.49	1.49	1.50
ϵ_ζ [%]	-	-9.61	-9.88	-9.49	-9.25

load-case (d) in Table 6.2, it is found that erroneous assumptions for the Young's moduli have a minimal effect on the identification accuracy of the cohesive zone parameters. The image residuals do not reveal any significant inadequacies (they are therefore not shown).

6.4 Experimental results

A real delamination experiment is conducted on the OLED-specimen by the micro-mechanical setup presented in Section 6.2.1, and imposing the load-case of Figure 6.8(d). A total of 44 images are acquired during the delamination process, of which examples are shown in Figure 6.12, together with the loading paths for the applied displacements U_x and U_y. Local boundary conditions are measured by global digital image correlation (GDIC) within four sub-regions of the images, employing fifth-order polynomial basis functions. Subsequently, the measured displacements are applied as local, Dirichlet boundary conditions within the corresponding four sub-regions of the FE-model used within the IDIC-framework, as explained in Section 6.3.1. Furthermore, since the PEN-substrate is glued to the mechanical setup, and there is a possibility that the glue layer deforms during the experiment, the bottom nodes of the modeled PEN-substrate are also measured by GDIC. This has not been done in the IDIC-analyses on the virtual experiments, described in 6.3.2, since the PEN-substrate was simply fixed in all directions during the virtual experiment, making it unnecessary to measure the associated zero displacements. The displacements within the region where the PEN-substrate is glued to the setup are measured by third-order polynomial basis functions along the full length within the field of view. Subsequently, as also explained in Section 6.3.1, all the corresponding bottom PEN-nodes in the model are prescribed by the measured displacements.

6.4.1 Sensitivity analysis

The kinematic sensitivity towards the parameters of interest: $G_{c,n}$, δ_c, and ζ, is evaluated by examining the correlation matrix M and its spectral decomposition matrices D and Q,

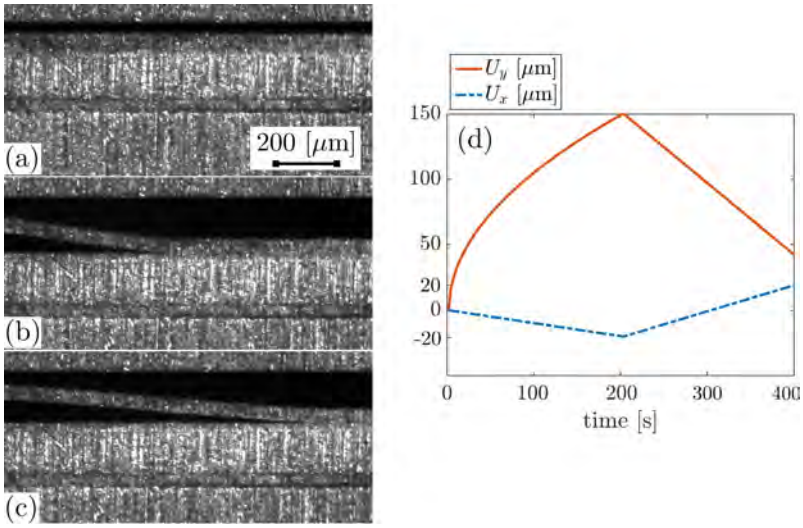

Figure 6.12. (a)-(c) Images of the deforming OLED-specimen, shown for three time increments during the mechanical experiment. A total of 44 images are used for IDIC. (d) The loading paths of the displacements U_x and U_y applied during the test, cf. Figure 6.1.

which are shown in Figure 6.13. The diagonal terms in M reveal that the optimization

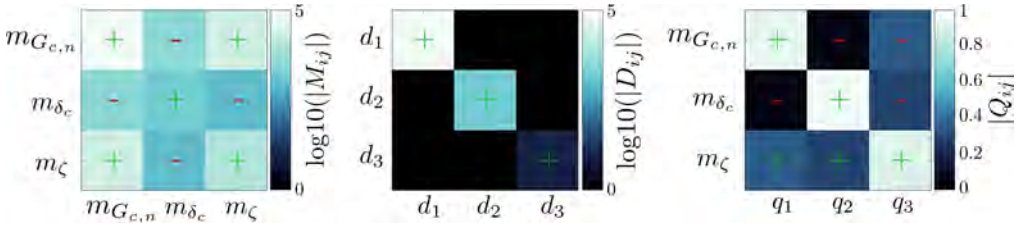

Figure 6.13. The sensitivity matrix M, its eigenvalue matrix D, and its eigenvector matrix Q, representing the kinematic sensitivity of IDIC towards the parameters of interest. The log-scales in M and D are used to improve the visible discreteness of the colors, and the signs of the values are plotted in each matrix element.

routine of IDIC is sensitive towards all parameters. Although the sensitivity m_{δ_c} is slightly lower than the sensitivity $m_{G_{c,n}}$, it is slightly higher than the sensitivity m_ζ. This is an even better scenario than for the virtual test-cases, in which m_{δ_c} was consistently lower than $m_{G_{c,n}}$ and m_ζ. Furthermore, the eigenvector matrix Q implies that the original sensitivity vectors m_i align with the orthogonal eigenvectors d_i, and, therefore, cross-sensitivity is only present to limited extent.

6.4.2 Identification results

To identify the three mixed-mode cohesive zone parameters, proper initial guess values are required to initialize the IDIC-routine. Since the analysis regards a real interface in an OLED-specimen without any knowledge on the cohesive zone parameters, the range in which the solution must lie is completely unknown. Only for the mixed-mode parameter ζ it can be said that its value is unlikely to stray far from $\zeta = 1$ [-]. The Gauss-Newton scheme underlying IDIC is known to only converge to an accurate solution when initialized relatively close to the global minimum of the objective function. Therefore, to estimate the range in which the solutions for $G_{c,n}$ and δ_c should be sought, a direct-search method is applied, before employing IDIC. To this end, displacement fields are simulated for a variety of parameter sets, and are subsequently used to compute the image residual, without employing the Gauss-Newton optimization scheme. Only the parameter space regarding $G_{c,n}$ and δ_c is scrutinized, while the mixed-mode parameter is taken as $\zeta = 1$ [-]. The landscape of the image residual is shown in Figure 6.14. From the residual landscape it becomes clear that,

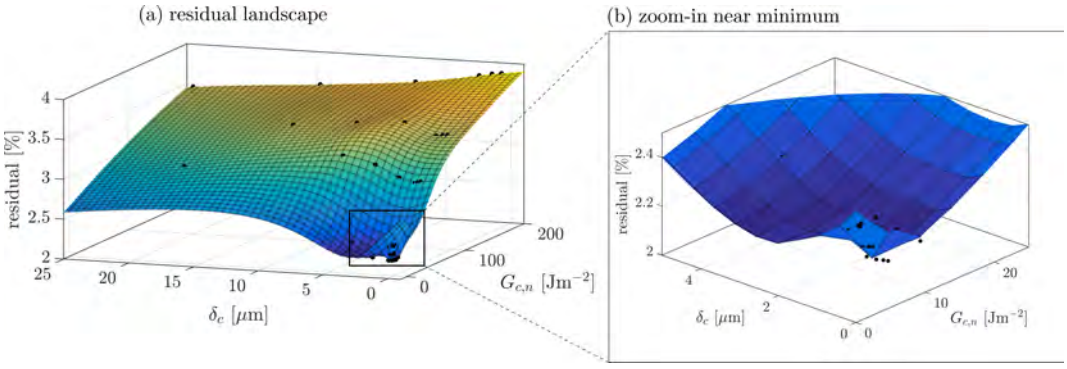

Figure 6.14. The residual landscape from direct-search simulations with a variety of parameter sets, where the black circles represent the calculated image residual [%] in the parameter space spanned by $G_{c,n}$ and δ_c. The colored surface is a visual aid, based on a regression through the data points. The mixed-mode parameter is taken as $\zeta = 1$ [-].

in case of $\zeta = 1$ [-], a global minimum exists, and that the solutions for $G_{c,n}$ and δ_c lie within the ranges of the axes in Figure 6.14(b).

Therefore, a total of seven IDIC-analyses are initialized with initial guess values within the ranges: $2 \leq G_{c,n}^i \leq 20$ [Jm^{-2}], $0.05 \leq \delta_c^i \leq 4.4$ [μm], and $1 \leq \zeta^i \leq 2.75$ [-]. The identification results are shown in Figure 6.15.

The mean values and corresponding standard deviations of the identified parameters are: $\bar{G}_{c,n} = 7.17 \pm 0.07$ [Jm^{-2}], $\bar{\delta}_c = 0.419 \pm 0.014$ [μm], $\bar{\zeta} = 1.001 \pm 0.001$ [-]. These small standard deviations demonstrate convergence to the same, global minimum. Interestingly, the ratio $\zeta = 1$ [-] implies that there is no difference between the work of separation in the normal and tangential direction for this OLED-specimen. Values for the work of separation that are equivalent for both the normal and tangential opening modes have also been found in [23, 130, 176]. In a relative sense, δ_c shows the largest standard deviation, which was anticipated by the relatively low corresponding sensitivity seen in the M-matrix of Figure 6.13.

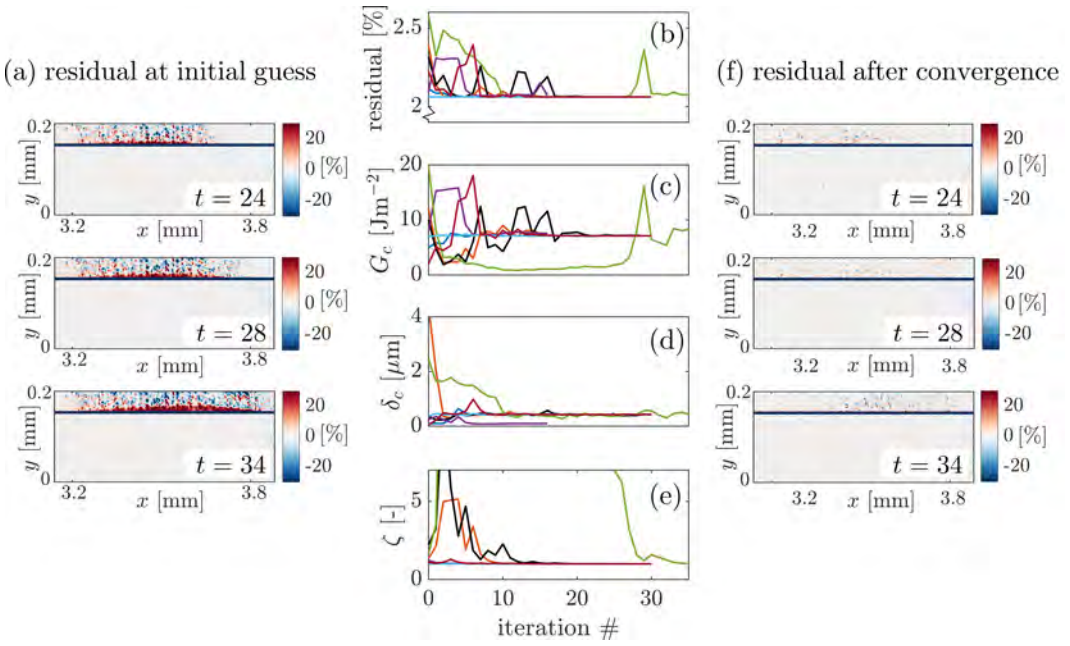

Figure 6.15. The convergence behavior of IDIC for different initial guess cases, in terms of (b) the image residual, in percentages [%] of the images' dynamic range, and (c)-(e) the mixed-mode cohesive zone parameter values. The lines are colored to distinguish between the optimization routines initialized with different initial guesses. (a) Examples of residual fields, at three time increments t at the initial guess of the IDIC-routine corresponding to the case represented by the green curve in (b)-(e), and after convergence (f). The blue band in the image residuals represents a masked region not taken into account in IDIC.

In one case, δ_c even converged to a solution significantly different from all other cases, see the purple line in Figure 6.15(d). The residual for this case seems to have been minimized when graphically evaluating Figure 6.15(b). However, examining it numerically, provides more insight. The mean image residual $\bar{r}$ and the standard deviation for all seven test-cases are: $\bar{r} = 2.133 \pm 0.003$ [%]. It is found that the purple case in Figure 6.15 has a residual that is 0.007% higher than $\bar{r}$, which is more than twice the standard deviation on $\bar{r}$. Furthermore, also the value for $G_{c,n}$ deviates from the mean $\bar{G}_{c,n}$ by twice the standard deviation on that mean. The combination of these discrepancies (in terms of the residual, and the solutions for $G_{c,n}$ and δ_c) with respect to the other cases implies that the respective optimization routine got stuck in a local minimum, and that the corresponding solution is less trustworthy than the solution found by the other IDIC-analyses. Its result is therefore not taken into account in the calculation of the mean values for the cohesive zone parameters, as reported above. The case represented by the green curve shows divergence up to iteration # 30, but eventually converges to a solution similar to the solutions found by the other cases (except the purple case). In all, the consistent results highlight the robustness of IDIC to converge to a global minimum for a range of initial guesses.

The image residual fields have been minimized properly and acceptably homogeneously, see Figures 6.15(a) and (f). The slightly remaining residuals are caused by the inevitability of modeling errors. As found from IDIC-analyses on the virtual experiment in Section 6.3.2, the consistent convergence for a range of initial guesses, and the homogeneously minimized image residual fields provide confidence in the accuracy of the identified mixed-mode cohesive zone parameters, given the assumed cohesive zone model and elasticity parameters of PEN and OCP.

6.5 Conclusion

Identifying relevant adhesion properties in microelectronic specimens is best done on the actual device, rather than on dedicated specimens. Using an actual device as a test-specimen restricts the possibility to employ test configurations that specifically target the measurement of adhesion properties, such as the double cantilever beam experiment. As a step towards realizing on-device measurement of adhesion properties, the full-field identification method of integrated digital image correlation (IDIC) was employed to identify mixed-mode cohesive zone parameters of a flexible OLED barrier stack, and the most challenging error sources were investigated. Delamination experiments were performed by a tri-axial mechanical testing rig, which allows for imposing arbitrary loading paths in all directions. It was found crucial to optimize the load-case, so that sufficient sensitivity towards the adhesion properties is triggered. Furthermore, because a high magnification is needed to visualize the kinematics by microscopic techniques, the loading conditions applied to the specimen typically fall outside the field of view. Local boundary conditions are therefore needed for the finite element model used within the IDIC-framework. These boundary conditions should adequately capture the kinematics imposed by the far-field load application, but care must be taken not to over-constrain the kinematics and thereby undermine the required sensitivity towards the parameters. No globally measured force data was used for the identification procedure. The known elasticity parameters of the elastically deforming material layers within the imaged field of view serve as an intrinsic force sensor. Erroneous assumptions for the Young's modulus of either PEN or OCP, within the expected measurement uncertainty, were shown to have a minor effect on the identification of the cohesive zone parameters.

The challenges regarding the local boundary conditions and the test configuration have been investigated by virtual experimentation. The virtual experiments allowed for evaluating and selecting a proper load-case and boundary conditions, so that all cohesive zone parameters could be accurately identified from a single, mechanical test. Sensitivity analysis, based on the correlation matrix M and its spectral decomposition matrices D and Q, has proven to be useful for anticipating the trustworthiness of the identification. Sufficient kinematic sensitivity towards the parameters of interest and minimal cross-sensitivity are crucial for identifying the cohesive zone parameters with satisfactory accuracy. The virtual experiments demonstrated that the identification results can be trusted to be accurate when: (1) consistent minimization towards similar image residuals occurs for IDIC-analyses employing different initial parameter guesses, (2) the remaining image residuals are homogeneous in space and time, (3) consistent convergence towards equivalent solutions are found for IDIC-analyses initialized with different initial parameter guesses.

The load-case and the boundary conditions, firstly optimized on the virtual experiments,

were subsequently employed for IDIC-analyses on a real mechanical experiment on a flexible OLED-specimen. Three mixed-mode cohesive zone parameters (i.e., $G_{c,n}$, δ_c, and ζ) were successfully identified from a single mechanical test, and the results were considered to be trustworthy by evaluating the convergence behavior and image residual fields.

The flexible specimen explored in this chapter exhibited significant deformation. For more rigid microelectronic material systems it will be even more challenging to achieve sufficient kinematic sensitivity, because of the limited amount of deformation. However, by using sufficient magnification, a proper load-case, and the full-field identification method of IDIC with local boundary conditions, rich kinematic data can be exploited to yield maximum sensitivity. The image residual fields constructing the objective function of the optimization routine in IDIC provide a direct measure for assessing the trustworthiness of the solution, making IDIC a promising technique for measuring relevant adhesion properties by on-device, mechanical experiments.

Acknowledgements

This research was carried out under project number M62.2.12472 in the framework of the Research Program of the Materials Innovation Institute (M2i) in the Netherlands (www.m2i.nl).

CHAPTER 7

Conclusions & future research

A numerical-experimental method for the full-field identification of relevant adhesion properties of interfaces in microelectronic devices was scrutinized in this dissertation. To this end, a micro-mechanical setup and an identification procedure, based on integrated digital image correlation, have been developed and investigated. The most important conclusions are listed below with references to the research questions (RQ) raised in the introduction. Subsequently, a summary of the remaining questions and a perspective on future research is given.

Conclusions:

1. Integrated digital image correlation (IDIC) and finite element model updating (FEMU) behave similarly under the influence of various error sources. However, for test-cases involving complex kinematics, small displacements, and image noise, the former method outperforms the latter (RQ.3 and RQ.4). The better performance of IDIC is mainly attributed to its one-step nature, in which critical regularization choices in the DIC algorithm are omitted, compared to the two-step method of FEMU, where essential choices, with difficult-to-anticipate consequences, are left to the user. Because deformation of small-scale, microelectronic specimens involves both complex kinematics and small displacements, IDIC is considered the most appropriate method for identifying the adhesion properties of interfaces in such material systems (RQ.4).

2. The accuracy of IDIC in identifying cohesive zone model parameters is strongly affected by the boundary conditions applied in the employed finite element model, constituting a critical error source (RQ.3). The method is, on the other hand, relatively insensitive to other error sources, such as an incorrectly assumed pre-crack length (in case of a double cantilever beam experiment), image noise, and erratic motion during an experiment.

3. The far-field locations where loads are applied in a micro-mechanical experiment typically fall outside the imaged field of view, due to the visual magnification required for capturing the governing kinematics at the scale of the micro-structure. Since boundary conditions are found to be the most critical source of error, this necessitates the

measurement of local boundary conditions that are subsequently used in the finite element model for the full-field identification procedure (RQ.1 and RQ.2).

4. The exact requirements for applying boundary conditions in the finite element (FE) model vary per test-case. The key challenge is to capture the local kinematics induced by the experimentally applied, far-field boundary conditions, and impose them in the model, while not over-constraining the model kinematics (RQ.2). General recommendations are, therefore, to kinematically prescribe a minimum number of FE-nodes at adequate locations, and to space the boundary condition nodes sufficiently to minimize local stress fluctuations in the FE-simulation (RQ.1). For an arbitrary test-case, computational analyses in the form of virtual experimentation, can be instrumental to acquire insight and establish adequate, local boundary conditions (RQ.1).

5. No force data is required for identifying cohesive zone model parameters when the elastic properties of one of the elastically deforming materials are known, and when that elastic deformation is contained within the visual data used for the full-field identification procedure (RQ.1).

6. Sensitivity maximization is essential for achieving sufficient identification accuracy. The analysis of the kinematic and/or force sensitivity is best done by evaluating the full-field sensitivity maps, even though this remains challenging in the presence of cross-sensitivity (RQ.2). Evaluating the correlation matrix and its eigenvalue decomposition can provide insightful information by which the experiment can be optimized to yield the highest sensitivity to the unknown parameters, while decreasing the corrupting effect of cross-sensitivity (RQ.1).

7. Cross-sensitivity may have a more detrimental effect on the accuracy of identified parameters, than insensitivity to a single parameter (RQ.3).

8. The mixed-mode conditions at the interface are difficult to control in an experiment (RQ.2). Even with highly specialized experimental equipment by which the globally imposed mix of normal and shear loads can be carefully controlled, the local degree of mode-mixedness along the fracture process zone of the delaminating interface was observed to vary strongly (Chapter 4). This fact was conveniently used in Chapter 4. Instead of conducting several experiments to identify the mixed-mode cohesive zone parameters, it was found that for this interface, one experiment in which an intermediate, global mode-mixedness is imposed, suffices. It is, however, important that the experiment sufficiently triggers both normal and shear opening components at the interface (RQ.1). Sensitivity analyses provide insight in selecting suitable test configurations, in terms of the globally imposed mix of normal and shear loads, for identifying mixed-mode cohesive zone parameters by integrated digital image correlation (RQ.1).

9. A micro-mechanical apparatus was realized that facilitates the investigation of mechanical, interfacial failure mechanisms in microelectronic devices or samples thereof (RQ.1) The device consists of two commercially available piezoelectric actuator stacks, and it can accomplish tri-axial force sensing and positioning. Despite lack of knowledge

regarding the commercial actuators' technical details, thorough calibration of the device's operational properties allows for converting piezoelectric motion actuators into force sensors. The setup is thereby dedicated to conduct versatile experiments with separate or combined loading capabilities in three directions by nanometer displacement control, and sub-millinewton force measurement. The setup demonstrated its capability to conduct in-situ tests with a variety of microscopic techniques, including optical and scanning electron microscopy, and optical profilometry (RQ.1). Any changes made to the micro-mechanical setup, such as the use of different specimen grippers, requires re-calibration of the setup's operational properties. In particular, the machine compliance must be carefully re-evaluated (RQ.1).

10. On-device testing limits the possible test configurations for adequately identifying relevant adhesion properties (RQ.2). Sensitivity analysis should be exploited to optimize the load-case for triggering the required kinematics, before real experiments are conducted (RQ.1).

11. The image residual is the most direct measure for evaluating the identification results. The trustworthiness of the solution can be assessed by examining the image residuals and the convergence behavior of the optimization routine underlying IDIC (RQ.1). The solution may be trusted to be accurate when (1) the image residual fields are low and homogeneous throughout space and time, and when (2) the optimization routine consistently converges to the same solution for different initial parameter guesses.

Remaining questions, challenges, and perspectives on future research:

1. The adequacy of local boundary conditions is evaluated by computational analysis of the relevant test-case in the form of virtual experimentation. However, the actual choices regarding the application of these boundary conditions, i.e., the number of prescribed nodes and their locations, is still rather arbitrary, although a pragmatic procedure for their selection has been proposed. A more rigorous approach to assess the application of adequate boundary conditions is desirable.

2. A step towards identifying adhesion properties of multi-layer interface systems has been established, although only for the case of a single interface failing in a stack during a mechanical test. To realize a more complete identification approach relevant for microelectronic material stacks, the method must be further developed to deal with multiple interfaces failing simultaneously. The intricacy of this situation could first be examined by virtual experimentation. This should focus on how the sensitivity of the identification method, towards the parameters of interest, is affected by the potentially interacting interfaces.

3. The currently developed methodology assumes homogeneous interfaces. The presence of heterogeneity along microelectronic interfaces may pose a realistic problem, due to the potentially heterogeneous, underlying microstructures of the interfacing materials. A future research question could therefore be: how can adhesion properties be identified for a heterogeneous interface? As a first approach, heterogeneity may be implemented into the identification method by subdividing the modeled interface into

regions, each exhibiting their own set of interface parameters (e.g., using a cohesive zone model). This would make the adhesion properties a function of a spatial coordinate, to be identified for each spatial subregion. The approach suggested here would, however, be limited by the arbitrary choices made in defining the spatial subregions. Once again, virtual experimentation would yield insight into the potential of dealing with the problem of heterogeneous interfaces.

4. This dissertation was concerned with two-dimensional, full-field measurement techniques, based on images of the specimen's surface, and from which a mixture of mode-I and mode-II properties were identified. It is relevant to inquire how the method can be extended to include the identification of adhesion properties from additional, out-of-plane, mode-III delamination. Digital image correlation is already being applied to measure three-dimensional kinematics from 3D imaging techniques or in a quasi-3D setting from surface metrology methods, such as optical profilometry (digital height correlation). It would be interesting to combine three-dimensional, mechanical experiments (yielding tri-axial force data) with three-dimensional simulations to recover the relevant adhesion properties. A key challenge therein would be to extract accurate, local boundary conditions from the available visual data for which the image resolution may still be insufficient at present.

5. The number of possible test configurations for on-device tests is limited by the predefined specimen geometry of actual microelectronic devices. In this work, the adhesion properties of a flexible OLED display have been successfully identified. To achieve this, significant efforts were required to select a proper load-case for the experiment. For more rigid microelectronic specimens, it is likely to be even more difficult to select the appropriate load-case that triggers sufficient kinematic sensitivity for identifying mechanical parameters. This problem must be tackled in order to achieve on-device adhesion measurements of microelectronics in general (not only flexible systems). The use of local boundary conditions allows for approaching the problem by employing a higher microscopic magnification, so that more small-scale kinematics can be visualized.

References

[1] S. Luryi, J. Xu, and A. Zaslavsky, editors. *Future Trends in Microelectronics*. John Wiley & Sons, Ltd, 2010.

[2] S.E. Thompson and S. Parthasarathy. Moore's law: the future of Si microelectronics. *Materials Today*, 9 (6):20 – 25, 2006. ISSN 1369-7021. doi: 10.1016/S1369-7021(06)71539-5.

[3] F.C. Krebs, S.A. Gevorgyan, and J. Alstrup. A roll-to-roll process to flexible polymer solar cells: model studies, manufacture and operational stability studies. *Journal of Materials Chemistry*, 19:5442–5451, 2009. doi: 10.1039/B823001C.

[4] N. Palavesam, S. Marin, D. Hemmetzberger, C. Landesberger, K. Bock, and C. Kutter. Roll-to-roll processing of film substrates for hybrid integrated flexible electronics. *Flexible and Printed Electronics*, 3(1):014002, 2018. doi: 10.1088/2058-8585/aaaa04.

[5] R.R. Søndergaard, M. Hösel, and F.C. Krebs. Roll-to-roll fabrication of large area functional organic materials. *Journal of Polymer Science Part B: Polymer Physics*, 51(1):16–34, 2013. doi: 10.1002/polb.23192.

[6] iSuppli. Flexible OLED market revenue forecast worldwide from 2013 to 2014 (in billion u.s. dollars). URL `https://www.statista.com/statistics/271193/flexible-oled-market-revenue-forecast-worldwide/`. Retrieved: February 6, 2019.

[7] Statistica. Flexible display shipments market revenue worldwide from 2015 to 2022 (in billion u.s. dollars). URL `https://www.statista.com/statistics/616114/flexible-display-market-worldwide`. Retrieved: February 6, 2019.

[8] W.D. van Driel, M.A.J. van Gils, R.B.R. van Silfhout, and G.Q. Zhang. Prediction of Delamination Related IC & Packaging Reliability Problems. *Microelectronics Reliability*, 45:1633–1638, 2005. doi: 10.1016/j.microrel.2005.07.065.

[9] G.Q. Zhang. *Challenges and Future Perspectives*, pages 537–563. Springer, Dordrecht, 2006. ISBN 978-1-4020-4935-4. doi: 10.1007/1-4020-4935-8_9.

[10] S. Zhao and X. Pang. Investigation of delamination control in plastic package. *Microelectronics Reliability*, 49(3):350–356, 2009. ISSN 0026-2714. doi: 10.1016/j.microrel.2009.01.001.

[11] G.A.O. Davies and R. Olsson. Impact on composite structures. *The Aeronautical Journal (1968)*, 108 (1089):541–563, 2004. doi: 10.1017/CBO9780511574504.

[12] D. Hull and Y.B. Shi. Damage mechanism characterization in composite damage tolerance investigations. *Composite Structures*, 23(2):99 – 120, 1993. ISSN 0263-8223. doi: 10.1016/0263-8223(93)90015-I.

[13] L.R. Sbriglia, A.M. Baker, J.M. Thompson, R.V. Morgan, A.J. Wachtor, and J.D. Bernardin. Embedding sensors in FDM plastic parts during additive manufacturing. In M. Mains, editor, *Topics in Modal Analysis & Testing, Volume 10*, pages 205–214, Cham, 2016. Springer International Publishing. doi: 10.1007/978-3-319-30249-2_17.

[14] O. van der Sluis, B. Vossen, J. Neggers, A.P. Ruybalid, K. Chockalingam, R. Peerlings, J.P.M. Hoefnagels, J. Remmers, V. Kouznetsova, P. Schreurs, and M.G.D. Geers. *Advances in Delamination Modeling of Metal/Polymer Systems: Continuum Aspects*, pages 83–128. Springer International Publishing, Cham, 2018. ISBN 978-3-319-90362-0. doi: 10.1007/978-3-319-90362-0_3.

[15] H. Ullah, A.R. Harland, and V.V. Silberschmidt. Damage in woven CFRP laminates under impact loading. *EPJ Web of Conferences*, 26:04004, 2012. doi: 10.1051/epjconf/20122604004.

[16] K.L. Mittal. Adhesion measurement of thin films. *Electrocomponent Science and Technology*, 3(1):21–42, 1976. doi: 10.1155/APEC.3.21.

[17] T. Andersson and A. Biel. On the effective constitutive properties of a thin adhesive layer loaded in peel. *International Journal of Fracture*, 141(1):227–246, 2006. ISSN 1573-2673. doi: 10.1007/s10704-006-0075-6.

[18] T. Andersson and U. Stigh. The stress - elongation relation for an adhesive layer loaded in peel using equilibrium of energetic forces. *International Journal of Solids and Structures*, 41:413–434, 2004. doi: 10.1016/j.ijsolstr.2003.09.039.

[19] P.G. Charalambides, J.J. Lund, A.G. Evans, and R.M. McMeeking. A test specimen for determining the fracture resistance of bimaterial interfaces. *Journal of Applied Mechanics*, 56(1):77 – 82, 1989. doi: 10.1115/1.3176069.

[20] L. Durix, M. Dreßler, D. Coutellier, and B. Wunderle. On the development of a modified button shear specimen to characterize the mixed mode delamination toughness. *Engineering Fracture Mechanics*, 84: 25–40, 2012. doi: 10.1016/j.engfracmech.2011.12.015.

[21] J.L. Högberg, B.F. Sørensen, and U. Stigh. Constitutive behaviour of mixed mode loaded adhesive layer. *International Journal of Solids and Structures*, 44(25 - 26):8335 – 8354, 2007. ISSN 0020-7683. doi: 10.1016/j.ijsolstr.2007.06.014.

[22] M. Kolluri, J.P.M. Hoefnagels, J.A.W. van Dommelen, and M.G.D. Geers. Irreversible mixed mode interface delamination using a combined damage-plasticity cohesive zone enabling unloading. *International Journal of Fracture*, 185(1):77–95, 2014. ISSN 1573-2673. doi: 10.1007/s10704-013-9899-z.

[23] J. Neggers, J.P.M. Hoefnagels, O. van der Sluis, O. Sedaghat, and M.G.D. Geers. Analysis of the dissipative mechanisms in metal-elastomer interfaces. *Engineering Fracture Mechanics*, 149:412 – 424, 2015. ISSN 0013-7944. doi: 10.1016/j.engfracmech.2015.06.056.

[24] B.F. Sørensen and P. Kirkegaard. Determination of mixed mode cohesive laws. *Engineering Fracture Mechanics*, 73(17):2642 – 2661, 2006. ISSN 0013-7944. doi: 10.1016/j.engfracmech.2006.04.006.

[25] C. Sun, M.D. Thouless, A.M. Waas, J.A. Schroeder, and P.D. Zavattieri. Ductile - brittle transitions in the fracture of plastically-deforming adhesively-bonded structures. Part I : Experimental studies. *International Journal of Solids and Structures*, 45(10):3059 – 3073, 2008. doi: 10.1016/j.ijsolstr.2008.01.011.

[26] A.A. Volinsky, N.R. Moody, and W.W. Gerberich. Interfacial toughness measurements for thin films on substrates. *Acta Materialia*, 50(3):441 – 466, 2002. doi: 10.1016/S1359-6454(01)00354-8.

[27] V. Gupta, R. Hernandez, J. Wu, and P. Charconnet. Interfacial adhesion and its degradation in selected metal/oxide and dielectric/oxide interfaces in multi-layer devices. *Vacuum*, 59(1):292–300, 2000. doi: 10.1016/S0042-207X(00)00282-7.

[28] J. W. Hutchinson and Z. Suo. *Mixed Mode Cracking in Layered Materials*, volume 29 of *Advances in Applied Mechanics*. 1991. doi: 10.1016/S0065-2156(08)70164-9.

[29] K.M. Liechti and Y.S. Chai. Asymmetric Shielding in Interfacial Fracture Under In-Plane Shear. *Journal of Applied Mechanics*, 59:295–304, 1992. doi: 10.1115/1.2899520.

[30] O. van der Sluis, Y.Y. Hsu, P.H.M. Timmermans, M. Gonzalez, and J.P.M. Hoefnagels. Stretching-induced interconnect delamination in stretchable electronic circuits. *Journal of Physics D: Applied Physics*, 44(3), 2011. doi: 10.1088/0022-3727/44/3/034008.

[31] B.G. Vossen, O. van der Sluis, P.J.G. Schreurs, M.G.D. Geers, J. Neggers, and J.P.M. Hoefnagels. On the role of fibril mechanics in the work of separation of fibrillating interfaces. *Mechanics of Materials*, 88:1 – 11, 2015. ISSN 0167-6636. doi: 10.1016/j.mechmat.2015.04.009.

[32] P.J.M. Janssen, J.P.M. Hoefnagels, Th.H. de Keijser, and M.G.D. Geers. Processing induced size effects in plastic yielding upon miniaturisation. *Journal of the Mechanics and Physics of Solids*, 56(8):2687 – 2706, 2008. ISSN 0022-5096. doi: 10.1016/j.jmps.2008.03.008.

[33] J. Zimmermann, S. Van Petegem, H. Bei, D. Grolimund, E.P. George, and H. van Swygenhoven. Effects of focused ion beam milling and pre-straining on the microstructure of directionally solidified molybdenum pillars: A laue diffraction analysis. *Scripta Materialia*, 62(10):746 – 749, 2010. ISSN 1359-6462. doi: 10.1016/j.scriptamat.2010.02.013.

[34] H.T Goldrein, S.J.P Palmer, and J.M Huntley. Automated fine grid technique for measurement of large-strain deformation maps. *Optics and Lasers in Engineering*, 23(5):305 – 318, 1995. ISSN 0143-8166. doi: 10.1016/0143-8166(95)00036-N.

[35] V.J. Parks. Strain measurement using grids. *Optical Engineering*, 21(4):663–669, 1982. doi: 10.1117/12.7972958.

[36] P.J. Sevenhuijsen, J.S. Sirkis, and F. Bremand. Current trends in obtaining deformation data from grids. *Experimental Techniques*, 17(3):22–26, 1993. doi: 10.1111/j.1747-1567.1993.tb00747.x.

[37] T.M. Kreis, M. Adams, and W.P.O. Jüptner. Methods of digital holography: a comparison. *Proc.SPIE*, 3098:224–233, 1997. doi: 10.1117/12.281164.

[38] U. Schnars and W.P.O. Jüptner. *Digital Holography - Digital Hologram Recording, Numerical Reconstruction, and Related Techniques*. Springer, Berlin, 2005.

[39] D.N. Borza and I.T. Nistea. High temporal and spatial resolution in time resolved speckle interferometry. *Optics and Lasers in Engineering*, 50(8):1075–1083, 2012. ISSN 0143-8166. doi: 10.1016/j.optlaseng.2012.01.022.

[40] C. Joenathan, B. Franze, P. Haible, and H.J. Tiziani. Large in-plane displacement measurement in dual-beam speckle interferometry using temporal phase measurement. *Journal of Modern Optics*, 45(9):1975–1984, 1998. doi: 10.1080/09500349808231715.

[41] P. Meinlschmidt, K.D. Hinsch, and R.S. Sirohi. *Selected Papers on Electronic Speckle Pattern Interferometry: Principles and Practice*. SPIE Milestone Series, volume MS132, 1996.

[42] G. Besnard, F. Hild, and S. Roux. "Finite-Element" displacement fields analysis from digital images: Application to Portevin-Le Châtelier bands. *Experimental Mechanics*, 46(6):789–803, 2006. doi: 10.1007/s11340-006-9824-8.

[43] P. Cheng, M.A. Sutton, H.W. Schreier, and S.R. McNeill. Full-field speckle pattern image correlation with B-spline deformation function. *Experimental Mechanics*, 42(3):344–352, 2002. doi: 10.1007/BF02410992.

[44] T.C. Chu, W.F. Ranson, and M.A. Sutton. Applications of digital-image-correlation techniques to experimental mechanics. *Experimental Mechanics*, 25(3):232–244, 1985. doi: 10.1007/BF02325092.

[45] F. Hild and S. Roux. Comparison of local and global approaches to digital image correlation. *Experimental Mechanics*, 52(9):1503–1519, 2012. doi: 10.1007/s11340-012-9603-7.

[46] W.H. Peters and W.F. Ranson. Digital imaging techniques in experimental stress analysis. *Optical Engineering*, 21(3):427–431, 1982. doi: 10.1117/12.7972925.

[47] Y. Sun, J.H.L. Pang, C.K. Wong, and F. Su. Finite element formulation for a digital image correlation method. *Applied Optics*, 44(34):7357–7363, 2005. doi: 10.1364/AO.44.007357.

[48] M. Sutton, W. Wolters, W. Peters, W. Ranson, and S. McNeill. Determination of displacements using an improved digital correlation method. *Image and Vision Computing*, 1(3):133–139, 1983. doi: 10.1016/0262-8856(83)90064-1.

[49] M. Grédiac and A. Vautrin. A new method for determination of bending rigidities of thin anisotropic plates. *Journal of Applied Mechanics*, 57(4):964–968, 1990. doi: 10.1115/1.2897668.

[50] M. Grédiac, F. Pierron, S. Avril, and E. Toussaint. The virtual fields method for extracting constitutive parameters from full-field measurements: a review. *Strain*, 42(4):233–253, 2008. doi: 10.1111/j.1475-1305.2006.tb01504.x.

[51] F. Pierron and M. Grédiac. *The Virtual Fields Method*. Springer New York, New York, NY, 2012. ISBN 978-1-4614-1823-8.

[52] D. Claire, F. Hild, and S. Roux. A finite element formulation to identify damage fields: the equilibrium gap method. *International Journal for Numerical Methods in Engineering*, 61(2):189–208, 2004. doi: 10.1002/nme.1057.

[53] J. Réthoré, S. Roux, and F. Hild. Optimal and noise-robust extraction of fracture mechanics parameters from kinematic measurements. *Engineering Fracture Mechanics*, 78(9):1827–1845, 2011. doi: 10.1016/j.engfracmech.2011.01.012.

[54] S. Roux and F. Hild. Digital image mechanical identification (DIMI). *Experimental Mechanics*, 48(4): 495–508, 2008. doi: 10.1007/s11340-007-9103-3.

[55] S. Andrieux and A.B. Abda. Identification of planar cracks by complete overdetermined data: inversion formulae. *Inverse Problems*, 12(5):553, 1996. doi: 10.1088/0266-5611/12/5/002.

[56] T. Bannour, A.B. Abda, and M. Jaoua. A semi-explicit algorithm for the reconstruction of 3D planar cracks. *Inverse Problems*, 13(4):899–917, 1997. doi: 10.1088/0266-5611/13/4/002.

[57] J.D. Collins, G.C. Hart, T.K. Haselman, and B. Kennedy. Statistical identification of structures. *AIAA Journal*, 12(2):185–190, 1974. doi: 10.2514/3.49190.

[58] K.T. Kavanagh and R.W. Clough. Finite element applications in the characterization of elastic solids. *International Journal of Solids and Structures*, 7(1):11–23, 1971. doi: 10.1016/0020-7683(71)90015-1.

[59] M.H.H. Meuwissen, C.W.J. Oomens, F.P.T. Baaijens, R. Petterson, and J.D. Janssen. Determination of the elasto-plastic properties of aluminium using a mixed numerical-experimental method. *Journal of Materials Processing Technology*, 75(1-3):204, 1998. doi: 10.1016/S0924-0136(97)00366-X.

[60] J.E. Mottershead and M.I. Friswell. Model updating in structural dynamics: a survey. *Journal of Sound and Vibration*, 167(2):347–375, 1993. doi: 10.1006/jsvi.1993.1340.

[61] C.W.J. Oomens, M.R. van Ratingen, J.D. Janssen, J.J. Kok, and M.A.N. Hendriks. A numerical-experimental method for a mechanical characterization of biological materials. *Journal of Biomechanics*, 26(4-5):617–621, 1993. doi: 10.1016/0021-9290(93)90024-9.

[62] E. Pagnacco, D. Lemosse, F. Hild, and F. Amiot. Inverse strategy from displacement field measurement and distributed forces using FEA. In *Proceedings of the 2005 SEM Annual Conference and Exposition on Experimental and Applied Mechanics*, pages 1079–1088, 2005. ISBN 0912053909.

[63] D. Simon and J.-D. Golinval. Use of whole-field displacement measurements for model updating of blades. *Proceedings of IMAC XXI*, (131):3–6, 2003.

[64] F. Hild, G. Besnard, J. . Lagrange, S. Roux, and C. Voltz. Characterization of necking phenomena in high-speed experiments by using a single camera. *Eurasip Journal on Image and Video Processing*, 2010, 2010. doi: 10.1155/2010/215956.

[65] J. Neggers, J.P.M. Hoefnagels, M.G.D. Geers, F. Hild, and S. Roux. Time-resolved integrated digital image correlation. *International Journal for Numerical Methods in Engineering*, 103(3):157–182, 2015. ISSN 1097-0207. doi: 10.1002/nme.4882.

[66] S. Roux and F. Hild. Stress intensity factor measurements from digital image correlation: Post-processing and integrated approaches. *International Journal of Fracture*, 140(1-4):141–157, 2006. doi: 10.1007/s10704-006-6631-2.

[67] S. Avril, M. Bonnet, A.-S. Bretelle, M. Grédiac, F. Hild, P. Ienny, F. Latourte, D. Lemosse, S. Pagano, E. Pagnacco, and F. Pierron. Overview of identification methods of mechanical parameters based on full-field measurements. In *Proceedings of the Society for Experimental Mechanics, Inc.*, volume 65, pages 381–402, 2008. doi: 10.1007/s11340-008-9148-y.

[68] M. Bonnet and A. Constantinescu. Inverse problems in elasticity. *Inverse Problems*, 21(2):R1–R50, 2005. doi: 10.1088/0266-5611/21/2/R01.

[69] M. Grédiac. The use of full-field measurement methods in composite material characterization: interest and limitations. *Composites Part A: Applied Science and Manufacturing*, 35(7-8):751–761, 2004. doi: 10.1016/j.compositesa.2004.01.019.

[70] M. Grédiac and F. Hild. *Full-Field Measurements and Identification in Solid Mechanics*. Wiley, 2012. ISBN 978-1-118-57847-6.

[71] J.-S. Affagard, F. Mathieu, J.-M. Guimard, and F. Hild. Identification method for the mixed mode interlaminar behavior of a thermoset composite using displacement field measurements and load data. *Composites: Part A*, 91:238–249, 2016. doi: 10.1016/j.compositesa.2016.10.007.

[72] M. Alfano, G. Lubineau, and G.H. Paulino. Global sensitivity analysis in the identification of cohesive models using full-field kinematic data. *International Journal of Solids and Structures*, 55:66–78, 2015. ISSN 0020-7683. doi: 10.1016/j.ijsolstr.2014.06.006.

[73] B. Blaysat, J.P.M. Hoefnagels, G. Lubineau, M. Alfano, and M.G.D. Geers. Interface debonding characterization by image correlation integrated with Double Cantilever Beam kinematics. *International Journal of Solids and Structures*, 55:79 – 91, 2015. doi: 10.1016/j.ijsolstr.2014.06.012.

[74] R. Fedele, B. Raka, F. Hild, and S. Roux. Identification of adhesive properties in glare assemblies using digital image correlation. *Journal of the Mechanics and Physics of Solids*, 57(7):1003 – 1016, 2009. ISSN 0022-5096. doi: 10.1016/j.jmps.2009.04.005.

[75] A.L. Gain, J. Carroll, G.H. Paulino, and J. Lambros. A hybrid experimental/numerical technique to extract cohesive fracture properties for mode-I fracture of quasi-brittle materials. *International Journal of Fracture*, 169(2):113–131, 2011. doi: 10.1007/s10704-010-9578-2.

[76] N. Valoroso, M. Sessa, S.and Lepore, and G. Cricrì. Identification of mode-I cohesive parameters for bonded interfaces based on DCB test. *Engineering Fracture Mechanics*, 104:56–79, 2013. ISSN 0013-7944. doi: 10.1016/j.engfracmech.2013.02.008.

[77] Y. Xu, X. Li, X. Wang, and L. Liang. Inverse parameter identification of cohesive zone model for simulating mixed-mode crack propagation. *International Journal of Solids and Structures*, 51(13):2400–2410, 2014. ISSN 0020-7683. doi: 10.1016/j.ijsolstr.2014.03.008.

[78] L.I.J.C. Bergers, J.P.M. Hoefnagels, and M.G.D. Geers. Characterization of time-dependent anelastic microbeam bending mechanics. *Journal of Physics D: Applied Physics*, 47(35):355306, 2014. doi: 10.1088/0022-3727/47/35/355306.

[79] G. Geymonat, F. Hild, and S. Pagano. Identification of elastic parameters by displacement field measurement. *Comptes Rendus - Mecanique*, 330(6):403–408, 2002. doi: 10.1016/S1631-0721(02)01476-6.

[80] A. Constantinescu. On the identification of elastic moduli from displacement-force boundary measurements. *Inverse Problems in Engineering*, 1(4):293–313, 1995. doi: 10.1080/174159795088027587.

[81] P. Ladeveze and D. Leguillon. Error estimate procedure in the finite element method and applications. *SIAM Journal on Numerical Analysis*, 20(3):485–509, 1983. doi: 10.1137/0720033.

[82] S. Avril and F. Pierron. General framework for the identification of constitutive parameters from full-field measurements in linear elasticity. *International Journal of Solids and Structures*, 44(14-15):4978–5002, 2007. doi: 10.1016/j.ijsolstr.2006.12.018.

[83] J. Réthoré. A fully integrated noise robust strategy for the identification of constitutive laws from digital images. *International Journal for Numerical Methods in Engineering*, 84(6):631–660, 2010. doi: 10.1002/nme.2908.

[84] H. Leclerc, J.N. Périé, S. Roux, and F. Hild. Integrated digital image correlation for the identification of mechanical properties. *Lecture Notes in Computer Science (including subseries Lecture Notes in Artificial*

Intelligence and Lecture Notes in Bioinformatics), 5496 LNCS:161–171, 2009. doi: 10.1007/978-3-642-01811-4_15.

[85] J. Réthoré, Muhibullah, T. Elguedj, M. Coret, P. Chaudet, and A. Combescure. Robust identification of elasto-plastic constitutive law parameters from digital images using 3D kinematics. *International Journal of Solids and Structures*, 50(1):73–85, 2013. doi: 10.1016/j.ijsolstr.2012.09.002.

[86] J. Réthoré, S. Roux, and F. Hild. An extended and integrated digital image correlation technique applied to the analysis of fractured samples. *European Journal of Computational Mechanics*, 18:285–306, 2009. doi: 10.3166/ejcm.18.285-306.

[87] F. Mathieu, F. Hild, and S. Roux. Identification of a crack propagation law by digital image correlation. *International Journal of Fatigue*, 36(1):146–154, 2012. doi: 10.1016/j.ijfatigue.2011.08.004.

[88] F. Mathieu, F. Hild, and S. Roux. Image-based identification procedure of a crack propagation law. *Engineering Fracture Mechanics*, 103:48–59, 2013. doi: 10.1016/j.engfracmech.2012.05.007.

[89] J. Réthoré and R. Estevez. Identification of a cohesive zone model from digital images at the micron-scale. *Journal of the Mechanics and Physics of Solids*, 61(6):1407–1420, 2013. doi: 10.1016/j.jmps.2013.01.011.

[90] F. Hild and S. Roux. Digital image correlation: From displacement measurement to identification of elastic properties - a review. *Strain*, 42(2):69–80, 2006. doi: 10.1111/j.1475-1305.2006.00258.x.

[91] J. Kajberg and G. Lindkvist. Characterisation of materials subjected to large strains by inverse modelling based on in-plane displacement fields. *International Journal of Solids and Structures*, 41(13):3439–3459, 2004. doi: 10.1016/j.ijsolstr.2004.02.021.

[92] M. Teaca, I. Charpentier, M. Martiny, and G. Ferron. Identification of sheet metal plastic anisotropy using heterogeneous biaxial tensile tests. *International Journal of Mechanical Sciences*, 52(4):572–580, 2010. doi: 10.1016/j.ijmecsci.2009.12.003.

[93] J. Kajberg, K.G. Sundin, L.G. Melin, and P. Stohle. High strain-rate tensile testing and viscoplastic parameter identification using microscopic high-speed photography. *International Journal of Plasticity*, 20(4-5): 561–575, 2004. doi: 10.1016/S0749-6419(03)00041-X.

[94] M. Meuwissen. *An Inverse Method for the Mechanical Characterisation of Metals*. Eindhoven University of Technology, 1998. doi: 10.6100/IR508723.

[95] F. Mathieu, H. Leclerc, F. Hild, and S. Roux. Estimation of elastoplastic parameters via weighted FEMU and Integrated-DIC. *Experimental Mechanics*, 55(1):105–119, 2015. doi: 10.1007/s11340-014-9888-9.

[96] P. Lava, S. Cooreman, S. Coppieters, M. De Strycker, and D. Debruyne. Assessment of measuring errors in DIC using deformation fields generated by plastic FEA. *Optics and Lasers in Engineering*, 47(7-8):747–753, 2009. doi: 10.1016/j.optlaseng.2009.03.007.

[97] H.A. Bruck, S.R. McNeill, M.A. Sutton, and W.H. Peters III. Digital image correlation using Newton-Raphson method of partial differential correction. *Experimental Mechanics*, 29(3):261–267, 1989. doi: 10.1007/BF02321405.

[98] M. Sutton, C. Mingqi, W. Peters, Y. Chao, and S. McNeill. Application of an optimized digital correlation method to planar deformation analysis. *Image and Vision Computing*, 4(3):143–150, 1986. doi: 10.1016/0262-8856(86)90057-0.

[99] B. Pan, H. Xie, B.-Q. Xu, and F.-L. Dai. Performance of sub-pixel registration algorithms in digital image correlation. *Measurement Science and Technology*, 17(6):1615–1621, 2006. doi: 10.1088/0957-0233/17/6/045.

[100] H.W. Schreier, J.R. Braasch, and M.A. Sutton. Systematic errors in digital image correlation caused by intensity interpolation. *Optical Engineering*, 39(11):2915–2921, 2000. doi: 10.1117/1.1314593.

[101] M. Bornert, F. Brémand, P. Doumalin, J.-C. Duprè, M. Fazzini, M. Grédiac, F. Hild, S. Mistou, J. Molimard, J.-J. Orteu, L. Robert, Y. Surrel, P. Vacher, and B. Wattrisse. Assessment of digital image correlation measurement errors: Methodology and results. *Experimental Mechanics*, 49(3):353–370, 2009. doi: 10.1007/s11340-008-9204-7.

[102] B.K.P. Horn and B.G. Schunck. Determining optical flow. *Artificial Intelligence*, 17(1-3):185–203, 1981. doi: 10.1016/0004-3702(81)90024-2.

[103] J. Neggers, B. Blaysat, J.P.M. Hoefnagels, and M.G.D. Geers. On image gradients in digital image correlation. *International Journal for Numerical Methods in Engineering*, 105(4):243–260, 2016. ISSN 1097-0207. doi: 10.1002/nme.4971.

[104] H.W. Schreier and M.A. Sutton. Systematic errors in digital image correlation due to undermatched subset shape functions. *Experimental Mechanics*, 42(3):303–310, 2002. doi: 10.1177/001448502321548391.

[105] J. Neggers, J.P.M. Hoefnagels, F. Hild, S. Roux, and M.G.D. Geers. Direct stress-strain measurements from bulged membranes using topography image correlation. *Experimental Mechanics*, 54(5):717–727, 2014. doi: 10.1007/s11340-013-9832-4.

[106] T. Elguedj, J. Réthoré, and A. Buteri. Isogeometric analysis for strain field measurements. *Computer Methods in Applied Mechanics and Engineering*, 200(1-4):40–56, 2011. doi: 10.1016/j.cma.2010.07.012.

[107] J. Réthoré, T. Elguedj, P. Simon, and M. Coret. On the use of nurbs functions for displacement derivatives measurement by digital image correlation. *Experimental Mechanics*, 50(7):1099–1116, 2010. doi: 10.1007/s11340-009-9304-z.

[108] R. Mahnken and E. Stein. Parameter identification for finite deformation elasto-plasticity in principal directions. *Computer Methods in Applied Mechanics and Engineering*, 147(1-2):17–39, 1997.

[109] S.M. Kleinendorst, J.P.M. Hoefnagels, C.V. Verhoosel, and A.P. Ruybalid. On the use of adaptive refinement in isogeometric digital image correlation. *International Journal for Numerical Methods in Engineering*, 104 (10):944–962, 2015. ISSN 1097-0207. doi: 10.1002/nme.4952.

[110] MSC Software Corporation. *Volume A: Theory and User Information*, 2013.

[111] M.A. Hopcroft, W.D. Nix, and T.W. Kenny. What is the Young's modulus of silicon? *Journal of Microelectromechanical Systems*, 19(2):229–238, 2010. doi: 10.1109/JMEMS.2009.2039697.

[112] B. Pan. Bias error reduction of digital image correlation using Gaussian pre-filtering. *Optics and Lasers in Engineering*, 51(10):1161–1167, 2013. doi: 10.1016/j.optlaseng.2013.04.009.

[113] B. Pan, H. Xie, Z. Wang, K. Qian, and Z. Wang. Study on subset size selection in digital image correlation for speckle patterns. *Optics express*, 16:7037–7048, 2008. doi: 10.1364/OE.16.007037.

[114] M. Kolluri, J.P.M. Hoefnagels, J.A.W. van Dommelen, and M.G.D. Geers. An improved miniature mixed-mode delamination setup for *in situ* microscopic interface failure analyses. *Journal of Physics D: Applied Physics*, 44(3):1–13, 2011. doi: 10.1088/0022-3727/44/3/034005.

[115] B.F. Sørensen and T.K. Jacobsen. Large-scale bridging in composites: R-curves and bridging laws. *Composites Part A: Applied Science and Manufacturing*, 29(11):1443 – 1451, 1998. ISSN 1359-835X. doi: 10.1016/S1359-835X(98)00025-6.

[116] U. Stigh, K.S. Alfredsson, T. Andersson, A. Biel, T. Carlberger, and K. Salomonsson. Some aspects of cohesive models and modelling with special application to strength of adhesive layers. *International Journal of Fracture*, 165(2):149–162, 2010. ISSN 1573-2673. doi: 10.1007/s10704-010-9458-9.

[117] L.I.J.C. Bergers, J.P.M. Hoefnagels, and M.G.D. Geers. On-wafer time-dependent high reproducibility nano-force tensile testing. *Journal of Physics D: Applied Physics*, 47(49):495306, 2014. doi: 10.1088/0022-3727/47/49/495306.

[118] A.P. Ruybalid, J.P.M. Hoefnagels, O. van der Sluis, and M.G.D. Geers. Comparison of the identification performance of conventional FEM updating and integrated DIC. *International Journal for Numerical Methods in Engineering*, 106(4):298–320, 2016. ISSN 1097-0207. doi: 10.1002/nme.5127.

[119] L. Wittevrongel, P. Lava, S.V. Lomov, and D. Debruyne. C^n-continuity in Digital Image Correlation: Implementation and Validation of C^{-1}, C^0 and C^1 Algorithms. *Strain*, 51(6):444–458, 2015. ISSN 1475-1305. doi: 10.1111/str.12156.

[120] G.I. Barenblatt. The mathematical theory of equilibrium cracks in brittle fracture. *Advances in Applied Mechanics*, 7(C):55–129, 1962. doi: 10.1016/S0065-2156(08)70121-2.

[121] M.J. van den Bosch, P.J.G. Schreurs, and M.G.D. Geers. An improved description of the exponential Xu and Needleman cohesive zone law for mixed-mode decohesion. *Engineering Fracture Mechanics*, 73:1220–1234, 2006. doi: 10.1016/j.engfracmech.2005.12.006.

[122] D.S. Dugdale. Yielding of steel sheets containing slits. *Journal of the Mechanics and Physics of Solids*, 8 (2):100–104, 1960. doi: 10.1016/0022-5096(60)90013-2.

[123] A. Hillerborg, M. Moder, and P.-E. Petersson. Analysis of crack formation and crack growth in concrete by means of fracture mechanics and finite elements. *Cement and Concrete Research*, 6(6):773–781, 1976. doi: 10.1016/0008-8846(76)90007-7.

[124] V. Tvergaard and J.W. Hutchinson. On the toughness of ductile adhesive joints. *Journal of the Mechanics and Physics of Solids*, 44(5):789 – 800, 1996. ISSN 0022-5096. doi: 10.1016/0022-5096(96)00011-7.

[125] X.P. Xu and A. Needleman. Void nucleation by inclusion debonding in a crystal matrix. *Modelling and Simulation in Materials Science and Engineering*, 1(2):111, 1993. doi: 10.1088/0965-0393/1/2/001.

[126] G. Alfano. On the influence of the shape of the interface law on the application of cohesive-zone models. *Composites Science and Technology*, 66(6):723–730, 2006. doi: 10.1016/j.compscitech.2004.12.024.

[127] N. Chandra, H. Li, C. Shet, and H. Ghonem. Some issues in the application of cohesive zone models for metalceramic interfaces. *International Journal of Solids and Structures*, 39(10):2827 – 2855, 2002. ISSN 0020-7683. doi: 10.1016/S0020-7683(02)00149-X.

[128] J.H. Rose, J. Ferrante, and J.R. Smith. Universal binding energy curves for metals and bimetallic interfaces. *Phys. Rev. Lett.*, 47:675–678, 1981. doi: 10.1103/PhysRevLett.47.675.

[129] B.A.E. van Hal, R.H.J. Peerlings, M.G.D. Geers, and O. van der Sluis. Cohesive zone modeling for structural integrity analysis of ic interconnects. *Microelectronics Reliability*, 47(8):1251 – 1261, 2007. ISSN 0026-2714. doi: 10.1016/j.microrel.2006.08.017. 2006 ROCS Workshop.

[130] M. Kolluri, J.P.M. Hoefnagels, M. Samimi, J.A.W. van Dommelen, O. van der Sluis, and M.G.D. Geers. An In Situ Experimental-Numerical Approach for Characterization and Prediction of Interface Delamination: Application to CuLF-MCE Systems. *Advanced Engineering Materials*, 14(11):1034–1041, 2012. ISSN 14381656. doi: 10.1002/adem.201200110.

[131] M. Ortiz and A. Pandolfi. Finite-deformation irreversible cohesive elements for three-dimensional crack-propagation analysis. *International Journal for Numerical Methods in Engineering*, 44(9):1267–1282, 1999. ISSN 1097-0207. doi: 10.1002/(SICI)1097-0207(19990330)44:9¡1267::AID-NME486¿3.0.CO;2-7.

[132] M. Kolluri, M.H.L. Thissen, J.P.M. Hoefnagels, J.A.W. van Dommelen, and M.G.D. Geers. In-situ characterization of interface delamination by a new miniature mixed mode bending setup. *International Journal of Fracture*, 158(2):183–195, 2009. doi: 10.1007/s10704-009-9356-1.

[133] A.P. Ruybalid, J.P.M. Hoefnagels, O. van der Sluis, and M.G.D. Geers. Image-based interface characterization with a restricted microscopic field of view. *International Journal of Solids and Structures*, 132-133:218–231, 2018. ISSN 0020-7683. doi: 10.1016/j.ijsolstr.2017.08.020.

[134] M. Samimi, J.A.W. van Dommelen, M. Kolluri, J.P.M. Hoefnagels, and M.G.D. Geers. Simulation of interlaminar damage in mixed-mode bending tests using large deformation self-adaptive cohesive zones. *Engineering Fracture Mechanics*, 109:387–402, 2013. ISSN 0013-7944. doi: 10.1016/j.engfracmech.2012.09.017.

[135] M.J. van den Bosch, P.J.G. Schreurs, and M.G.D. Geers. Identification and characterization of delamination in polymer coated metal sheet. *Journal of the Mechanics and Physics of Solids*, 56(11):3259 – 3276, 2008. ISSN 0022-5096. doi: 10.1016/j.jmps.2008.07.006.

[136] B. Morgan, F. Hild, and S. Roux. On the identifiability of the Hill-1948 model with one uniaxial tensile test. *Strain*, 53(5):e12233–n/a, 2017. ISSN 1475-1305. doi: 10.1111/str.12233.

[137] B. Kolman and D.R. Hill. *Elementary Linear Algebra*. Pearson, 2004.

[138] C. Du, J.P.M. Hoefnagels, L.I.J.C. Bergers, and M.G.D. Geers. A uni-axial nano-displacement micro-tensile test of individual constituents from bulk material. *Experimental Mechanics*, 57(8):1249–1263, 2017. ISSN 1741-2765. doi: 10.1007/s11340-017-0299-6.

[139] D.S. Gianola and C. Eberl. Micro- and nanoscale tensile testing of materials. *Journal of the Minerals, Metals, and Materials society*, 61(3):24, 2009. doi: 10.1007/s11837-009-0037-3.

[140] O. Kraft and C.A. Volkert. Mechanical Testing of Thin Films and Small Structures. *Advanced Engineering Materials*, 3(3):99–110, 2001. ISSN 14381656. doi: 10.1002/1527-2648(200103)3:3¡99::AID-ADEM99¿3.3.CO;2-U.

[141] M.F. Pantano, H.D. Espinosa, and L. Pagnotta. Mechanical characterization of materials at small length scales. *Journal of Mechanical Science and Technology*, 26(2):545–561, 2012. ISSN 1738-494X. doi: 10.1007/s12206-011-1214-1.

[142] M.A. Haque and M.T.A. Saif. A review of MEMS-based microscale and nanoscale tensile and bending testing. *Experimental Mechanics*, 43(3):248–255, 2003. ISSN 0014-4851. doi: 10.1007/BF02410523.

[143] K.J. Hemker and W.N. Sharpe. Microscale Characterization of Mechanical Properties. *Annual Review of Materials Research*, 37(1):93–126, 2007. ISSN 1531-7331. doi: 10.1146/annurev.matsci.36.062705.134551.

[144] V.T. Srikar and S.M. Spearing. A critical review of microscale mechanical testing methods used in the design of microelectromechanical systems. *Experimental Mechanics*, 43(3):238–247, 2003. ISSN 0014-4851. doi: 10.1007/BF02410522.

[145] H.E. Aviles, J.A. Gregory, H.A. Panissidi, and H.E. Wattenbarger. Tri-axial force transducer for a manipulator gripper. *US Patent number: 4478089*, 1984. URL `http://www.freepatentsonline.com/4478089.html`.

[146] S. Hogreve and K. Tracht. Design and implementation of multiaxial force sensing gripper fingers. *Production Engineering*, 8(6):765–772, 2014. doi: 10.1007/s11740-014-0563-x.

[147] H.J. Pandya, J. Sheng, and J.P. Desai. MEMS-based flexible force sensor for tri-axial catheter contact force measurement.

[148] H. Huang, H Zhao, B Wu, S Wan, and C. Shi. A novel two-axis load sensor designed for in situ scratch testing inside scanning electron microscopes. *Sensors (Basel)*, 13(2):2552–65, 2013. doi: 10.3390/s130202552.

[149] Y. Seymen, B. Güler, and M. Efe. Large strain and small-scale biaxial testing of sheet metals. *Experimental Mechanics*, 56(9):1519–1530, 2016. doi: 10.1007/s11340-016-0185-7.

[150] W. O'Brien. *Piezoresistive Sensors Facilitate High-Speed Nanopositioning*. Laurin Publishing, 2003.

[151] A. Arnau and D. Soares. *Fundamentals on Piezoelectricity. In: Arnau Vives A. (eds) Piezoelectric Transducers and Applications*. Springer, Berlin, Heidelberg, 2004.

[152] S. Ozeri and D. Shmilovitz. Static force measurement by piezoelectric sensors. In *2006 IEEE International Symposium on Circuits and Systems*, pages 4 pp.–, 2006. doi: 10.1109/ISCAS.2006.1693799.

[153] J. Liu, X. Luo, J. Liu, M. Li, and L. Qin. Development of a commercially viable piezoelectric force sensor system for static force measurement. *Measurement Science and Technology*, 28(9):095103, 2017. doi: 10.1088/1361-6501/aa7dc0.

[154] M. Lord and D.M. Smith. Static response of a simple piezoelectric load cell. *Journal of Biomedical Engineering*, 5(2):162 – 164, 1983. ISSN 0141-5425. doi: 10.1016/0141-5425(83)90037-7.

[155] S.D. Pekarek. System and method for measuring quasi-static force with a piezoelectric system, 2011. US Patent 7,997,144 B1.

[156] J.-S. Park, H. Chae, H.K. Chung, and S.I. Lee. Thin film encapsulation for flexible am-oled: a review. *Semiconductor Science and Technology*, 26(3):034001, 2011. doi: 10.1088/0268-1242/26/3/034001.

[157] P. van de Weijer, H.B. Akkerman, P.C.P. Bouten, P. Panditha, P.J.M. Klaassen, and A. Salem. Side leakage into the organic interlayer of unstructured hybrid thin-film encapsulation stacks and lifetime implications for roll-to-roll produced organic light-emitting diodes. *Organic Electronics*, 53:256–264, 2018. ISSN 1566-1199. doi: 10.1016/j.orgel.2017.11.019.

[158] A. Bagchi, G.E. Lucas, Z. Suo, and A.G. Evans. A new procedure for measuring the decohesion energy for thin ductile films on substrates. *Journal of Materials Research*, 9(7):1734–1741, 1994. doi: 10.1557/JMR.1994.1734.

[159] S.J. Bull and E.G. Berasetegui. An overview of the potential of quantitative coating adhesion measurement by scratch testing. *Tribology International*, 39(2):99–114, 2006. doi: 10.1016/j.triboint.2005.04.013.

[160] P.J. Burnett and D.S. Rickerby. The relationship between hardness and scratch adhession. *Thin Solid Films*, 154(1):403 – 416, 1987. doi: 10.1016/0040-6090(87)90382-8.

[161] J. Chen and S.J. Bull. Modelling the limits of coating toughness in brittle coated systems. *Thin Solid Films*, 517(9):2945 – 2952, 2009. doi: 10.1016/j.tsf.2008.12.054.

[162] A.G. Evans and J.W. Hutchinson. On the mechanics of delamination and spalling in compressed films. *International Journal of Solids and Structures*, 20(5):455–466, 1984. doi: 10.1016/0020-7683(84)90012-X.

[163] A. Favache, L. Libralesso, P.J. Jacques, J.-P. Raskin, C. Bailly, B. Nysten, and T. Pardoen. Fracture toughness measurement of ultra-thin hard films deposited on a polymer interlayer. *Thin Solid Films*, 550: 464–471, 2014. doi: 10.1016/j.tsf.2013.10.052.

[164] M.D. Kriese, W.W. Gerberich, and N.R. Moody. Quantitative adhesion measures of multilayer films: Part II. indentation of W/Cu, W/W, Cr/W. *Journal of Materials Research*, 14(7):3019–3026, 1999. doi: 10.1557/JMR.1999.0405.

[165] M. Li, C.B. Carter, M.A. Hillmyer, and W.W. Gerberich. Adhesion of polymer-inorganic interfaces by nanoindentation. *Journal of Materials Research*, 16(12):3378–3388, 2001. doi: 10.1557/JMR.2001.0466.

[166] D.B. Marshall and A.G. Evans. Measurement of adherence of residually stressed thin films by indentation. I. mechanics of interface delamination. *Journal of Applied Physics*, 56(10):2632–2638, 1984. doi: 10.1063/1.333794.

[167] S.K. Venkataraman, J.C. Nelson, N.R. Moody, D.L. Kohlstedt, and W.W. Gerberich. Micro-mechanical characterization of tantalum nitride thin films on sapphire substrates. In *Materials Research Society Symposium - Proceedings*, volume 343, pages 587–602, 1994. doi: 10.1557/PROC-343-597.

[168] S. Zhang and X. Zhang. Toughness evaluation of hard coatings and thin films. *Thin Solid Films*, 520(7): 2375 – 2389, 2012. doi: 10.1016/j.tsf.2011.09.036.

[169] S. Raghavan, I. Schmadlak, G. Leal, and S.K. Sitaraman. Mixed-mode cohesive zone parameters for submicron scale stacked layers to predict microelectronic device reliability. *Engineering Fracture Mechanics*, 153:259 – 277, 2016. ISSN 0013-7944. doi: 10.1016/j.engfracmech.2015.12.013.

[170] A.P. Ruybalid, J.P.M. Hoefnagels, O. van der Sluis, M.P.F.H.L. van Maris, and M.G.D. Geers. Mixed-mode cohesive zone parameters from integrated digital image correlation on micrographs only. *International Journal of Solids and Structures*, 156 - 157:179 – 193, 2019. ISSN 0020-7683. doi: 10.1016/j.ijsolstr.2018.08.010.

[171] A.P. Ruybalid, J.P.M. Hoefnagels, O. van der Sluis, and M.G.D. Geers. An *in-situ*, micro-mechanical setup with accurate, tri-axial, piezoelectric force sensing and positioning, 2019. Submitted to journal.

[172] H.B. Akkerman, R.K. Pendyala, P. Panditha, A. Salem, J. Shen, P. van de Weijer, P.C.P. Bouten, S.H.P.M. de Winter, K. van Diesen-Tempelaars, G. de Haas, S. Steudel, C.-Y. Huang, M.-H. Lai, Y.-Y. Huang, M.-H. Yeh, A.J. Kronemeijer, P. Poodt, and G.H. Gelinck. High-temperature thin-film barriers for foldable AMOLED displays. *Journal of the Society for Information Display*, 26(4):214–222, 2018. doi: 10.1002/jsid.647.

[173] S. Harkema, R. K. Pendyala, C.G. Geurts, P.L. Helgers, J.W. Levell, J.S. Wilson, and D. MacKerron. Light management in flexible OLEDs. In *Organic Light Emitting Materials and Devices XVIII*, volume 9183, page 91831H, 2014. doi: 10.1117/12.2061777.

[174] A. Salem, H.B. Akkerman, P. van de Weijer, P.C.P. Bouten, J. Shen, S.H. de Winter, and L.M. Toonen. Thin-film flexible barriers for PV applications and OLED lighting. In *Photovoltaic Specialists Conference (PVSC) 2017 IEEE 43rd*, pages 1661–1663, 2017.

[175] R.J. Visser, L. Moro, X. Chu, J.R. Chen, P. van de Weijer, H.B. Akkerman, S. Graham, M. Söderlund, A. Perrotta, and M.A. Creatore. *Thin Film Encapsulation*, pages 1–51. Springer Japan, 2018. ISBN 978-4-431-55761-6. doi: 10.1007/978-4-431-55761-6_26-1.

[176] O. van der Sluis, T. Vermeij, J. Neggers, J. Vossen, M. van Maris, J. Vanfleteren, M. Geers, and J. Hoefnagels. From Fibrils to Toughness: Multi-Scale Mechanics of Fibrillating Interfaces in Stretchable Electronics. *Materials*, 11(2):231, 2018. doi: 10.3390/ma11020231.

[177] M.L. Benzeggagh and M. Kenane. Measurement of mixed-mode delamination fracture toughness of unidirectional glass/epoxy composites with mixed-mode bending apparatus. *Composites Science and Technology*, 56(4):439 – 449, 1996. doi: 10.1016/0266-3538(96)00005-X.

[178] A. Kuhl and J. Qu. A technique to measure interfacial toughness over a range of phase angles. *Journal of Electronic Packaging, Transactions of the ASME*, 122(2):147–151, 2000. doi: 10.1115/1.483147.

[179] N.A. Warrior, A.K. Pickett, and N.S.F. Lourenço. Mixed-Mode Delamination - Experimental and Numerical Studies. *Strain*, 39(4):153–159, 2003. doi: 10.1046/j.1475-1305.2003.00088.x.

[180] A. Xiao, L. G. Wang, W. D. Van Driel, L. J. Ernst, O. Van Der Sluis, D. G. Yang, and G. Q. Zhang. Characterization and modeling of thin film interface strength considering mode mixity. In *Proceedings - Electronic Components and Technology Conference*, pages 1925–1930, 2007.

[181] M.J. van den Bosch, P.J.G. Schreurs, and M.G.D. Geers. A cohesive zone model with a large displacement formulation accounting for interfacial fibrilation. *European Journal of Mechanics - A/Solids*, 26(1):1 – 19, 2007. ISSN 0997-7538. doi: 10.1016/j.euromechsol.2006.09.003.

[182] O. Rokoš, J.P.M. Hoefnagels, R.H.J. Peerlings, and M.G.D. Geers. On micromechanical parameter identification with integrated DIC and the role of accuracy in kinematic boundary conditions. *International Journal of Solids and Structures*, 146:241–259, 2018. ISSN 0020-7683. doi: 10.1016/j.ijsolstr.2018.04.004.

[183] MCB website. https://www.mcb.eu/en/downloads. Online: accessed 18 July 2017.

APPENDIX A

Single cantilever beam bending experiment

To validate the local boundary condition application method of Chapter 3, a fully-defined test-case with a single cantilever beam is studied. A load, in the form of a fixed mass of 51.3×10^{-3} [kg], is applied to the left end of an aluminum beam (modeled by a point load of 0.503 [N] in the corresponding FE-model), while the right end is clamped (see Figure A.1(a)). The clamped, right-hand side of the specimen is firstly modeled by fixing the corresponding nodes. Subsequently, the strategy as explained in Section 3.5, is employed: the physical boundary conditions are replaced by boundary conditions at the selected nodes, but that do not correspond to the physical application of the boundary conditions. To this end, displacements are first measured by a DIC pre-step in a subregion at the clamped edge (right-hand side in the image), and subsequently the corresponding nodes on the neutral axis of the beam model are kinematically prescribed. The number of prescribed nodes is varied. The length, width and thickness dimensions of the beam are, respectively: $144.5 \times 20.15 \times 1.99$ [mm^3]. In this experiment, the load application falls within the field of view, so the proposed method for applying boundary conditions in a restricted field of view can thereby be properly assessed. The goal is to conduct IDIC to identify Young's modulus E, which is initialized with a value of $E^i = 70$ [GPa]. The results for Young's modulus E are presented in Figure A.1. The Young's modulus of this aluminum alloy (EN AW-6082) has been specified to have the value of $E = 70 \pm 1$ [GPa] [183].

When the clamped side is modeled as a real fixture (fully constraining the corresponding nodes), the identification result is the least accurate (red line). Similar oscillatory behavior of the parameter convergence was also observed in the results for the DCB experiment in Figure 3.3(b) of Section 3.3. Increasing the number of prescribed nodes improves the parameter identification and from these results it is validated that IDIC with a FE-model employing four kinematically prescribed nodes is most accurate, yielding a Young's modulus: $E = 69 \pm 1$ [GPa]. The stated uncertainty is based on the uncertainty of the geometric parameters used in the finite element model, the uncertainty of the applied force (in the form of a calibrated mass), and the uncertainty of measurement of the local boundary conditions by digital image correlation.

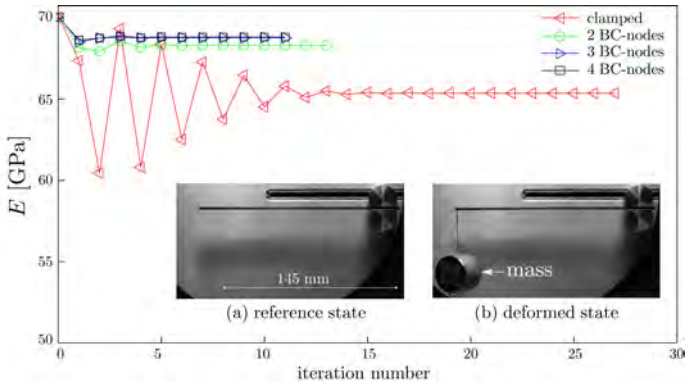

Figure A.1. Results from IDIC on two images (a) and (b) of a single cantilever beam experiment. The number of prescribed nodes at the fixed end (on the right) is varied in the corresponding FE-model.

APPENDIX B

Digital image correlation "pre-step"

The digital image correlation (DIC) "pre-step", used in Chapter 4 to measure the kinematic boundary conditions for the local finite element model, utilizes global 2D polynomial basis functions up to the fourth degree [105]. Results of the DIC pre-step are presented in terms of the remaining image residuals after convergence (expressed in [%] of the dynamic range of the images). Figure B.1 shows two examples of such image residuals for the DIC pre-step conducted on the top-right subregion (see Figure 4.4) of images of virtually deformed artificial speckle patterns with different pixel resolutions. Using the images described in

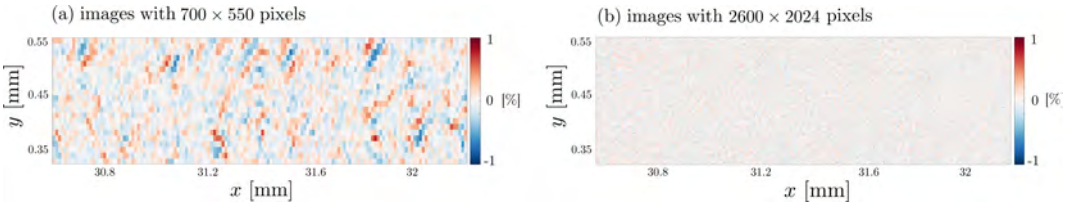

Figure B.1. Residual fields of the DIC pre-step on the top-right subregion (see Figure 4.4) of images with different pixel resolutions. The fields shown here are the residuals between the reference image and the final image (final time increment).

Section 4.2.2, with 700 × 550 pixels, relatively large image residual fields remain after convergence of the DIC pre-step. The residual artifacts seen in Figure B.1(a) indicate that the corresponding DIC pre-step is too inaccurate for boundary condition extraction (discussed below). In a separate virtual test-case with artificially rotated images, similar artifacts were observed in the image residual fields (not shown). Various global DIC-routines with different image interpolation schemes were tested, yielding the conclusion that such residual artifacts are caused by interpolation errors and can be diminished by increasing the pixel resolution [96, 100, 101], effectively increasing the number of pixels per speckle pattern feature. When the pixel resolution was increased to images comprising 2600 × 2024 pixels, the image residuals of the DIC pre-step were significantly reduced, see Figure B.1(b).

Since the simulated displacements are of great importance for the accuracy of the IDIC-routine, the errors on the simulated displacements due to inaccuracies in the DIC pre-step are quantified and investigated. To this end, the error fields ϵ_{h_x} and ϵ_{h_y} between the nodal

displacements h_x and h_y simulated by the virtual experiment (VE) and the local finite element model with local boundary conditions measured by the DIC pre-step are evaluated. This is done for the spatial domain corresponding to the region of interest that will be used for IDIC (see the IDIC ROI in Figure 4.4). The two cases with the low resolution images of 700 × 550 pixels and the high resolution images of 2600 × 2024 pixels are compared. The difference fields are calculated as follows:

$$\epsilon_{h_x} = h_{x,\mathrm{VE}} - h_{x,\mathrm{local}}, \tag{B.1}$$

$$\epsilon_{h_y} = h_{y,\mathrm{VE}} - h_{y,\mathrm{local}}, \tag{B.2}$$

and are subsequently divided by the pixel size: 10.7 [μm] for the low resolution images and 2.7 [μm] for the high resolution images, in order to evaluate the difference fields in terms of pixels [px]. The difference fields are shown in Figure B.2 for three time increments t and for a single y-cross-section for all (thirty) time increments. These results confirm that when

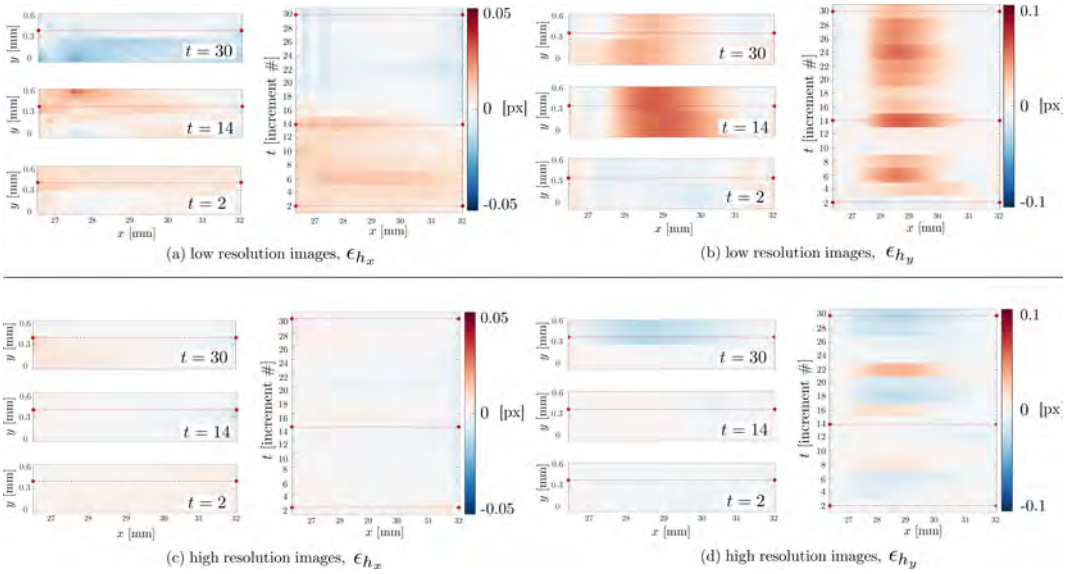

Figure B.2. The x- and y-components of the displacement difference fields from the virtual experiment and the finite element simulation with local boundary conditions extracted from low resolution (a)-(b) and high resolution (c)-(d) images. The error fields are shown for three time increments, and for a single y-cross-section for all time increments.

high resolution images are used for the DIC pre-step, the resulting error in the displacement with respect to the reference displacement from the virtual experiment is smaller than when low resolution images are used. Besides the interpolation errors improving, the DIC pre-step accuracy, typically ~ 0.01 [px] [45, 96], is determined by the pixel size and is improved in the case of smaller pixels. The average of the displacement errors in Figures B.2(c)-(d) for the case of high resolution images is 5.4×10^{-3} [px], which corresponds to 15 [nm].

Word of thanks

Like many others, I'm sure, I've experienced my Ph.D.-project as a long climb up the intellectual mountain, with few vantage points, many near-vertical parts, and numerous overhanging cliffs that block the view of the treacherous path that lies ahead. Although the actual hike must be ventured alone, the summit can't be reached without the guidance and support of others. I would like to take this opportunity to express my gratitude to the wonderful people around me.

To my promotor Marc Geers: thank you for keeping a clear overview of the road map, for providing advice at the right moments as to which route to take, and for teaching me the crucial importance of constant, critical reflection.

To my supervisor Olaf van der Sluis: many thanks for your efforts in sharing your expertise in computational modeling and numerical simulations, and for acknowledging my struggles and providing reassurance during more difficult times.

To my supervisor Johan Hoefnagels: thanks for showing me your exquisitely keen way of putting scientific research into perspective, and for always keeping your door open, even when you were out of the office. I am extremely grateful for your readiness to assist me at the most critical times: writing and revising papers together at 2 o'clock in the morning, when submission deadlines demanded our close collaboration in order to achieve our ambitious goals, even when they seemed impossible until the very end of the climb. Your faith in me and in our research, together with your openness during discussion have contributed to the most supporting supervision I could have wished for.

To our lab technician Marc van Maris: thank you for sharing your extremely valuable experimental expertise. It has aided my development in out-of-the-box thinking and practical skills. Without proper gear and practical training the steep slopes of the mountain cannot be overcome. You are a PhD.-student's lifeline in experimental science, providing confidence during our climb and catching us when we fall.

To my friends from various offices and the Multi-Scale lab: thank you for your companionship, and for providing the essential stress-outlets in the form of intense foosball games and nights out. In particular, I would like to thank Tom de Geus and Jan Neggers for all your practical help, even when you were extremely busy yourselves. Siavash: thank you for your openness, and for the warm discussions about the mystertrees of life. Franz and Maxime: thanks for your friendship and for all the fun times we shared during our salsa dancing period. Tarek, Prakhyat, and Varun, thanks for all the healthy breaks you've shared with me.

To my trusted friend Salman: thanks for your brotherhood during our studies and scientific adventures. When feeling demotivated I only had to look over my shoulder to see you bravely climbing your own mountain besides mine, which gave me the comforting realization that I did not have to walk alone.

To The Hot Jalapeños: thanks for providing me with the feeling of being part of a tight group of friends, on which I can always count.

To my cousin Maik: thank you for sharing your philosophical views and associated questions. Our discussions have been highly inspiring to me and have helped me understand my view on the world (including this project).

To Kirsten: thank you for helping me shape my values as a person, in particular during the first few years of this PhD.-project, which has majorly contributed to growing up and maturing into a researcher.

To Ron van den Bergh: thank you for the thought-provoking trips we took together, lightening the final stretch of my climb. Your structured way of thinking is something I strongly value, and which has provided me with new insights and tools to explore and develop.

To mom and dad: thank you for your unconditional love and support in various forms, for keeping faith, and for reminding me that hard work does pay off in the end. Your love, comfort, and wisdom have allowed me to grow into the person I am today, and like a great safety net at the foot of the mountain, they provide the confidence that I need to take on any challenge that lies ahead.

To my dearest Fleur: thank you for the privilege of receiving all your warmth, for your heartfelt love, and for your willingness to help and support me in every possible way. Your view on appreciating life by being conscious and thankful for the things that make you happy, no matter how small, while staying true to your heart's compass, inspires me every day. You are my highest ambition, and I believe I can climb any mountain, no matter how steep, together with you.

Andre
Veldhoven, April 2019

Curriculum vitae

Andre Ruybalid was born on October 26$^{\text{th}}$, 1987, in Farmington, New Mexico, U.S.A. He finished secondary school (VWO) in 2006 at St.-Janscollege in Heerlen, the Netherlands, after which he enrolled in the Bachelor program of Mechanical Engineering at Eindhoven University of Technology in the Netherlands. Continuing his education, he enrolled in the Master program of Mechanical Engineering at the same university. As part of his curriculum he completed a traineeship in the group of Dr. Michelle Dickinson at the University of Auckland, New Zealand, on "Characterization of the mechanical properties of leptin receptor-deficient mice vertebrae, using nanoindentation tests". In 2013, he obtained his MSc.-degree *with great appreciation* within the Mechanics of Materials group of Professor Marc Geers, with his thesis entitled "A novel bending test methodology for the investigation of mechanical failure behavior of flexible electronics". In the same year, he started his PhD.-research project entitled "In-situ identification of interface properties within 3D microelectronic devices" within the same group, under the supervision of Professor Marc Geers, Dr. Johan Hoefnagels, and Dr. Olaf van der Sluis, of which the results are presented in this dissertation. As part of the program he completed the graduate school of Engineering Mechanics. In 2014 he was awarded the prize for *best presentation* at the symposium of this graduate school and received the *best poster award* at the same symposium in the year of 2015.

List of publications

Journal publications (this thesis)

A.P. Ruybalid, O. van der Sluis, M.G.D. Geers and J.P.M. Hoefnagels. Full-field identification of mixed-mode adhesion properties in a flexible, multi-layer microelectronic material system. *Submitted to journal (2019).*

A.P. Ruybalid, J.P.M. Hoefnagels, O. van der Sluis and M.G.D. Geers. An *in-situ*, micromechanical setup with accurate, tri-axial, piezoelectric force sensing and positioning. *Submitted to journal (2019).*

A.P. Ruybalid, J.P.M. Hoefnagels, O. van der Sluis, M.P.F.H.L. van Maris and M.G.D. Geers (2019). Mixed-mode cohesive zone parameters from integrated digital image correlation on micrographs only. *International Journal of Solids and Structures*, 156-157, pp. 179-193, doi: 10.1016/j.ijsolstr.2018.08.010.

A.P. Ruybalid, J.P.M. Hoefnagels, O. van der Sluis and M.G.D. Geers (2018). Image-based interface characterization with a restricted microscopic field of view. *International Journal of Solids and Structures*, 132-133, pp. 218-231, doi: 10.1016/j.ijsolstr.2017.08.020.

A.P. Ruybalid, J.P.M. Hoefnagels, O. van der Sluis and M.G.D. Geers (2016). Comparison of the identification performance of conventional FEM-updating and integrated DIC. *International Journal for Numerical Methods in Engineering*, 106(4), pp. 298-320, doi: 10.1002/nme.5127.

Journal publications (other)

J.P.M. Hoefnagels, A.P. Ruybalid and C.A. Buizer (2015). A small-scale, contactless, pure bending device for in-situ testing. *Experimental Mechanics*, 55(8), pp. 1511-1524, doi: 10.1007/s11340-015-0046-9.

S.M. Kleinendorst, J.P.M. Hoefnagels, C.V. Verhoosel and A.P. Ruybalid (2015). On the use of adaptive refinement in isogeometric digital image correlation. *International Journal for Numerical Methods in Engineering*, 104(10), pp. 944-962, doi: 10.1002/nme.4952.

Book chapter

O. van der Sluis, B.G. Vossen, J. Neggers, A.P. Ruybalid, K. Chockalingam, R.H.J. Peerlings, J.P.M. Hoefnagels, J.J.C. Remmers, V. Kouznetsova, P.J.G. Schreurs and M.G.D. Geers (2017). *Advances in delamination modeling of metal/polymer systems: continuum aspects. In J. Morris (Ed.), Nanopackaging.* Dordrecht: Springer, doi: 10.1007/978-3-319-90362-0_3.

Conference proceedings

S.M. Kleinendorst, B.J. Verhaegh, J.P.M. Hoefnagels, A.P. Ruybalid, O. van der Sluis and M.G.D. Geers (2018). On the boundary conditions and optimization methods in integrated digital image correlation. In M.-T. Lin, C. Sciammarella, L. Lamberti and C. Furlong (Eds.), *Advancement of Optical Methods in Experimental Mechanics, Volume 3 (pp. 55-61). (Conference Proceedings of the Society for Experimental Mechanics Series book series (CPSEMS))*. Dordrecht: Springer, doi: 10.1007/978-3-319-63028-1_9.

J.P.M. Hoefnagels, S.M. Kleinendorst, A.P. Ruybalid, C.V. Verhoosel and M.G.D. Geers (2017). Self-adaptive isogeometric global digital image correlation and digital height correlation. In S. Yoshida, C. Sciammarella and L. Lamberti (Eds.), *Advancement of Optical Methods in Experimental Mechanics - Proceedings of the 2016 Annual Conference on Experimental and Applied Mechanics (pp. 165-172). (Conference Proceedings of the Society for Experimental Mechanics Series).* Springer, doi: 10.1007/978-3-319-41600-7_20.

A.P. Ruybalid, J.P.M. Hoefnagels, O. van der Sluis and M.G.D. Geers (2017). Full-field identification methods: comparison of FEM updating and integrated DIC. In S. Yoshida, C. Siammarella and L. Lamberti (Eds.), *Advancement of Optical Methods in Experimental Mechanics, Volume 3 (pp. 191-197). (Conference Proceedings of the Society for Experimental Mechanics Series, No. 2017).* Dordrecht: Springer, doi: 10.1007/978-3-319-41600-7_24.

A.P. Ruybalid, J.P.M. Hoefnagels, O. van der Sluis and M.G.D. Geers (2017). Full-field identification of interfaces in microelectronic devices. In J. Hay, N. Karanjgaokar and L.V. Starman (Eds.), *Micro and Nanomechanics, Volume 5 (pp. 9-13). (Conference Proceedings of the Society for Experimental Mechanics Series, No. 2017).* Dordrecht: Springer, doi: 10.1007/978-3-319-42228-2_2.

A.P. Ruybalid, J.P.M. Hoefnagels, O. van der Sluis and M.G.D. Geers (2016). Performance assessment of integrated digital image correlation versus FEM updating. *Conference Proceedings of the Society for Experimental Mechanics Series (pp. 11-15).* Springer, doi: 10.1007/978-3-319-21765-9_2.